

VERTEX MODELS ON RANDOM GRAPHS

Von der Fakultät für Physik und Geowissenschaften
der Universität Leipzig

genehmigte

D I S S E R T A T I O N

zur Erlangung des akademischen Grades

doctor rerum naturalium

(Dr. rer. nat.)

vorgelegt

von *Diplom-Physiker Martin Weigel*

geboren am *6. September 1972* in *Neustadt a. d. Weinstraße*

Gutachter: *Prof. Dr. W. Janke, Universität Leipzig*

Prof. Dr. D. A. Johnston, HW University, Edinburgh

Prof. Dr. B. Petersson, Universität Bielefeld

Tag der Verleihung: *21. Oktober 2002*

Bibliographische Beschreibung

Weigel, Martin

Vertex Models on Random Graphs

Universität Leipzig, Dissertation

290 S., 279 Lit., 92 Abb., 24 Tab.

Referat

Diese Arbeit befaßt sich mit der Koppelung von Vertex-Modellen an die planaren ϕ^4 -Zufallsgraphen des Zugangs zur Quantengravitation über dynamische Polygonifizierungen. Das betrachtete System hat eine doppelte Bedeutung, einerseits als die Koppelung einer konformen Feldtheorie mit zentraler Ladung $C = 1$ an zweidimensionale Euklidische Quantengravitation, andererseits als Anwendung von geometrischer, “annealed” Unordnung auf ein prototypisches Modell der statistischen Mechanik. Da das Modell mit Hilfe einer großangelegten Reihe von Monte Carlo Simulationen untersucht wird, müssen entsprechende Techniken für die Simulation von dynamischen Quadrangulierungen bzw. die dualen ϕ^4 -Graphen entwickelt werden. Hierzu werden verschiedene Algorithmen und die dazugehörigen Züge vorgeschlagen und hinsichtlich ihrer Ergodizität und Effizienz untersucht. Zum Vergleich mit exakten Ergebnissen werden die Verteilung der Koordinationszahlen bzw. bestimmte Analoga davon konstruiert. Für Simulationen des F -Modells auf ϕ^4 -Zufallsgraphen wird ein Ordnungsparameter für den antiferroelektrischen Phasenübergang mit Hilfe einer Plakettenspindarstellung formuliert. Ausführliche “finite-size scaling”-Analysen des Kosterlitz-Thouless-Phasenübergangs des F -Modells auf dem Quadratgitter und auf Zufallsgraphen werden vorgestellt und die Positionen der jeweiligen kritischen Punkte sowie die dazugehörigen kritischen Exponenten werden bestimmt. Die Rückreaktion des Vertex-Modells auf die Zufallsgraphen wird in Form der Koordinationszahlverteilung, der Verteilung der “Baby-Universen” und dem daraus resultierenden String-Suszeptibilitäts-Exponenten sowie durch die geometrische Zweipunktfunktion analysiert, die eine Schätzung der intrinsischen Hausdorff-Dimension des gekoppelten Systems liefert.

Bibliographic Information

Weigel, Martin

Vertex Models on Random Graphs

Universität Leipzig, Dissertation

290 p., 279 ref., 92 fig., 24 tab.

Abstract

In this thesis, the coupling of ice-type vertex models to the planar ϕ^4 random graphs of the dynamical polygonifications approach to quantum gravity is considered. The investigated system has a double significance as a conformal field theory with central charge $C = 1$ coupled to two-dimensional Euclidean quantum gravity and as the application of a special type of annealed connectivity disorder to a prototypic model of statistical mechanics. Since the model is analyzed by means of large-scale Monte Carlo simulations, suitable simulation techniques for the case of dynamical quadrangulations and the dual ϕ^4 random graphs have to be developed. Different algorithms and the associated update moves are proposed and investigated with respect to their ergodicity and performance. For comparison to exact results, the co-ordination number distribution of the dynamical polygonifications model, or certain analogues of it, are constructed. For simulations of the 6-vertex F model on ϕ^4 random graphs, an order parameter for its anti-ferroelectric phase transitions is constructed in terms of a “plaquette spin” representation. Extensive finite-size scaling analyses of the Kosterlitz-Thouless point of the square-lattice and random graph F models are presented and the locations of the critical points as well as the corresponding critical exponents are determined. The back-reaction of the coupled vertex model on the random graphs is investigated by an analysis of the co-ordination number distribution, the distribution of “baby universes” and the string susceptibility exponent as well as the geometric two-point function, yielding an estimate for the internal Hausdorff dimension of the coupled system.

Contents

1	Introduction	1
2	The DTRS Approach to Quantum Gravity	7
2.1	Path Integrals and Geometric Theories	7
2.1.1	Path integrals and quantum paths	7
2.1.2	Random surfaces and strings	9
2.1.3	Quantum gravity	10
2.1.4	The case of two dimensions	13
2.2	Simplicial Quantum Gravity	14
2.2.1	Random walks and the Wiener measure	14
2.2.2	Discretising quantum gravity	16
2.2.3	Dynamical triangulations and the discretised action	19
2.3	Analytical Results for the Discretised Theory	24
2.3.1	Existence of the discretised partition function	25
2.3.2	String susceptibility, mass gap and string tension	27
2.3.3	The combinatorial solution	30
2.3.4	Matrix models	33
2.3.5	Fractal structure of the lattices	36
2.3.6	Further results and the transfer matrix	40

2.3.7	The continuum limit	42
2.4	Dressing Dynamical Triangulations	44
2.4.1	Annealed and quenched disorder	44
2.4.2	The KPZ/DDK solution	46
2.4.3	Matrix model examples	49
3	The Simulation of Dynamical Graphs	51
3.1	Graph Ensembles	52
3.1.1	Triangulations and ϕ^3 graphs	52
3.1.2	Quadrangulations and ϕ^4 graphs	55
3.2	Simulation of Dynamical Polygonifications	57
3.2.1	Moves and ergodicity	58
3.2.2	Detailed balance and pseudo grand-canonical simulations	62
3.2.3	Generalization to quadrangulations	64
3.2.4	Necessary checks and implementation details	68
3.3	The Co-Ordination Number Distribution	74
3.3.1	Counting planar graphs	75
3.3.2	Comparison to simulation results	83
3.4	The Two-Link Flip for ϕ^4 Graphs	91
3.5	Enhancing the Efficiency	96
3.5.1	Autocorrelation times	96
3.5.2	The baby-universe surgery method	103
4	Vertex Models and Their Simulation	112
4.1	Square-Lattice Vertex Models	113
4.1.1	Definition and basic properties	113

4.1.2	Exact solution of the zero-field cases	116
4.1.3	Transformations and specializations	121
4.2	The Loop Algorithm	124
4.2.1	Idea and outline	125
4.2.2	Choice of the breakup probabilities	128
4.2.3	Practical application and tests	131
4.3	Vertex Models on Random ϕ^4 Graphs	135
4.3.1	Additional symmetry	135
4.3.2	The order parameter	137
4.3.3	Implementation of the simulation scheme	142
5	The 6-Vertex Model on Random ϕ^4 Graphs	147
5.1	Analytical Results	148
5.1.1	The case of regular lattices	148
5.1.2	Vertex models coupled to quantum gravity	151
5.2	The Anti-Ferroelectric Phase Transition	156
5.2.1	Scaling at an infinite order phase transition	157
5.2.2	The square-lattice F model	159
5.2.3	The F model on planar ϕ^4 random graphs	172
5.3	Dynamical Scaling and Autocorrelation Times	199
5.3.1	Local update	200
5.3.2	Surgery update	206
5.4	Geometrical Properties	210
5.4.1	The co-ordination number distribution	211
5.4.2	The string susceptibility exponent	216
5.4.3	The Hausdorff dimension	226

6	Conclusions and Outlook	240
A	Methods of Simulation and Data Analysis	246
A.1	The Monte Carlo Process	246
A.1.1	Simple sampling	246
A.1.2	Importance sampling	247
A.2	Autocorrelations and Dynamical Scaling	249
A.3	Binning and the Jackknife	252
A.3.1	The binning technique	252
A.3.2	Jackknife bias and variance estimates	253
A.4	Estimation of Autocorrelation Times	257
A.5	Histogram Reweighting	260
B	Graph Embedding and Visualization	263
	Bibliography	266
	Acknowledgements	289
	Curriculum Vitae	290

List of Figures

2.1	A small patch of a random triangulation embedded in the plane	17
2.2	0-, 1-, 2- and 3-simplices.	19
2.3	Excess and deficit angles of a geodesic triangle	22
2.4	Visualization of a two-dimensional dynamical triangulation with 5000 triangles — smooth example	25
2.5	The generation of dynamical triangulations by matrix models	34
2.6	Visualization of a two-dimensional dynamical triangulation with 5000 triangles — “fractal” example	37
3.1	Self-energy contributions in triangulations	52
3.2	Tadpole contributions in triangulations	53
3.3	Singular contributions in quadrangulations	55
3.4	A double link in a ϕ^4 graph	56
3.5	Alexander moves for triangulations	59
3.6	The (k, l) moves in two dimensions	60
3.7	One-link flip move for quadrangulations	65
3.8	Ways of breakup for ϕ^4 vertices	66
3.9	Insertion and deletion moves for quadrangulations	68
3.10	Touching link test	70
3.11	Uniquely connected test	71

3.12	Double link test	72
3.13	Insertion technique for the co-ordination number distribution	77
3.14	Co-ordination numbers for Poissonian and QG random lattices	79
3.15	Insertion technique for quadrangulations	83
3.16	Co-ordination number distribution for dynamical triangulations	84
3.17	Co-ordination number distribution for singular triangulations	85
3.18	Partition function ratios for dynamical triangulations	86
3.19	Partition function ratios for dynamical triangulations and incomplete exclusion of singularities	87
3.20	Co-ordination number distribution of dynamical quadrangulations	89
3.21	Partition function ratios for dynamical quadrangulations (one-link flip only)	90
3.22	Necessity of the two-link flip for quadrangulations	92
3.23	Partition function ratios for dynamical quadrangulations (one- and two-link flip)	93
3.24	Specific heat of an Ising model on dynamical ϕ^4 graphs	95
3.25	Finite-size scaling of autocorrelation times for the link-flip dynamics	101
3.26	Integrated autocorrelation times associated with the co-ordination number distribution of ϕ^3 graphs	102
3.27	A minBU surgery step on a dynamical ϕ^3 graph	104
3.28	Finding the minBU necks containing a given link of the graph	105
3.29	Finite-size scaling of autocorrelation times for the minBU surgery dynamics	110
4.1	Arrow configurations of the 6-vertex model	114
4.2	Additional arrow configurations of the 8-vertex model	115
4.3	The worldline representation for vertex models	116
4.4	The phase diagram of the 6-vertex model	117

4.5	Ferroelectric and anti-ferroelectric ground states of the 6-vertex model	118
4.6	The worldline representation of the XYZ quantum chain	123
4.7	Vertex breakups of the loop algorithm	126
4.8	A loop cluster for the 6-vertex model	127
4.9	Loop-algorithm simulation of a 4×4 F model — thermal averages . .	133
4.10	Loop-algorithm simulation of a 4×4 F model — autocorrelation times	134
4.11	The phase diagram of the 8-vertex generalized F model	137
4.12	Internal energy of the KDP model on random ϕ^4 graphs	138
4.13	Transformation of the 6-vertex model to a spin model on the dual lattice	139
4.14	Anti-ferroelectric ground state in the plaquette spin representation . .	141
4.15	Insertion moves for the 6-vertex model on ϕ^4 graphs	145
5.1	Loop gas representation of the F model	152
5.2	Example of a loop gas configuration on a random ϕ^4 graph	153
5.3	Specific heat of the square-lattice F model	162
5.4	Peak locations of the polarizability of the square-lattice F model . . .	164
5.5	Peak locations of the polarizability of the square-lattice F model — log-log corrections	167
5.6	FSS of the critical polarizability of the square-lattice F model	168
5.7	Peaks of the polarizability of the square-lattice F model	170
5.8	Thermal scaling of the polarizability of the square-lattice F model . .	171
5.9	Specific heat of the F model on planar ϕ^4 random graphs	173
5.10	Peak locations of the polarizability of the F model on planar ϕ^4 ran- dom graphs	174
5.11	Constrained fits to the peak locations of the polarizability of the F model on planar ϕ^4 random graphs	177

5.12 FSS of the peak locations of the polarizability of the F model on singular ϕ^4 random graphs	179
5.13 FSS of the mean square extents of the F model on the square lattice and on ϕ^4 random graphs	180
5.14 Comparison of scaling corrections for the square-lattice and ϕ^4 graph F models	181
5.15 Temperature dependence of the internal energy of the square-lattice and random graph F models	184
5.16 FSS of the peak heights of the polarizability of the F model on ϕ^4 random graphs	188
5.17 FSS of the polarizability at $\beta = \ln 2$ of the F model on ϕ^4 random graphs	190
5.18 FSS of the spontaneous polarization at the peak locations of the polarizability of the F model on ϕ^4 random graphs	192
5.19 FSS of the spontaneous polarization at the asymptotic critical coupling $\beta = \ln 2$ of the F model on ϕ^4 random graphs	193
5.20 Peaks of the polarizability of the F model on ϕ^4 random graphs	194
5.21 Thermal scaling of the polarizability of the F model on ϕ^4 random graphs	196
5.22 Configuration snapshots of the F model coupled to ϕ^4 random graphs — high-temperature phase	197
5.23 Configuration snapshots of the F model coupled to ϕ^4 random graphs — low-temperature phase	198
5.24 Integrated autocorrelation times of the mean square extent of pure ϕ^4 random graphs and of ϕ^4 graphs coupled to the F model	202
5.25 Integrated autocorrelation times of the mean square extent of ϕ^4 random graphs coupled to the F model — local update	203
5.26 Integrated autocorrelation times of the internal energy of the F model coupled to ϕ^4 random graphs — local update	204

5.27	Integrated autocorrelation times of the spontaneous polarization of the F model coupled to ϕ^4 random graphs — local update	205
5.28	Integrated autocorrelation times of the F model coupled to ϕ^4 random graphs as a function of the inverse temperature — local update	207
5.29	Integrated autocorrelation times of the mean square extent of ϕ^4 random graphs coupled to the F model — global update	208
5.30	Integrated autocorrelation times of the spontaneous polarization of the F model coupled to ϕ^4 random graphs — global update	210
5.31	Integrated autocorrelation times of the spontaneous polarization of the F model coupled to ϕ^4 random graphs as a function of the inverse temperature — global update	211
5.32	Co-ordination number distribution of ϕ^4 random graphs coupled to the F model	212
5.33	Fraction of loops of length two of ϕ^4 random graphs coupled to the F model as a function of the inverse temperature	213
5.34	Inverse pseudo-critical temperatures defined by the maximum of the fraction of loops of length two of ϕ^4 graphs coupled to the F model	215
5.35	Distribution of minBUs of the dynamical quadrangulations model with $N_2 = 1024$ quadrangles	219
5.36	String susceptibility exponent of ϕ^4 random graphs coupled to the F model as a function of the inverse temperature	222
5.37	String susceptibility exponent of the F model on ϕ^4 random graphs in the critical phase as a function of the graph size	225
5.38	Example of the geometrical two-point function for pure ϕ^4 random graphs	227
5.39	FSS plots of the peak positions and heights of the two-point function of pure ϕ^4 random graphs	228
5.40	Mean extent of ϕ^4 random graphs coupled to the F model as a function of the inverse temperature	229
5.41	Collapse of the re-scaled two-point functions of ϕ^4 random graphs coupled to the F model at $\beta = 0.2$	238

B.1 Adaptive unification of edge lengths 265

List of Tables

3.1	Critical values μ_0 for the dynamical polygonifications model	57
3.2	Integrated autocorrelation times for the link-flip dynamics for ϕ^4 graphs	99
3.3	Integrated autocorrelation times for the mixed dynamics for ϕ^4 graphs	109
5.1	Fit results for the peak locations of the polarizability of the square-lattice F model	163
5.2	Fit results for the peak locations of the polarizability of the square-lattice F model — corrections	165
5.3	Fit results for the peak locations of the polarizability of the F model on ϕ^4 random graphs	175
5.4	Fit results for the peak locations of the polarizability of the F model on ϕ^4 random graphs — corrections	176
5.5	Fit results for the peak heights of the polarizability of the F model on ϕ^4 random graphs	187
5.6	Fit results for the polarizability of the F model on ϕ^4 random graphs at $\beta = \ln 2$	189
5.7	Fit results for the spontaneous polarization of the F model on ϕ^4 random graphs	191
5.8	Integrated autocorrelation times of the mean square extent of ϕ^4 random graphs coupled to the F model for the link-flip dynamics	201
5.9	Integrated autocorrelation times of the spontaneous polarization for the link-flip and combined link-flip/surgery dynamics for the F model on ϕ^4 graphs	209

5.10	Maxima of the fraction of two-loops of ϕ^4 graphs coupled to the F model	214
5.11	Influence of the lower cut-off B_{\min} on the fit results for the minBU distribution for pure ϕ^4 graphs with $N_2 = 1024$ sites	220
5.12	Parameters of fits to the distribution of minBUs for pure ϕ^4 random graphs	221
5.13	Parameters of fits to the distribution of minBUs for the F model coupled to ϕ^4 random graphs at $\beta = 1.4$	223
5.14	Parameters of fits to the distribution of minBUs for the F model coupled to ϕ^4 random graphs at $\beta = \ln 2$	224
5.15	Parameters of FSS fits to the peak locations of the geometrical two-point function of ϕ^4 graphs coupled to the F model at $\beta = 0.2$	230
5.16	Parameters of fits to the peak locations and heights of the two-point function of ϕ^4 graphs coupled to the F model at $\beta = 0.2$, $\beta = \ln 2$ and $\beta = 1.4$	231
5.17	Parameters of improved fits to the peak locations of the two-point function of ϕ^4 graphs coupled to the F model at $\beta = 0.2$, $\beta = \ln 2$ and $\beta = 1.4$	232
5.18	Fit parameters for the scaling of the mean extent of pure ϕ^4 random graphs	234
5.19	Estimates for the shift and Hausdorff dimension of pure ϕ^4 random graphs	235
5.20	Parameters of fits to the mean extent of ϕ^4 graphs coupled to the F model at $\beta = 0.2$, $\beta = \ln 2$ and $\beta = 1.4$	236
5.21	Parameters of improved fits to the mean extent of ϕ^4 graphs coupled to the F model at $\beta = 0.2$, $\beta = \ln 2$ and $\beta = 1.4$	237

Chapter 1

Introduction

The construction of a quantum theory of gravity is one of the fundamental open questions in theoretical physics. Einstein gravity being perturbatively non-renormalizable as a field theory, this problem calls for novel, non-perturbative approaches. As it has turned out in the past few years, the investigation of fluctuating, multi-dimensional manifolds is a promising theoretical framework for this task. Ambitious approaches in this direction include the theories of strings, branes etc. [1]. Despite their success, however, these theories have severe problems of projecting the results of the involved high-dimensional models back to the physical four-dimensional space-time.

Starting from early ideas about the formulation of a *discretised* theory of quantum gravity [2], the introduction of the framework of *dynamical triangulations* by Ambjørn *et al.* [3], David [4] and Kazakov *et al.* [5] has led to a successful theory of Euclidean quantum gravity, for reviews see [6–12]. Although the model can be formulated for an arbitrary number of dimensions, the focus of the analytical and most of the numerical work in the field has been — mostly for technical reasons — put on the exploration of the properties of the two-dimensional model. The dynamical triangulations scheme starts out with the formal attempt to quantize the Einstein-Hilbert action of general relativity with the path-integral method. The thus formulated prescription to integrate over all possible choices of the metric tensor consistent with certain constraints or, equivalently, over a suitable class of *random (hyper-)surfaces* is replaced by a sum over discretised approximations of such surfaces in order to regularize the considered path integral. In the dynamical triangulations approach, these discrete surfaces are taken to be *simplicial* or *combinatorial manifolds* [13,14], i.e., surfaces glued together from simplicial building blocks subject to certain reg-

ularity constraints. For the case of two dimensions these surfaces are nothing but random triangulations composed of equilateral triangles. In this way, the problem of Euclidean quantum gravity is reduced to a combinatorial one.

For the case of two dimensions, the resulting random-surface model can be explicitly solved to a quite complete degree. The summation over the triangulations can be performed, alternatively, by early developed graph-theoretical methods for the counting of triangulations [15], or by exploiting the equivalence of this counting problem to a perturbative expansion of certain *matrix integrals* [16–18] originally considered in the context of the planar approximation to QCD [19], which count the orientable, “fat” ϕ^3 graphs dual to the triangulations. For an excellent review of the methods applied in this context see Ref. [10]. Apart from that, a numerical treatment of the model is possible via Monte Carlo simulations of the fluctuating surfaces [20–22]. Applying these methods, the model is found to exhibit a continuous phase transition as a function of the fugacity controlling the number of triangles and the corresponding continuum limit, corresponding to a diverging size of the triangulations, coincides with the *Liouville theory* of two-dimensional Euclidean quantum gravity [6, 23, 24]; however, the information that can be extracted from the discrete dynamical triangulations model goes beyond that of the continuum Liouville theory. The critical exponents governing the scaling in the vicinity of this phase transition can be determined exactly [10, 16, 25–28]. A key point in the understanding of the properties of the model is given by the finding that the occurring triangulations can be considered as *self-similar fractals*, composed of “baby universes” attached to the main body of the lattice via a small number of links, i.e., via “bottlenecks” [29]. The corresponding fractal or Hausdorff dimension is found to be $d_h = 4$ [26–28], thus largely exceeding the topological dimension two of the model.

The continuum theory predicts a renormalization of the critical exponents of conformal minimal matter with central charge $0 \leq C < 1$ coupled to the Liouville field expressed by the KPZ/DDK formula [30–32]. In the discrete framework of the dynamical triangulations approach, a decoration of the lattice with matter variables can be conveniently expressed in terms of suitably adapted matrix models. Some of the resulting integrals could be explicitly performed, including the cases of the Ising model [33–35], the q -states Potts model [36–39] and the $O(n)$ loop model [40–44] coupled to two-dimensional discrete, Euclidean quantum gravity. These and further models have been analyzed numerically via Monte Carlo simulations of the combined system of dynamical triangulations and coupled matter variables, see, e.g.

Refs. [45–52]. The critical exponents resulting from all these model studies coincide with those predicted by the KPZ formula. The KPZ/DDK solution breaks down for central charge $C > 1$, such that for this region the information about the theory is still rather incomplete. Speculations about the behaviour of the dynamical triangulations model on crossing this “ $C = 1$ barrier” have caused quite some discussions [53, 54]. For $C \rightarrow \infty$ the geometry of the model is known to collapse to a *branched polymer* phase, i.e., to configurations of planar tree graphs [53] with Hausdorff dimension $d_h = 2$. However, the breakdown of the model for $C > 1$ is still not completely understood [12]. Thus, the limiting case $C = 1$ is of obvious special interest.

Vertex models of statistical mechanics, placed on *regular* lattices, exhibit an exceptionally rich phase structure, including lines of first- and second-order phase transitions as well as critical and multi-critical points [55]. A multitude of models known from statistical mechanics can be transformed to or formulated as limiting cases of the 6- or 8-vertex models, cf. Refs. [55–58]. This series of models includes the Ising and q -states Potts models as well as various graph colouring problems and quantum spin models. Hence, vertex models can be considered as prototypes for models of phase transitions in two dimensions. The zero-field, square-lattice 8-vertex model has been solved exactly by Baxter [59, 60], revealing a peculiar type of continuous phase transitions with continuously varying critical exponents. The 6-vertex model is found to correspond to a critical surface in the phase diagram of the 8-vertex model. A special slice of the 6-vertex case, the anti-ferroelectric F model [61, 62], exhibits an infinite-order phase transition of the Kosterlitz-Thouless type [63, 64], whereas other specializations undergo first-order phase transitions.

On the basis of the well-known results of universality and scaling for models of statistical mechanics and condensed matter theory, the analysis of the effect of *disorder* onto the behaviour of those systems has received an increasing amount of attention during the last decades. The thus described area comprises a wide range of separate subjects, including such different topics as spin glasses [65, 66], the effect of random fields on magnetic systems [66], disordered electronic systems [67] or the analysis of generic random graphs and random networks [68], each of which is a prominent field of research in condensed matter physics. For the lattice spin models of statistical mechanics two major types of disorder are distinguished, namely

annealed randomness, where the disorder varies on the same time scale as the spin variables such as the cases considered in this thesis, and *quenched* disorder, where the random degrees of freedom are frozen on the time scale of variation of the spins, which is the case, e.g., for random-bond models and spin glasses. Depending on these types of randomness, different predictions regarding possible changes of the order and characteristics of the occurring phase transitions on application of the disorder have been made [66, 69–71]. In this context, an investigation of the properties of spin models coupled to the random surfaces of the dynamical triangulations model constitutes an analysis of the effect of a specific type of *annealed* geometrical or *connectivity disorder* onto the considered lattice systems.

Vertex models coupled to the lattices of the dynamical triangulations model allow one to study the effect of this geometrical type of disorder on prototypic models of statistical mechanics. Since the most interesting of these models, the 6- and 8-vertex models are defined on a four-valent lattice, the dynamical triangulations model has to be generalized to a *dynamical quadrangulations* model, i.e., a model of surfaces composed of squares, whose dual “fat” ϕ^4 random graphs can be decorated by vertex model arrows in the way prescribed for the 6- and 8-vertex models. For the case of the 6-vertex model the lack of a global sense of orientation on the random graphs reduces the range of sensible choices of vertex weights to the parameter space of the F model of an anti-ferroelectric. Its critical regime corresponds to a conformal field theory of central charge $C = 1$, such that the resulting *vertex model on random graphs* corresponds to the limiting case of the “ $C = 1$ barrier” of discrete Euclidean quantum gravity. This model can be formulated in terms of a matrix integral and an asymptotic solution can be found by a saddle-point method [72, 73], yielding partial information about its content of scaling dimensions. In this thesis, we analyze this model by means of an extensive set of Monte Carlo simulations of the combined system of dynamical, planar ϕ^4 random graphs and the coupled vertex model. A general exploration of its phase diagram is followed by a detailed scaling analysis of the matter- and graph-related observables of the system and a comparison of the outcomes to the results of Refs. [72, 73] as well as the KPZ/DDK framework of Refs. [30–32].

The outline of this thesis is as follows. Chapter 2 is devoted to an introduction to the dynamical triangulations model. We review the steps taken from the path-integral

ansatz for the quantization of gravity and the related string models to the formulation of simplicial quantum gravity and collect the most important analytical results available for the two-dimensional model as well as the most prominent methods that have been employed to achieve them. Finally, the predictions of KPZ/DDK [30–32] for the effect of coupling matter systems to Euclidean quantum gravity in two dimensions are reported.

The methods for a numerical, Monte Carlo simulation of dynamical triangulations are considered in Chapter 3. We distinguish different ensembles of triangulations resp. the dual ϕ^3 graphs with respect to the extent of allowed singular contributions, consider the classic sets of update moves for simulations in the canonical and grand-canonical ensembles and discuss the aspects of ergodicity and detailed balance. Ideas for a generalization of this simulation scheme to the case of dynamical *quadrangulations* resp. the dual ϕ^4 random graphs first presented in Refs. [49, 74] are picked up and elaborated in depths. As it turns out, for most of the considered ensembles the update moves resulting from an *ad hoc* generalization of the moves used in the triangulation model have to be augmented by a second type of moves to ensure ergodicity. To have exact, finite-graph results at hand for comparison to the simulation outcomes, we construct the co-ordination number distribution or certain analogues of it for the triangulation as well as the quadrangulation model from the graph counting results of the matrix model approach. To alleviate the known problem of critical slowing down of the considered type of dynamics, we adapt and generalize the “minBU surgery algorithm” put forward in Ref. [75] to the case of dynamical quadrangulations resp. ϕ^4 random graphs. We conduct a dynamical scaling analysis of the autocorrelation times of the different algorithms considered to evaluate their performance.

Chapter 4 we start by a survey of the known exact results for vertex models on regular lattices, focusing on the structure of their phase diagrams and the type of the occurring phase transitions. The simulation of vertex models can be most efficiently performed by algorithms of the cluster type, the most prominent of which is the so-called *loop algorithm* [76]. While its use is well documented for the case of regular lattices, the intended application for the simulation of vertex models on random graphs calls for some modifications and adaptations. For the case of the F model considered, the definition of an order parameter for the anti-ferroelectric phase transition on a random lattice requires a reformulation of the vertex model in terms of “plaquette spins”.

In Chapter 5 we address the problem of the F model coupled to planar ϕ^4 random graphs. After a short exposition of the exceptionally important position of vertex models in the context of integrable models and conformal field theory in two dimensions and a comparison of the situations on regular and random lattices, we report the analytical results found for the system in Refs. [72, 73]. Noting the surprising lack of numerical work on the 6-vertex model on the square-lattice and in order to calibrate our set of simulation and analysis tools, we analyze the Kosterlitz-Thouless point of the square-lattice F model via a set of Monte Carlo simulations. With the thus gained insight, we perform large-scale simulations of the F model on ϕ^4 random graphs and analyze the phase structure and the scaling properties in the vicinity of its critical point. The outcomes are compared to the predictions of the KPZ formula. The dynamical properties of the used combined link-flip, minBU surgery and loop algorithm update are determined by a scaling analysis of the autocorrelation times of several observables. The back-reaction of the matter degrees of freedom on the properties of the random graphs is investigated by considering the distribution of “baby universes” and extracting the string susceptibility exponent as well as an analysis of the geometrical two-point function of the graphs, resulting in an estimate of the Hausdorff dimension of the lattices.

Finally, Chapter 6 contains a summary of the results obtained and some outlook on ongoing and future work.

Chapter 2

The Dynamical Triangulations Approach to Quantum Gravity

The dynamical triangulations approach to quantum gravity is a simplicial or lattice regularization of the path integral formulation of the theory of gravity. Independently, for the case of two dimensions the same type of expressions occur when discretising the Polyakov interpretation of the bosonic string. While for the case of general dimensions very few exact results are available, the quantum gravity model in two dimensions, corresponding to string theory embedded in $D = 0$ dimensions, can be solved exactly by several complementary combinatorial techniques. Within the framework of Liouville theory one can find semi-exact results for the coupling of $C < 1$ unitary conformal matter to the gravitating space time, corresponding to the Polyakov string embedded in $0 \leq D \leq 1$ dimensions.

2.1 Path Integrals and Geometric Theories

2.1.1 Path integrals and quantum paths

The path integral approach of Dirac [77] and Feynman [78] has proved to be a successful and physically appealing formulation of the quantization problem in physics (for an introduction see, e.g., Ref. [79]). While algebraic schemes like canonical or BRST quantization give quantization prescriptions which look rather arbitrary on the operator level, the path integral approach is based intuitively on the funda-

mental principles of quantum mechanics. Furthermore, it offers various technical advantages like the inherent covariance of the formulation or the quite natural expression of renormalization theory in terms of path integrals.

In quantum mechanics, the transition amplitude of a point particle to move from position x_1 to x_2 in \mathbb{R}^d can be expressed in the path integral language as

$$G(x_1, x_2) = \int_{x_1}^{x_2} \mathcal{D}[x(t)] e^{i \int_{t_1}^{t_2} dt L(x, \dot{x})/\hbar}, \quad (2.1)$$

where

$$S[x(t)] = \int_{t_1}^{t_2} dt L(x, \dot{x}) \quad (2.2)$$

denotes the *classical* action of the problem in terms of the Lagrangian L . That is, the propagator is given by the functional integral over all possible classical paths of the particle weighted by $\exp(iS/\hbar)$. The classical limit follows naturally as $\hbar \rightarrow 0$ since at the classical solution one has $\delta S = 0$, such that the phase factors are wildly varying and thus destructively interfering everywhere but in the vicinity of the classical path. Proceeding further, in second quantization the functional integral $\mathcal{D}x$ over paths $x(t)$ is formally replaced by an integral of fields $\phi(x)$, i.e.

$$\mathcal{D}x \rightarrow \mathcal{D}\phi(x). \quad (2.3)$$

Since the world lines $x(t)$ being summed in the functional integral (2.1) are (simple) geometric objects, it is natural to think of Eq. (2.1) as an integral over geometries and formulate the action (2.2) in terms of the geometric properties of the world lines. Instead of the explicit parameterization $x(t)$, we consider an abstract path $P(x_1, x_2) \in \mathcal{P}(x_1, x_2)$, where $\mathcal{P}(x_1, x_2)$ denotes the set of all smooth paths connecting x_1 and x_2 . The simplest reparameterization-invariant choice of action is then obviously given by

$$S[P(x_1, x_2)] = m \int_{P(x_1, x_2)} dl, \quad (2.4)$$

i.e., the length of the world line $P(x_1, x_2)$, where m denotes a coupling parameter. In terms of the parameterization $x(t)$ this becomes

$$S[x(t)] = m \int_{t_1}^{t_2} dt \sqrt{(\dot{x}^\mu)^2}, \quad (2.5)$$

such that the classical equations of motion are those of a free relativistic particle,

$$\frac{\delta S}{\delta x^\mu(t)} = \frac{d}{dt} \left(\frac{\dot{x}^\mu}{|\dot{x}|} \right) = 0, \quad (2.6)$$

solved by straight lines $\dot{x}^\mu = \text{const}$. Thus, the free relativistic particle has an elegant co-ordinate free description via the functional integral

$$G(x_1, x_2) = \int_{\mathcal{P}(x_1, x_2)} \mathcal{D}[P(x_1, x_2)] e^{im \int_{P(x_1, x_2)} dl/\hbar}, \quad (2.7)$$

which is formulated entirely in terms of the geometry of the paths. Obviously, the integral over paths $P(x_1, x_2)$ should be over *equivalence classes* of paths instead of individual paths, i.e. reparameterizations

$$x(t) \rightarrow x(f(t)), \quad \dot{f} > 0, \quad (2.8)$$

should not be counted as different paths.

2.1.2 Random surfaces and strings

A natural generalization of this concept replaces the zero-dimensional particle sweeping out curves in time by one-dimensional *strings* sweeping out two-dimensional surfaces, the so-called *world sheets*. For simplicity we consider closed strings, i.e. world sheets $M(\gamma_1, \gamma_2)$ spanned between two boundary strings γ_1, γ_2 of topology S^1 . The obvious generalization of the action (2.4) then is

$$S[M(\gamma_1, \gamma_2)] = \mu \int_{M(\gamma_1, \gamma_2)} dA, \quad (2.9)$$

with a string coupling μ , such that the action is given by the *area* of the world sheet and the propagator now is represented as

$$G(\gamma_1, \gamma_2) = \int_{\mathcal{M}(\gamma_1, \gamma_2)} \mathcal{D}[M(\gamma_1, \gamma_2)] e^{iS[M(\gamma_1, \gamma_2)]/\hbar}. \quad (2.10)$$

Then, different interpretations of such a system are in place. First, if the swept out manifolds M are considered as parameterized surfaces $X : S^1 \times [0, 1] \rightarrow \mathbb{R}^D$, with co-ordinates $(\xi^1, \xi^2) = \xi \mapsto x = (x^1, \dots, x^D)$, the action (2.9) becomes

$$\begin{aligned} S_{\text{NG}}[X; \mu] &= \mu \int dA(\xi) = \mu \int d^2\xi \sqrt{|\det h|} \\ &= \mu \int d^2\xi \sqrt{\left(\frac{\partial x^\mu}{\partial \xi^1}\right)^2 \left(\frac{\partial x^\mu}{\partial \xi^2}\right)^2 - \left(\frac{\partial x^\mu}{\partial \xi^1} \frac{\partial x^\mu}{\partial \xi^2}\right)^2}, \end{aligned} \quad (2.11)$$

where h denotes the metric on the embedded world sheet induced by the mapping X , i.e.,

$$h_{\alpha\beta} = \frac{\partial x^\mu}{\partial \xi^\alpha} \frac{\partial x^\mu}{\partial \xi^\beta}. \quad (2.12)$$

This is the celebrated *Nambu-Goto* action of string theory [80]. Inserted in the path integral (2.10), the formal integral over surfaces $M(\gamma_1, \gamma_2)$ then becomes an integral over equivalence classes of maps X under diffeomorphisms. On the other hand, introducing an *internal* metric $g_{\alpha\beta}$ on M , Brink, di Vecchia and Howe [81] proposed the following re-write of the action,

$$S_P[X, g; \mu] = \frac{1}{2} \int d^2\xi \sqrt{|\det g|} g^{\alpha\beta} (h_{\alpha\beta} + \mu g_{\alpha\beta}), \quad (2.13)$$

which is known as the *Polyakov* string action. As indicated by the double argument of S_P , the integration of Eq. (2.10) should now be performed independently with respect to both variables X and g as was proposed by Polyakov [82]. It can be seen by a simple calculation that the actions (2.11) and (2.13) are equivalent at the classical level; in a quantized theory, however, their equivalence is not at all obvious (see, e.g., Ref. [10]).

2.1.3 Quantum gravity

Of course, the Nambu-Goto and Polyakov actions are only the simplest possible actions for random surfaces; for a physical theory one might add further terms, probably involving either the extrinsic curvature H in terms of the induced metric h or intrinsic curvature terms R^k , $k = 1, 2, \dots$, resulting from the internal metric g . For a *quantum theory of gravity* in d dimensions, the natural action to start with is the *Einstein-Hilbert* action of classical gravity,

$$S_{\text{EH}}[g; \mu, \lambda] = \int_M d^d\xi \sqrt{|\det g|} (\mu - \lambda R), \quad (2.14)$$

which, as expected for a gravity theory, does not refer to an embedding space, but is entirely formulated in terms of the internal metric properties. The first term is still the area term (generalized to d dimensions), now written as a function of the internal metric g , while the second term introduces the scalar curvature R derived from g . In this context, μ gains the meaning of a *cosmological constant* and λ denotes the *gravitational coupling constant*. The action (2.14) is explicitly invariant under diffeomorphisms $\xi^\alpha \mapsto \tilde{\xi}^\alpha$ of the co-ordinates, since the determinant of g transforms as

$$\sqrt{|\tilde{g}(\tilde{\xi})|} = \det \left(\frac{\partial \xi^\alpha}{\partial \tilde{\xi}^\beta} \right) \sqrt{|g(\xi)|}, \quad (2.15)$$

such that the additional determinant just cancels the determinant stemming from the transformation of the measure $d^d\xi$ (R , of course, transforms as a scalar). Since

for the case of quantum gravity we do not any more have the propagation of strings in mind, the path integral is naturally performed over *closed* surfaces M instead of “tubes” $S^1 \times [0, 1]$ and we thus define the partition function of the system as

$$Z(\mu, \lambda) = \int \mathcal{D}[g] e^{i S_{\text{EH}}[g; \mu, \lambda]/\hbar}, \quad (2.16)$$

where the functional integral covers all diffeomorphically inequivalent metrics g of closed, smooth manifolds.

If the quantum gravity path integral (2.16) should be more than a symbolic expression of a quantization programme, even from superficial consideration several fundamental problems and the need for interpretation of Eq. (2.16) come to mind:

1. Eq. (2.16) prescribes a state sum over a complex phase factor. Such sums, however, are generally divergent, see, e.g. Ref. [83]. Furthermore, Riemannian manifolds and thus metrics offer a variety of technical advantages over the Lorentzian metrics we are instructed to sum over.
2. The integral over equivalence classes of metric tensors g is not obviously *a priori* well-defined. How is the over-counting due to diffeomorphically equivalent metrics accounted for? What about different differentiable structures and different topologies of the manifolds?
3. Since the curvature term of the action (2.14) can become arbitrarily large, the Einstein-Hilbert action is in general unbounded from below. This obviously renders the path integral (2.16) ill-defined, unless the measure term $\mathcal{D}[g]$ gives negligible weight to such configurations.

The complex phase factor is commonly circumvented by the formal substitution

$$t \rightarrow i\tau \quad (2.17)$$

of the time-like co-ordinate of the metric g . Under this *Wick rotation* the phase factor changes as

$$e^{i S_{\text{EH}}/\hbar} \rightarrow e^{-S_{\text{EH}}/\hbar}, \quad (2.18)$$

thus making the path integral Euclidean and therewith potentially convergent. After performing the integration, a Lorentzian signature of the metric is supposed to be recovered by analytic continuation in τ or, alternatively, an explicit back-rotation.

While this prescription is a well-established trick in quantum field theory on a fixed (Minkowski) background based on the Osterwalder-Schrader reconstruction theorem (see, e.g., [84]), it has been noted [85–87] that the possibility of a Wick back-rotation is far from obvious in quantum gravity. For a dynamical and spatially varying metric a Wick (back-)rotation cannot be given by the simple prescription (2.17) which is obviously not invariant under diffeomorphisms; from the space of metrics to be integrated over almost all will have no geometrically apparent notion of time [87]. In fact, the class of metrics and thus manifolds in the sense of the path integral (2.16) compatible with a Lorentzian signature is different from the class of metrics with Euclidean signature. Thus, the substitution (2.18) is an *ad hoc* assumption that (as it turns out) changes the theory. We will speak about “Euclidean quantum gravity” in contrast to “Lorentzian quantum gravity” when referring to the Wick rotated theory.

As far as the over-counting of diffeomorphically equivalent metrics in the path integral (2.16) resp. its Euclidean counterpart is concerned, two possible solutions come to mind [11]: either only one representative of each equivalence class of metrics is counted in the functional integral, which is, however, practically quite impossible. Or the integral should be performed over *all* metrics, taking care of the over-counting by dividing out the “volume” of the diffeomorphism group in the measure, i.e., one should make the following replacement:

$$\int \mathcal{D}[g] \rightarrow \int \frac{\mathcal{D}[g]}{\text{Vol}[\text{Diff}(g)]} \quad (2.19)$$

The precise meaning of this transformation depends on the methods applied to further develop the problem. In a continuum theory this additional factor corresponds to the Fadeev-Popov determinant, whereas in the discretised models considered below, the symmetry with respect to diffeomorphisms of metrics transforms to a permutation symmetry of discrete objects.

A sum over different topologies of manifolds, which should be in principle included in the path integral (2.16), is quite intractable for the case of general dimensions, since for $d \geq 3$ there is no obvious classification of topologies in terms of a finite set of parameters. For $d \geq 4$ there additionally occurs the problem of diffeomorphically inequivalent differentiable structures for the same manifold. Also for those reasons we now turn to the case of two-dimensional quantum gravity.

2.1.4 The case of two dimensions

In two dimensions the topology of a closed surface M_h is uniquely characterized by its *genus*¹ h given in terms of the *Euler characteristic* by $\chi = 2 - 2h$. Taking the discussion of the previous section into account, the partition function of two-dimensional Euclidean quantum gravity reads

$$Z(\mu, \lambda) = \sum_{h=0}^{\infty} \int \frac{\mathcal{D}[g_h]}{\text{Vol}[\text{Diff}(g_h)]} e^{-S_{\text{EH}}[g_h; \mu, \lambda]}, \quad (2.20)$$

with the action of Eq. (2.14). Here, we have set $\hbar = 1$ for simplicity. Since the Euler characteristic is a topological invariant and related to the integral over the scalar curvature as

$$\int_{M_h} d^2\xi \sqrt{|\det g_h|} R = 4\pi\chi = 8\pi(1 - h), \quad (2.21)$$

which is the celebrated *Gauß-Bonnet* theorem (see, e.g., Ref. [88]), the path integral (2.20) can be reduced to

$$Z(\mu, \lambda) = \sum_{h=0}^{\infty} e^{4\pi\chi(h)\lambda} Z^h(\mu), \quad (2.22)$$

where the partition function $Z^h(\mu)$ at fixed genus h is given by

$$Z^h(\mu) = \int \frac{\mathcal{D}[g_h]}{\text{Vol}[\text{Diff}(g_h)]} e^{-\mu V_{g_h}}, \quad (2.23)$$

where $V_{g_h} = \int_{M_h} d^2\xi \sqrt{|\det g_h|}$ is the volume of the universe M_h . Taking into account the topological triviality of two-dimensional gravity, we note that the Polyakov string action (2.13) can be alternatively interpreted as two-dimensional quantum gravity coupled to the D independent scalar fields $h_{\alpha\beta}$. The topological triviality of the Einstein-Hilbert action in two dimensions results in a boundedness of the action for any *fixed* topology; it remains to be checked, whether a summation over topologies can be performed after solving the problem at fixed topology. This leads to the so-called *double-scaling limit* to be discussed below in Section 2.3.7.

A field-theoretic solution of the problem of two-dimensional quantum gravity is based on the uniformization theorem [89] for two-dimensional Riemannian surfaces which states that every Riemannian surface is conformally equivalent to (see, e.g., Ref. [23])

¹Here, h should not be confused with the external metric $h = h_{\alpha\beta}$ above.

- \mathbb{CP}^1 , the Riemann sphere, or
- H , the Poincaré upper half plane, or
- a quotient of H by a discrete subgroup $\Gamma \subset \text{SL}(2, \mathbb{R})$,

such that the metric g can be written as

$$g = e^{\gamma\phi} \hat{g} \tag{2.24}$$

with respect to some reference metric \hat{g} on one of the above spaces. Thus, two-dimensional gravity can be formulated in terms of the single *Liouville field* ϕ ; this Liouville field theory can be treated analytically on the quantized level, see Refs. [6, 23, 24] for reviews. However, the discretised theories presented below can be solved exactly and yield results going beyond those of the continuum approach; the results from both approaches coincide whenever they overlap.

2.2 Simplicial Quantum Gravity

While the continuum Liouville theory sketched above develops the problem covariantly to introduce a short-distance cut-off only at the end, a *discretisation* of the problem makes the involved expressions finite from the beginning. After solving the discretised theory, the relevant coupling constant(s) should be tuned such as to define a proper continuum limit of the theory; this involves a renormalization of relevant parameters.

However, a discretisation of the geometries to be integrated over, either by a lattice model or the simplicial building blocks described below, has to ensure that the sum over discretisations covers all metrics to be summed over in Eq. (2.20). That is, the discretised metrics have to be something like a dense subset of the original space of metrics. Such a property can be guaranteed for the case of “quantum gravity” in one dimension. The discussion of the next section follows Ref. [10].

2.2.1 Random walks and the Wiener measure

Let $f_0(x)$ be the initial distribution of a cloud of particles in \mathbb{R}^D coupled to a heat bath. Its diffusive spread in time is in the simplest approximation described by the

diffusion equation,

$$\frac{\partial f}{\partial t} = \frac{1}{2} \Delta f, \quad (2.25)$$

subject to the initial condition $f(x, 0) = f_0(x)$, which is solved by [90]

$$f(x, t) = \int_{\mathbb{R}^d} dy G_t(x, y) f_0(y), \quad (2.26)$$

where the *heat kernel* $G_t(x, y)$ is defined as

$$G_t(x, y) = \frac{1}{(2\pi t)^{D/2}} e^{-\frac{|x-y|^2}{2t}}. \quad (2.27)$$

From Gaussian integration we have the following decomposition property of $G_t(x, y)$:

$$G_t(x_0, x_N) = \int dx_1 \cdots dx_{N-1} G_{t/N}(x_N, x_{N-1}) \cdots G_{t/N}(x_1, x_0), \quad (2.28)$$

for any $N \geq 1$. Now, consider the piecewise linear path $\omega : [0, t] \rightarrow \mathbb{R}^D$ connecting the points (x_0, \dots, x_N) ,

$$\omega(s) = x_{k-1} + \frac{x_k - x_{k-1}}{t/N} \left(s - \frac{k-1}{N}t\right), \quad \frac{k-1}{N}t \leq s \leq \frac{k}{N}t, \quad 1 \leq k \leq N. \quad (2.29)$$

Then, the expression

$$D_t^N \omega = \left(2\pi \frac{t}{N}\right)^{-\frac{D}{2}N} dx_1 \cdots dx_{N-1} \quad (2.30)$$

may be considered as a measure on the space $\Omega_{N,t}(x, y)$ of all such paths connecting x and y . Using the identity

$$\sum_{k=1}^N \frac{|x_k - x_{k-1}|^2}{t/N} = \sum_{k=1}^N \frac{t}{N} \left(\frac{|x_k - x_{k-1}|}{t/N}\right)^2 = \int_0^t |\dot{\omega}(s)|^2 ds \quad (2.31)$$

in Eq. (2.28), the propagator $G_t(x, y)$ can be written in a form reminiscent of a path integral as

$$G_t(x, y) = \int_{(x,y)} D_t^N \omega \exp\left(-\frac{1}{2} \int_0^t |\dot{\omega}(s)|^2 ds\right), \quad (2.32)$$

which is called the *random-walk representation* of $G_t(x, y)$ on $\Omega_{N,t}(x, y)$. The expression (2.32), which is a conventional integral of a finite number of variables, can be viewed as a discrete approximation to a true path integral, i.e., there exists a measure $D_t \omega$ on the space $\Omega_t(x, y)$ of all *continuous* paths $\omega : [0, t] \rightarrow \mathbb{R}^D$ connecting x

and y , such that [91]

$$\begin{aligned} \int_{(x,y)} D_t^N \omega \exp\left(-\frac{1}{2} \int_0^t |\dot{\omega}(s)|^2 ds\right) f\left[\omega\left(\frac{1}{N}t\right), \dots, \omega\left(\frac{N-1}{N}t\right)\right] \\ = \int_{(x,y)} D_t \omega f\left[\omega\left(\frac{1}{N}t\right), \dots, \omega\left(\frac{N-1}{N}t\right)\right] \end{aligned} \quad (2.33)$$

for all bounded and continuous functions $f : \mathbb{R}^{(N-1)D} \rightarrow \mathbb{R}$ and arbitrary $N \geq 1$; i.e., the discrete measures are identical to $D_t \omega$ with respect to functions f uniquely defined by their values at the reference points $\frac{k}{N}t$. The measure $D_t \omega$ is called the *Wiener measure* on $\Omega_t(x, y)$. Thus, we have constructed a path integral measure from the set of piecewise linear paths. Reversing the view, one can ask for the behaviour and convergence of different discrete approximations to the Wiener measure. Obviously, given a path $\omega \in \Omega_t(x, y)$, we can define discretised paths $\omega_N \in \Omega_{N,t}(x, y)$ by $\omega_N(kt/N) = \omega(kt/N)$, $k = 0, \dots, N$, such that $\omega_N \rightarrow \omega$ uniformly on $[0, t]$ and in view of Eq. (2.33) the measures

$$\begin{aligned} D_t^N \omega \exp[-S(\omega)] \quad , \\ S(\omega) = \frac{1}{2} \int_0^t |\dot{\omega}(s)|^2 ds, \end{aligned} \quad (2.34)$$

can be considered as approximations to the Wiener measure $D_t \omega$ for $N \rightarrow \infty$. In fact, it can be shown that not only for $S(\omega)$ given above but for rather general actions one has convergence $D_t^N \omega \exp[-S(\omega)] \rightarrow D_t \omega$ of the measures; in statistical physics terms such a property is known as *universality* with respect to “microscopic realizations”. Thus, according to this *theorem of Donsker* (see, e.g., Ref. [92]) for the case of one-dimensional manifolds, i.e. curves, a whole variety of discretisations of the path integral can be chosen which all properly converge to the continuum formulation in terms of the integral measures.

2.2.2 Discretising quantum gravity

In more than one dimension there is no analogue of Donsker’s theorem that could guarantee different discretisations to converge to the continuum formulation. Nevertheless, discretisations similar to the random-walk representation of the Wiener measure are possible.

A discretisation for the Nambu-Goto string of Eq. (2.11) embedded in \mathbb{R}^d is perhaps most naturally defined by considering random surfaces on a hypercubic lattice \mathbb{Z}^d .

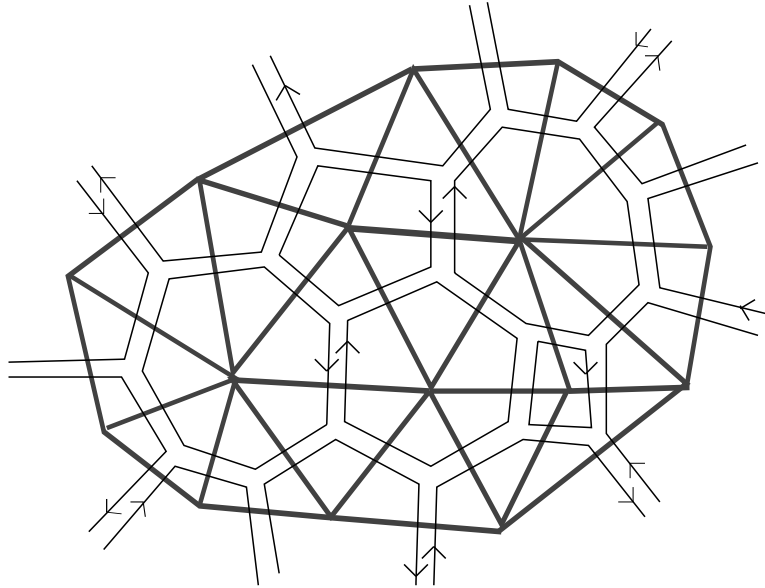


Figure 2.1: A small patch of a random triangulation (thick lines) embedded in the plane. The dual graph (thin double lines) of the lattice is a ϕ^3 graph of the same topology.

Here, the lattice surface is defined as a set of plaquettes in \mathbb{Z}^d , each consisting of four cyclically ordered vertices in \mathbb{Z}^d , i.e. a set of squares of the lattice, usually connected to a closed surface. Due to the over-exponential growth of the number of these (self-intersecting) surfaces with the number of vertices, the problem is only well-defined for fixed topology, usually that of planar graphs. This *lattice random surface* (LRS) model has been considered in early approaches towards discretising quantum gravity initiated by Weingarten [2]. We will not discuss this model further here, for a review see Ref. [10].

A suitable discretisation of the intrinsic, not embedded geometry occurring in the d -dimensional quantum gravity model is given by the concept of *piecewise linear* (PL) manifolds, i.e. d -dimensional simplicial complexes subject to suitable regularity conditions. In the case of two dimensional quantum gravity the simplices of maximal dimension are 2-simplices glued together along their edges, such that the complex can be depicted as a closed *random triangulation*. Fig. 2.1 shows a patch of such a triangulation embedded in the plane. Such discrete approximations to quantum

gravity have originally been proposed by Regge [93] for a co-ordinate free description of (classical) gravity. Given these fundamental building blocks, the summation over triangulations should in principle include a variation of the *edge lengths* of the triangles as well as the *connectivity* of the simplicial complex². Simultaneous variation of both of these properties is possible and the corresponding ansatz is known as the “dynamical Regge approach” [94, 95]. However, historically two limiting cases of this general scheme have been more intensively developed:

- (a) Starting from the original discretisation attempt of Regge [93] and Regge and Ponzano [96] the *Regge calculus* approach to quantum gravity [97–100] performs the sum over metrics by considering a triangulation of *fixed connectivity* and *varying the edge lengths* of the triangles. The effect of this variation then has to be incorporated in the path integral measure, which led to some discussion about how this should be done [101, 102]. This approach has been followed mainly by numerical methods, including studies of the resulting geometry [103, 104], the effect of the coupling of matter to the gravitating universe [105] and extensions to the four-dimensional case [106].
- (b) Stressing the combinatorial aspect of PL manifolds, the theory of *dynamically triangulated random surfaces* (DTRS) considers triangulations consisting of *equilateral* triangles, integrating over all possible gluings of a given number of triangles to a (usually) closed surface of a given topology. Thus, its dynamic aspect comes from the *connectivity* of the complex instead of from the edge lengths. This model, originally proposed independently as a model for quantum gravity in two dimensions by Ambjørn *et al.* [3], David [4] and Kazakov *et al.* [5], can be solved exactly for the case of two dimensions in the pure case and also for the coupling of certain kinds of matter to it, cf. the discussion below.

The Regge calculus approach (a) will not be discussed further here. Instead, we concentrate on the DTRS approach (b) and discuss the properties of the considered simplicial manifolds and the therewith discretised action of two-dimensional quantum gravity.

²Since in quantum gravity we do not consider an *embedding* of the surfaces, the mentioned edge lengths should be considered as properties of the internal metric.

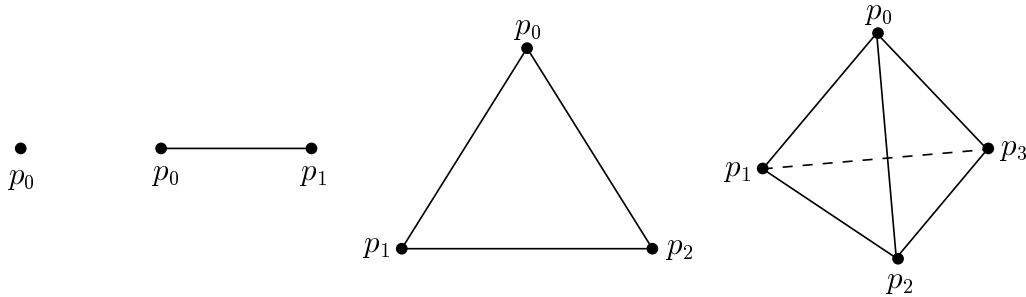


Figure 2.2: 0-, 1-, 2- and 3-simplices.

2.2.3 Dynamical triangulations and the discretised action

An r -dimensional *simplex* $\sigma_r = \langle p_0 \dots p_r \rangle$ is the point set in \mathbb{R}^d defined by [88]

$$\sigma_r = \left\{ x \in \mathbb{R}^d \mid x = \sum_{i=0}^r c_i p_i, c_i \geq 0, \sum_{i=0}^r c_i = 1 \right\}, \quad (2.35)$$

with geometrically independent points $p_i \in \mathbb{R}^d$. A q -face of $\sigma_r = \langle p_0 \dots p_r \rangle$ is the simplex $\sigma_q = \langle p_{i_0} \dots p_{i_q} \rangle$. Fig. 2.2 shows the simplices of lowest dimension. A *simplicial complex* K is a finite set of simplices, such that (i) all faces of each simplex of K belong to K and (ii) the intersection of any two simplices of K is either a simplex of K or the empty set. The dimension of K equals the maximum of the dimensions of the simplices it contains. The *star* $\text{star}_K(\sigma)$ of a simplex $\sigma \in K$ is the union of all simplices of K of which σ is a face; the *link* $\text{link}_K(\sigma)$ is the union of all faces σ_f of all simplices in $\text{star}_K(\sigma)$ satisfying $\sigma_f \cap \sigma = \emptyset$. The point set $|K| = \cup_{\sigma \in K} \sigma$ is called the *polyhedron* of K , which provides the underlying topological space of the complex; the polyhedron $|K|$ is said to be triangulated by K . A *subdivision* K' of K is a simplicial complex such that $|K'| = |K|$ and each r -simplex of K' is contained in an r -simplex of K .

Then, a piecewise linear or *PL manifold* M is a polyhedron such that each point in M has a neighbourhood which is simplicially isomorphic to an open set in \mathbb{R}^d , where “simplicially isomorphic” means that the corresponding map is invariant under subdivisions. On the other hand, a *simplicial manifold* is a d -dimensional complex K such that $\text{link}(\sigma_r) \simeq S^{d-r-1}$ [14]. Thus, simplicial manifolds are abstract, combinatorial representations (triangulations) of PL manifolds. However, in the DTRS scheme triangulations are not deduced *a posteriori* as triangulations of manifolds, but constructed independently by *gluings* [13]. There, a set of simplices is endowed with identifications of faces of different simplices such that each face is subject to exactly

one gluing procedure. In two dimensions, i.e., when gluing triangles in the indicated way, the resulting simplicial complex is a simplicial manifold³. In general, the gluing of d -simplices to a simplicial manifold M has to obey the *Dehn-Sommerville* relations,

$$\chi(M) = \sum_{i=0}^d (-1)^i N_i(M), \quad (2.36)$$

$$\sum_{i=2k-1}^d (-1)^i \frac{(i+1)!}{(i-2k+2)!(2k-1)!} N_i(M) = 0 \quad , \quad (2.37)$$

if d is even, where $1 \leq k \leq d/2$. Whereas if d is odd the second equation reads

$$\sum_{i=2k}^d (-1)^i \frac{(i+1)!}{(i-2k+1)!2k!} N_i(M) = 0, \quad (2.38)$$

where $1 \leq k \leq (d-1)/2$ and $N_i(M)$ is the number of i -simplices in M . Eq. (2.36) is the well-known way to compute the Euler characteristic for a simplicial surface; for the case of $d=2$ the second equation reduces to the simple property

$$2N_1(M) = 3N_2(M), \quad (2.39)$$

expressing the fact that each link is shared between exactly two triangles. Note that for the $d=2$ case the combination of Eqs. (2.36) and (2.37) leaves only one independent variable, for example the number of triangles $N_2(M)$. For $d=3, 4$ one has one additional independent variable, say the number of $(d-2)$ -simplices (*bones*) $N_{d-2}(M)$.

Now, a d -dimensional *dynamical triangulation* T_a can be defined as a triangulation (subdivision) of a simplicial manifold M built by gluing $N_d(T_a)$ d -simplices with a common, fixed edge length a . Here, a serves as cut-off for the discretisation of the path integral (2.20). As far as the discretisation programme is concerned, it can unfortunately be shown that not every topological manifold can be triangulated in general dimensions [13]. Thus, as mentioned above there is no analogue of Donsker's theorem for $d > 1$. However, one can prove an approximation theorem which states that for any Riemannian manifold M of bounded geometry there is a cut-off a and numbers of d - and $d-2$ -simplices $N_d(T_a)$ and $N_{d-2}(T_a)$ such that there exists a dynamical triangulation $T_{a, N_d, N_{d-2}}$ with a distance from M in the *Gromov-Hausdorff*

³In dimensions $d > 2$ the result will in general only be a *pseudo-manifold* [14].

metric smaller than a given arbitrary, positive number [14]. Stated in other words, any such manifold can be approximated with arbitrary precision by dynamical triangulations. Note that this result is much weaker than Donsker's theorem in the one-dimensional case.

Given the concept of a dynamical triangulation, the notions of differential calculus necessary for the formulation of general relativity should be transferred to the discrete language. This programme has been first carried out by Regge in the seminal paper [93] and later on adapted to the view of dynamical triangulations in [98]. The basic properties which have to be translated are those of (geodesic) distance, of area (or volume for $d > 2$) and of curvature. The classic distance definition stemming from Regge calculus [93] is the continuation of the generic, flat metrics of the interior of the simplices of the simplicial manifold to the whole of the complex; the resulting metric, however, is obviously singular at the vertices. Instead, considering the simplicial complexes as combinatorial objects, the metric should be defined in terms of the simplicial building blocks of the triangulation, i.e. its faces, edges and vertices. The distance between vertices p_1 and p_2 in T_a can be conveniently defined as

$$d(p_1, p_2) = a \min_{l(p_1, p_2)} |l(p_1, p_2)|, \quad (2.40)$$

where the minimum is taken over all discrete curves $l(p_1, p_2) = (p_1 = p_{i_1}, p_{i_2}, \dots, p_{i_n} = p_2)$ for arbitrary $n \leq N_0(T_a)$ such that $\langle p_{i_k}, p_{i_{k+1}} \rangle$ is a link belonging to T_a and $|l(p_1, p_2)| = n$. Since the edge length is a constant, we will frequently consider $d(p_1, p_2)/a$. Analogously, one can define the distance between edges as the minimum number of edges of the dual lattice one has to travel to connect them and, similarly, distances between simplices of larger dimension. On the grounds of universality (cf. Section 2.2.1) we expect the precise definition of distance to make no difference as long as a continuum limit can be defined (i.e., the model exhibits a continuous phase transition). Note that all of those distances are *geodesic* for the discrete surfaces and can thus be used in the places where the theory of relativity refers to geodesic distances.

To discretise the notion of curvature, we concentrate on the case of *two-dimensional* simplicial manifolds. Recall that (one of the versions of) the Gauß-Bonnet theorem states that for a *geodesic n-angle* t with angles β_i on a smooth surface the integral over the *scalar curvature* R ,

$$\frac{1}{2} \int_t R \, dA = \sum_i \beta_i - (n - 2)\pi \equiv \epsilon_t, \quad (2.41)$$

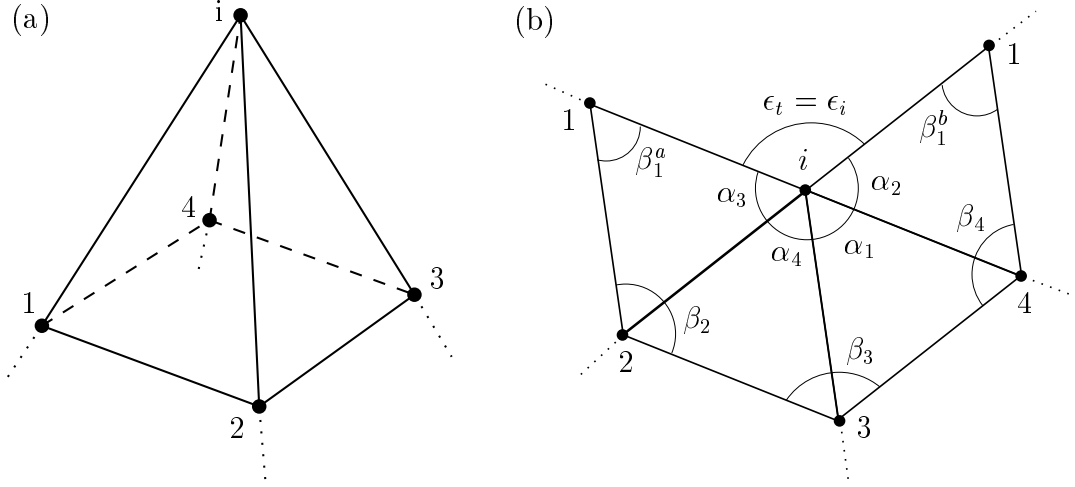


Figure 2.3: The excess angle ϵ_t of the geodesic rectangle (1234) is equal to the deficit angle ϵ_i of vertex i . (a) The geodesic triangle (1234) and an interior vertex i . (b) Embedding of the surroundings of i into the plane, after cutting the triangulation open along the link (1i).

does in general not vanish (as in flat space); instead, the n -angle t has an *excess angle* ϵ_t . Alternatively stated, the parallel transport of a vector around the triangle will rotate it by the excess angle ϵ_t [93]. On the discretised surface, the interior of simplices is flat; since scalar curvature is an intrinsic property which does not depend on the embedding (this is the “*Theorema Egregium*” of Gauß), curvature can also not be attributed to the edges, because the simplicial surface can be *bent* along the edges without changing the intrinsic properties. Thus, curvature has to be associated with the *vertices* of the simplicial manifold. If for each vertex we define the *deficit angle* ϵ_i as

$$\epsilon_i \equiv 2\pi - \sum_{\langle p_i, p_j, p_k \rangle \in T_a} \alpha_i[\langle p_i, p_j, p_k \rangle], \quad (2.42)$$

we read off from Fig. 2.3(b) that $\epsilon_i = \epsilon_t$. Thus, from Eq. (2.41) we have

$$\frac{1}{2} \int_t R dA = \sum_{p_i \in T_a} \epsilon_i = \sum_{p_i \in T_a} R_i A_i, \quad (2.43)$$

where the area A_i and curvature R_i associated to the vertex p_i are defined as

$$A_i = \frac{1}{3} \sum_{\langle p_i, p_j, p_k \rangle \in T_a} A[\langle p_i, p_j, p_k \rangle], \quad R_i = \frac{2\epsilon_i}{A_i}, \quad (2.44)$$

i.e., the area of each triangle $\langle p_1, p_2, p_3 \rangle$ is equally distributed between its vertices p_i . For the case of equilateral triangles occurring in the DTRS scheme all angles equal $\pi/3$ and therefore $\epsilon_i = (6 - q_i)\pi/3$, where q_i denotes the *co-ordination number* of the vertex p_i . Eq. (2.44) then reads

$$A_i = \frac{\mathbf{a}^2}{3}q_i, \quad R_i = \frac{2\pi(6 - q_i)}{q_i\mathbf{a}^2}, \quad (2.45)$$

where $\mathbf{a}^2 = a^2\sqrt{3}/4$. Now, the integral over curvature can be evaluated as

$$\sum_{p_i \in T_a} A_i R_i = \frac{2\pi}{3} \sum_{p_i \in T_a} (6 - q_i) = 4\pi[N_0(T_a) - N_2(T_a)/2] = 4\pi\chi(T_a), \quad (2.46)$$

where we have used the Dehn-Sommerville relation (2.39) in the last step and $\chi(T_a)$ is given by (2.36). This proves the discrete analogue of the Gauß-Bonnet theorem. Writing the total area of the surface as

$$\sum_{p_i \in T_a} A_i = \mathbf{a}^2 N_2(T_a), \quad (2.47)$$

the path integral of two-dimensional simplicial quantum gravity is given by

$$Z(\mu, \lambda; a) = \sum_{h=0}^{\infty} e^{4\pi\chi(h)\lambda} \sum_{N_2=1}^{\infty} e^{-\mu\mathbf{a}^2 N_2} \sum_{T_a \in \mathcal{T}_a(h, N_2)} \frac{1}{C(T_a)}. \quad (2.48)$$

In the following, we absorb the ‘‘lattice spacing’’ \mathbf{a} formally into the coupling constant μ , until in Section 2.3.7 the continuum limit of the discrete theory is discussed. The $C(T_a)$ denote the symmetry factors associated with dynamical triangulations of genus h and with N_2 triangles, that is, the volume of the corresponding symmetry group. Thus, two-dimensional simplicial quantum gravity is reduced to the purely combinatorial problem of determining the number $\mathcal{N}[T_a(h, N_2)]$ of triangulations of a given topology and size and the corresponding symmetry factors $C(T_a)$. They encode the over-counting of metrics in the path integral measure due to equivalent metrics, i.e., metrics connected by an orientation-preserving diffeomorphism. For *labelled* triangulation as they naturally occur in computer simulations of DTRS models (see Chapter 3 below), $C(T_a)$ is simply given by the factorial $N_0(T_a)!$ reflecting the number of possible re-labellings of the vertices [11]. In general, the space of equivalence classes of metrics can be characterized by a finite-dimensional *Teichmüller space* (see, e.g., Ref. [88]) of metrics $\hat{g}(t_1, \dots, t_m)$, $t_i \in \mathbb{C}$, such that any metric g on a manifold M is equivalent to

$$e^{\phi} \hat{g}(t_1, \dots, t_m), \quad (2.49)$$

where ϕ is a function on M . Here, the parameters t_i correspond to the combinatorial freedom in the gluing of simplices, whereas the conformal factor e^ϕ encodes additional invariants such as volume and curvature. Without discussion we mention that the discretised Einstein-Hilbert action of a simplicial manifold T in dimensions $d > 2$ is given by [107, 108]

$$S_T[\kappa_d, \kappa_{d-2}] = \kappa_d N_d(T) - \kappa_{d-2} N_{d-2}(T), \quad (2.50)$$

where κ_d and κ_{d-2} are suitable combinations of the cosmological and gravitational coupling constants (see, e.g., Ref. [9]). Also, the additional term h_{ab} in the Polyakov action Eq. (2.13) adds a term

$$\frac{1}{2} \sum_{\langle p_i p_j \rangle \in T_a} (x_i - x_j)^2 \quad (2.51)$$

to the discretised action, where the x_k are additional co-ordinates in \mathbb{R}^D associated to the vertices of the lattice. This justifies the claim presented above, that the Polyakov string (at fixed topology) can be viewed as two-dimensional quantum gravity coupled to D Gaussian fields.

2.3 Analytical Results for the Discretised Theory

In the following we concentrate on the case of the DTRS model in two dimensions, such that, unless otherwise stated, all results cited apply to the case $d = 2$. Having defined a discretised theory of two-dimensional Euclidean quantum gravity in terms of dynamical triangulations, one has to ensure the existence of a continuum limit for the theory to become a possible candidate for the quantum theory of gravity. If such a limit exists, we expect certain observables to scale according to power laws in the vicinity of the critical point, thus defining universal critical exponents of the theory. In a cursory survey, we present the methods which have been successfully applied to solve the combinatorial problem exactly and the main results of the analysis. First of all, one has to check, whether the sum of Eq. (2.48) over dynamical triangulations is well-defined (that is, finite) such as to have a chance to define a continuum limit. To entertain the reader and stimulate her imagination regarding the objects to be summed over, Fig. 2.4 shows a sample two-dimensional dynamical triangulation embedded in \mathbb{R}^3 .

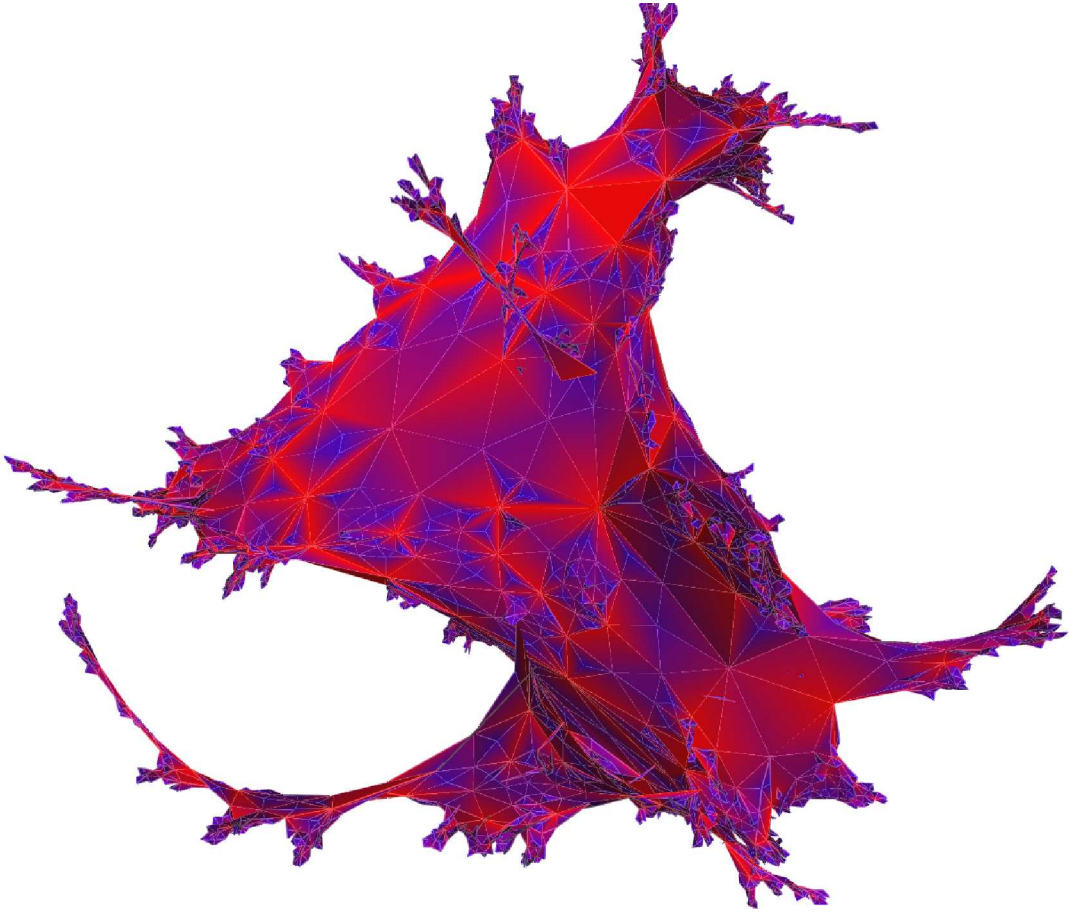


Figure 2.4: Embedding of a two-dimensional dynamical triangulation with $N_2 = 5000$ triangles in \mathbb{R}^3 (projected to \mathbb{R}^2 for obvious reasons). The colour of the triangles encodes the local curvature of the surface according to Eq. (2.45); blue regions have curvature $R > 0$, red patches denote $R < 0$. The embedding was generated with an adaptive algorithm described in Appendix B.

2.3.1 Existence of the discretised partition function

Adopting the interpretation of the Polyakov string action (2.13) as two-dimensional quantum gravity coupled to D Gaussian fields, we consider the discretised m -loop function at fixed topology,

$$G_\mu^h(l_1, \dots, l_m) = \sum_{N_2=1}^{\infty} e^{-\mu N_2} \sum_{T_a \in \mathcal{T}_a(h, N_2; l_i)} \frac{1}{\tilde{C}(T_a)} \int \prod_{p_i \in T_a} dx_i e^{-\frac{1}{2} \sum_{\langle ij \rangle} (x_i - x_j)^2}. \quad (2.52)$$

Here, the l_i denote fixed boundary loops consisting of $n_i = n(l_i)$ links of the triangulation. The $G_\mu(l_1, \dots, l_m)$ are quite general functionals, which include the m -point

functions $G_\mu(p_i, \dots, p_m)$ when contracting the loops l_i to points p_i and the partition function Z_μ for $m = 0$. The symmetry factors $\tilde{C}(T_a)$ in general depend on the number m of fixed loops or points and are thus not identical to the factors $C(T_a)$ of Eq. (2.48). If we include the sum over topologies,

$$G_\mu(l_1, \dots, l_m) = \sum_{h=0}^{\infty} e^{4\pi\chi(h)\lambda} G_\mu^h(l_1, \dots, l_m), \quad (2.53)$$

where $\lambda = 0$ for the Polakov string, the number of such triangulations can be shown to have a *lower* bound of the form [10]

$$(cN_2)!, \quad (2.54)$$

which grows faster than any exponential. Since the fields x_i will result for a fixed triangulation in a free energy $F \leq fN_2$ for some $f > 0$, it is obvious that

$$G_\mu^h(l_1, \dots, l_m) \geq \sum_{N_2=1}^{\infty} (cN_2)! e^{\text{const} \times N_2}, \quad (2.55)$$

which is divergent. Thus, including the sum over topologies, the m -loop functions are ill-defined for any value of the coupling μ due to the *entropy* of the triangulations. We thus concentrate on the problem at fixed topology. A possible inclusion of the sum over topologies using matrix models is discussed below in Section 2.3.7.

For the case of triangulations of fixed genus h the situation is fortunately more pleasant: it can be shown that the number $|\mathcal{T}_a(h, N_2)|$ of such inequivalent triangulations is exponentially bounded with respect to the number of triangles [8], i.e.,

$$|\mathcal{T}_a(h, N_2)| \leq e^{\text{const} \times N_2}. \quad (2.56)$$

Then, for a *spanning tree* on a given triangulation T_a the Gaussian integral in Eq. (2.52) can be easily performed due to the absence of closed loops to yield the bound [10]

$$\int \prod_{p_i \in T_a} dx_i e^{-\frac{1}{2} \sum_{\langle ij \rangle} (x_i - x_j)^2} \leq (2\pi)^{N_2(T_a)D/2}, \quad (2.57)$$

such that $G_\mu^h(l_1, \dots, l_m)$ is finite for $\mu > \frac{D}{2} \log 2\pi$. Thus, for given h and a given number of boundary loops l_1, \dots, l_m there is a $\mu_0(l_1, \dots, l_m) > 0$ such that the m -loop functions are finite and analytic for $\mu > \mu_0(l_1, \dots, l_m)$ and divergent for $\mu < \mu_0(l_1, \dots, l_m)$ (this includes, of course, the partition function of the model). Furthermore, it can be proved that $\mu_0(l_1, \dots, l_m) = \mu_0$ does not depend on the

choice of boundary loops l_i and is even independent of the genus h [3, 109, 110]. Since for μ right above the limiting value μ_0 the sum over N_2 in (2.52) is dominated by the large- N_2 terms, the limit $\mu \downarrow \mu_0$ is the obvious candidate for the continuum limit of the model.

For the case of simplicial quantum gravity in dimensions $d > 2$ a similar property could only quite recently be proved [111–113]; also there, the number of non-isomorphic triangulations with a given number of d -simplices is exponentially bounded with N_d .

2.3.2 String susceptibility, mass gap and string tension

Integrating over the marked vertices in the m -point function, the *susceptibilities* are defined as

$$\chi_{(m)}^h(\mu) = \int dx_2 \cdots dx_m G_\mu^h(0, x_2, \dots, x_m). \quad (2.58)$$

In the thermodynamic limit $N_2 \rightarrow \infty$ their singular part can also be expressed as derivative of the partition function,

$$\chi_{(m)}^h(\mu) \sim (-1)^m \frac{d}{d\mu^m} Z^h(\mu), \quad (2.59)$$

since in view of Eq. (2.52) differentiating with respect to μ will pull down a factor of $-N_2$, which is, in the limit of a large number of triangles, the same effect as fixing an additional vertex in the triangulations in going from $G_\mu^h(0, x_2, \dots, x_{m-1})$ to $G_\mu^h(0, x_2, \dots, x_m)$. The differences for small N_2 stem from the different symmetry factors associated with the triangulations. Since $Z^h(\mu)$ is singular at the special point $\mu = \mu_0$, the susceptibility is expected to scale with the *string susceptibility exponent* γ_s as

$$\chi^h(\mu) \equiv \chi_{(2)}^h \sim (\mu - \mu_0)^{-\gamma_s^h}. \quad (2.60)$$

It turns out that the *critical exponent* γ_s^h indeed does depend on the genus h of the triangulations.

By separating out the minimum of the Gaussian action,

$$S_{\min}(T_a) \equiv \min_{(x_1, \dots, x_D)} \frac{1}{2} \sum_{\langle ij \rangle} (x_i - x_j)^2, \quad (2.61)$$

the Gaussian integral in Eq. (2.52) can be written as

$$\int \prod_{p_i \in T_a} dx_i e^{-\frac{1}{2} \sum_{\langle ij \rangle} (x_i - x_j)^2} = e^{-S_{\min}(T_a)} \left(\frac{(2\pi)^{N_2(T_a \setminus \partial T_a)}}{\det C_{T'_a}^0} \right)^{D/2}. \quad (2.62)$$

Here, $C_{T'_a}$ is the *adjacency matrix* of the triangulation T'_a constructed by removing all boundary links from T_a and identifying all boundary sites with one vertex given the label 0 and

$$(C_{T'_a})_{ij} = \begin{cases} -q_{ij} & \text{if } i \neq j \\ q_i & \text{if } i = j \end{cases}, \quad (2.63)$$

where q_i is the co-ordination number of vertex p_i and q_{ij} is the number of links connecting vertices p_i and p_j (i.e., either 0 or 1 for simplicial manifolds). The modified adjacency matrix $C_{T'_a}^0$ is defined by deleting the row and column indexed by 0. The representation (2.62) allows a continuation of the theory to non-integer and even negative embedding dimensions D ; especially to the case $D = -2$, which can be solved analytically, see Refs. [5, 21, 114–116]. Inserting (2.62) into the definition of the susceptibility (2.59), $\chi^h(\mu)$ can be expressed in terms of the determinant $\det C_{T'_a}^0$. Using the fact that this determinant is additive with respect to “gluings” of two spherical universes along two of their boundary lines l_i , for $h = 0$ one can prove the inequality [117]

$$\gamma_s^0 \leq \frac{1}{2}, \quad (2.64)$$

which is one of the most general results for the DTRS models; this mean-field like bound is supposed to hold for any random surface model with local interactions. Especially, via the extension of Eq. (2.62) to non-integer and negative dimensions D , this result is valid for the coupling of conformal matter of any central charge to two-dimensional Euclidean quantum gravity. The mean-field limit in statistical mechanics is usually found to be equivalent to the limit of infinite dimensionality of space. Considering $D \rightarrow \infty$ in the DTRS model, from Eq. (2.62) obviously configurations minimizing the determinant $\det C_{T'_a}^0$ will dominate; as it turns out, this minimal weight is attached to configurations of *branched polymers*, i.e. planar tree graphs. The branched polymer model (see, e.g., Refs. [118, 119]) can be solved exactly and not surprisingly yields the limiting value $\gamma_s^0 = 1/2$. In Section 2.3.3 we will see that for pure gravity, i.e. the case $D = 0$, a value different from mean-field behaviour, namely $\gamma_s^0 = -1/2$ is realized. Bounds similar to (2.64) can be found for higher-genus surfaces, see Ref. [10] and references therein.

Considering the long-distance behaviour of the m -loop or m -point functions, we define the inverse correlation length or *mass gap* $m(\mu)$ as the limit⁴

$$m^h(\mu) = - \lim_{r \rightarrow \infty} \frac{\ln G_\mu^h(r)}{r}, \quad (2.65)$$

where $G_\mu^h(r) = G_\mu^h(0, x)$, $|x| = r$. The proof of the existence of the indicated limit is technically somewhat intricate [7, 10]. It follows from a sub-additivity property of the two-point function, namely

$$G_\mu^h(r_1 + r_2) \geq G_\mu^h(r_1)G_\mu^h(r_2). \quad (2.66)$$

Qualitatively, the origin of this relation is quite obvious if we consider the (suitably normalized) 2-loop function $G_\mu^h(l_1, l_2)$ as the probability of the propagation of a string from l_1 to l_2 , where $|l_1| = |l_2|$. Then, the probability of the string to propagate from l_1 to l_2 through a *fixed* intermediate position, corresponding to the rhs of Eq. (2.66), is naturally smaller than the probability for it to propagate through *any possible* intermediate position, represented by the lhs of (2.66) [8]. It can also be shown that $m^h(\mu) \geq 0$ for $\mu > \mu_0$ and $m^h(\mu)$ is a decreasing function of μ . It is not proved (for the most general case), but almost certainly true, that $m^h(\mu)$ really vanishes at $\mu = \mu_0$, i.e. that the correlation length $1/m^h(\mu)$ diverges at the critical point μ_0 .

From the definition (2.65) of the mass gap we infer the following long distance behaviour of the correlator

$$G_\mu^h(r) \sim e^{-m^h(\mu)r}, \quad r \gg 1/m^h(\mu). \quad (2.67)$$

If the mass scales to zero, which is essential for the existence of a well-defined continuum limit, we associate this scaling with the critical exponent ν :

$$m^h(\mu) \sim (\mu - \mu_0)^{\nu^h}. \quad (2.68)$$

The exponent ν is expected to be independent of the genus h . As will be demonstrated in Section 2.3.5 ν is related to the fractal structure of the lattices characterized by the Hausdorff dimension d_H as $\nu = 1/d_H$. The exponents ν or d_H are not known exactly for the general case, i.e., two-dimensional quantum gravity coupled to conformal matter with central charge $C = D$. On the other hand, the short distance behaviour of the 2-point function defines the *anomalous dimensions* η^h as

$$G_\mu^h(r) \sim r^{d-1} \frac{1}{r^{d-2+\eta^h}}, \quad r \ll 1/m^h(\mu), \quad (2.69)$$

⁴For the quantum gravity (and not the string theory) point of view, the two-point function will be explicitly defined in terms of geodesic distance, see below Section 2.3.5.

where the additional factor r^{d-1} stems from the average over spherical shells implied in considering $G_\mu^h(r)$. In view of the scaling of the mass $m^h(\mu)$ to zero at the critical point $\mu = \mu_0$, the limits of long and short distance considered in Eqs. (2.67) and (2.69) can be alternatively interpreted in terms more natural for statistical physicists: since the region $r \ll 1/m^h(\mu)$ eventually covers the whole triangulation as $\mu \rightarrow \mu_0$, (2.69) describes the correlator in the vicinity of the critical point (the scaling region), whereas the exponential decay (2.67) is valid off criticality. Combining the definition (2.58) of the susceptibility with the scaling properties (2.60), (2.68) and (2.69) we find

$$(\mu - \mu_0)^{-\gamma_s^0} \sim \int dr G_\mu^0(r) = \int_0^{1/m^0(\mu)} dr r^{1-\eta} \propto (1/m^0(\mu))^{2-\eta} \sim (\mu - \mu_0)^{-\nu(2-\eta)}, \quad (2.70)$$

i.e. the *Fisher scaling relation*

$$\gamma_s^0 = \nu^0(2 - \eta^0). \quad (2.71)$$

Finally, considering the exponential decay of the 1-loop function $G_\mu^0(l)$ for a large planar loop l enclosing an area A ,

$$G_\mu^0(l) \sim A^{\beta^0} e^{-\sigma^0(\mu)A}, \quad (2.72)$$

defines the *string tension* for spherical surfaces, $\sigma^0(\mu)$, which can be interpreted as the surface tension of a membrane attached to the “frame” l . It can be shown [120] that the string tension $\sigma^0(\mu) \geq 1$, such that it does *not* scale to zero as $\mu \rightarrow \mu_0$. As will be shown below in Section 2.3.7 this implies that the physical, re-scaled string tension defined from the continuum limit becomes infinite.

2.3.3 The combinatorial solution

The problem of the Polyakov string (2.13) embedded in $D = 0$ dimensions, i.e. pure Euclidean quantum gravity in two dimensions can be solved exactly with a generating function technique known as the *loop equation*. An alternative formulation of this system in term of a *matrix integral*, which can also be performed analytically, will be sketched in the next section.

To dynamically control the presence and weight of boundaries in the triangulations, we add a *boundary term* to the discretised Einstein-Hilbert action of Eq. (2.48) at

fixed topology h , i.e.

$$S_T[\mu; \kappa_1, \dots, \kappa_b] = \mu N_2 + \sum_{i=1}^b \kappa_i n_i \quad (2.73)$$

should denote the action of a simplicial manifold T with b punctures enclosed by boundary polygons of geodesic lengths $n_i = n(l_i)$; the κ_i thus play the rôle of *boundary cosmological constants*. Using the abbreviations

$$w_{N_2, n_1, \dots, n_b}^h = \sum_{T_a \in \mathcal{T}_a(h, N_2; n_i)} \frac{1}{\tilde{C}(T_a)} \quad (2.74)$$

for the number of triangulations of genus h with b boundaries of lengths n_i and defining *fugacities* of triangles and boundary links,

$$\mathbf{m} = e^{-\mu}, \quad \mathfrak{k}_i = e^{\kappa_i}, \quad (2.75)$$

the loop functions (2.52) for fluctuating loop lengths n_i and at $D = 0$ now read

$$G_{\mathbf{m}}^h(\mathfrak{k}_1, \dots, \mathfrak{k}_b) = \sum_{N_2} \sum_{n_1, \dots, n_b} w_{N_2, n_1, \dots, n_b}^h \mathbf{m}^{N_2} \mathfrak{k}_1^{-n_1} \dots \mathfrak{k}_b^{-n_b}, \quad (2.76)$$

whereas the loop functions for fixed boundary lengths⁵ n_i , the *Hartle-Hawking wave functionals* [121], are given by

$$G_{\mathbf{m}}^h(n_1, \dots, n_b) = \sum_{N_2} w_{N_2, n_1, \dots, n_b}^h \mathbf{m}^{N_2}. \quad (2.77)$$

Obviously both kinds of loop functions are related by a Laplace transform as

$$G_{\mathbf{m}}^h(\mathfrak{k}_1, \dots, \mathfrak{k}_b) = \sum_{n_1, \dots, n_b} \mathfrak{k}_1^{-n_1} \dots \mathfrak{k}_b^{-n_b} G_{\mathbf{m}}^h(n_1, \dots, n_b) \quad (2.78)$$

From a combinatorial point of view, the $G_{\mathbf{m}}^h(\mathfrak{k}_1, \dots, \mathfrak{k}_b)$ can thus be considered as the *generating functions* of the numbers $w_{N_2, n_1, \dots, n_b}^h$.

Considering the effect of simple surgery operations on the triangulations that change the number of triangles or the number of boundary links by units of one, corresponding to a multiplication by factors of \mathbf{m} , \mathbf{m}^{-1} , \mathfrak{k} or \mathfrak{k}^{-1} , one can derive the following recursion relation for the generating function for planar triangulations ($h = 0$) [15]⁶:

$$g_0(\mathbf{m}, \mathfrak{k}) = \mathbf{m} \mathfrak{k} g_0(\mathbf{m}, \mathfrak{k}) + \frac{1}{\mathfrak{k}} g_0^2(\mathbf{m}, \mathfrak{k}), \quad (2.79)$$

⁵Note that the $n(l_i)$ are diffeomorphism invariant quantities.

⁶The relation originally derived by Tutte [15] is for a slightly different class of triangulations and includes corrections for the smallest triangulations; it thus look slightly more complicated than the relation given.

where

$$g_h(\mathbf{m}, \mathfrak{k}_1, \dots, \mathfrak{k}_b) = G_{\mathbf{m}}^h(\mathfrak{k}_1, \dots, \mathfrak{k}_b) \mathfrak{k}_1^{-1} \cdots \mathfrak{k}_b^{-1}. \quad (2.80)$$

Eq. (2.79), known as the *loop equation* (a form of the Dyson-Schwinger equation), should be understood order by order in the variables \mathbf{m} and \mathfrak{k} . This type of equation can be used to iteratively generate the numbers $w_{N_2, n_1, \dots, n_b}^h$. In the limit of large N_2 closed-form expressions can be given (for a review see, e.g. Ref. [10]); for the case of closed triangulations of general genera h one finds [25]

$$w_{N_2}^h \sim N_2^{\theta_h} e^{\mu_0 N_2} [1 + O(N_2^{-1})], \quad (2.81)$$

where

$$\theta_h = \frac{5h - 7}{2}. \quad (2.82)$$

The number of closed triangulations with N_2 triangles grows exponentially as indicated in Section 2.3.1 with a power-law correction characterized by the exponents θ^h . These exponents are related to the string susceptibility exponents γ_s^h as follows. Consider the partition function at fixed topology

$$Z^h(\mu) = \sum_{N_2=0}^{\infty} e^{-\mu N_2} \mathcal{Z}^h(N_2), \quad (2.83)$$

where $\mathcal{Z}(N_2) = w_{N_2}^h$ denotes the *canonical* partition function at fixed volume. Inserting the expression (2.81) into this equation, we have⁷

$$Z^h(\mu) \sim \sum_{N_2=0}^{\infty} e^{-(\mu - \mu_0) N_2} N_2^{\theta_h} \sim (\mu - \mu_0)^{-(\theta_h + 1)}. \quad (2.84)$$

Recalling that via Eqs. (2.59) and (2.60) $Z^h(\mu) \sim (\mu - \mu_0)^{2 - \gamma_s^h}$, it follows that $\theta^h = \gamma_s^h - 3$ and thus

$$\gamma_s^h = \frac{5h - 1}{2}. \quad (2.85)$$

Especially, for planar surfaces $h = 0$, one finds $\gamma_s^0 = -1/2$ in contrast to the mean-field result $\gamma_s^0 = 1/2$. Along the same lines also the counting of surfaces consisting not only of triangles, but of arbitrary polygons, is possible [122, 123].

⁷Concerning the last equality, consider the continuum expression

$$\int_0^{\infty} dN_2 e^{-(\mu - \mu_0) N_2} N_2^{\theta_h} = \frac{\Gamma(\theta_h + 1)}{(\mu - \mu_0)^{\theta_h + 1}}.$$

2.3.4 Matrix models

An alternative path of derivation of the central result (2.81) for the number of triangulations of a given number of triangles is given by the analysis of *matrix integrals* (for reviews see, e.g., Refs. [6, 23, 124]), originally considered by 't Hooft for the large- N limit of QCD [19]; in fact, the concept of “loop equations” has been originally developed in the context of matrix models.

Consider the Taylor expansion of the zero-dimensional field theory integral

$$\int d\phi e^{-\frac{1}{2}\phi^2 + \frac{g}{3}\phi^3} = \sum_{k=0}^{\infty} \int d\phi e^{-\frac{1}{2}\phi^2} \frac{1}{k!} \left(\frac{g\phi^3}{3} \right)^k \equiv \sum_{k=0}^{\infty} \frac{1}{k!} \left(\frac{g}{3} \right)^k \langle \phi^{3k} \rangle, \quad (2.86)$$

where ϕ is a simple, real-valued variable. Introducing an external source J , the occurring terms can be written as

$$\int d\phi e^{-\phi^2/2} \phi^n = (-i)^n \frac{\partial^n}{\partial J^n} \int d\phi e^{-\phi^2/2 + iJ\phi} \Big|_{J=0} = \frac{\partial^n}{\partial J^n} e^{-J^2/2} \Big|_{J=0}. \quad (2.87)$$

Since each derivative $\partial/\partial J$ brings down a factor of J , after setting $J = 0$ only *pairs* of such derivatives give contributions without factors of J , which thus do not vanish. Therefore, one has a zero-dimensional version of *Wick's theorem* (see, e.g., Ref. [125]),

$$\langle \phi_1 \cdots \phi_n \rangle = \sum_{\text{perm}(i_1, \dots, i_n)} \langle \phi_{i_1} \phi_{i_2} \rangle \cdots \langle \phi_{i_{n-1}} \phi_{i_n} \rangle. \quad (2.88)$$

Associating with each factor $\phi^3/3$ a vertex with three external lines,



the expansion of (2.86) corresponds to the pairwise connection of vertices via links. The resulting ϕ^3 Feynman graphs are generic, “thin” graphs without an orientation of the plaquettes; this is obviously not enough structure for the triangulation of Riemannian surfaces (even though these graphs are interesting in their own right, see e.g. Refs. [126–128]). Therefore, consider the more general integral

$$W(g, N) \equiv \int d\phi e^{-\frac{1}{2}\text{Tr}\phi^2 + \frac{g}{3\sqrt{N}}\text{Tr}\phi^3} \equiv \sum_{k=0}^{\infty} \frac{1}{k!} \left(\frac{g}{3\sqrt{N}} \right)^k \langle \text{Tr}\phi^{3k} \rangle, \quad (2.89)$$

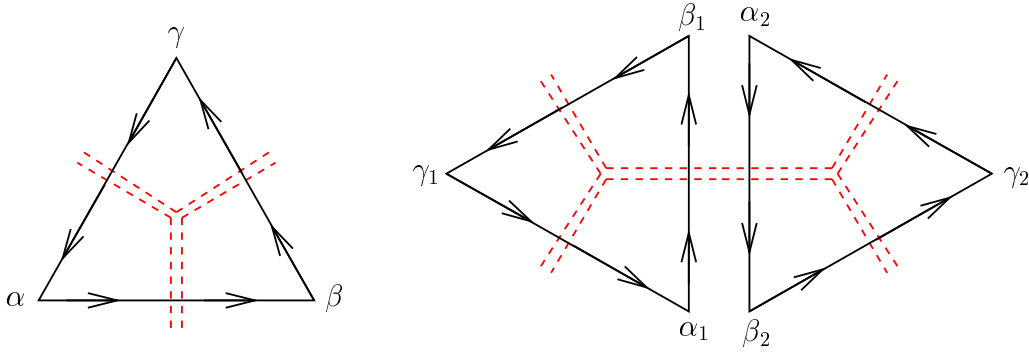


Figure 2.5: The Wick expansion of the matrix integral (2.89) corresponds to the gluing of oriented triangles mediated by the matrix indices.

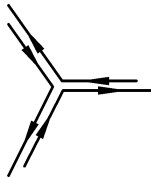
where now ϕ is a $N \times N$ Hermitian matrix and

$$d\phi \equiv \prod_{\alpha \leq \beta} d \operatorname{Re} \phi_{\alpha\beta} \prod_{\alpha < \beta} d \operatorname{Im} \phi_{\alpha\beta}. \quad (2.90)$$

Then, again, the expansion is given by the combination of all possible Wick contractions of $(\operatorname{Tr} \phi^3)^k$ and the two-point function is

$$\langle \phi_{\alpha\beta} \phi_{\alpha'\beta'} \rangle = \int d\phi e^{-\frac{1}{2} \sum_{\alpha\beta} |\phi_{\alpha\beta}|^2} \phi_{\alpha\beta} \phi_{\alpha'\beta'} = \delta_{\alpha\beta'} \delta_{\beta\alpha'} \quad (2.91)$$

Then, via the pairing of the indices of ϕ , the corresponding vertices receive a ribboned, “fat” structure,



leading to orientable plaquettes of the surface. In terms of the triangulation, i.e. the dual lattice of the ϕ^3 graph, the “fat” structure can be understood as follows: to each factor $\operatorname{Tr} \phi^3$ we associate a triangle and to each term $\phi_{\alpha\beta} \phi_{\beta\gamma} \phi_{\gamma\alpha}$ contributing to $\operatorname{Tr} \phi^3$ a labelling of the vertices of the triangle by α, β, γ in cyclic order; thus, the element $\phi_{\alpha\beta}$ corresponds to the oriented link between vertices α and β . Then the Kronecker δ symbols of Eq. (2.91) ensure that each link (α, β) is identified with an oppositely oriented link (β', α') . This is illustrated in Fig. 2.5.

In this way, the integral (2.89) corresponds to a sum over closed, orientable triangulations of $N_2(T) = k$ triangles, which are, however, possibly disconnected. Making

use of a common trick in field-theory [125], taking the *logarithm* of (2.89) kills all disconnected contributions, leaving only connected surfaces. Summing over Eq. (2.91) it is obvious that each vertex of the triangulation picks up a factor of N , such that the overall weight of a triangulation T is given by

$$g^{N_2(T)} N^{N_0(T) - N_2(T)/2} \frac{1}{C(T)} = g^{N_2(T)} N^{\chi(T)} \frac{1}{C(T)}. \quad (2.92)$$

Note that the factorial $k!$ in (2.89) is partially cancelled against the number of permutations of the triangles, resulting in the symmetry factor $1/C(T)$. In view of Eq. (2.48), the identifications

$$N = e^{4\pi\lambda}, \quad g = e^{-\mu} \quad (2.93)$$

let us conclude that

$$Z(\mu, \lambda) = \ln \frac{W(g, N)}{W(0, N)} \quad (2.94)$$

is the partition function of the two-dimensional Euclidean quantum gravity problem. Note that the Hermiticity of the considered matrices is essential for the orientability of the triangles and thus the surfaces; using real symmetric matrices instead makes the two indices α and β indistinguishable, thus generating both orientable and non-orientable triangulations. From the weights (2.92) it is obvious that the *planar limit* $N \rightarrow \infty$ leaves only triangulations with minimal $\chi = 2 - 2h$, i.e. with $h = 0$. On the other hand, in the limit $N = 1$ we recover the case of generic, “thin” graphs, where all genera come with equal weights. From the discussion up to this point it should be clear that the partition function $Z(\mu, \lambda)$ defined in this way — as a sum over topologies — is divergent and should therefore be considered as a symbolic representation of the collection of all orders of a large- N expansion,

$$Z(\mu = -\ln g, \lambda = \frac{\ln N}{4\pi}) = \sum_{h=0}^{\infty} N^{2-2h} Z^h(\mu) = \sum_{h=0}^{\infty} N^{2-2h} \sum_{N_2=0}^{\infty} g^{N_2} \mathcal{Z}^h(N_2). \quad (2.95)$$

The leading term of this expansion, i.e. the limit $N \rightarrow \infty$ (the planar theory), can be computed exactly via the saddle-point method to give [16]

$$\mathcal{Z}^0(N_2) = \frac{8^{N_2} \Gamma(\frac{3}{2}N_2)}{(N_2 + 2)! \Gamma(\frac{1}{2}N_2 + 1)} \stackrel{N_2 \rightarrow \infty}{\sim} N^{-7/2} e^{N_2 \ln 12\sqrt{3}}. \quad (2.96)$$

Comparing with the result (2.81) we find agreement for the planar case and the additional information that the critical value of the cosmological constant for this particular model is given by

$$\mu_0 = \ln(12\sqrt{3}). \quad (2.97)$$

As mentioned above, the matrix model approach is very closely related to the combinatorial ansatz leading to the loop equations. For example, the numbers $g_h(g = \mathbf{m}, \mathbf{k}_1, \dots, \mathbf{k}_b)$ can be directly computed within the matrix model scheme. If we denote (in contrast to the above notation) by $\langle \cdot \rangle$ an average with respect to the measure

$$W^{-1}(g, N) e^{-\frac{1}{2}\text{Tr}\phi^2 + \frac{g}{3\sqrt{N}}\text{Tr}\phi^3} d\phi, \quad (2.98)$$

the generating function g_h is given by

$$g_h(g, \mathbf{k}_1, \dots, \mathbf{k}_b) = N^{b-2} \sum_{k_1, \dots, k_b} \frac{\langle \text{Tr} \phi^{k_1} \dots \phi^{k_b} \rangle_{\text{conn}}}{\mathbf{k}_1^{k_1+1} \dots \mathbf{k}_b^{k_b+1}}, \quad (2.99)$$

where $\langle \cdot \rangle_{\text{conn}}$ denotes the connected part of the correlation function.

With the same technique further models can be considered by changing the matrix potential. Re-writing (2.89) more generally as

$$W(g, N) = \int d\phi e^{-N\text{Tr}V(\phi, g)}, \quad V(\phi, g) = \frac{1}{2}\phi^2 - \frac{g}{3}\phi^3 \quad (2.100)$$

which involves a re-scaling $\phi \rightarrow \sqrt{N}\phi$ for technical purposes, it can be easily seen that, for example, the quartic potential,

$$V(\phi, g) = \frac{1}{2}\phi^2 - \frac{g}{4}\phi^4, \quad (2.101)$$

generates the ensemble of “fat” ϕ^4 graphs, i.e. the dual lattices of *quadrangulations*. Matrix potentials with more than one matrix or with non-Hermitian matrices correspond to a dressing of the random graphs with matter variables, see Section 2.4.3.

2.3.5 Fractal structure of the lattices

Considering the features of geometrical observables on random triangulations of the introduced type, it quickly becomes clear that the intrinsic geometry of the lattices is far from smooth; instead they have a very ragged and highly detailed structure reminiscent of *fractals*. This can most eye-catchingly be demonstrated by considering an embedding of the two-dimensional lattices in \mathbb{R}^3 trying to faithfully reproduce the property of equal edge lengths of the triangles, cf. Fig. 2.6.

The prevailing parameter characterizing the “fractality” of a structure is the *Hausdorff dimension* with respect to a given metric, which defines how a suitably defined

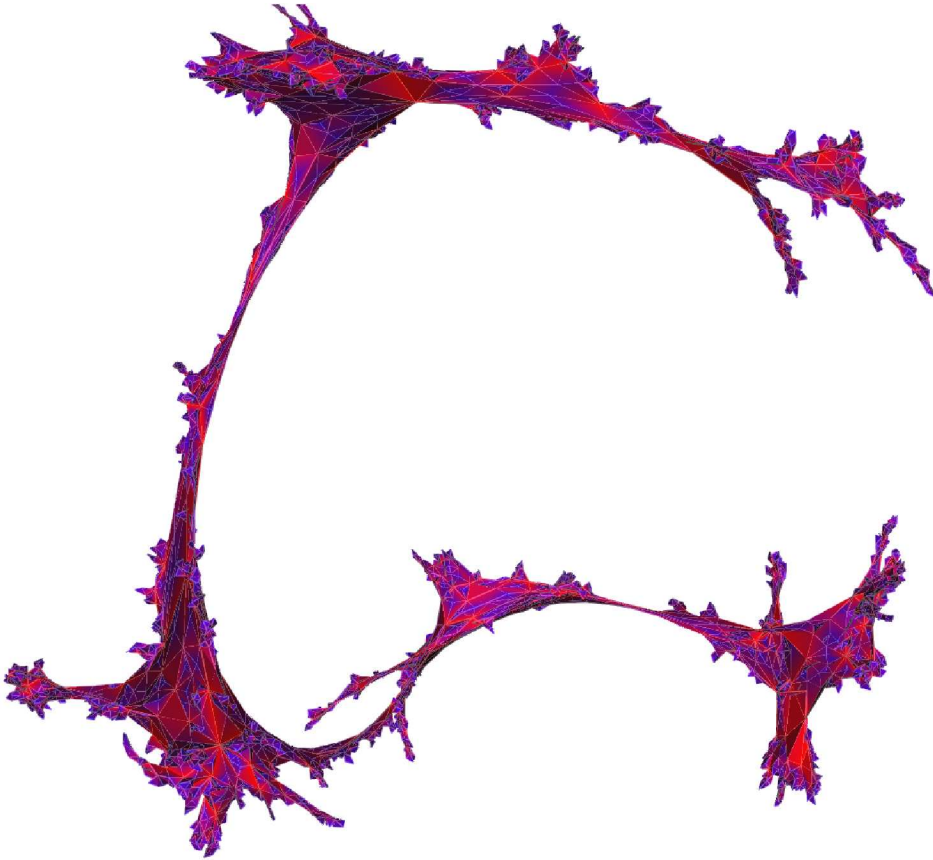


Figure 2.6: Embedding of a two-dimensional dynamical triangulation with $N_2 = 5000$ triangles in \mathbb{R}^3 . The triangulation is taken from the same ensemble as the more smooth looking example of Fig. 2.4. The embedding was generated with an adaptive algorithm trying to avoid edge intersections while uniformizing the edge lengths, cf. Appendix B.

measure of linear length of the structure scales in terms of its volume. For the case of the Polyakov string embedded in \mathbb{R}^D the *mean square extent* with respect to distances in the embedding space and in the *grand-canonical ensemble* of a varying number of triangles N_2 is defined as

$$\langle x^2 \rangle_\mu \equiv \frac{\int dx x^2 G_\mu^h(0, x)}{\int dx G_\mu^h(0, x)}. \quad (2.102)$$

Then, define the average number of triangles in this ensemble as

$$\langle N_2 \rangle_\mu \equiv - \frac{\int dx \frac{\partial}{\partial \mu} G_\mu^h(0, x)}{\int dx G_\mu^h(0, x)}, \quad (2.103)$$

since differentiating (2.52) with respect to μ brings down a factor of $-N_2$. In the limit

$$d_H = \frac{1}{2} \lim_{\mu \rightarrow \mu_0} \frac{\ln \langle x^2 \rangle_\mu}{\ln \langle N_2 \rangle_\mu} \quad (2.104)$$

exists, it is called the *external Hausdorff dimension* of the considered ensemble of random surfaces; otherwise, we set $d_H = \infty$. Alternatively, it can be defined in the canonical ensemble of a fixed number of triangles N_2 as

$$d_H = \frac{1}{2} \lim_{N_2 \rightarrow \infty} \frac{\ln \langle x^2 \rangle_{N_2}}{\ln N_2}. \quad (2.105)$$

Thus, the average area of the surfaces asymptotically scales as

$$\langle N_2 \rangle_\mu \sim \langle x^2 \rangle_\mu^{d_H/2}, \quad \mu \rightarrow \mu_0. \quad (2.106)$$

For the case of pure quantum gravity, no embedding in a target space (apart from illustrative purposes) is available. Recall from (2.52) that the two-point function in $D = 0$ is defined as

$$G_\mu^h(r) = \sum_{N_2=1}^{\infty} e^{-\mu N_2} \sum_{T_a \in \mathcal{T}_a(h, N_2; p_1, p_2)} \delta(d(p_1, p_2) - r), \quad (2.107)$$

where $d(p_1, p_2)$ denotes the internal geodesic distance of Eq. (2.40). Then, we define the analogue of the mean square extent as

$$\langle r^2 \rangle_\mu \equiv \frac{\sum_{r=0}^{\infty} r^2 G_\mu^h(r)}{\sum_{r=0}^{\infty} G_\mu^h(r)}, \quad (2.108)$$

and the average number of triangles by

$$\langle N_2 \rangle_\mu \equiv - \frac{\sum_{r=0}^{\infty} \frac{\partial}{\partial \mu} G_\mu^h(r)}{\sum_{r=0}^{\infty} G_\mu^h(r)}. \quad (2.109)$$

Then, the *internal Hausdorff dimension*⁸ d_h is given by

$$d_h = \frac{1}{2} \lim_{\mu \rightarrow \mu_0} \frac{\ln \langle r^2 \rangle_\mu}{\ln \langle N_2 \rangle_\mu}. \quad (2.110)$$

Obviously, a similar definition of an intrinsic Hausdorff dimension can also be given for the case of the Polyakov string. Both dimensions are not necessarily equal; instead, it can be shown that $d_h \leq d_H$, which is intuitively obvious since in the

⁸Note the use of upper case and lower case subscripts H resp. h to distinguish the external and internal Hausdorff dimensions.

embedding space one does not have to follow the surface to travel between two points, such that distances are shorter there.

It should be emphasized that there are several slightly different definitions of internal Hausdorff dimensions which have been used in the literature (see, e.g. Refs. [7, 10, 11]). It is possible, for instance to drop the summation over r in (2.109) and consider

$$\langle N_2(r) \rangle_\mu = -\frac{\frac{\partial}{\partial \mu} G^h_\mu(r)}{G^h_\mu(r)} = \frac{\partial}{\partial \mu} \ln G^h_\mu(r) \sim r^{d_h}, \quad r \rightarrow \infty, \quad m(\mu)r = \text{const.} \quad (2.111)$$

From the definition of the mass $m(\mu)$ Eq. (2.67) and its scaling as $\Delta\mu \rightarrow 0$ Eq. (2.68), we have

$$\langle N_2(r) \rangle_\mu \sim \frac{\partial m(\mu)}{\partial \mu} r \sim m(\mu)^{\frac{\nu-1}{\nu}} r \propto r^{1/\nu}, \quad (2.112)$$

where we have used the scaling assumption $m(\mu)r = \text{const}$ above. Thus we have the scaling relation

$$\nu = 1/d_h, \quad (2.113)$$

which together with the Fisher scaling relation (2.71) determines the number of independent exponents.

Numerically, the intrinsic Hausdorff dimension of two-dimensional simplicial quantum gravity is observed to be much larger than the topological dimension $d = 2$; in fact, from the transfer-matrix approach described below, it is known that $d_h = 4$ for pure quantum gravity in two dimensions. This is related to the structure of the lattices as depicted in Fig. 2.6. The triangulation appears as composed from “blobs” of all length scales attached to the main surface through *necks* of only a few links; in this way, the whole “universe” can be decomposed into a tree of *baby universes*, which are (apart from the cut-off a) similar to the whole graph [29]. The relation between the “baby universes” and the fractal dimension can be understood by means of the real space renormalization group approach [11, 129, 130]. Defining an elementary blocking transformation by cutting from the original ensemble a all last generation *minimal neck baby universes* (minBUs), i.e. those at the leafs of the “baby universe” tree, to result in a renormalized ensemble b , the scales of lengths and areas are related asymptotically as [11]

$$\frac{\langle N_2 \rangle_b}{N_{2,a}} \sim \left(\frac{\langle r^2 \rangle_b}{\langle r^2 \rangle_a} \right)^{d_r/2}, \quad N_2 \rightarrow \infty, \quad (2.114)$$

where the averages are here performed in the canonical, fixed N_2 ensemble. The dimension d_r is numerically found to approach $d_h = 4$ for large graphs; thus, the

“baby-universe” structure of the triangulations is closely related to their fractal structure.

Two further dimensions are commonly considered in connection with random surfaces, see e.g. Refs. [11, 12]. Let $n_{T_a}(r)$ be the number of vertices p_i of a given triangulation T_a which have a distance $d(0, p_i) \leq r$ from a marked point 0. Then the *branching dimension* d_b describes the scaling of the average of the number of disconnected components $n_0(r)$ of the *boundary* of the ball of volume $n_{T_a}(r)$,

$$\langle n_0(r) \rangle \sim r^{d_b}, \quad N_2 \rightarrow \infty. \quad (2.115)$$

Numerical simulations give results of $d_b \gtrsim 2.5$, signalling indeed a large rate of branching. Finally, to define the *spectral dimension* d_s consider, in the continuum theory, the diffusion of a test particle on the surface; in the short-time limit, the average probability density for the particle to return to its initial point scales as

$$\langle P(t) \rangle \sim t^{-d_s/2}, \quad t \rightarrow 0. \quad (2.116)$$

Surprisingly, it can be shown that, despite of the rather large Hausdorff dimension, the spectral dimension stays at the flat-space value $d_s = 2$ for quantum gravity with $C \leq 1$ [131]. However, the fractal structure of the triangulations (i.e., the dimension d_h) can still be seen also in the diffusion process, namely in the scaling of the travelled distance of the particle with time,

$$\langle r \rangle_t \sim t^{1/d_h}, \quad t \rightarrow \infty. \quad (2.117)$$

2.3.6 Further results and the transfer matrix

Considering the scaling relations (2.71) and (2.113) and the exact values of the string susceptibility exponent of Eq. (2.85), one needs one further exponent, either d_H , η or ν for a complete description of the critical behaviour of the two-dimensional quantum gravity problem. This missing information can be extracted from a differential equation for the generating functions of the b -loop function mentioned above in Section 2.3.3 [28] or, alternatively, from a *transfer-matrix* formulation of the problem [26, 27].

Starting from the general generating function (2.76), one can again derive a recursion relation of the Schwinger-Dyson type with respect to elementary operations at the entrance and exit loops of the correlators known as the “peeling” and “slicing”

decomposition of the triangulations, see, e.g., Ref. [10]. Then, writing down and solving a differential equation mimicking the elementary steps used, the correlator in the scaling limit is found to be [28],

$$G_\mu^0(r) \sim \frac{\cosh [\beta(\Delta\mu)^{1/4}r]}{\sinh^3 [\beta(\Delta\mu)^{1/4}r]}, \quad (2.118)$$

where $\beta = \sqrt{6} \exp(\mu_0)$. In the two limits considered in Section 2.3.2 this reduces to

$$G_\mu^0(r) \sim e^{-2(\Delta\mu)^{1/4}\beta r}, \quad r \gg 1/m(\mu), \quad (2.119)$$

and

$$G_\mu^0(r) \sim r^{-3}, \quad r \ll 1/m(\mu), \quad (2.120)$$

such that from the definitions (2.67), (2.69) and (2.68) we read off the exponents $\nu = 1/4$ and $\eta^0 = 4$. From the scaling relation $d_h = 1/\nu$ we infer an internal Hausdorff dimension $d_h = 4$.

Using the above-mentioned slicing decomposition, which divides a triangulation in spherical shells of triangles of equal geodesic distance from a given point or loop, it is possible to write down a transfer-matrix formulation of the problem. Besides deriving the result (2.118), this method even yields the so-called *loop distribution function* $\rho^0(r, l)$ for spherical topology, that is: $\rho(r, l)dl$ is the average number of loops of lengths between l and $l + dl$ at the boundary of a ball with radius r on the triangulations. In the thermodynamic limit $N_2 \rightarrow \infty$ of the canonical ensemble of planar lattices ($h = 0$) it is given by [26]

$$\rho^0(l, r) = \frac{3}{7\sqrt{\pi}r^2} \left[x^{-5/2} + \frac{1}{2}x^{-3/2} + \frac{14}{3}x^{1/2} \right] e^{-x}, \quad (2.121)$$

where $x = r^2/l$ is a scaling variable. From this very detailed result, it is also possible to derive the scaling dimensions $d_h = 4$ and $d_b = 3$ which are related to the singular behaviour of the distribution. In view of the possibility of a transfer-matrix formulation, the question arose, whether one could find the quantum Hamiltonian corresponding to the continuum limit of the transfer matrix which would yield a completely new description of two-dimensional quantum gravity. There, proper time is identified with the geodesic distance of the slicing decomposition. Approaches in this direction can be found in Refs. [132, 133].

2.3.7 The continuum limit

As usual in lattice field theory, for the definition of a proper continuum limit the mass $m(\mu)$ (the inverse correlation length) has to scale to zero as μ approaches μ_0 , since only then the resulting continuum expressions become independent of the chosen cut-off. As mentioned above, the scaling of the mass cannot be proven analytically for the string model and thus has to be assumed there; for the quantum gravity model, on the other hand, from the continuum expression of the two-point function Eq. (2.118), the scaling of the mass is obvious. For the case of the string model, the edge length \mathfrak{a} of the simplicial manifolds corresponds to a length scale cut-off ϵ in the physical embedding space \mathbb{R}^D . For a non-vanishing physical mass m_{phy} with dimension $1/[\text{length}]$ to appear, the coupling μ has to be sent to μ_0 depending on ϵ such that

$$m(\mu(\epsilon)) = m_{\text{ph}}\epsilon, \quad (2.122)$$

i.e., we take the limit $\epsilon \rightarrow 0$ and $\mu \rightarrow \mu_0$ in a correlated way, keeping m_{ph} fixed. Alternatively, the continuum limit can be considered in terms of the intrinsic cut-off $\mathfrak{a} \rightarrow 0$ of the triangulations. The relation between the scaling of both quantities is found from inserting the physical area of the surface $A = N_2 \mathfrak{a}^2$ and the physical distance $x_{\text{phy}} = x\epsilon$ into Eq. (2.106) to give

$$\mathfrak{a}^2 \sim \epsilon^{d_H}. \quad (2.123)$$

The physical string tension σ_{phy} as a surface tension has the dimension of $1/\epsilon^2$, such that it should obey

$$\sigma(\mu(\epsilon)) = \sigma_{\text{phy}}\epsilon^2. \quad (2.124)$$

Since, as mentioned in Section 2.3.2 $\sigma(\mu) \geq 1$, this equation can only be fulfilled for $\sigma_{\text{phy}} = \infty$. Physically, this means that the imagined membrane attached to the frame of a loop l is flat up to spiky outgrowths of almost no area. This corresponds to the picture of a branched polymer model, which is known to be the right description in the mean-field limit of large target dimensionality D . In terms of the equivalent model of quantum gravity coupled to D Gaussian fields, this corresponds to the observed collapse of the geometry to a branched polymer phase for central charge $C = D > 1$. Obviously, a physically sensible string theory would consider physical dimensions $D > 1$. However, a scaling of the string tension can be possibly established by adding higher (extrinsic) curvature terms H^k , $k = 1, 2, 3, \dots$ to the action (2.13), see Ref. [10].

In the quantum gravity model, we want a physical cosmological constant μ_{phy} , which has dimension $1/[\text{length}]^2$. Thus, the renormalization condition is

$$\mu - \mu_0 = \mu_{\text{phy}} \mathbf{a}^2, \quad (2.125)$$

which from the scaling of the mass implies that

$$m(\mu(a)) = m_{\text{phy}} \mathbf{a}^{2\nu} = m_{\text{phy}} \mathbf{a}^{2/d_h}, \quad (2.126)$$

equivalent to Eq. (2.122)⁹. Then, in terms of the intrinsic cut-off \mathbf{a} , the continuum distance is $r_{\text{phy}} = r \mathbf{a}^{2\nu}$ and the continuum propagator $G^h(r_{\text{phy}}, \mu_{\text{phy}})$ should be defined as

$$G^h(r_{\text{phy}}, \mu_{\text{phy}}) = \lim_{a \rightarrow 0} a^{2\nu(1-\eta^h)} G_{\mu(a)}^h(r_{\text{phy}} a^{-2\nu}), \quad (2.127)$$

which from Eqs. (2.69) and (2.67) yields the intended asymptotic behaviour

$$\begin{aligned} G^h(r_{\text{phy}}, \mu_{\text{phy}}) &\sim r_{\text{phy}}^{1-\eta^h}, & r_{\text{phy}} &\ll m_{\text{phy}}^{-1}, \\ G^h(r_{\text{phy}}, \mu_{\text{phy}}) &\sim e^{-m_{\text{phy}} r_{\text{phy}}}, & r_{\text{phy}} &\gg m_{\text{phy}}^{-1}. \end{aligned} \quad (2.128)$$

The summation over topology Eq. (2.53) is divergent without further modifications. Thus, there is no naïve scaling with respect to the gravitational coupling λ . Within the matrix model formulation (2.89), the sum over topologies translates into the large- N expansion in the dimension of the matrices given in Eq. (2.95). It turns out that the critical points $g_0^h = e^{\mu_0^h}$ of the fixed-topology partition functions do not depend on the genus h [10]. From the dependence (2.85) of the string susceptibility exponent on the genus,

$$(2 - \gamma_s^h) = (2 - \gamma_s^0)(1 - h) = (2 - \gamma_s^0)\chi(h)/2, \quad (2.129)$$

and the scaling of the fixed genus partition functions,

$$Z^h(\mu) \sim f^h(\mu - \mu_0)^{2-\gamma_s^h}, \quad (2.130)$$

it is obvious that the contribution of the higher genus surfaces increases as $\mu \rightarrow \mu_0$. Thus it might make sense to take the limits $\mu \rightarrow \mu_0$ and $N \rightarrow \infty$ in a correlated manner. Renormalizing the gravitational coupling constant as

$$e^{\lambda_{\text{phy}}} = N(\mu - \mu_0)^{(2-\gamma_s^0)/2}, \quad (2.131)$$

⁹Note, however, that here in contrast to Eq. (2.122), the intrinsic Hausdorff dimension has to be used.

the scaling limit of the all genus partition function Eq. (2.95) can be written as

$$Z(\mu, \lambda) \sim \sum_{h=0}^{\infty} N^{\chi(h)} (\mu - \mu_0)^{(2-\gamma_s^0)\chi(h)/2} \sim \sum_{h=0}^{\infty} e^{\lambda_{\text{phy}} \chi(h)} f_h. \quad (2.132)$$

This limit, i.e. $\mu \rightarrow \mu_0$ and $N \rightarrow \infty$ with $\lambda_{\text{phy}} = \text{const}$ is known as the *double scaling limit* of the matrix model Eq. (2.89) [134–136]. To give an interpretation to this representation, one can, for example, define a matrix model which has the same perturbation expansion as the one given above, but is convergent. It turns out, however, that there are no real solutions to the resulting *Painlevé I equation* [10]. Thus, the problem of a non-perturbative definition of the sum over topologies is still unsolved.

2.4 Dressing Dynamical Triangulations

As mentioned several times, the D -dimensional Polyakov string can be interpreted as two-dimensional quantum gravity coupled to conformal matter of central charge $C = D$. Most of the results presented above, however, only apply to the case of pure gravity, i.e. $D = 0$. As discussed in Section 2.3.2, the limit $D \rightarrow \infty$ corresponds to the mean-field limit of the model, which has $\gamma_s^0 = 1/2$ indicating the collapse of geometry to branched polymers. On the other hand, the opposite limit $D \rightarrow -\infty$ corresponds to the classical or Liouville limit of the theory with surfaces regular up to a finite number of points with defects, which has $\gamma_s^h = -\infty$. Additionally, the non-unitary case $D = -2$ can be solved exactly due to a cancellation in the determinant (2.62) to give $\gamma_s^0 = -1$, $d_H = \infty$ [21]¹⁰. The behaviour in between these two extremal cases and the question, where transitions between the different types of behaviour occur, will be discussed now.

2.4.1 Annealed and quenched disorder

Concerning disorder in systems of statistical mechanics, two fundamentally different scenarios are commonly distinguished. Symbolically expressing the probability distribution of the disorder degrees of freedom by P and the partition function for

¹⁰Note that $d_H = \infty$ makes a proper continuum scaling impossible due to the relation (2.123).

a given realization of the disorder by $Z(\{\mu_i\}; P)$, the partition function for the full disordered system is given by

$$Z(\{\mu_i\}) = [Z(\{\mu_i\}; P)]_P, \quad (2.133)$$

where the square brackets indicate averaging with respect to P and the μ_i are some coupling parameters. Expectation values can usually be expressed as derivatives of the free energy, i.e.

$$\langle A \rangle_{\text{annealed}} \sim \frac{\partial^k \ln Z(\{\mu_i\})}{\partial \mu_{i_1} \cdots \partial \mu_{i_k}}. \quad (2.134)$$

Thus, the thermal and disorder averages are performed on the same level; this scenario is commonly referred to as that of *annealed disorder*. On the other hand, one can compute expectation values on the level of the partition function $Z(\{\mu_i\}; P)$ and perform the disorder average afterwards, i.e.

$$\langle A \rangle_{\text{quenched}} \sim \left[\frac{\partial^k \ln Z(\{\mu_i\}; P)}{\partial \mu_{i_1} \cdots \partial \mu_{i_k}} \right]_P, \quad (2.135)$$

defining the notion of *quenched disorder*. Physically, both schemes correspond to limiting cases with respect to the time scales of fluctuation of thermal and disorder related properties. While in the annealed scenario both types of variables fluctuate on the same time scale, quenched disorder can be considered as an approximation to the situation that the disorder degrees of freedom fluctuate so much slower than the thermal variables that they can effectively be considered as fixed on the time scale of thermal fluctuation.

The relevance of the application of quenched disorder to a system of statistical mechanics undergoing a continuous phase transition in terms of a change of the universal critical properties such as critical exponents depends on the rate at which the fluctuations of the pseudo-critical couplings induced by the disorder die out in the thermodynamic limit. A systematic analysis of this observation leads to the Harris [69] and Harris-Luck [71] criteria for the relevance of quenched disorder. For the case of a first-order phase transition of the model on regular lattices, one can expect a disorder-induced weakening to a continuous transition. Numerical simulations of Potts models on the quenched ensemble of random planar ϕ^3 graphs indicate a change of the critical exponents in the cases with a second-order phase transition and a softening to continuous phase transitions of the first-order cases [137, 138]. An attempt to calculate the exponents for the quenched case from those observed in the annealed case via use of the *replica trick* (see, e.g., Ref. [139]) can be found in Ref. [140].

The scenario of annealed disorder in the framework of dynamical triangulations corresponds to the coupling of matter to the gravitating universe such that the geometry induces effects on the matter, which in turn has a *back-reaction* onto the geometry of space-time. The corresponding partition function at fixed topology is very similar to the expression for the loop correlator (2.52) and reads

$$Z(\mu, \{\beta_i\}; a) = \sum_{N_2=1}^{\infty} e^{-\mu a^2 N_2} \sum_{T_a \in \mathcal{T}_a(h, N_2)} \frac{1}{C(T_a)} \int \prod_{i=1}^{N_2} d\sigma_i e^{-S_{\text{matter}}[\{\sigma_i\}; \{\beta_i\}]}, \quad (2.136)$$

where the σ_i are matter variables located on the triangles of the simplicial manifold and the β_i are matter-related coupling parameters¹¹. For annealed disorder, the general relevance criteria of Harris and Luck do not apply. However, it is found that the coupling of $C \leq 1$ conformal matter to two-dimensional gravity is always relevant and, even more, it can be demonstrated, how the scaling dimensions of the matter part renormalize due to the coupling to gravity.

2.4.2 The KPZ/DDK solution

According to Polyakov, the bosonic string can be interpreted as two-dimensional quantum gravity coupled to D bosonic fields. Since the action (2.13) does not contain any coupling constants to tune, it describes a *critical* theory of central charge $C = D$. Thus, solving the Polyakov string model or an approximation to it is directly related to the problem of quantum gravity coupled to matter. By considering the problem in the light-cone gauge and making some *ad hoc* assumptions, Knizhnik, Polyakov and Zamolodchikov [30] could evaluate the partition function of the coupled system for the planar case $h = 0$. This solution was later on re-derived in the conformal gauge and extended to higher genera by David [31] and Distler and Kawai [32]. For the string susceptibility exponent γ_s^h they find¹²

$$\gamma_s^h - 2 = \chi(h) \frac{D - 25 - \sqrt{(25 - D)(1 - D)}}{24}. \quad (2.137)$$

Furthermore, if we consider a primary field ϕ of the matter theory which has conformal weight Δ before coupling it to the gravitating surface, the operator picks up

¹¹It is, of course, also possible to place the matter variables on other types of fundamental building blocks of the simplicial complex such as the vertices or the edges.

¹²Note, that the number 25 (and in the following 24) occurring in this formula is related to the fact that the Polyakov string is critical in $D = 26$, where the gravity theory essentially decouples from the matter part.

a gravitational dressing leading to a new weight $\tilde{\Delta}$ satisfying the KPZ equation [30],

$$\tilde{\Delta} - \Delta = -\frac{1}{2}\alpha^2\tilde{\Delta}(\tilde{\Delta} - 1), \quad (2.138)$$

where

$$\alpha = -\frac{1}{2\sqrt{3}}(\sqrt{25-D} - \sqrt{1-D}). \quad (2.139)$$

Solving for $\tilde{\Delta}$, we have

$$\tilde{\Delta} = \frac{\sqrt{1-D+24\Delta} - \sqrt{1-D}}{\sqrt{25-D} - \sqrt{1-D}}. \quad (2.140)$$

Note that from the formulae (2.137) and (2.140) γ_s^h and $\tilde{\Delta}$ pick up imaginary parts as $D > 1$, such that the considered calculation breaks down in this limit. The case $D = 1$ is marginal and therefore logarithmic corrections to scaling are expected. This effect is known as the $C = 1$ barrier of two-dimensional quantum gravity. Note that due to this effect this calculation does not shed much light on the string theory originally considered since, of course, there dimensions $D > 1$ constitute the case of interest. However, from the point of view of coupling matter to quantum gravity it is highly valuable, since most of the interesting “toy models” of matter have central charge $C \leq 1$. Especially, consider the unitary conformal *minimal models* of Ref. [141] with central charge

$$C = 1 - \frac{6}{m(m+1)}, \quad m \in \mathbb{N}, \quad m \geq 2, \quad (2.141)$$

which include the critical versions of, e.g., the Ising model ($C = 1/2$) and the 3-state Potts model ($C = 4/5$). Within the minimal series of models, a theory is completely described by the central charge C . In contrast, for the limiting case $C = 1$ there are several inequivalent realizations such as the 4-state Potts model, a single massless scalar field or the 6-vertex model. For the minimal series, from Eq. (2.137) we have $\gamma_s^0 = -1/m$.

On the same lines of argumentation, i.e. within the Liouville scheme of quantum gravity, by considering diffusion on a fluctuating geometry an expression for the intrinsic Hausdorff dimension of the coupled system can be derived [142],

$$d_h = 2 \frac{\sqrt{25-C} + \sqrt{49-C}}{\sqrt{25-C} + \sqrt{1-C}}, \quad (2.142)$$

where $0 \leq C \leq 1$. However, an alternative conjecture was made based on matrix model calculations reading [143]

$$d_h = \frac{24}{\sqrt{1-C}(\sqrt{1-C} + \sqrt{25-C})}. \quad (2.143)$$

Both formulas agree for $C = 0$, i.e. pure gravity, but yield different results for the other cases. In contradiction to both results, numerical simulations are consistent with a constant $d_h = 4$ for all $0 \leq C \leq 1$ [51, 144]. For non-unitary matter $C < 0$ the predictions of Eq. (2.142) agree with numerical results for $C = -2$ [116]. Also, the classical limit $C \rightarrow -\infty$ yields $d_h = 2$ as expected. Thus Eq. (2.142) could be correct for $C < 0$.

What happens beyond the $C = 1$ barrier? Numerically, in all cases studied the string susceptibility exponent is found to become positive [54], accompanied by a divergence of the sizes of the “baby universes” in the thermodynamic limit¹³. For $C \gtrsim 4$ the value of γ_s^0 seems to approach the branched polymer value $1/2$. However, the question whether the collapse to branched polymers takes place exactly at $C = 1$ or at some larger “critical” central charge is still unsettled. However, a renormalization group study of the problem revealed that the systems probably collapse to the branched polymer phase as C exceeds 1 [53]; but the attraction to the new fixed point is only logarithmic, explaining that numerically one has to go to rather large central charges $C \gtrsim 4$ to see the branched polymer phase. The mechanism leading to the geometry of branched polymers, is physically very plausible for the case of multiple copies of spin models generating $C > 1$. First, the interaction between geometry and matter is strongest in the vicinity of the critical point, since only there the spins are correlated on a macroscopic scale. Now, in the critical region typical spin configurations consist of clusters of differently oriented spins of all sizes, such that a considerable amount of the total free energy of the system is “stored” in the surfaces (i.e., closed curves in two dimensions) separating patches of different spin alignments. Since the corresponding free energy is approximately proportional to the *area* (or length) of the phase boundaries, it is energetically favourable to have minimal length boundaries between patches of equal spin alignment. On a regular lattice, the minimal surface of a patch of fixed volume cannot become arbitrarily small, but is just given by the shape of a sphere. On a dynamical triangulation, however, at each point there can grow a *baby universe* of arbitrarily large volume connected to the mother universe only via a very small number of links. Thus, if only the energies associated to the matter interactions are strong enough (i.e., if C is large enough), the free energy of the critical system will be minimal for lattices composed of “blobs” (“baby universes”) decorated with

¹³Note that, since the central charge is additive, large C can be generated by coupling several copies of, say, Ising models to the lattices.

spins of equal alignment and connected to each other by a minimal number of links. This is exactly the geometry of branched polymers.

2.4.3 Matrix model examples

As mentioned above in Section 2.3.4, changing the matrix potential of Eq. (2.89) allows for the representation of decorated random graphs. For the case of an Ising type decoration this was first noted by Kazakov [33, 145], who considered a two-matrix model with the potential

$$V(\phi_1, \phi_2; c, g) = \frac{1}{2}(\phi_1^2 + \phi_2^2) - c\phi_1\phi_2 - \frac{g}{4}(\phi_1^4 + \phi_2^4), \quad (2.144)$$

where the matrix integral (2.100) should now be performed with respect to both Hermitian $N \times N$ matrices ϕ_1 and ϕ_2 . Obviously, the quartic terms $\phi_{1/2}^4$ generate “fat” graphs with vertices of co-ordination number four instead of three, the dual lattices of which correspond to dynamical *quadrangulations* instead of triangulations. Remembering that the propagators $\text{Tr } \phi^2$ correspond to the *links* of the graphs, there are now two types of such bonds,

$$\begin{aligned} \langle \text{Tr } \phi_1^2 \rangle &= \langle \text{Tr } \phi_2^2 \rangle = \frac{1}{1 - c^2}, \\ \langle \text{Tr } \phi_1 \phi_2 \rangle &= \frac{c}{1 - c^2}. \end{aligned} \quad (2.145)$$

Setting $c = \exp(-2\beta)$, we have

$$\begin{aligned} \langle \text{Tr } \phi_{1/2}^2 \rangle &= \frac{\sqrt{c}}{1 - c^2} \exp(\beta), \\ \langle \text{Tr } \phi_1 \phi_2 \rangle &= \frac{\sqrt{c}}{1 - c^2} \exp(-\beta), \end{aligned} \quad (2.146)$$

such that one can interpret the two types of vertices as the two alignments of Ising spins placed on the ϕ^4 vertices and the bond (or propagator) weights correspond to those of the Ising model up to the common factor $\sqrt{c}/(1 - c^2)$ which is just an overall shift of the energy scale. Using the methods developed in [17, 18] one can derive a set of parametric equations in the planar limit $N \rightarrow \infty$ which, to each order in the number of vertices, allows to compute the partition function of the Ising model coupled to planar ϕ^4 graphs [145]. In the limit of diverging graph size, the model is found to exhibit a continuous, third-order phase transition at the critical coupling

$$\beta_c = \ln 2, \quad (2.147)$$

and with matter-related critical exponents $\alpha = -1$, $\beta = 1/2$ and $d_h\nu = 3$ [34], which differ from the Onsager exponents for the Ising model on a flat lattice of $\alpha = 0$, $\beta = 1/8$ and $d_h\nu = 2$.¹⁴ The exponents found agree with those predicted from the KPZ equation (2.140). The string susceptibility exponent is found to stay at the pure gravity value $\gamma_s^0 = -1/2$ everywhere except at the critical point $\beta = \beta_c$, where it is shifted to $\gamma_s^0 = -1/3$. Thus, only at the critical point the back-reaction of the matter part on the fluctuating lattices is strong enough to influence their universal properties. It turns out that the slightly generalized matrix potential

$$V(\phi_1, \phi_2; , c, g, h) = \frac{1}{2}(\phi_1^2 + \phi_2^2) - c\phi_1\phi_2 - \frac{g}{4}(e^h \phi_1^4 + e^{-h} \phi_2^4), \quad (2.148)$$

which obviously corresponds to the additional application of a magnetic field h to the Ising spins, still corresponds to a solvable matrix integral, leading to the remarkable fact that the two-dimensional Ising model in the field can be solved exactly when coupled to fluctuating planar random lattices, in contrast to the usual static square lattice case. From the above discussion it should be obvious that a very similar treatment is possible for the case of the Ising model coupled to planar ϕ^3 graphs, i.e., the duals of dynamical triangulations. The critical exponents found there do not differ from the ϕ^4 case as expected [34]. When considering a torus of genus $h = 1$, the critical exponents of the matter part remain unchanged and $\gamma_s^1 = 2$ as expected from (2.137) [146]. Note that $\gamma_s^1 = 2$ is valid for *all* inverse temperatures β since according to (2.137) for $h = 1$, γ_s does not depend on the central charge. This effect is connected to the speciality of $h = 1$ that it has a logarithmically diverging partition function.

More complicated systems can be expressed in terms of non-Hermitian matrix models. For instance, the 6-vertex model coupled to “fat” ϕ^4 graphs is described by the matrix potential [72, 73]

$$V(\phi, \phi^\dagger; b, c) = \phi\phi^\dagger - b\phi^2\phi^{\dagger 2} - \frac{c}{2}(\phi\phi^\dagger)^2. \quad (2.149)$$

This will be discussed further in Chapter 5 below.

¹⁴It has been noted that the new exponents actually coincide with those of the *spherical model* in three dimensions. It is not clear, however, whether this has a physical explanation.

Chapter 3

The Simulation of Dynamical Graphs

The combination of methods presented in the previous chapter led to a rather complete solution of the pure two-dimensional Euclidean quantum gravity problem. Quite a few of these results could only be achieved by the guidance of numerical work, i.e., Monte Carlo (MC) simulations of dynamical triangulations. Furthermore, the exact information about the coupling of matter to random lattices is by far not as complete as in the pure case, such that numerical simulations are still very well in place.

Since the final objective of this thesis are simulations of the 6-vertex model, which necessarily lives on a four-valent lattice, the well-known methods for simulations of dynamical triangulations and the dual ϕ^3 graphs have to be generalized and adapted to the cases of dynamical quadrangulations resp. the dual ϕ^4 graphs. As it turns out, the main issue in this context is the ergodicity of the chosen set of update moves. This will be tested against known exact results for the cases of pure gravity and an Ising model coupled to the graphs. An analysis of the autocorrelation times of the algorithm calls for more sophisticated update procedures found in the baby-universe surgery method. If not stated otherwise, all discussions of the present chapter exclusively apply to the case of dynamical polygonifications and their dual graphs in two dimensions.

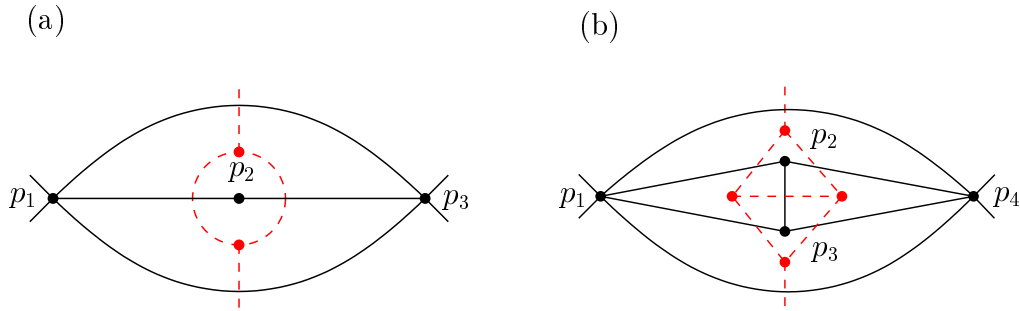


Figure 3.1: Singular contributions of the *self-energy type* in a non-combinatorial triangulation. Black solid lines show the triangulation part, red dashed lines indicate the corresponding ϕ^3 graphs. (a) The three points p_1 , p_2 and p_3 define two distinct triangles; the two points p_1 and p_3 define two distinct links. The dual ϕ^3 graph has a local self-energy contribution. (b) The points p_1 and p_4 define two distinct links, but all triangles are combinatorially unique. The dual ϕ^3 has a non-local self-energy contribution or non-trivial two-point subgraph.

3.1 Graph Ensembles

3.1.1 Triangulations and ϕ^3 graphs

In the theoretical discussions of the previous chapter we have omitted some necessary comments on how the considered triangulations or the dual ϕ^3 graphs look like in detail. The notion of simplicial manifolds presented in Section 2.2.3 describes the “naïve” picture of a triangulation composed entirely of regular, non-degenerate triangles, which is in agreement with the representation of Fig. 2.1. Formally, the regularity of the triangulations was described in Section 2.2.3 by the fact that the reference points defining an r -simplex should be geometrically independent in \mathbb{R}^d and their considered linear combination (2.35) should be convex. On the other hand, similar assumptions were obviously not made when considering the matrix integrals of Section 2.3.4; there, *all* orientable graphs of a given topology that can be formed by connecting a given number of vertices with three links each were considered, including possibly occurring degeneracies.

Consider the case of two-dimensional dynamical triangulations. In combinatorial terms, the question of singular contributions can be split into two parts. First, in a *regular* triangulation the simplicial building blocks of the manifold, i.e. the links and triangles, are uniquely defined by two (links) or three (triangles) vertices. The

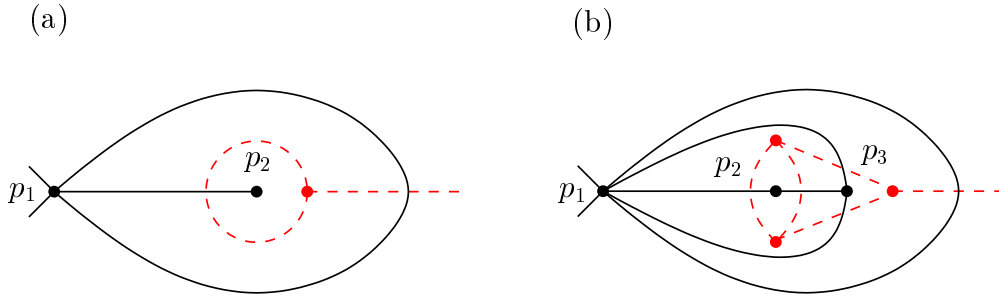
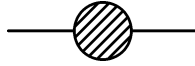


Figure 3.2: Singular contributions of the *tadpole type* in a non-combinatorial triangulation. (a) A triangle is defined by only two points p_1 and p_2 ; p_1 corresponds to two identified points, the link $\langle p_1 p_2 \rangle$ represents two identified links. The dual graph has a tadpole contribution. (b) The point p_1 corresponds to two identified points, but no links are identified. The dual ϕ^3 graph contains a one-point subgraph.

degenerate cases of two vertices defining two distinct links or three vertices defining two distinct triangles can occur in the same situation, which is depicted in Fig. 3.1(a). It corresponds to the possibility that two triangles share *two* links instead of one. The dual graph of this situation is called a *self-energy* contribution, that is, a loop of length two in the ϕ^3 graph. More generally, considering only degenerate *links* of the triangulation, these singularities are described as double links of the triangulation or (non-trivial) two-point subgraphs of the dual ϕ^3 graph, cf. Fig. 3.1(b). A two-point subgraph is a component of a graph which can be disconnected by deleting two edges.

The second singular contribution stems from the possibility of vertices to loose not only their geometrical independence, but to become actually *identified*, which leads to an originally degenerate triangle as depicted in Fig. 3.2(a), where also two links have become identified. In the ϕ^3 graph this situation corresponds to a *tadpole insertion*, alternatively described as a loop of length one. Relaxing the condition of identified links, a general singularity of this type is given by a degenerate triangle (without identification of links) or, in the dual graph, a one-point subgraph, cf. 3.2(b). By “one-point subgraph” we mean a subgraph that can be cut off from the rest of the graph by deleting one vertex.

From the point of view of the ϕ^3 graphs, the most general singular contributions can be considered as “dressings” of the elementary self-energy and tadpole diagrams. Thus, a non-trivial two-point subgraph can be depicted as a dressed self-energy,



and a one-point subgraph corresponds to a dressed version of the tadpole graph,



In the following, the short terms “self-energy” and “tadpole” will be often used synonymously for the contributions depicted above.

Note that degenerate triangles or one-point subgraphs can only occur when the graph also contains non-trivial two-point subgraphs¹, whereas the latter are independent of the existence of one-point subgraphs. Thus, it makes sense to consider the following hierarchy of three ensembles of triangulations and dual ϕ^3 graphs:

- (a) The exclusion of all singular contributions to the triangulations defines the *regular ensemble* of dynamical triangulations and their dual ϕ^3 graphs. All simplicial building blocks of the triangulations are combinatorially distinct, no double links or degenerate triangles occur. In the dual ϕ^3 graphs, non-trivial two-point insertions and one-point subgraphs are forbidden.
- (b) Allowing two vertices of the triangulation to define two distinct links and three vertices to define two distinct triangles, but still excluding degenerate triangles, defines a set of triangulations which we call *restricted singular ensemble*. There, the triangulations can contain double links, and the dual ϕ^3 graphs include non-trivial two-point subgraphs as depicted in Fig. 3.1.
- (c) In addition including degenerate triangles, i.e., triangles defined by only two points, one arrives at the *singular ensemble* of dynamical triangulations. The corresponding ϕ^3 graphs are unrestricted and contain non-trivial two-point subgraphs as well as the one-point subgraphs depicted in Fig. 3.2.

Obviously, the regular ensemble corresponds to the class of triangulations considered in the context of simplicial manifolds in the previous chapter. On the other hand,

¹This is obvious from Fig. 3.2(b), where the right vertex of the ϕ^3 graph has to be connected to a two-point subgraph to become a co-ordination point of the graph.

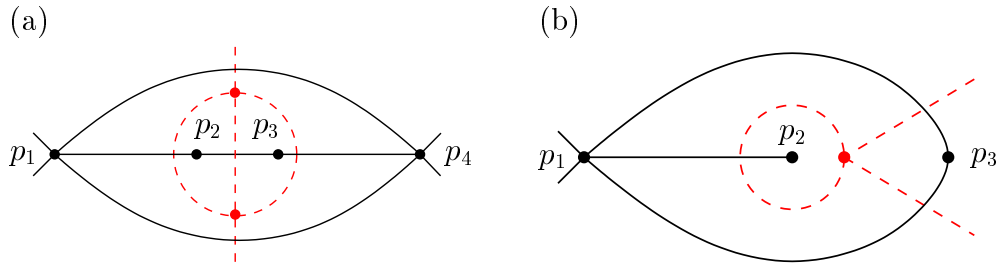
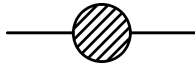


Figure 3.3: Singular contributions in a non-combinatorial quadrangulation (black solid lines) and the dual ϕ^4 graph (red dashed lines). (a) The points p_1 and p_4 define two distinct links; the points p_1, \dots, p_4 define two distinct quadrangles. The ϕ^4 graph contains a self-energy subgraph. (b) The points p_1, p_2 and p_3 define a degenerate quadrangle. The dual ϕ^4 graph contains a tadpole insertion.

the matrix models of Section 2.3.4 naturally generate graphs of the singular ensemble. Especially, the result (2.96) for the partition function of pure, two-dimensional Euclidean quantum gravity and the critical value $\mu_0 = \ln(12\sqrt{3})$ of the cosmological constant are for triangulations of the singular ensemble. The restricted singular ensemble can be considered as an interpolation between the other two extremal cases.

3.1.2 Quadrangulations and ϕ^4 graphs

The notion of combinatorial uniqueness is easily generalized to the case of more general polygonifications of manifolds. Here, we consider the case of *quadrangulations* and their dual ϕ^4 graphs. Figure 3.3 shows the local versions of singular insertions of the self-energy and tadpole types². The general, non-local versions of these subgraphs change slightly. The dressed self-energy subgraph is the same as before,



but the dressed tadpole graph now has two external lines,



²The tadpole-type contribution for the ϕ^4 case is sometimes also called *seagull* graph.

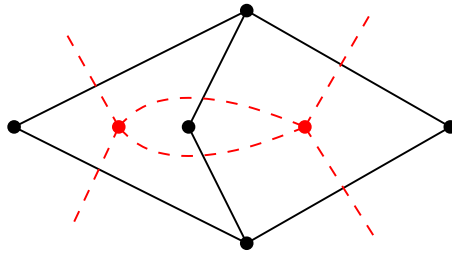


Figure 3.4: A double link in a random ϕ^4 graph (red dashed lines) does not correspond to a singularity of the corresponding quadrangulation (black solid lines), but indicates that two quadrangles share two edges instead of one. These configurations are forbidden in the “strict” ensemble.

Note from Fig. 3.3(a) that the local self-energy contribution is now no longer represented by a double link, but a triple link in the dual graph. Double links in the ϕ^4 graphs can nevertheless occur and correspond to quadrangles sharing two sides instead of one as depicted in Fig. 3.4. Thus, in the quadrangulation they do not correspond to singular contributions in the sense of a loss of the combinatorial distinctness of the fundamental building blocks. However, it turns out that in certain situations it is favourable to also exclude double links from the ϕ^4 graphs. Thus, for the case of quadrangulations or ϕ^4 graphs we define an additional ensemble:

- (a’) Quadrangulations of the *strict* ensemble are those quadrangulations of the regular ensemble that do not contain neighbouring quadrangles sharing more than one side. The dual ϕ^4 graphs do not have any multiple links and no one-point or non-trivial two-point subgraphs.

The notion of universality of critical phenomena implies that results for the continuum limit of the theory do not depend on the details of the chosen discretisation, i.e., universal quantities such as critical exponents and universal amplitude ratios should not depend on whether one uses triangulations or quadrangulations and which restrictions on the inclusion of singular contributions are imposed. This has been explicitly checked by matrix model calculations for the case of pure two-dimensional quantum gravity [16, 21] and, among other cases, for the coupling of an Ising model to dynamical triangulations and quadrangulations [34, 35]. Even the rather crude restriction of the dynamical triangulation model to vertices with coordination numbers 5, 6 and 7 does not change its critical behaviour [147]; the same is true when adding an additional R^2 (higher curvature) term to the action [148]. As

ensemble	ϕ^3	ϕ^4
regular	$\ln \frac{256}{27} \approx 2.249$	$\ln \frac{27}{4} \approx 1.910$
restricted singular	$\ln \frac{27}{2} \approx 2.603$	$\ln \frac{196}{27} \approx 1.982$
singular	$\ln 12\sqrt{3} \approx 3.034$	$\ln 12 \approx 2.485$

Table 3.1: Critical value μ_0 of the cosmological constant for the pure two-dimensional dynamical polygonifications model for the cases of triangulations resp. ϕ^3 graphs and quadrangulations resp. ϕ^4 graphs for various graph ensembles. The numbers are taken from Ref. [151]. For the case of the strict ensemble of ϕ^4 graphs there is no exact result available.

mentioned above, the naïve matrix model ansatz counts ϕ^3 resp. ϕ^4 diagrams including all possible singular insertions, that is, it corresponds to the *singular* ensemble of the above classification. Results for the less singular ensembles can be found by explicit renormalization techniques that kill the tadpole and self-energy contributions [16, 149–151]. Alternatively, it can be shown on quite general grounds that the inclusion or exclusion of singular graph contributions does not change the critical behaviour of matrix model theories [152]. Non-universal properties, on the other hand, naturally depend on the ensemble considered. Especially, the critical value μ_0 of the cosmological constant for the case of pure quantum gravity in two dimensions is only given by the value of Eq. (2.97) for the singular ensemble of ϕ^3 graphs. For reference, the values for the other cases are given in Table 3.1.³ Nevertheless, simulations including (at least some) singular contributions in the polygonifications or dual graphs can have some advantages over those in the regular or strict ensembles, since situations have been observed where the finite-size effects decreased with the inclusion of singular contributions [50]. This will be discussed further in Section 3.3.2.

3.2 Simulation of Dynamical Polygonifications

As for regular lattices also for the case of dynamical polygonifications and random graphs a statistical, but exact method for the determination of expectation values

³A value for the *strict* ensemble in the ϕ^4 case is not available since in the Dyson-Schwinger approach of Ref. [151], double links are only *part* of the contribution of dressed four-point vertices which are removed in one step.

and the analysis of phase transitions is given by the Monte Carlo integration technique. There, from a given probability distribution, states are sampled by setting up a Markov chain in the configuration space of the model. Successive states of the Markovian process are connected by a given set of (often local) changes to the system state, which are commonly called the *moves* associated with a specific Monte Carlo dynamics. A proper convergence of this sampling scheme can be guaranteed, when the conditions of *ergodicity* and *detailed balance* are fulfilled. The most important formulae are collected in Appendix A.1. For general introductions see, e.g., Refs. [153–155]. In the next two sections we consider the aspects of ergodicity and detailed balance for the dynamical triangulations (or ϕ^3) model only. The generalization of these results to the case of dynamical quadrangulations of ϕ^4 graphs is presented in Section 3.2.3.

3.2.1 Moves and ergodicity

While ensuring detailed balance is just a matter of correctly setting up the transition probabilities associated to the considered moves, ergodicity is a property of the class of applied moves itself. Stated a bit sloppily, a set of update moves is ergodic, iff starting from an arbitrary point in the state space all of the other points are touched by the Markov chain with finite probability and in finite time⁴. For the simulation of the dynamical triangulations problem, a set of update moves thus must ensure that, for a finite number of simplices, all topologically equivalent triangulations can be generated from each other by a finite series of update moves. This implies that we consider the problem at *fixed topology*, which will be the case for the rest of this thesis.

The notion of equivalence of triangulations is not unique. First, triangulations can be considered homeomorphically equivalent, i.e., connected by a topological homeomorphism. On the other hand, two triangulations are called combinatorially equivalent, iff they can be subdivided into the same triangulation (up to a re-labelling of the simplices), see Section 2.2.3. The claim that both notions itself are equivalent is the “Hauptvermutung” of topology and has been proved true for two and three dimensions, but false for $d \geq 5$. It is true in general dimensions, however, for the case of *smooth* triangulations; on the other hand, for dimensions four and above,

⁴For systems with continuous variables this condition can obviously not be fulfilled. There, one has to consider probability densities instead of probabilities.

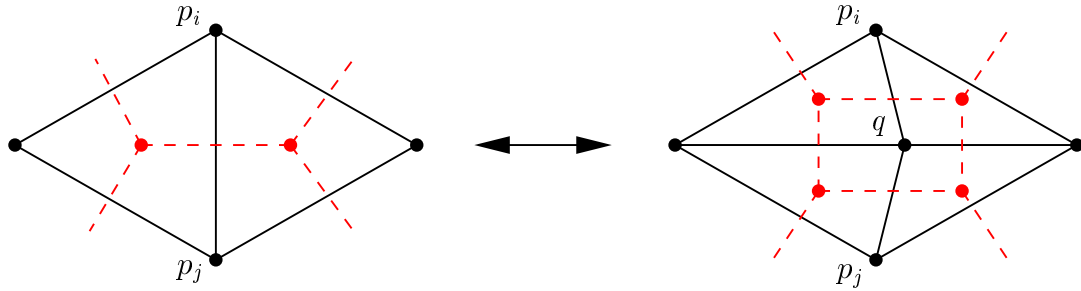


Figure 3.5: Application of the Alexander move [157] to a two-dimensional simplicial manifold (black solid lines) and its dual ϕ^3 graph (red dashed lines). The vertex q is inserted along the link $\langle p_i p_j \rangle$ and its surroundings are triangulated. In the reversed move q is deleted together with the sub-division it generated.

not every topological manifold admits a smooth triangulation, for details see Ref. [156] and references therein. Since we are mainly interested in the case of two dimensions, we can safely concentrate on the notion of combinatorial equivalence. Thus, a set of Monte Carlo update moves will be considered ergodic, if it generates all combinatorially equivalent triangulations.

Such a set of moves has been proposed (in a different context, though) by Alexander [157] for d -dimensional simplicial manifolds. For each face σ of a simplicial manifold M we symbolically write

$$M = \sigma P + Q, \quad (3.1)$$

such that σP denotes all components of M that contain the face σ and Q the complement of σP in M . Then, with respect to a face σ of $M = \sigma P + Q$, the Alexander move is defined by

$$\sigma P + Q \rightarrow q \bar{\sigma} P + Q, \quad (3.2)$$

where q is an additional vertex originally not contained in M and $\bar{\sigma}$ denotes the *boundary* of σ . It turns out [157] that one can concentrate on the case of a link $\sigma = \langle p_i p_j \rangle$ without loss of generality. Here and in the following, we use the notation $\langle p_0 \cdots p_r \rangle$ to symbolize an r -simplex, cf. Section 2.2.3 for a precise definition of this concept. Then, the rule (3.2) instructs one to insert a new vertex q on the link $\langle p_i p_j \rangle$ and re-triangulate the surroundings of the new point. Correspondingly, in the reverse move q and the created parts of the sub-division have to be deleted. This is depicted for the case of two dimensions in Fig. 3.5. It has been shown that all combinatorially equivalent simplicial manifolds can be generated from each other by

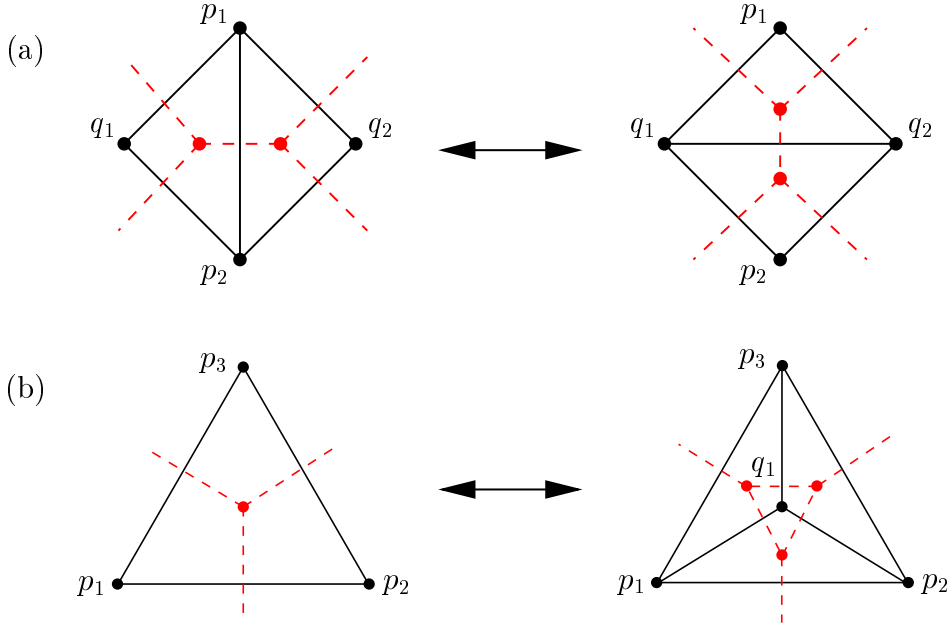


Figure 3.6: The (k, l) moves in two dimensions applied to a simplicial manifold (black solid lines) and the dual ϕ^3 graph (red dashed lines). (a) The $(2, 2)$ or flip move. The product $\langle p_1 p_2 \rangle \overline{\langle q_1 q_2 \rangle} = \langle p_1 p_2 q_1 \rangle + \langle p_1 p_2 q_2 \rangle$ is replaced by $\overline{\langle p_1 p_2 \rangle} \langle q_1 q_2 \rangle = \langle p_1 q_1 q_2 \rangle + \langle p_2 q_1 q_2 \rangle$ and vice versa for the reversed move. (b) The $(3, 1)$ (insertion) and $(1, 3)$ (deletion) moves. In the $(3, 1)$ move the product $\langle p_1 p_2 p_3 \rangle \overline{\langle q_1 \rangle} = \langle p_1 p_2 p_3 \rangle$ is replaced by $\overline{\langle p_1 p_2 p_3 \rangle} \langle q_1 \rangle = \langle p_1 p_2 q_1 \rangle + \langle p_2 p_3 q_1 \rangle + \langle p_3 p_1 q_1 \rangle$.

a series of these Alexander moves [157]. However, for computer simulations these moves are not very convenient, since it is computationally demanding to locally find links and vertices where the moves can be applied, especially in dimensions $d > 2$. Apart from that, they do not allow simulations in the canonical ensemble of a fixed number of triangles.

Therefore, a different set of moves is much more commonly used in numerical simulations. The (k, l) or Pachner moves proposed in Ref. [156] are in d dimensions given by the substitution

$$\langle p_1 \cdots p_l \rangle \overline{\langle q_1 \cdots q_k \rangle} \rightarrow \overline{\langle p_1 \cdots p_l \rangle} \langle q_1 \cdots q_k \rangle, \quad (3.3)$$

where $k + l = d + 2$, $k = 1, \dots, d + 1$. Here, overlining of a simplex denotes the application of the boundary operator to it, where the boundary of an oriented r -

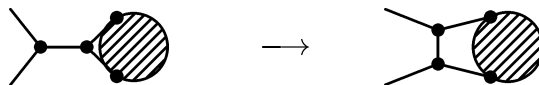
simplex $\langle p_0 \cdots p_r \rangle$ is given by,

$$\overline{\langle p_0 \cdots p_r \rangle} \equiv \sum_{i=0}^r (-1)^i \langle p_0 \cdots \hat{p}_i \cdots p_r \rangle, \quad (3.4)$$

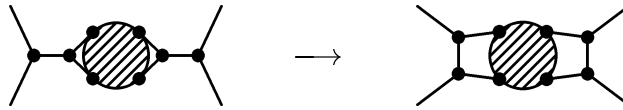
where the vertex p_i under “ $\hat{}$ ” is omitted. The (k, l) move (3.3) is, obviously, only defined if $\langle p_1 \cdots p_l \rangle \overline{\langle q_1 \cdots q_k \rangle}$ is and $\overline{\langle p_1 \cdots p_l \rangle}$ is not originally part of the simplicial manifold. Thus, a (k, l) move replaces the product of an $l - 1$ -simplex and the boundary of a $k - 1$ -simplex with a configuration where the boundary operator is exchanged between the two parts. The inverse of a (k, l) move is an (l, k) move. In two dimensions, one arrives at a $(2, 2)$ move which is its own inverse and a set of mutually inverse moves $(3, 1)$ and $(1, 3)$. These are depicted in Fig. 3.6. The (k, l) moves are known to be equivalent to the Alexander moves in dimensions 2, 3 and 4 [156]. An argument for general dimensions has been given in Ref. [158]. The case of two dimensions is special in the respect that the $(2, 2)$ or flip move alone is known to be ergodic for simulations of the canonical ensemble of a fixed number of triangles N_2 [21, 157]. This ensemble is much more convenient for numerical simulations and, apart from that, provides the possibility of making use of the powerful *finite-size scaling* (FSS) techniques.

Although the presented discussion concentrated on updating the triangulations, it should be obvious from Figs. 3.5 and 3.6 that the Alexander and Pachner moves translate in a natural way to moves in the dual ϕ^3 graphs. Considering the graphs in their own right, by duality the presented statements about ergodicity hold true. For the present work all simulations were performed directly in the language of the graphs.

Note that the mentioned proofs of ergodicity apply to simplicial manifolds only, i.e., in the language of the previous section only for simulations in the *regular ensemble* of dynamical triangulations ergodicity of the (k, l) moves is proven. To proof ergodicity at fixed N_2 for the *restricted singular* and *singular* ensembles also, it suffices to show that every triangulation containing degenerate links or triangles can be transformed to a regular, combinatorial triangulation via a series of flip moves. The possibility to do this can be most easily seen in the dual ϕ^3 graph language. There, a one-point subgraph can be reduced to a regular contribution by a flip move on the vertices adjacent to the external line,



thus removing the singularity. The right vertex of the original graph belongs to the one-point subgraphs, but is drawn outside of it for illustrative purposes. Of course, it can happen that the two external lines of the diagram are themselves connected to the same point, thus producing another one-point subgraph after the flip. However, the flips can always be continued, until the subgraph is connected by at least two lines. For the case of non-trivial two-point subgraphs a similar transformation can be found,



which connects the subgraph by at least three lines to the “mother universe”. Note that the flip move applied in this way cannot produce tadpole insertions, such that one does not leave the restricted singular ensemble if one starts from it. Thus the $(2, 2)$ flip move is ergodic for dynamical triangulations of a fixed number of triangles and the dual ϕ^3 graphs in all of the defined ensembles.

3.2.2 Detailed balance and pseudo grand-canonical simulations

As far as the condition of *detailed balance* is concerned it is obvious, e.g., from Eq. (2.48) that for a fixed number of triangles the weight factors for single triangulations are trivial. Up to overall factors, the only remaining weights are the symmetry factors $C(T_a)$ of the triangulations. However, for labelled triangulations which naturally occur in the context of computer simulations, these are just given by $C(T_a) = N_2!$, which is a constant for fixed N_2 . Therefore, all weight factors are equal, unless additional matter is coupled to the triangulations. The detailed balance condition is then trivially fulfilled for the $(2, 2)$ flip move, such that for simulations in the canonical ensemble each proposed move compatible with the chosen ensemble is accepted.

For simulations in the grand-canonical ensemble of a varying number of triangles, however, a detailed balance check has to be implemented. The Boltzmann weight of a labelled triangulation T is given by

$$W(T) = \frac{1}{N_2(T)!} \frac{\exp[-\mu N_2(T)]}{Z(\mu)}. \quad (3.5)$$

Now, consider a (3, 1) insertion move to a triangulation T' consisting of $N_2(T') = N_2(T) + 2$ triangles. The detailed balance condition for this move reads

$$\frac{e^{-\mu N_2}}{N_2! Z(\mu)} P(T \rightarrow T') = \frac{e^{-\mu(N_2+2)}}{(N_2+2)! Z(\mu)} P(T' \rightarrow T). \quad (3.6)$$

The transition probability $P(T \rightarrow T')$ consists of two parts,

$$P(T \rightarrow T') = P_{\text{apriori}}(T \rightarrow T') P_{\text{akz}}(T \rightarrow T'), \quad (3.7)$$

where P_{apriori} is the probability to randomly select a specific move and P_{akz} is the acceptance probability for the proposed update. For the insertion move we choose a triangle at random, which then is split into three triangles as shown in Fig. 3.6(b); thus,

$$P_{\text{apriori}}(T \rightarrow T') = \frac{1}{N_2(T)}. \quad (3.8)$$

For the opposite (1, 3) deletion move we randomly choose a vertex with co-ordination number three, and the adjacent triangles are replaced by a single triangle. In the dual graph language this corresponds to finding a loop of length three and contracting it to a point; if there are $n_3(T')$ of such loops, we have

$$P_{\text{apriori}}(T' \rightarrow T) = \frac{1}{n_3(T')}. \quad (3.9)$$

Thus, for the detailed balance condition (3.6) to hold, the acceptance probabilities should fulfil

$$\frac{P_{\text{akz}}(T \rightarrow T')}{P_{\text{akz}}(T' \rightarrow T)} = \frac{e^{-2\mu}}{[N_2(T) + 2][N_2(T) + 1]} \frac{N_2(T)}{n_3(T')}. \quad (3.10)$$

Note that this expression is not symmetric with respect to the original and reversed moves. Therefore, the usual Metropolis rule for the acceptance probabilities cannot be applied; instead, we choose $P_{\text{akz}} = r = \text{const}$ for one of the moves and adapt the probability of the opposite move accordingly.

In this thesis we will mainly apply canonical simulations, exploiting their conceptual and technical advantages. However, as will become obvious in Section 3.3, we have some interest in the determination of *ratios* $\mathcal{Z}(N_2)/\mathcal{Z}(N_2 - 2)$ of canonical partition functions. These can be sampled with a different and simpler variant of simulations with varying number of triangles which we call *pseudo grand-canonical* simulations. Suppose that we allow variations of N_2 only in a window $N_{2,\min} \leq N_2 \leq N_{2,\max}$. Then, we consider the sampling of dynamical triangulations in a non-Boltzmann grand-canonical ensemble at $\mu = 0$ with weights

$$\tilde{W}(T) \equiv \frac{1}{Z'(0)}, \quad (3.11)$$

where

$$Z'(0) = \sum_{N_2=N_{2,\min}}^{N_{2,\max}} \mathcal{Z}(N_2). \quad (3.12)$$

In this ensemble, the probability of the appearance of a triangulation with N_2 triangles is

$$P(N_2) = \sum_{T \in \mathcal{T}_{N_2}} \tilde{W}(T) = \frac{\mathcal{Z}(N_2)}{Z'(0)}, \quad (3.13)$$

such that ratios of partition functions can be estimated by

$$\frac{\langle \hat{H}(N_2) \rangle}{\langle \hat{H}(N'_2) \rangle} = \frac{P(N_2)}{P(N'_2)} = \frac{\mathcal{Z}(N_2)}{\mathcal{Z}(N'_2)}, \quad (3.14)$$

where $\hat{H}(N_2)$ denotes the sampled frequency (or histogram) of the occurrence of triangulations with N_2 triangles in the sampling process. Obviously, in this ensemble one has to delimit N_2 at least from above, since otherwise N_2 would diverge (until hitting some computer memory constraints) in the Monte Carlo process of the proposed ensemble. The detailed balance condition for this ensemble reads

$$\frac{1}{N_2(T)} P_{\text{akz}}(T \rightarrow T') = \frac{1}{n_3(T')} P_{\text{akz}}(T' \rightarrow T), \quad (3.15)$$

which is solved by $P_{\text{akz}}(T \rightarrow T') = r$, $r < 1$, and

$$P_{\text{akz}}(T' \rightarrow T) = r \frac{n_3(T')}{N_2(T)} = r \frac{n_3(T')}{N_2(T') - 2}, \quad (3.16)$$

such that the insertion move is accepted with a constant probability r and the acceptance probability of the deletion move can be computed entirely in terms of the properties of T' . If $N_2 = N_{2,\max}$ and an insertion move is tried or $N_2 = N_{2,\min}$ and a deletion move is attempted, the moves are rejected (but nevertheless counted as links of the Markov chain). Since the reversed variants of these moves cannot occur either, detailed balance is not violated. A method related to the approach presented here has been proposed in Ref. [159].

3.2.3 Generalization to quadrangulations

While simulations of dynamical triangulations have been widely applied (see, e.g., Refs. [21, 159–161]), also for the more special cases of modified gravity actions [147, 162] and the coupling of various types of matter to the lattices (see, e.g., Refs.

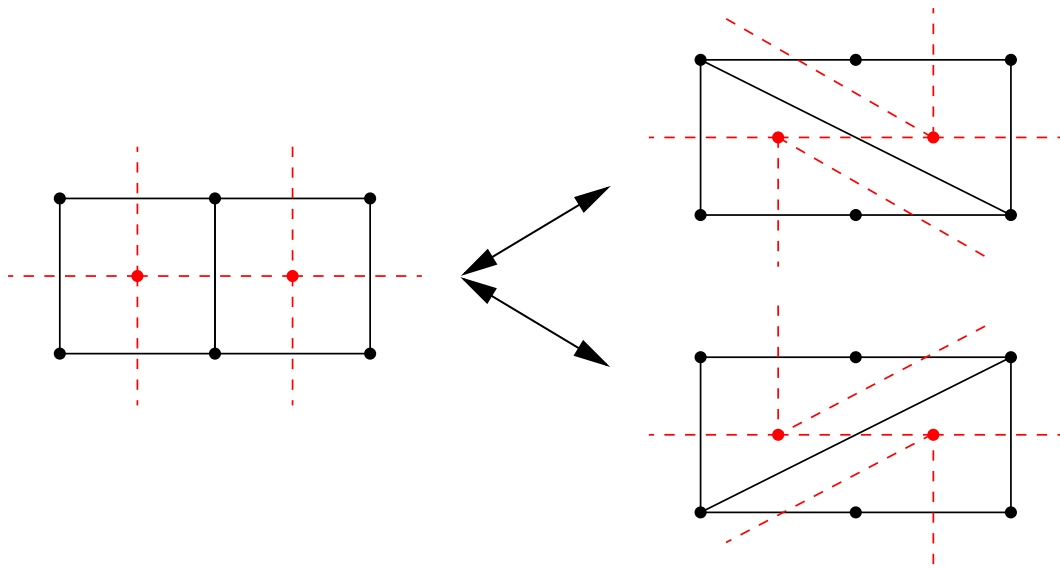
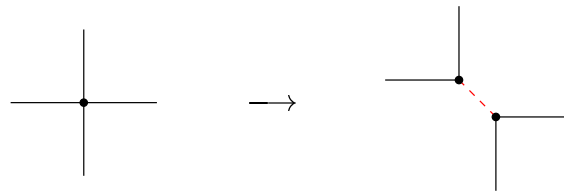


Figure 3.7: Generalization of the $(2, 2)$ link flip move for dynamical triangulations to the case of a random quadrangulation (black solid lines) and the dual ϕ^4 graph (red dashed lines). Note that, in contrast to the triangulation case, there are two inequivalent ways to flip the link between the two squares.

[45, 46, 48, 50–52, 163]), other dynamical polygonifications have attracted much less attention. The only simulations of dynamical quadrangulations we know of are reported in Refs. [49, 74].

As with the simulation of dynamical triangulations, the main issue for the quadrangulation case is the necessity of update moves that ergodically sweep out the space of quadrangulations and the dual ϕ^4 graphs. The rather obvious generalization of the $(2, 2)$ flip move was first proposed in Ref. [49] and is depicted in Fig. 3.7. In Ref. [74] Baillie and Johnston give a justification for this choice of moves in terms of a break-up of the squares of the quadrangulation into triangles. Obviously, each vertex of the dual ϕ^4 graph can be broken up into two connected ϕ^3 vertices,



Taking into account the two possibilities to do such a break-up, one ends up with four possible break-ups of the dual diagram of two adjacent squares as shown in Fig.

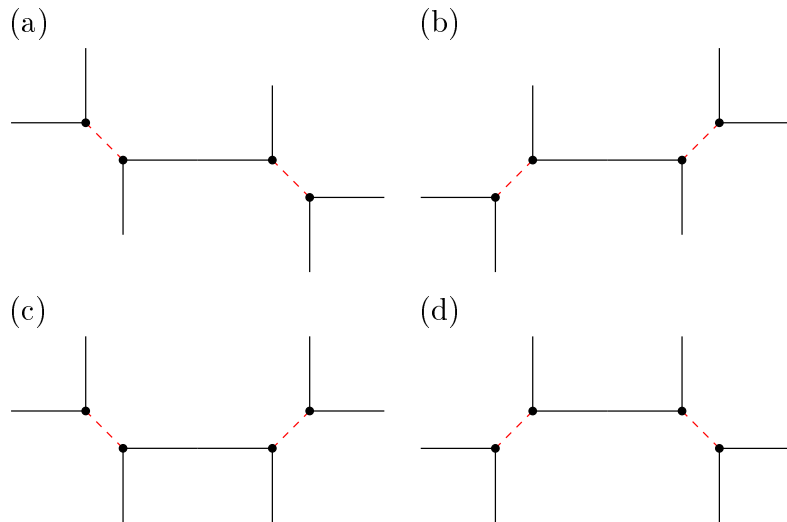


Figure 3.8: The four possible ways to break the dual ϕ^4 graph of two adjacent squares up into a ϕ^3 graph. The red dashed lines denote the newly introduced links along which the vertices have been broken up.

3.8. Now, one can apply the usual ϕ^3 flip move to the resulting graphs. Doing so, one notes that some of the flips connect two of the newly introduced, dashed links to the same vertex. To retain the possibility of contracting the ϕ^3 graph back to a ϕ^4 diagram again, these moves should obviously be forbidden. The remaining moves on the diagrams of Figs. 3.8(a)-(d) either leave them unchanged or produce exactly the ϕ^4 flip moves shown in Fig. 3.7 after contracting back to the ϕ^4 language. Furthermore, both orientations of the resulting ϕ^4 flip move come with equal frequency. Thus, the flip move for quadrangulations or ϕ^4 graphs can be traced back to the (2, 2) flip move for triangulations.

Let us consider the question of ergodicity of such flip moves in the different ensembles of quadrangulations and ϕ^4 graphs. Obviously, every ϕ^4 graph can be transformed to a ϕ^3 graph in the way described above. If the ϕ^4 graph was taken from the *strict* ensemble, the resulting ϕ^3 graph will not contain any singular contributions. Since the (2, 2) link flip for ϕ^3 graphs is ergodic in the space of *regular* triangulations, one might argue that thus the corresponding ϕ^4 link flip is ergodic in the ensemble of *strict* graphs. This is the view advocated in Ref. [74]. While numerical simulations show that this is very probably true (see Ref. [74] and the results presented below), we would like to point out that to our opinion this argument cannot be considered a proof of ergodicity. This is due to the fact that in the language of the broken-up

diagrams of Fig. 3.8 some of the ϕ^3 flip moves are disallowed in order to guarantee the possibility of a contraction to a ϕ^4 graph after the flip. In a regular ϕ^3 graph with only one kind of links, however, these moves would be possible. Theoretically, it is very well possible, though, that the exclusion of these flips raises barriers in the configuration space of those ϕ^3 graphs that can be contracted to strict ϕ^4 graphs, thus breaking the ergodicity of the proposed flip move. Ergodicity could be shown if one could set up a one-to-one correspondence between ϕ^4 graphs of the strict ensemble and ϕ^3 graphs of the regular ensemble. This question is naturally related to the question of the existence of a *perfect matching* of the ϕ^3 graphs. A perfect matching of a graph is a subset of its edges, such that no two of these edges meet at a vertex, but each vertex of the graph is an end of one of the edges of the matching. This question in turn is related to a three-colouring problem for the links of the ϕ^3 graphs; if such a three-colouring is possible, one can contract all pairs of ϕ^3 vertices connected by a link of, say, colour one to end up with a proper ϕ^4 graph. In fact, as a consequence of the celebrated proof of the four-colouring conjecture it can be shown that every planar ϕ^3 graph from the regular ensemble is three-link-colourable (this is the so-called ‘‘Petersen-Tait theorem’’, see, e.g., Ref. [164]). However, it turns out that the contractions defined in this way can lead to singular contributions in the resulting ϕ^4 graph even though the ϕ^3 is regular. Thus, the problem is that of a mixing of the different ensembles, such that it seems not to be obvious how to prove ergodicity of the ϕ^4 flip move for a given (more or less restricted) ensemble. The problem of ergodicity of the ϕ^4 moves will be analyzed more thoroughly by numerical means below.

The insertion and deletion moves of the triangulation case have their obvious generalization in the moves depicted in Fig. 3.9. Move (a) is applicable to quadrangulations and ϕ^4 graphs of all ensembles, whereas move (b) cannot be applied in the strict ensemble. However, as far as the deletion move is concerned, it is obviously rather improbable to find a configuration as the one shown in Fig. 3.9(a), such that this type of move suffers from very small acceptance rates. Since we will not perform (pseudo) grand-canonical simulations in the strict ensemble, we concentrate on the moves shown in Fig. 3.9(b). The detailed balance condition for simulations in the pseudo grand-canonical ensemble, Eq. (3.16), is almost unchanged for the case of quadrangulations,

$$P_{\text{akz}}(T' \rightarrow T) = \frac{r n_2(T')}{2 N_2(T)} = \frac{r n_2(T')}{2 N_2(T') - 1}, \quad (3.17)$$

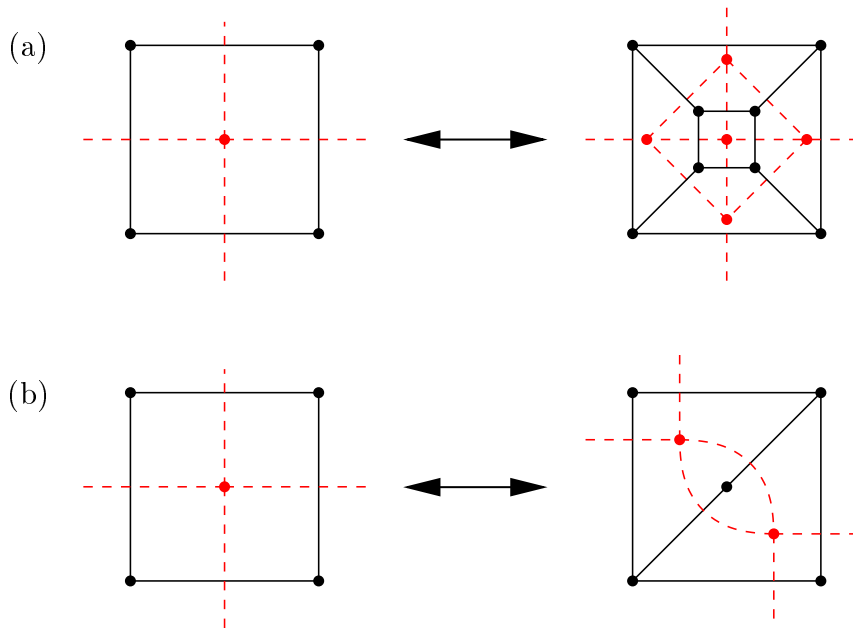


Figure 3.9: Two variants of insertion and deletion moves for dynamical quadrangulations (black solid lines) and ϕ^4 graphs (red dashed lines). (a) Insertion of an additional square that adds four vertices to the ϕ^4 graph and its inverse deletion. These moves are applicable in all of the defined ensembles. (b) Insertion of a single vertex on the diagonal of the square, which adds only one vertex to the graph. This move and its inverse are not allowed in the *strict* ensemble.

where now $n_2(T')$ is the number of two-loops of the quadrangulation T' . The additional factor $1/2$ appearing here as compared to (3.16) stems from the fact that there are two combinatorially distinct possibilities to insert a point on the diagonal of the square, cf. Fig. 3.9(b), whereas the insertion move for triangulations was unique up to re-labellings of the vertices.

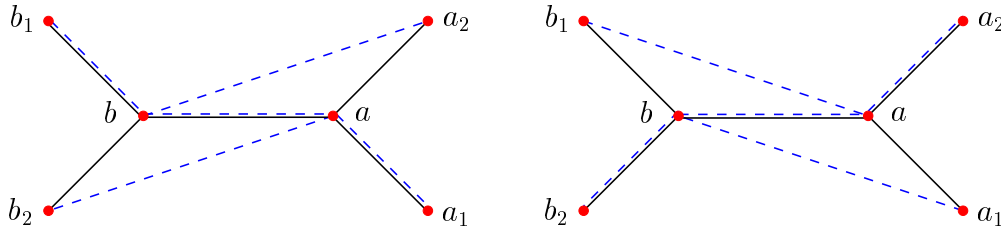
3.2.4 Necessary checks and implementation details

Up to now, we have not discussed how one ensures that the flip move dynamics for canonical simulations always generates polygonifications or graphs of the same consistent ensemble. That this is guaranteed, however, was taken for granted in the discussion of the ergodicity properties at least in the case of triangulations. It is obvious that, starting from a polygonification of the strict or regular ensembles some of the flips can produce multiple links; furthermore, as soon as those appear,

degenerate triangles resp. squares can be produced by flip moves. We will discuss the case of triangulations first and then generalize to quadrangulations.

Triangulations and ϕ^3 graphs

In the *regular* ensemble of triangulations or ϕ^3 graphs it suffices to prevent the appearance of double links in the triangulation or, equivalently, the appearance of non-trivial two-point subgraphs in the dual diagram. Degenerate polygons resp. one-point subgraphs can only be produced by link flips from an ensemble that already contains degenerate links resp. non-trivial two-point subgraphs. In terms of the flip move for triangulations, one has to ensure that the vertices q_1 and q_2 of Fig. 3.6(a) are not already connected by a link before the flip move. Concerning the dual graph, we distinguish two ways of the flip move,



which we label with a “chirality” variable χ to indicate the direction of rotating the links of the vertices a and b as $\chi = +1$ (left diagram) and $\chi = -1$ (right diagram). Here, and in the following, the black solid lines denote the graph before the flip and the blue dashed lines indicate the flipped diagram. For un-labelled graphs, these two flips are identical, since they can be mapped onto each other by an exchange $a \leftrightarrow b$; since the computer code has to work with labelled triangulations, we nevertheless distinguish them. Then, on comparing the above diagrams with the corresponding pair of triangles of Fig. 3.6(a), it becomes obvious that the check for the creation of a double link of the triangulation translates into the graph language as the check, whether the *faces* (or *loops*) adjacent to the links $\langle bb_1 \rangle$ and $\langle aa_1 \rangle$ have a common link before the flip⁵. This *touching link test* is illustrated in Fig. 3.10. Note that in terms of the ϕ^3 graph this check is non-local since the considered faces can be arbitrarily large. In contrast, the corresponding check for the triangulation is local. If the touching link test fails (or one of the other tests described below), the move

⁵Note that, by definition, we always traverse the faces or loops of the graphs along their links counter-clockwise; that is, at each vertex we turn left.

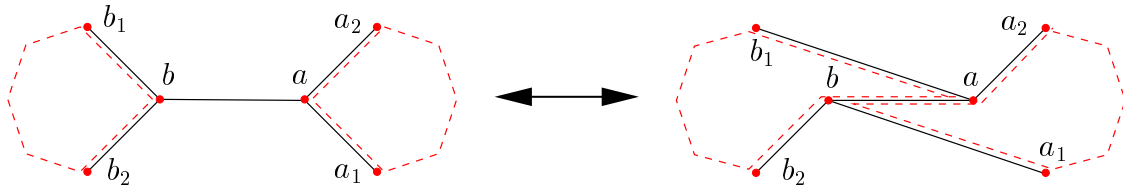


Figure 3.10: The loops (faces) adjacent to the links $\langle bb_1 \rangle$ and $\langle aa_1 \rangle$ (red dashed lines) acquire a common link by applying the $\chi = -1$ link flip move to a ϕ^3 diagram. If both loops already have a common link before the flip, a non-trivial two-point subgraph characterized by two loops sharing more than one link, is generated. In the triangulation this corresponds to a double link. The check for the $\chi = +1$ move is identical to the presented one.

is rejected, but the unchanged configuration is nevertheless counted as new state of the Monte Carlo Markov chain.

Once we allow degenerate links in the triangulation or non-trivial two-point subgraphs in the dual graph, but still want to exclude degenerate triangles resp. one-point subgraphs, i.e. for simulations in the *restricted singular* ensemble, another check has to be applied. A one-point subgraph is produced by a flip move, if one of the points a and b would become a co-ordination point of the graph after the flip; this is demonstrated in Fig. 3.11. The checks are identical for both of the ϕ^3 flip move variants $\chi = \pm 1$ given above. In practice, one checks whether any loop (face) emerging from $\langle bb_1 \rangle$ and $\langle aa_2 \rangle$ or their reversal links arrives back at one of those four links, i.e., whether $\langle bb_1 \rangle$ and $\langle aa_2 \rangle$ are *uniquely connected* to each other (and similarly for the links $\langle bb_2 \rangle$ and $\langle aa_1 \rangle$).

Finally, for the *singular* ensemble no specific conditions have to be fulfilled for a flip move to be allowed, such that the flip move acceptance rate is 100% there. To summarize, we present a C++ code snippet from the simulation program coded for the simulations of ϕ^3 and ϕ^4 graphs of this thesis, that contains function calls for the necessary checks on the link flip move performed on a randomly chosen link l of a ϕ^3 graph:

```
template<> bool Graph<3>::check_flip_move(const Link<3>& l, int chir)
{
    // exclude 2-point subgraphs (and thus 1-point subgraphs)
    if(umode() < restricted_singular && touching_link(l+1, r1+1) )
        return false;
```

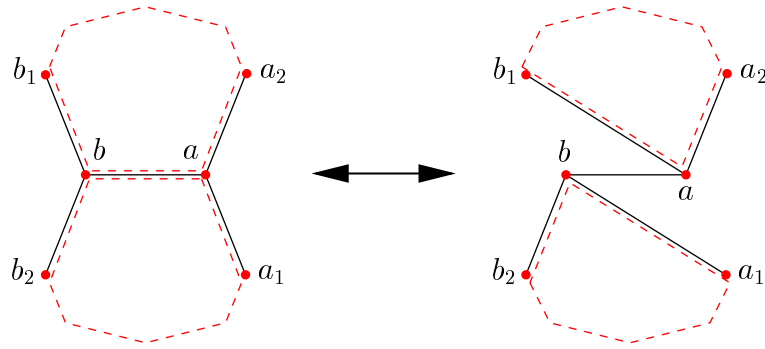


Figure 3.11: If one of the shown loops (red dashed lines) is exclusively connected to the rest of the graph via the links $\langle bb_1 \rangle$ and $\langle aa_2 \rangle$ (upper loop) resp. $\langle bb_2 \rangle$ and $\langle aa_1 \rangle$ (lower loop), the shown flip move transforms it to a one-point subgraph, since removing one of the vertices a or b would disconnect it from the rest of the “universe”. In the triangulation this corresponds to a degenerate triangle.

```

else if(umode() == restricted_singular) {
    // exclude 1-point subgraphs
    if( uniquely_connected(l-1, r1+1) ) return false;
    if( uniquely_connected(l+1, r1-1) ) return false;
}

return true;
}

```

Here, $\text{umode}()$ denotes the used graph ensemble, $\mathbf{r1}$ is the reverse link of \mathbf{l} and the “+” and “-” signs symbolize counter-clockwise and clockwise traversal of the links adjacent to a vertex, respectively⁶. Thus, in the notation of the previous figures, \mathbf{l} is given by the link $\langle ab \rangle$, $\mathbf{l}+1$ by $\langle aa_1 \rangle$ etc.

Quadrangulations and ϕ^4 graphs

Using labelled quadrangulations or graphs we have four distinct variants of flip moves in the ϕ^4 graph language, namely (cf. Fig. 3.7),

⁶Note that due to the “fat” structure of the graphs we can always assign such a cyclic order to the links emerging from a vertex.

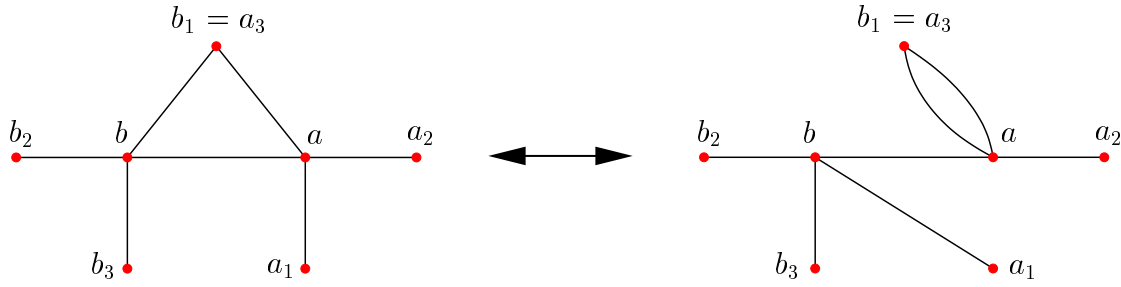
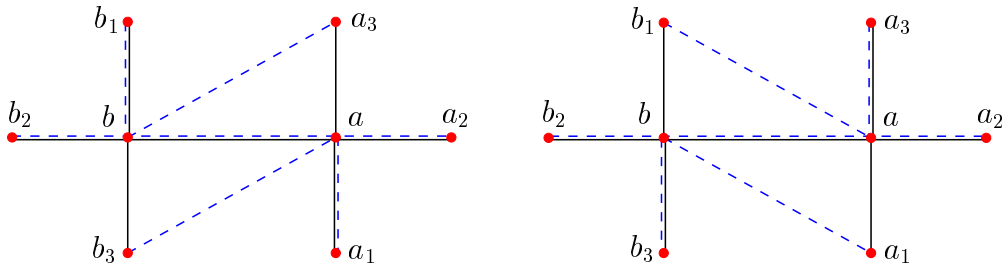
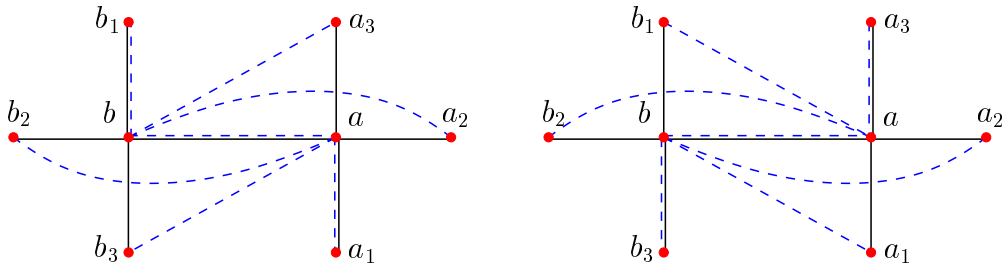


Figure 3.12: Production of a double link by a ϕ^4 flip move of type $\chi = -1$. To prevent the occurrence of double links, one has to ensure that $a_1 \neq b_3$ and $a_3 \neq b_1$ for $\chi = \pm 1$.



labelled by $\chi = +1$ (left) and $\chi = -1$ (right), and additionally the flips



referred to by $\chi = +2$ (left) and $\chi = -2$ (right). The latter two correspond to an exchange of the labelled vertices $a \leftrightarrow b$. In the singular ensemble they are equivalent to the double application of the $\chi = \pm 1$ flips. Furthermore, it can be easily seen by inspection that the necessary checks on the flip moves for the different ensembles always give the same result for $\chi = \pm 2$ as for a $\chi = \pm 1$ move. Thus, the inclusion of the $\chi = \pm 2$ moves cannot generate graphs different from those generated by the $\chi = \pm 1$ moves alone; also, numerically we find no improvement in the de-correlation of the links of the Markov chain. Therefore, we restrict ourselves to the $\chi = \pm 1$ moves.

The necessary geometry tests to rule out disallowed flips for the *regular*, *restricted singular* and *singular* ensembles for the ϕ^4 case are almost identical to those of the

ϕ^3 or triangulations case; the only difference is given by the fact that the loops to be considered for the “touching link” test now depend on the chosen variant of move⁷ $\chi = \pm 1$. The *strict* ensemble, which additionally excludes the appearance of double links in the ϕ^4 graph, needs an additional check which is depicted in Fig. 3.12. Note that, in contrast to the other three ensembles, this additional check is not sufficient to also rule out the appearance of the next singular contributions, i.e., non-trivial two-point subgraphs. Again, the necessary checks on the flip moves are summarized in the following code segment for the case of simulations of ϕ^4 graphs:

```
template<> bool Graph<4>::check_flip_move(const Link<4>& l, int chir)
{
    if(umode() == strict) {
        // exclude double link a3=b1/a1=b3
        if( target(l+1) == target(r1-1) ) return false;
        if( target(l-1) == target(r1+1) ) return false;
        // exclude 2-point subgraphs (and thus 1-point subgraphs)
        if( touching_link(l+1+(chir>0), r1+1+(chir>0)) ) return false;
    }
    else if(umode() == regular)
        if( touching_link(l+1+(chir>0), r1+1+(chir>0)) ) return false;
    else if(umode() == restricted_singular) {
        // exclude 1-point subgraphs
        if( uniquely_connected(l-1, r1+1) ) return false;
        if( uniquely_connected(l+1, r1-1) ) return false;
    }

    return true;
}
```

We note the technical point that it is crucial for an acceptable performance of the program code that both, the ϕ^3 or ϕ^4 graph *and* the polygonification, given by the faces or loops of the graph joined by the corresponding links, are held up-to-date during the Monte Carlo process. This is due to the fact that the information of the faces or loops is needed for the “touching link” and “uniquely connected” type of tests during the update.

⁷The details can be seen from the piece of code shown below.

Finally, it should be noted that also the grand-canonical moves have to be subject to some geometry tests in order not to leave the chosen ensemble of graphs. The insertion moves in both the ϕ^3 and ϕ^4 cases do not need any additional checks. This holds true for the deletion move of Fig. 3.6(b) for the ϕ^3 case. The ϕ^4 deletion move of Fig. 3.9, however, can produce one-point subgraphs which have to be excluded unless simulating in the singular ensemble. The corresponding geometry test is similar to those presented for the flip moves. It will not be discussed in detail here, since (pseudo) grand-canonical simulations are only used for auxiliary purposes in this thesis.

3.3 The Co-Ordination Number Distribution

Given the rather non-trivial complexity of the restrictions on the flip moves for the simulation of dynamical graphs or polygonifications, it is highly desirable to have exact results for the models at hand to compare them with the simulation outcomes. An obvious candidate for this comparison are the exactly known critical exponents of the dynamical triangulations model presented in the previous chapter or, alternatively, the critical exponents of the Ising model coupled to dynamical polygonifications found in Refs. [34,35]. However, in view of the observed pronounced robustness of the model, i.e. the universality of the critical behaviour between the ϕ^3 and ϕ^4 cases and even with respect to such drastic changes as the restriction of co-ordination numbers to the values 5, 6 and 7 reported in Ref. [147], the critical exponents are not expected to react very sensitively on “bugs” in the program code, unless they are really of paramount importance.

There are mainly two areas, where defects in the simulation of dynamical graphs could show up. First, a faulty implementation of the necessary checks on the flip moves in the ensembles with restrictions could lead to the appearance of disallowed graph contributions. This possibility is easily ruled out by checking the whole graph for such disallowed contributions after each update move. Also, the possibility of the graph to change topology from the (usually) planar case⁸ to higher genera by a destruction of the cyclic order of the links around vertices in the updating process, can be easily checked for and excluded by the application of graph planarity tests

⁸Obviously, the notions of planarity and spherical topology of a graph are identical, since one can always blow up one of the faces of a spherical graph to enclose the whole diagram and then embed it in the plane.

(see, e.g., Ref. [164]). Here, a combination of the Euler and Dehn-Sommerville relations Eqs. (2.36) and (2.37) is very useful. While this kind of difficulty can arise in any sufficiently complex simulation program, there is an additional and more subtle problem, which is not so familiar from, e.g., spin model simulations on regular lattices, namely the question of ergodicity of the update moves. Especially for the case of ϕ^4 graphs, where no ergodicity proofs are available, such problems of non-ergodicity of the updating scheme can arise. Depending on how “much” non-ergodic the moves are, the resulting deviations from the true results can be very small and are thus extremely hard to detect, unless the appropriate observable is considered. Therefore, a very sensitive, local property of the graphs or polygonifications has to be used. An excellent candidate for such a quantity is given by the probability distribution of the co-ordination numbers of the polygonifications, which can be computed exactly in some special cases.

In the following, we speak synonymously about the co-ordination number distribution of the dynamical polygonifications model or the distribution of loop lengths of the corresponding dual ϕ^3 or ϕ^4 graph representation. Since every link of the graph corresponds to a link of the polygonification it should be obvious from (almost) any of the figures presented in this chapter that the number of sides of a face of the graph (the loop length) is identical to the co-ordination number of the vertex of the polygonification which is dual to the considered face of the graph.

3.3.1 Counting planar graphs

The ϕ^3 regular case

Matrix model techniques allow the exact solution of the counting problem for closed, planar ϕ^3 and ϕ^4 graphs (cf. Section 2.3.4 above). While originally matrix models count graphs of the *singular* ensemble, the calculations can be extended to the case of the regularized graphs. In addition, it is not only possible to count *closed* graphs (or *vacuum diagrams*), but also graphs with a given number of external lines. For planar ϕ^3 and ϕ^4 diagrams of the singular and regular ensembles this has been first done by matrix model techniques in Ref. [16]. Making use of these results, Boulatov *et al.* [21] have proposed a method for deriving the co-ordination number distribution of dynamical triangulations from the calculated graph numbers. Consider the partition function of the dynamical triangulations model in the *regular ensemble* with one of

the N_0 vertices, p_0 say, marked and held fixed; this is obviously by symmetry equal to $N_0 \mathcal{Z}(N_2)$, where $\mathcal{Z}(N_2)$ denotes the canonical partition function of the dynamical triangulation model for “universes” with a fixed number N_2 of triangles, cf. Section 2.3.3. On the other hand, it can also be expressed as [21]

$$N_0 \mathcal{Z}(N_2) = \sum_q \frac{1}{q} Q_q^{(N_2)}, \quad (3.18)$$

where $Q_q^{(N_2)}$ denotes the contribution of triangulations that have q triangles joining at the marked vertex p_0 . This implies that the co-ordination number distribution for dynamical triangulations is given by

$$P_{N_2}(q) = \frac{Q_q^{(N_2)}}{q N_0 \mathcal{Z}(N_2)}. \quad (3.19)$$

Cutting out the q triangles meeting at the marked vertex p_0 from the triangulation, one is left with an open triangulation with $N_2 - q$ triangles. In terms of the dual ϕ^3 graph this corresponds to a diagram with $N_2 - q$ vertices and q external lines. Then, the cut out part can be re-inserted again in one of q possible ways, accounting for the factor $1/q$ in (3.19). This is illustrated in Fig. 3.13(a). Therefore, $Q_q^{(N_2)}$ is equal to the number $G_{q, N_2 - q}^{(c)}$ of connected, planar ϕ^3 graphs with $N_2 - q$ vertices and q external lines. The restriction to connected diagrams stems from the fact that, for the regular ensemble, a closed graph cannot become disconnected on removing a “ring” sub-diagram of the form indicated in Fig. 3.13(a).

On the other hand, the partition function can be expressed in terms of the number $G_{3, N_2 - 1}^{(c)}$ of diagrams with three external lines as

$$\mathcal{Z}(N_2) = \frac{1}{3} \frac{1}{N_2} G_{3, N_2 - 1}^{(c)}, \quad (3.20)$$

where the factor $1/3$ accounts for the three distinct ways to close the graphs by the insertion of a single ϕ^3 vertex. Thus, the co-ordination number distribution for the regular ensemble of planar dynamical triangulations is given by [21]

$$P_{N_2}(q) = \frac{3N_2}{q(N_2/2 + 2)} \frac{G_{q, N_2 - q}^{(c)}}{G_{3, N_2 - 1}^{(c)}}, \quad (3.21)$$

where we have used that $N_0 = N_2/2 + 2$ for planar triangulations, which follows from the Euler and Dehn-Sommerville relations (2.36) and (2.37). The graph numbers $G_{q, N_2}^{(c)}$ can be found exactly as the coefficients of a power series expansion [16]. If we

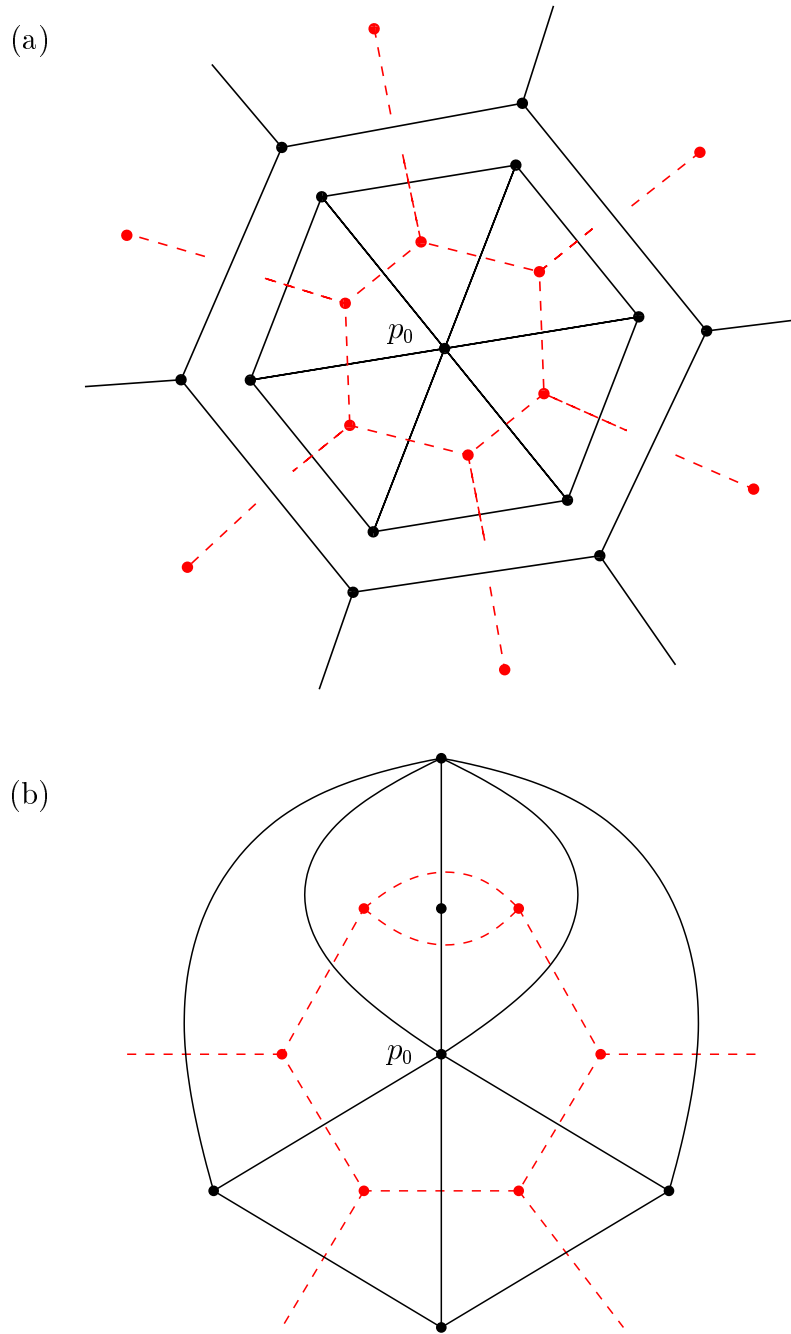


Figure 3.13: Construction of the co-ordination number distribution of the dynamical triangulations model from the number of ϕ^3 diagrams with a given number of vertices and external lines. Solid lines show the triangulation, dashed lines indicate the dual ϕ^3 graph. (a) *Regular ensemble*: removing the marked vertex p_0 and its q adjacent triangles from the triangulation leaves, in terms of the dual ϕ^3 graph, a diagram with $N_2 - q$ vertices and q external lines. Re-inserting the ring diagram of length q cut out before results in an additional symmetry factor of $1/q$ for the q distinct external legs of the ring. (b) *Other ensembles*: degenerate links of the triangles adjacent to the marked vertex p_0 enhance the symmetry factor associated with the insertion of the ring diagram.

write for the generating function of the number of connected, regular ϕ^3 graphs the following expansion [16, 151],

$$G^{(c)}(z, g) = \sum_{q=1, N_2=0}^{\infty, \infty} z^{q-1} g^{N_2} G_{q, N_2}^{(c)}, \quad (3.22)$$

the coefficients $G_{q, N_2}^{(c)}$ are exactly the numbers of such graphs with q external lines and N_2 vertices. This expansion can be explicitly performed [151] and one finds, e.g., for $q = 2$,

$$\begin{aligned} G_1^{(c)}(g) = & 1 + g + g^3 + 3g^5 + 13g^7 + 68g^9 + 399g^{11} + 2530g^{13} \\ & + 16965g^{15} + 118668g^{17} + 857956g^{19} + 6369883g^{21} + 48336171g^{23} \\ & + 373537388g^{25} + 2931682810g^{27} + 23317105140g^{29} + O(g^{31}) \end{aligned} \quad (3.23)$$

Inserting these numbers in Eq. (3.21) yields the exact co-ordination number distribution for finite triangulations. Finally, for the limit $N_2 \rightarrow \infty$ one has the explicit expression [16, 21]

$$P_\infty(q) = 16 \left(\frac{3}{16} \right)^q \frac{(q-2)(2q-2)!}{q!(q-1)!}. \quad (3.24)$$

This distribution of co-ordination numbers is shown in comparison to that of Poissonian random lattices constructed by the Voronoï-Delaunay prescription [165] in Fig. 3.14. While the co-ordination number distribution of Voronoï-Delaunay random lattices is peaked around the mean value 6, the distribution (3.24) is monotonous; especially, in the latter case many more vertices have co-ordination numbers 3 and 4 and the distribution exhibits a long tail for large co-ordination numbers q . The distribution of Poissonian random lattices falls off as $\exp(-\sigma q \ln q)$ with $\sigma \approx 2$ as $q \rightarrow \infty$ [165], whereas the distribution (3.24) declines much slower proportional to $\exp(-\sigma q)$ with $\sigma = \ln 4/3 \approx 0.3$ [21]. On the other hand, both distributions have the same mean, since in any closed triangulation each triangle appears in the co-ordination number of each of its three vertices, such that

$$\langle q \rangle = \frac{1}{N_0} \sum_{p_i} q(p_i) = \frac{3N_2}{N_0} = 6 \frac{N_2}{N_2 + 4}, \quad (3.25)$$

which approaches 6 as $N_2 \rightarrow \infty$.

ϕ^3 graphs with singular contributions

For the more singular graph ensembles it is still possible to calculate the graph numbers $G_{q, N_2}^{(c)}$ either in the matrix model scheme of Refs. [16, 149] or by writing down

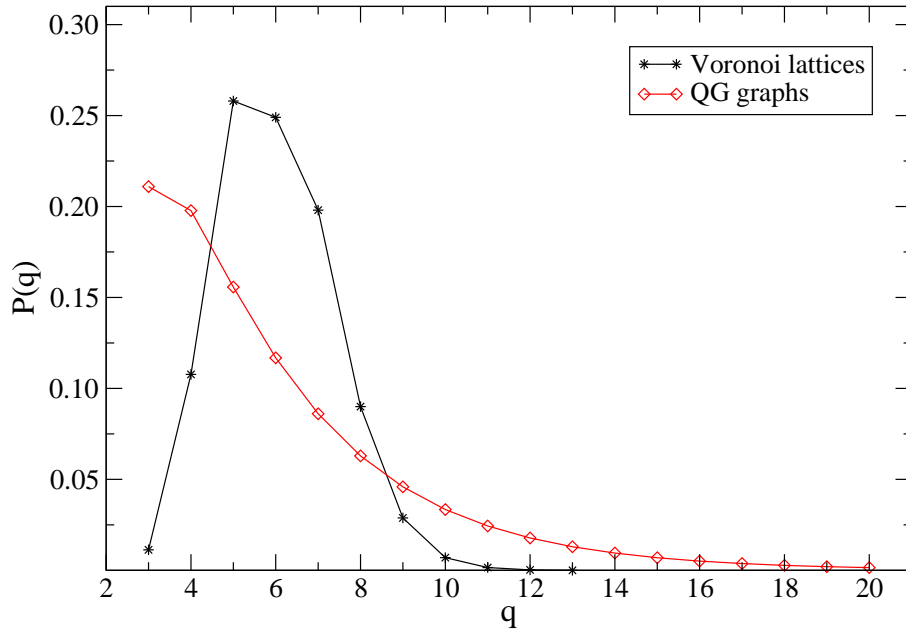


Figure 3.14: Co-ordination number distribution of Poissonian random lattices built by the Voronoï-Delaunay construction in comparison to the co-ordination number distribution of planar random triangulations (QG) from the DTRS model according to Eq. (3.24). Both distributions are for the limit of infinite-size lattices. The results for Poissonian lattices are taken from Ref. [165].

equations of the Schwinger-Dyson type for the graph counting, see Ref. [151]. However, the “cut-out and re-insert” prescription for the calculation of the co-ordination number distribution described for the case of regular triangulations does not simply carry over to situations when singular graph contributions are present. The general problem is that the symmetry factor $1/q$ associated with the insertion of the ring diagram depicted in Fig. 3.13(a) changes when the inserted ring itself contains multiple links or tadpoles. Consider the case of a double link present in the restricted singular and singular ensembles as shown in Fig. 3.13(b). While the co-ordination number of the considered vertex of the triangulation is still equal to q , the inserted ring diagram has only $q - 1$ external lines, which destroys the symmetry arguments used in writing down Eq. (3.19), since diagrams with varying numbers of external lines mix.

For the *restricted singular* ensemble, however, it is still possible to apply the same formula Eq. (3.21) for the co-ordination number distribution with the graph numbers

$G_{q,N_2}^{(c)}$ replaced by the number G_{q,N_2} of (possibly) *disconnected* diagrams including non-trivial two-point subgraphs. Possibly disconnected graphs have to be taken into account since with the presence of non-trivial two-point subgraphs, cutting out a ring diagram of the type shown in Fig. 3.13 can leave the remaining graph in several disconnected pieces. The gluing picture of Fig. 3.13 is still valid since — in the restricted singular ensemble — there is a one-to-one correspondence between graphs with q external lines that one can paste the ring of Fig. 3.13(a) into and graphs with $q - 1$ external lines, which can be closed by rings of the type shown in Fig. 3.13(b). This is due to the fact that one can always pair off two of the external lines of a graph with q external lines to end up with a graph with the same symmetry and $q - 1$ external lines. This reduced graphs are still of the same, restricted singular ensemble, since no two of the q external lines are allowed to originate from the same vertex, which would represent a disallowed one-point subgraph. If the latter would be allowed, the pairing of two external lines could lead to a tadpole contribution which is forbidden in the restricted singular ensemble. Since the same reasoning can be put up for the cases of several double links present on the ring diagram to be inserted, the co-ordination number distribution can be calculated in the same way as for the regular ensemble. There is one exceptional point where this reasoning breaks down: if $q = N_2$, which is obviously the maximum allowed co-ordination number, one is left with a single closed ring-diagram with alternating single and double links; this configuration can obviously not be decomposed in the way described above.

As soon as one-point subgraphs are allowed to appear in the graphs, the described “cut-out and re-insert” rule can no longer be used to calculate the co-ordination number distribution for general q . While it still works for small q , the calculation breaks down due to a mixing of symmetry factors for the general case. Note also that the definition of a co-ordination number is ambiguous for the singular ensemble. Besides the number of triangles meeting at a vertex, one could consider the number of *links* joining at a vertex. While these two definitions coincide for the regular and restricted singular ensembles, the appearance of one-point subgraphs in the singular ensemble results in the fact that a vertex can have more incident links than triangles.

A special case of the co-ordination number distribution is given by the ratio of partition functions for N_2 and $N_2 - 2$ triangles, which is by Eqs. (3.20) and (3.21)

$$\frac{\mathcal{Z}(N_2)}{\mathcal{Z}(N_2 - 2)} = \frac{N_2 - 2}{N_2} \frac{G_{3,N_2-1}}{G_{3,N_2-3}}, \quad (3.26)$$

where the graph numbers G should be suitably chosen to match the ensemble under

consideration, i.e., connected and regular for the regular ensemble and disconnected and with the corresponding type of singularities for the restricted singular and singular ensembles. Since the transformation $N_2 \rightarrow N_2 \pm 2$ corresponds to the grand-canonical moves presented above, this relation can be used in all of the ensembles for comparison to results from the pseudo grand-canonical method. Alternatively, the ratios $\mathcal{Z}(N_2)/\mathcal{Z}(N_2 - 2)$ can be determined from simulations in the canonical ensemble by considering the number of *possible* insertion or deletion moves in the following way. With respect to the insertion and deletion moves of Fig. 3.6(b), one can write [159]

$$\frac{\mathcal{Z}(N_2)}{\mathcal{Z}(N_2 - 2)} = \left\langle \frac{P(N_2 - 2 \rightarrow N_2)}{P(N_2 \rightarrow N_2 - 2)} \right\rangle_{N_2}, \quad (3.27)$$

where $P(N_2 - 2 \rightarrow N_2)$ denotes the total probability of performing an insertion move $N_2 - 2 \rightarrow N_2$ if the probability for each single, allowed insertion move is a constant. Analogously, $P(N_2 \rightarrow N_2 - 2)$ denotes the cumulated probability for a deletion step $N_2 \rightarrow N_2 - 2$. The thermal average is supposed to be taken in the *canonical* ensemble, i.e., the insertion and deletion steps are never really performed, but only the number of such possible moves is counted. An insertion move can be performed on each of the $N_2 - 2$ vertices of the smaller ϕ^3 graph and a deletion move is possible for each of the n_3 three-loops of the larger graph. Therefore, we have,

$$\left\langle \frac{P(N_2 - 2 \rightarrow N_2)}{P(N_2 \rightarrow N_2 - 2)} \right\rangle_{N_2} = \frac{N_2 - 2}{\langle n_3 \rangle_{N_2}}. \quad (3.28)$$

Finally, noting that $\langle n_3 \rangle_{N_2}$ corresponds to the number of vertices of the triangulation that have co-ordination number three, one can write

$$\frac{\mathcal{Z}(N_2)}{\mathcal{Z}(N_2 - 2)} = \frac{N_2 - 2}{\langle n_3 \rangle_{N_2}} = \frac{N_2 - 2}{N_2/2 + 2} \frac{1}{P_{N_2}(3)}. \quad (3.29)$$

This relation can be used in all of the ensembles to determine $P_{N_2}(3)$.

ϕ^4 graphs

Boldly generalizing the discussion of the previous paragraph, one might be tempted to write down an analogue of the expression (3.21) for the co-ordination number distribution,

$$P_{N_2}(q) = \frac{4N_2}{q(N_2 + 2)} \frac{G_{2q, N_2 - q}}{G_{4, N_2 - 1}}, \quad (3.30)$$

where now $G_{2q, N_2 - q}$ denotes the number of (connected or disconnected) planar ϕ^4 graphs of the considered ensemble. The corresponding graph numbers can be found order-by-order for the regular and singular ensembles in Ref. [16] and for all but the strict ensembles in Ref. [151] from a different approach. Finally, Ref. [150] gives explicit, closed-form expressions for the graph numbers for all of the ensembles but the strict one. However, as will be shown in the next Section, this approach does not give the correct co-ordination number distribution in the general case. In view of Eqs. (3.26) and (3.29) one can write

$$\frac{\mathcal{Z}(N_2)}{\mathcal{Z}(N_2 - 1)} = \frac{N_2 - 1}{N_2} \frac{G_{4, N_2 - 1}}{G_{4, N_2 - 2}} = \frac{N_2 - 1}{\langle n'_2 \rangle_{N_2}} \quad (3.31)$$

which uses the analogue of Eq. (3.20) for quadrangulations resp. ϕ^4 graphs, namely

$$\mathcal{Z}(N_2) = \frac{1}{4} \frac{1}{N_2} G_{4, N_2 - 1}. \quad (3.32)$$

Here, n'_2 denotes the number of two-loops of the ϕ^4 graph that can be deleted without leaving the considered ensemble. For the regular and singular ensembles one has $n'_2 = n_2$, i.e., all deletion moves are allowed. In the restricted singular ensemble, however, the removal of a two-loop belonging to a triple link (self-energy diagram) produces a disallowed seagull contribution, such that there $n'_2 \neq n_2$ in general. Therefore, the relation

$$\frac{\mathcal{Z}(N_2)}{\mathcal{Z}(N_2 - 1)} = \frac{2(N_2 - 1)}{N_2 + 2} \frac{1}{P_{N_2}(2)}, \quad (3.33)$$

is only valid for the regular and singular ensembles. These relations are again not applicable for the strict ensemble, since the used ratio of partition functions corresponds to the insertion or deletion of a loop of length two, which is forbidden in the strict case. For the graph numbers in Eq. (3.32), disconnected graphs should only be considered in the singular ensemble, since only there the removal of a single vertex can split the graph.

The reason for the failure of the ansatz (3.30) for general q is similar to that of the corresponding formula for singular ϕ^3 graphs. The situation is even more complicated though, since the analogue of the ring diagram of Fig. 3.13(a) now has $2q$ paired external lines as depicted in Fig. 3.15. Thus, even if the graph numbers for the strict ensemble would be available, the insertion process would lead to the appearance of double links. Even worse, for all of the ensembles the appearance of double links alters the symmetry factor $1/q$ as in the restricted singular ϕ^3 case; however,

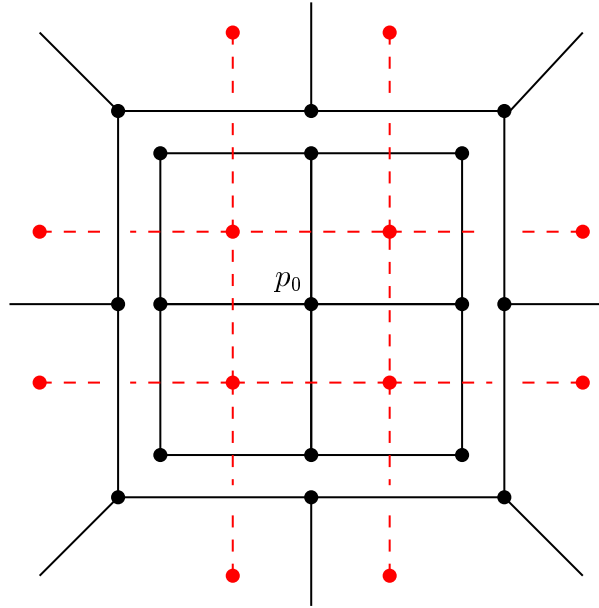


Figure 3.15: A ϕ^4 ring diagram (dashed lines) and the corresponding part of the quadrangulation (solid lines) as a candidate for the construction of the co-ordination number distribution of quadrangulations. The marked vertex p_0 has co-ordination number four. In contrast to the ϕ^3 case each ring vertex has *two* external lines.

in contrast to the latter situation, for ϕ^4 graphs of all ensembles it is possible for two of the q external lines of the outside graph (i.e., the graph the ring diagram is pasted into) to originate from the same vertex. This destroys the symmetry assumption of the insertion process. Thus, for checks of simulations of ϕ^4 graphs one has to entirely rely on the partition function ratio method of Eqs. (3.31) and (3.33).

3.3.2 Comparison to simulation results

For the measurement of co-ordination numbers two types of simulations were performed. Firstly, direct measurements of the co-ordination number distribution and the number of deletion moves n_3 resp. n'_2 by simulations in the canonical ensemble of a fixed number of ϕ^3 or ϕ^4 vertices. Secondly, simulations in the pseudo grand-canonical ensemble, delimiting the range of allowed numbers N_2 to a small band around the values N_2 and $N_2 - 2$ resp. N_2 and $N_2 - 1$ needed for the comparison with Eqs. (3.26) and (3.31). All simulations were directly performed in terms of the dual ϕ^3 or ϕ^4 graphs. Since ergodicity problems and code bugs are expected to show

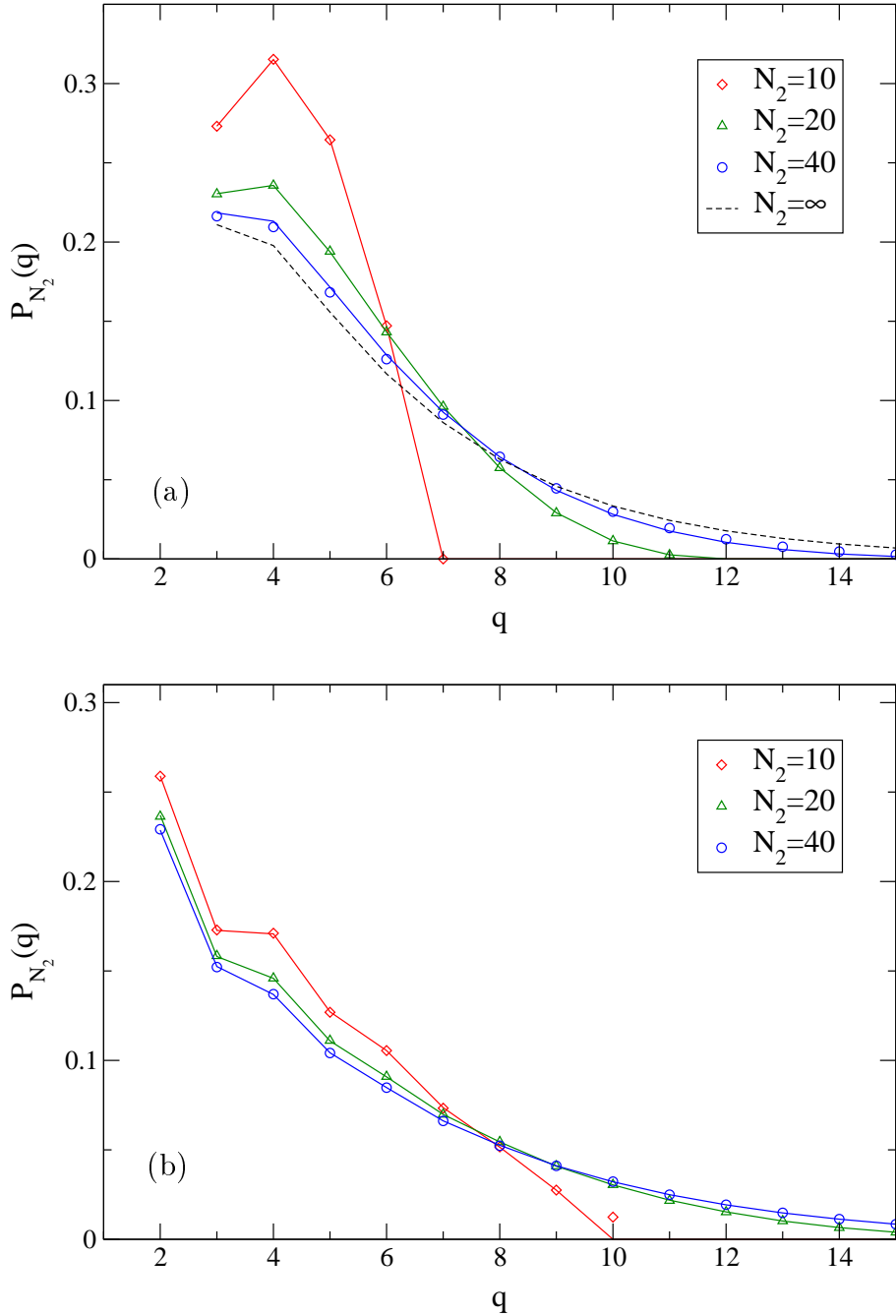


Figure 3.16: Distribution of co-ordination numbers of dynamical triangulations with N_2 triangles from canonical simulations of ϕ^3 graphs with the (2, 2) flip move. (a) Results for graphs of the *regular* ensemble compared to the exact expression (3.21) evaluated with the exact ϕ^3 graph numbers for the indicated graph sizes (solid lines). The dashed line indicates the infinite-volume result (3.24). (b) The distribution for graphs of the *restricted singular* ensemble. The solid lines denote the outcome of inserting the number of (possibly) disconnected ϕ^3 graphs of the restricted singular ensemble into Eq. (3.21). As explained in the text, this formula is correct apart from the value for the maximum possible co-ordination number. The statistical errors are of similar size as the symbols.

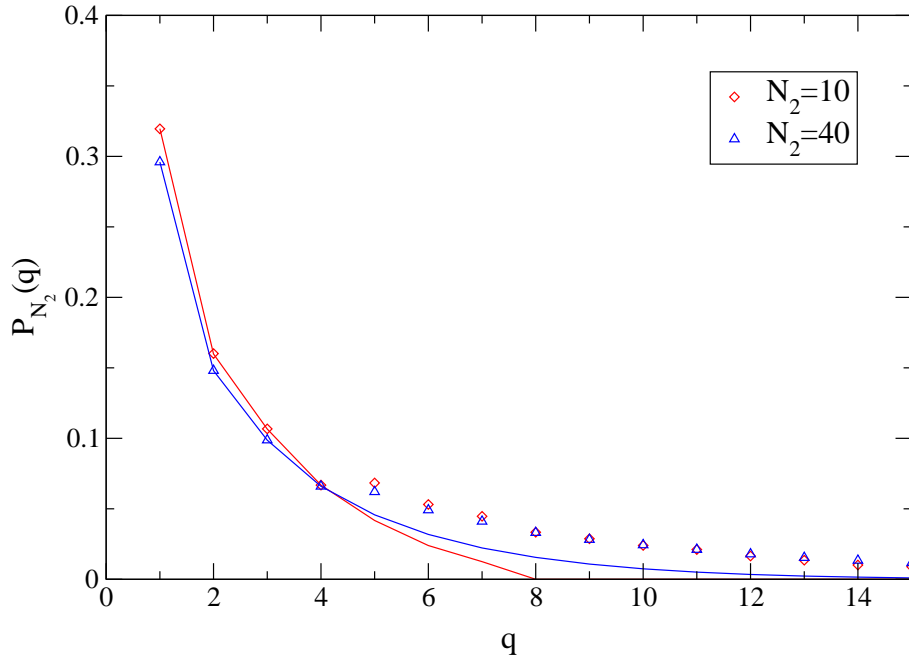


Figure 3.17: Co-ordination number distribution for dynamical triangulations with N_2 triangles of the *singular ensemble* from MC simulations. The solid lines indicate the values conjectured by inserting the number of possibly disconnected, singular ϕ^4 graphs into Eq. (3.21). As explained in the text, this formula is not generally applicable here due to a symmetry reduction in the inserted ring diagrams containing tadpoles and double links.

up especially pronounced for the smallest graph sizes, most of the results presented in this section are for graphs with $N_2 \lesssim 40$ vertices.

Triangulations and ϕ^3 graphs

According to the above explanations, we expect the co-ordination number distribution to be correctly predicted by Eq. (3.21) for the *regular* and *restricted singular* ensembles. In contrast, due to symmetry problems with the described “cut-out and re-insert” technique, the distribution of loop lengths for the ϕ^3 singular ensemble will not be correctly conjectured by the described ansatz. These expectations are completely met by the simulation outcomes, which are presented in Fig. 3.16 for the regular and restricted singular ensembles and in Fig. 3.17 for the singular ensemble. The presented data result from Monte Carlo simulations of planar ϕ^3 graphs with a

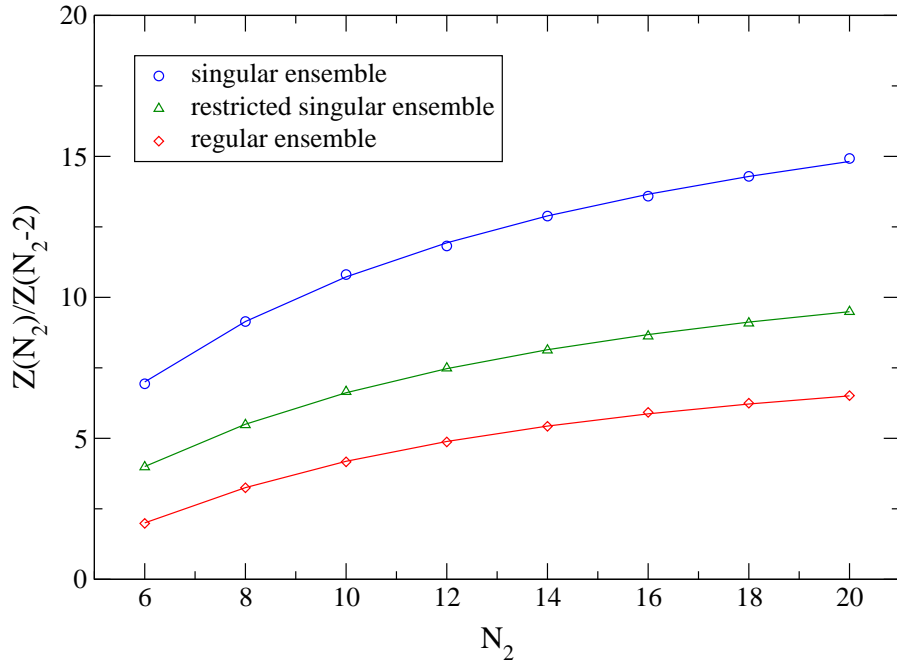


Figure 3.18: The ratio $\mathcal{Z}(N_2)/\mathcal{Z}(N_2 - 2)$ of canonical partition functions for the dynamical triangulations model from pseudo grand-canonical simulations of planar ϕ^3 graphs of the various ensembles. The solid lines show the exact expressions from Eq. (3.26) and the graph counting results of Refs. [16, 151].

fixed number of vertices N_2 applying the ergodic (2, 2) link flip move in accordance with the geometry restrictions described in Section 3.2.4. The co-ordination number distribution was sampled after each “sweep” of flip moves of the graph, where a sweep consists of one attempted flip move per vertex of the graph. The data of Figs. 3.16 and 3.17 correspond to 50 000 of such samples. Although, as will be discussed below in Section 3.5.1, the considered flip move dynamics is subject to rather pronounced critical slowing down effects, the lattice sizes considered here are so small that these effects can be safely neglected. A detailed error analysis was not performed for these check-only simulations; however, a comparison of independent simulations reveals that the error bars are comparable in size to the used plotting symbols.

When comparing the co-ordination number distributions for the three considered ensembles, note that the small non-monotonicities of the function $P_{N_2}(q)$ for small co-ordination numbers q and graph sizes N_2 for the cases of the regular and restricted singular ensembles, as depicted in Fig. 3.16, reflect the geometric restrictions present

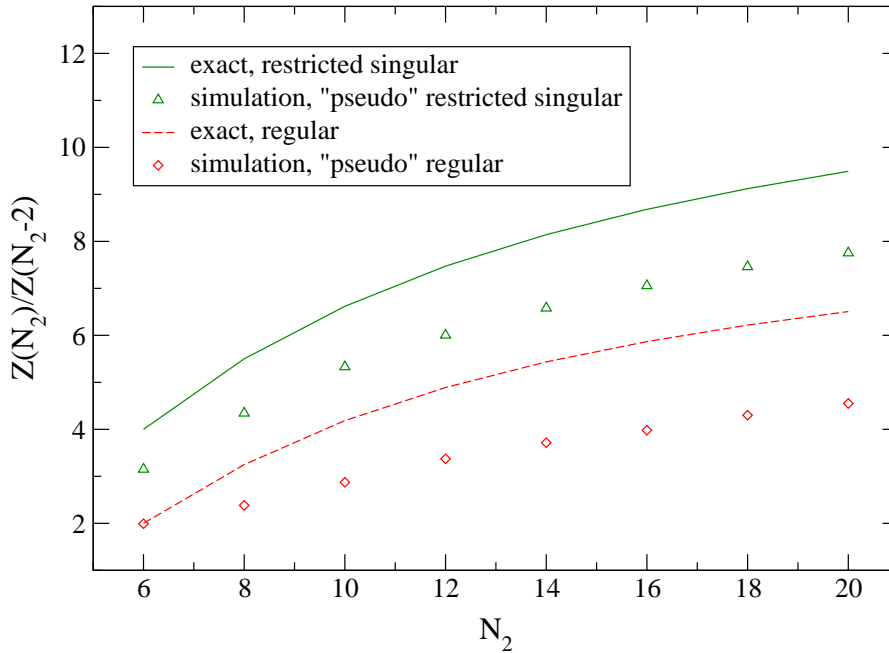


Figure 3.19: Partition function ratios from simulations of planar ϕ^3 graphs belonging to “pseudo” restricted singular and regular ensembles that exclude the local singularities, i.e. tadpoles and double links, but not more general one- and two-point subgraphs. The deviation from the exact results for the proper restricted singular and regular ensembles is apparent.

in these ensembles. Also, it is obvious that the present restrictions introduce hard cut-offs on the allowed values of q . While all $q \geq 1$ occur in the singular ensemble, the restricted singular ensemble excludes loops of length one, i.e. $q \geq 2$; finally, the regular ensemble does not allow loops of length two either, that is $q \geq 3$ there (as is obvious in the dual regular triangulation). Comparing the results for the different numbers N_2 of ϕ^3 vertices for the regular ensemble to the $N_2 \rightarrow \infty$ result of Eq. (3.24) it is obvious that finite-size effects are rather weak for the case of $P_{N_2}(q)$. This is typical for *local* quantities such as $P_{N_2}(q)$; in contrast, global properties such as the mean square extent of the graphs (cf. Section 2.3.5 above) usually suffer from strong finite-size corrections, see e.g. Refs. [51, 166]. Furthermore, comparing Figs. 3.16(a) and (b) and Fig. 3.17, it is obvious that the size of finite-size corrections is reduced as more of the singular contributions are included in the graphs. This effect has been observed before, see e.g. Refs. [50, 167]. The physical reason behind this observation lies in the structure of the “universes” of dynamical triangulations

as trees of “baby universes” inter-connected by minimal necks [29]. Depending on the amount of singularities allowed, the average length of the “baby universe” necks varies. While in the singular ensembles the smallest necks are of length one or two, the minimal neck in the regular ensemble is given by a loop of length three. Thus, one has an intrinsic length scale for the neck structure, whose size — compared to the size of the “universe” — partly determines the strength of finite-size effects.

As an alternative comparison to exact results and to test the code for the singular ensemble, we additionally performed simulations in the pseudo grand-canonical ensemble in order to estimate the partition function ratios of Eq. (3.26). As shown in Fig. 3.18 this test gives perfect agreement with the exact results of Eq. (3.26) for all three ensembles, now including the singular one. To probe the sensitivity of the partition function ratios to various possible code bugs and ergodicity problems, we additionally simulated graphs in “pseudo” restricted singular and regular ensembles. There, only the local singular contributions, i.e. tadpoles and self-energies, were excluded, but one- and (non-trivial) two-point subgraphs on larger length scales were not taken care of. As can be seen in Fig. 3.19 such a change can be detected very easily by a comparison to the exact results.

Quadrangulations and ϕ^4 graphs

Using the generalization of the (2, 2) link flip move to quartic planar graphs, the co-ordination number distribution of planar quadrangulations was determined from simulations with the same parameters as in the ϕ^3 case. In addition to the previously considered ensembles, for the ϕ^4 graphs simulations were also performed in the *strict* ensemble without double links. Fig. 3.20 shows the measured distributions for the extremal cases of the strict and singular ensembles. Again, the reduction of finite-size effects on including singular contributions is apparent. Also, in the singular ensemble the fraction of vertices with large co-ordination numbers is enhanced as compared to the strict ensemble, which is another indication for a reduction of finite-size effects, since vertices with large co-ordination numbers typically occur in the vicinity of the baby-universe bottlenecks. Note that, analogous to Eq. (3.25) for triangulations, for quadrangulations the average co-ordination number is a constant for a fixed number of squares, given by

$$\langle q \rangle = \frac{1}{N_0} \sum_{p_i} q(p_i) = \frac{4N_2}{N_0} = 4 \frac{N_2}{N_2 + 2}. \quad (3.34)$$

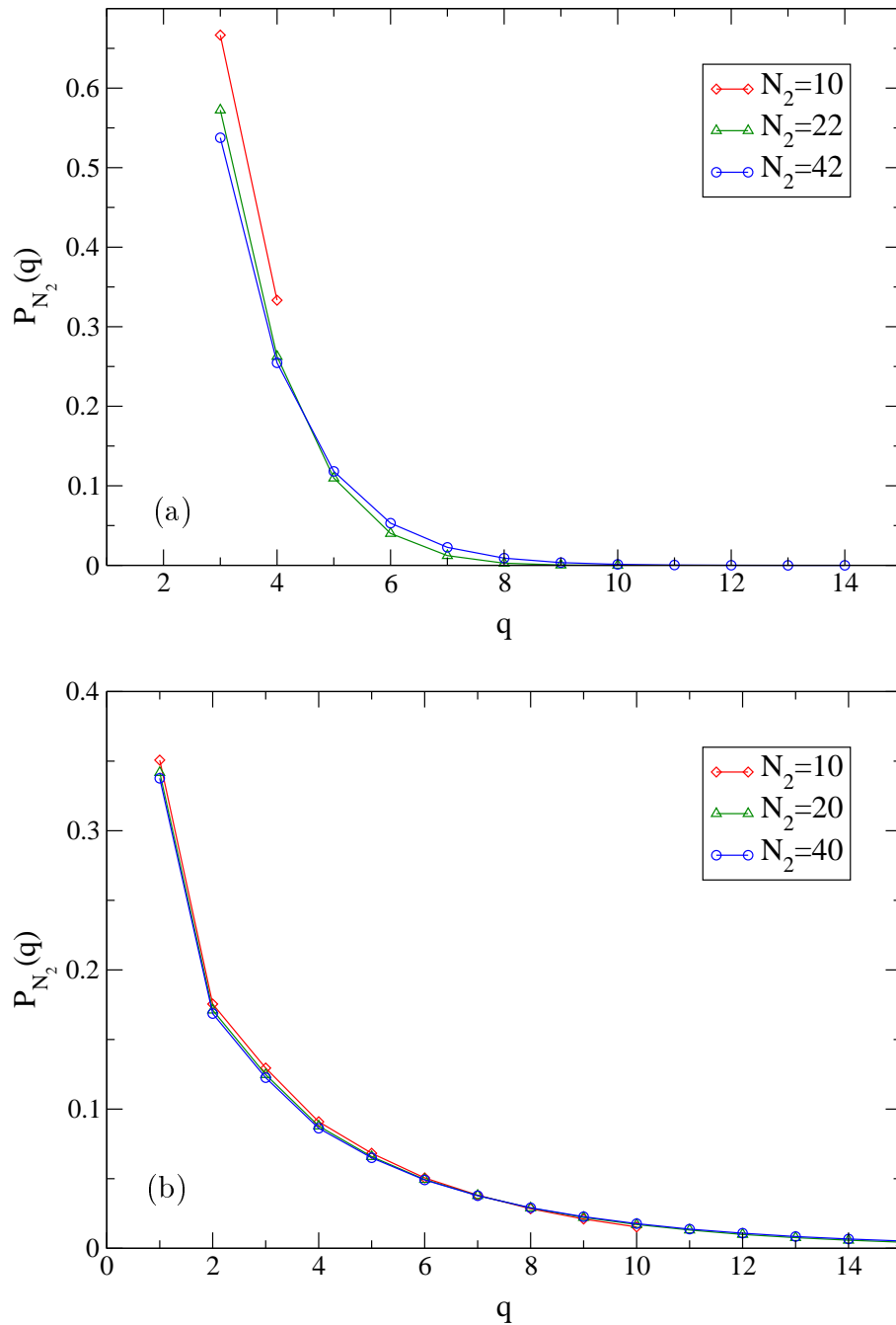


Figure 3.20: Co-ordination number distribution of dynamical quadrangulations from canonical simulations utilizing the generalized (2, 2) link flip move. The simulations were performed in the *strict* (a) and *singular* (b) ensembles. In contrast to the figures for ϕ^3 graphs, the solid lines do not show exact results, but are merely interpolations between the data points to guide the eye.

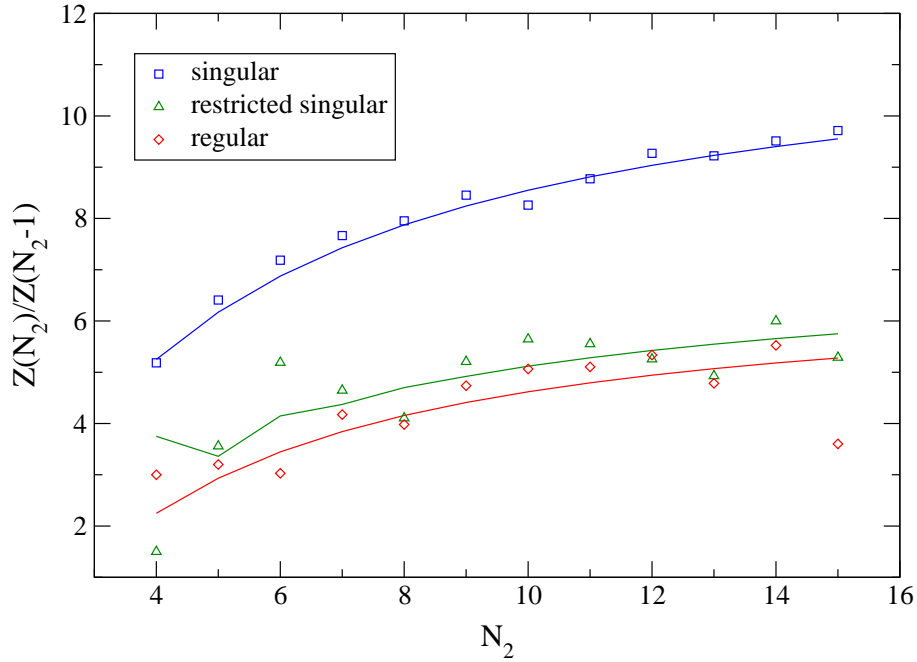


Figure 3.21: Partition function ratios $\mathcal{Z}(N_2)/\mathcal{Z}(N_2-1)$ of the dynamical quadrangulations model from simulations using the generalized $(2, 2)$ link flip. The simulations were performed in the *canonical* ensemble, measuring $\langle n'_2 \rangle_{n_2}$ and using Eq. (3.31) to infer $\mathcal{Z}(N_2)/\mathcal{Z}(N_2-1)$. The *statistical* error bars are of the size of the plotting symbols, the apparent fluctuations stem from the strong dependence on the starting configuration, which is due to the non-ergodicity of the update.

Thus, in the thermodynamic limit $N_2 \rightarrow \infty$ on average four squares meet at each vertex of the quadrangulation.

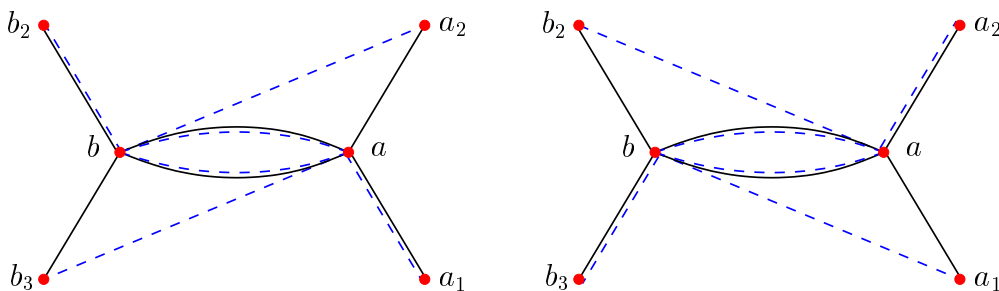
To check the simulation program, a comparison to the exactly known partition function ratios of Eq. (3.31) had to be performed. Using Eq. (3.31) and the graph enumeration results of Refs. [16,150,151], the partition function ratios $\mathcal{Z}(N_2)/\mathcal{Z}(N_2-1)$ can be evaluated exactly for small graph sizes N_2 and all of the considered ensembles apart from the strict one. While pseudo grand-canonical simulations yield results in agreement with the thus calculated partition function ratios, the “indirect” method of performing *canonical* simulations and applying Eqs. (3.31) and (3.33) to extract the ratios $\mathcal{Z}(N_2)/\mathcal{Z}(N_2-1)$ from the measured averages $\langle n'_2 \rangle_{N_2}$ yields strong deviations from the exact results as indicated in Fig. 3.21. These deviations are far from being covered by the statistical errors, which are again comparable in size to the used plotting symbols. Furthermore, the sign and strength of deviation is

strongly correlated to the used starting configuration for the canonical simulations of ϕ^4 graphs with N_2 vertices. Thus, they indicate a non-ergodicity of the used generalized (2, 2) link flip dynamics. In contrast, although there are no exact results for comparison, for the strict ensemble no such strong fluctuations occur. It seems that, in contrast to the ϕ^3 case, the link flip move alone is not ergodic for simulations of ϕ^4 graphs with a fixed number of vertices apart from graphs of the strict ensemble. Grand-canonical simulations, however, i.e. the inclusion of insertion and deletion moves, seem to work ergodically with the proposed dynamics.

3.4 The Two-Link Flip for ϕ^4 Graphs

What exactly are the barriers in the configuration space of dynamical ϕ^4 graphs preventing the generalized (2, 2) link flip move from being ergodic for canonical simulations? In fact, one can easily find ϕ^4 graph configurations which cannot be mapped to each other by link flip moves. Consider, e.g., the configurations depicted in Fig. 3.22, which can occur in all of the ensembles but the strict one. Obviously, in order to connect the left and right configurations one would have to perform a sequence of (2, 2) flip moves. However, no matter where it is performed, the first move produces a tadpole (or seagull) contribution in the graph of Fig. 3.22(b). Thus, no move is possible for the regular and restricted singular ensembles. For graphs of the singular ensemble, the first move is allowed, but there is nevertheless no sequence of flip moves connecting the two diagrams. A proof of this more general statement follows as a corollary from considerations about a two-colouring of the vertices of the quadrangulations discussed below in Section 4.3.3.

On the other hand, the two shown diagrams are still connected to each other by a kind of flip move. It corresponds to a flip move of the ϕ^3 type, where the interconnection between vertices a and b is a double link, i.e.



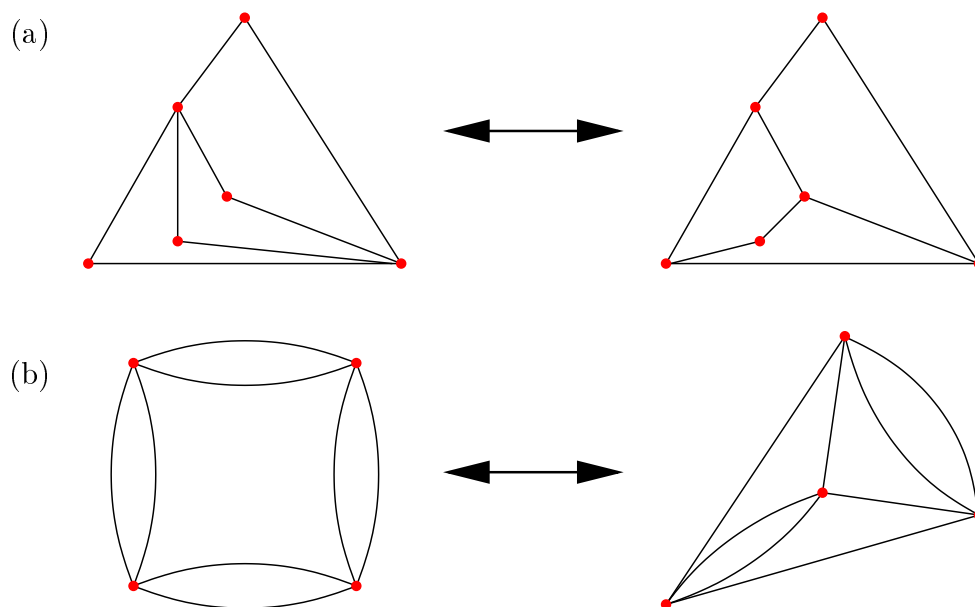


Figure 3.22: Configurations of a regular quadrangulation (a) and its dual ϕ^4 graph (b) that cannot be connected by a generalized $(2, 2)$ link flip move without producing a tadpole contribution.

which again comes in two chiralities, $\chi = +1$ (left) and $\chi = -1$ (right)⁹. This “two-link flip” connects not only the configurations of Fig. 3.22, but — as it turns out — removes all of the observed barriers in configuration space. As far as the necessary geometry tests are concerned, inspection of the two-link flip move shows that it cannot produce two-point subgraphs in the regular ensemble, but disallowed one-point subgraphs can be produced in the restricted singular ensemble. Thus, an additional test must only be implemented for the regular ensemble. Guaranteeing detailed balance when including the new move is no issue for the regular and restricted singular ensembles, since there *only* two-link flips are allowed along double links and therefore a two-link flip is always tried when encountering a double link between vertices a and b . For the singular ensemble, on the other hand, on hitting a double link one has to choose between the two possibilities of performing a “normal” $(2, 2)$ link flip (thus producing a seagull) or doing a two-link flip instead. One of the possibilities to do this in a way consistent with detailed balance is to treat double links between a and b as normal one-link flips during the update process and to introduce the two-link flip as an additional type of update that is performed between

⁹Strictly speaking, there are *four* chiralities if one takes the two possible configurations of the double link between a and b into account.

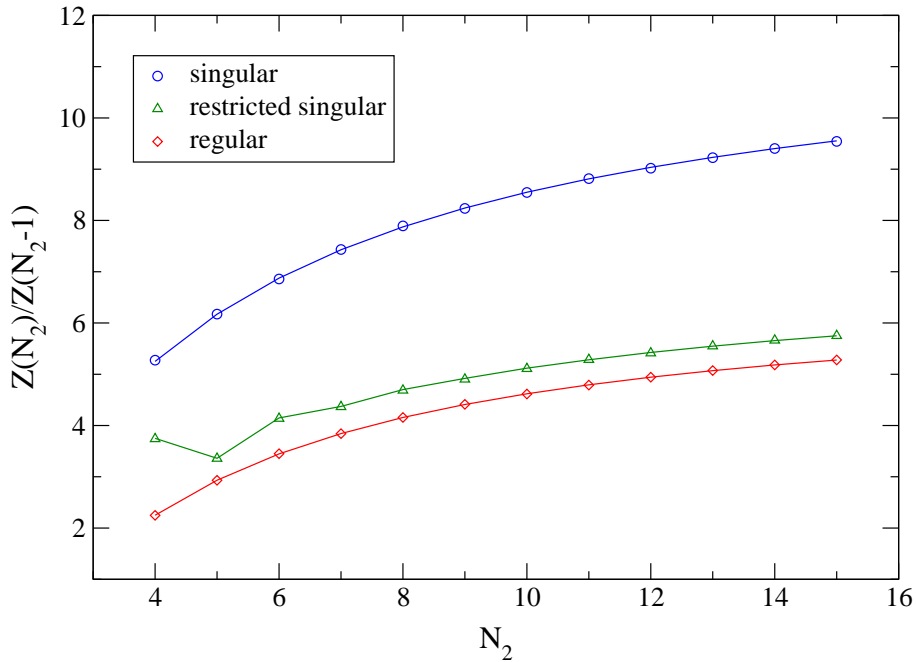


Figure 3.23: Partition function ratios $\mathcal{Z}(N_2)/\mathcal{Z}(N_2 - 1)$ for the planar quadrangulations model from MC simulations as compared to the exact result from Eq. (3.31) and the graph enumeration results of Refs. [16, 150, 151]. The simulations were performed in the canonical ensemble utilizing relation (3.31) for the estimation of the ratios. The data result from 50 000 samples.

the others at a constant frequency. Since the number of double links changes during the simulation, one chooses one of the double links irrespective of the number of double links present.

Applying the two-link flip additionally to the one-link flip in canonical simulations seems to ensure ergodicity also for simulations of a fixed number of vertices (recall that simulations in the (pseudo) grand-canonical ensemble already were ergodic with only the one-link flip). Although we cannot present an analytic proof for this claim, comparison of the indirectly sampled partition function ratios $\mathcal{Z}(N_2)/\mathcal{Z}(N_2 - 1)$ from Eq. (3.31) to the exact results from the graph enumeration technique of Refs. [16, 150, 151] now shows perfect agreement as illustrated in Fig. 3.23. Note that the number of samples taken in the Monte Carlo update is identical between the data shown in Figs. 3.21 and 3.23; thus, the apparent difference is solely due to the restoration of ergodicity and not a matter of a reduction of the statistical fluctuations.

To summarize, for the ϕ^3 and ϕ^4 graphs of the different ensembles and the different types of simulations the following statements about ergodicity can be made:

- (a) The (2, 2) link flip move is ergodic for simulations of dynamical triangulations and the dual ϕ^3 graphs at a fixed number of triangles resp. vertices of the ϕ^3 graph. This has been proved for the case of combinatorial triangulations, corresponding to the regular ensemble in our scheme, in Refs. [21, 156]. Taking the discussion of Section 3.2.1 into account, this result generalizes to the restricted singular and singular ensembles as well. For variants of the grand-canonical simulation method, adding the (3, 1) and (1, 3) insertion and deletion moves to the (2, 2) link flip ensures ergodicity in the space of triangulations with a varying number of triangles. The proof can be found for the regular ensemble in Ref. [156]. Since every triangulation or ϕ^3 graph of the more singular ensembles can be transformed to a regular one by successive applications of the link flip move, ergodicity of the grand-canonical set of moves for the restricted singular and singular ensembles is guaranteed by the arguments given in Section 3.2.1.
- (b) For simulations of dynamical quadrangulations and the dual ϕ^4 graphs, the information about ergodicity is mainly numerical. The generalization of the (2, 2) link flip move to ϕ^4 graphs is *not* ergodic for canonical simulations as can be easily proved. An exception to this statement is given by the strict ensemble, where no double links occur. There, the one-link flip dynamics seems to suffice to ensure ergodicity. Augmenting the one-link flip by a *two-link* flip around double links obviously restores ergodicity also for the regular, restricted singular and singular ensembles. In contrary, for simulations in the grand-canonical type of ensembles of a varying number of ϕ^4 vertices, the generalization of the (3, 1) and (1, 3) insertion and deletion moves together with the one-link flip are seemingly ergodic. That is, the possibility to change the number of ϕ^4 vertices or quadrangles circumvents the configuration space barriers seen by the canonical one-link flip dynamics.

Although the information about the ergodicity of simulations of dynamical quadrangulations or the dual ϕ^4 graphs is only numerical, it has been demonstrated that the considered partition function ratios (being related to the small- q limit of the coordination number distribution) constitute an observable which is highly sensitive to

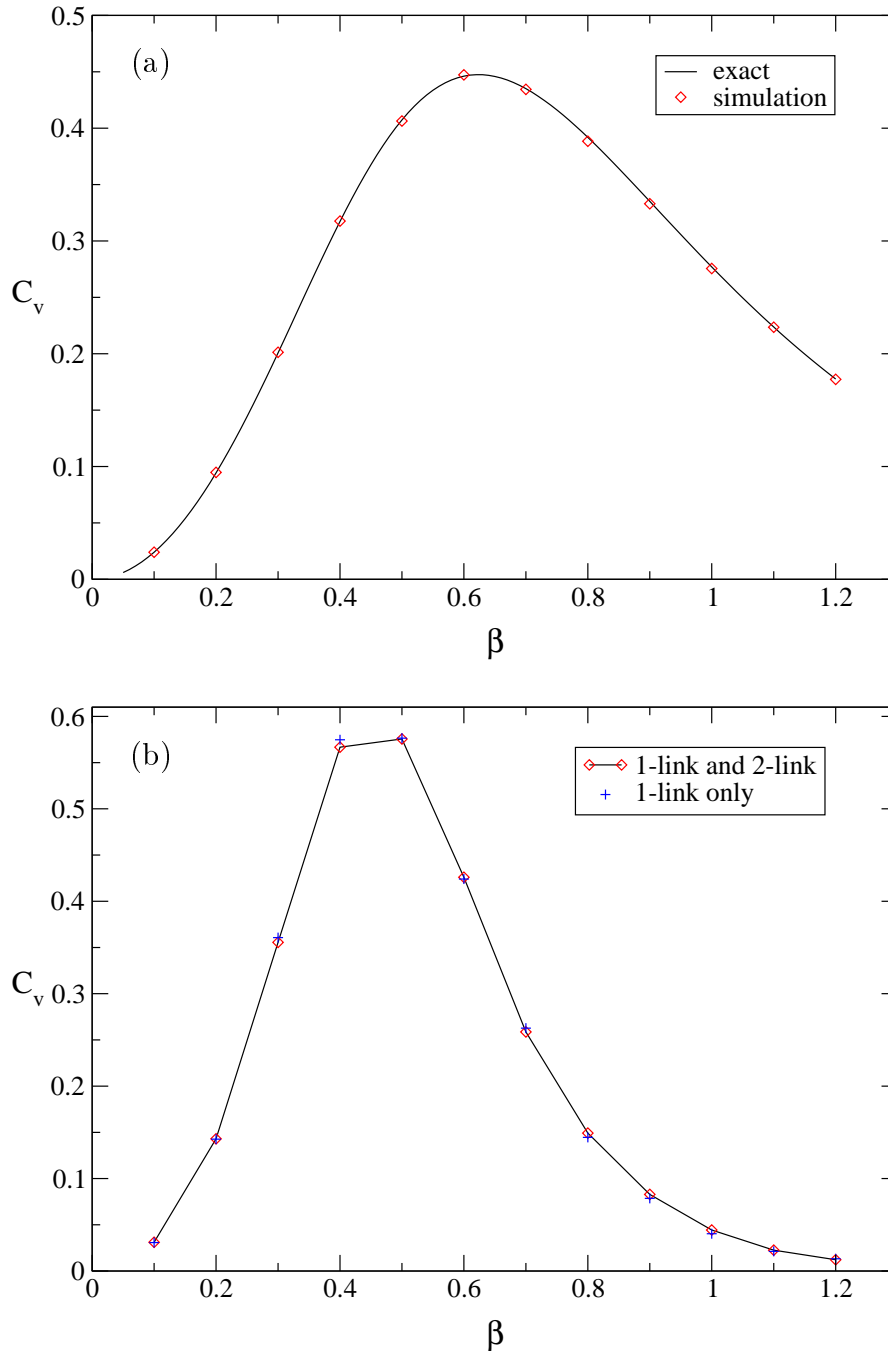


Figure 3.24: The specific heat C_v per vertex of an Ising model coupled to planar ϕ^4 random graphs with $N_2 = 10$ vertices as a function of the coupling $\beta = 1/k_B T$. The Ising model part was updated on the same time-scale as the graphs using the Wolff single cluster algorithm [168]. (a) Application of the non-ergodic one-link flip dynamics to graphs of the singular ensemble. The solid line shows the exact result of Refs. [33, 34, 145]. The model undergoes a third-order phase transition at $\beta_c = \ln 2 \approx 0.693$. (b) Comparison between simulations with the non-ergodic one-link flip dynamics and the ergodic, combined one- and two-link flip update for graphs of the regular ensemble. The solid line is only an interpolation to guide the eye.

a non-ergodicity of the considered update. This is, of course, intuitively rather obvious, since the partition function of the dynamical polygonifications model simply counts the number of polygonifications or graphs of a given ensemble. To demonstrate how much less sensitive other observables can be to this kind of ergodicity problems, as an aside in Fig. 3.24 we present the outcome of simulations of an Ising model coupled to planar ϕ^4 graphs. The simulations were performed either with the one-link flip alone and thus were not ergodic, or with the almost certainly ergodic combination of one- and two-link flips. For the singular ensemble and simulations with the non-ergodic one-link flip alone, we find nevertheless perfect agreement with the exact solution of the problem found in Refs. [33, 34, 145], cf. Fig. 3.24(a). Remembering that the non-ergodicity effect of the one-link flip was more pronounced in the regular ensemble, we also compared simulations for the Ising model on regular ϕ^4 graphs with the non-ergodic and ergodic set of moves as shown in Fig. 3.24(b). Also there, no obvious deviations are visible.

3.5 Enhancing the Efficiency

Once the question of ergodicity of the considered update is settled, the issue of *performance* of the suggested algorithm deserves some interest. Since in the canonical ensemble of a fixed number of polygons the dynamical polygonifications model should be considered as critical for all values of N_2 , we expect the algorithm to be hampered by *critical slowing down*. Additionally, the considered update is local, such that fairly large dynamical critical exponents can be expected. This is indeed the case, such that more sophisticated, less local algorithms are highly desirable. A class of such updates is given by the *baby-universe surgery* method.

3.5.1 Autocorrelation times

Monte Carlo simulations in the important sampling scheme are governed by an artificial dynamics characterized by the used set of update moves and the corresponding energy changes that determine the move acceptance rate via the Metropolis rule, cf. Appendix A.1. Of major interest for the analysis of static behaviour such as thermal averages is the *integrated autocorrelation time* $\tau_{\text{int}}(A)$, which determines the variance of the mean $\sigma^2(\bar{A})$ and thus the accuracy of the estimate \bar{A} of $\langle A \rangle$ from

a time series of length N . The relevant relation is given by:

$$\sigma^2(\bar{A}) \approx \frac{\sigma^2(A)}{N/2\tau_{\text{int}}(A)}, \quad (3.35)$$

that is, in presence of autocorrelations the number of independent measurements is effectively reduced to $N/2\tau_{\text{int}}(A)$, cf. Appendix A.2. Numerically, there are several methods for the determination of integrated autocorrelation times, the most popular being a direct numerical integration of the normalized autocorrelation function and the application of a combined binning/jackknifing technique. Especially, the estimation of variances of the autocorrelation time estimate itself is computationally non-trivial; the relevant formulae are given in Appendix A.4. Since in both approaches some subjective decision about the degree of convergence of the respective estimates must still be taken, we apply both methods in parallel to be able to detect runaway results via a lack of consistency between the two outcomes.

As indicated in Eq. (3.35), the integrated autocorrelation time depends on the considered observable A . As far as the efficiency of the used Monte Carlo dynamics is concerned, one is mainly interested in the *slowest mode* of the update, i.e., one is looking for the observable with the largest autocorrelation times since these times can be taken as the autocorrelation times of the MC process as a whole. In view of the locality of the considered flip-move dynamics, quantities that depend on the global structure of the graphs are the obvious candidates for such observables. The main global observable discussed in Chapter 2 was the *mean square extent* of the polygonifications or dual graphs, which is, as shown in Section 2.3.5, directly related to the global structure of the lattices, being described as a tree of “baby universes”. The definition of the mean square extent used in the simulations is still slightly different from the versions used in the analytical considerations of Section 2.3.5. In the canonical ensemble of a fixed number of vertices used in the simulations, we decompose the polygonifications into spherical shells of vertices of equal geodesic distance r from a randomly chosen reference vertex p_0 ; the number of such points is denoted by $G_{11}(r)$, i.e.,

$$G_{11}(r) = \# \text{ vertices with a geodesic link distance } r \text{ from } p_0. \quad (3.36)$$

Then, the mean square extent of the polygonification or the dual graph is defined to be

$$\langle r^2 \rangle_{N_2} = \left\langle \frac{\sum_{r=0}^{r_{\text{max}}} r^2 G_{11}(r)}{\sum_{r=0}^{r_{\text{max}}} G_{11}(r)} \right\rangle_{N_2}, \quad (3.37)$$

where the maximal occurring distance r_{\max} is determined by the current graph configuration and, for dynamical graphs, varies between measurements¹⁰. Here, the average $\langle \cdot \rangle_{N_2}$ denotes the thermal average in the canonical ensemble of a fixed number N_2 of graph vertices. Since the pure dynamical polygonifications model at a fixed number N_2 of polygons has no free coupling parameter, it can be considered critical for all values of N_2 . Therefore, the well-known arguments of dynamical scaling apply. Especially, the integrated autocorrelation times $\tau_{\text{int}}(r^2)$ are expected to scale with the size N_2 of the system as

$$\tau_{\text{int}}(r^2) = A_{r^2} N_2^{z_{r^2}/d_h}, \quad (3.38)$$

cf. Appendix A.2. In contrast to the *dynamical critical exponent* $z = z_{\text{exp}}$ defined from the scaling of the *exponential* autocorrelation times τ_{exp} , which is on the basis of universality arguments believed to be independent from the observable under consideration, see e.g. Ref. [169], the exponent $z_A = z_{\text{int},A}$ associated to the scaling of the integrated autocorrelation time of an observable A can in general depend on the choice of A , cf. Appendix A.2.

Exploiting the given relations, one can extract the critical exponent z_{r^2} from the MC simulations of dynamical graphs. Since the focus of this work lies on ϕ^4 graphs, only this type of graphs is considered in detail here, divided into the different ensembles with respect to the inclusion of singularities described in Section 3.1. The simulations were performed in the canonical ensemble of a fixed number N_2 of ϕ^4 vertices. To generate the initial configurations, starting from an octahedron, i.e. a regular eight-sided polygon consisting of six vertices, insertion moves of the type described in Section 3.2.3 were performed until the desired graph size was reached. From the following series of (one- and two-link) flip-move updates at least the first 500 $\tau_{\text{int}}(r^2)$ sweeps¹¹ were discarded for equilibration¹². The remaining time series of (almost) equilibrium measurements of r^2 was then analyzed with the methods described in Appendix A.4 to extract the integrated autocorrelation time $\tau_{\text{int}}(r^2)$. Simulations were performed for different lattice sizes up to 8192 vertices to allow for a finite-size

¹⁰Here, one could also consider averaging on the level of $G_{11}(r)$ instead of the indicated average. For a proper analysis of variances and autocorrelation times, however, this would require the recording of a huge amount of data.

¹¹Here and in the following, a *sweep* of flip moves refers to one attempted flip move per vertex of the ϕ^4 (or ϕ^3) graph.

¹²Obviously, this has to be done in a self-consistent way via an *a posteriori* check, since $\tau_{\text{int}}(r^2)$ is not known *a priori*.

N_2	strict		regular		restricted singular	
	$\tau_{\text{int}}(r^2)$	$\tau_{\text{int}}^{\text{jack}}(r^2)$	$\tau_{\text{int}}(r^2)$	$\tau_{\text{int}}^{\text{jack}}(r^2)$	$\tau_{\text{int}}(r^2)$	$\tau_{\text{int}}^{\text{jack}}(r^2)$
64	0.708(40)	0.718(46)	0.551(16)	0.546(35)	0.613(20)	0.624(38)
128	0.937(55)	0.919(49)	0.681(27)	0.677(33)	0.763(31)	0.715(60)
256	1.38(11)	1.33(11)	0.943(81)	0.871(46)	1.062(78)	1.029(50)
512	2.19(32)	2.28(23)	1.43(12)	1.47(12)	1.534(95)	1.513(83)
1024	3.10(11)	3.12(18)	2.27(13)	2.27(09)	2.32(11)	2.290(77)
2048	4.90(35)	4.61(24)	3.37(13)	3.47(14)	3.66(24)	3.80(17)
4096	7.16(33)	7.40(36)	5.37(14)	5.51(23)	5.27(16)	4.90(21)
8192			8.07(104)	8.66(85)		

Table 3.2: Integrated autocorrelation times of the mean square extent $\langle r^2 \rangle$ for the (one- and two-link) flip-move dynamics for ϕ^4 random graphs of the strict, regular and restricted singular ensembles. The graph sizes range from 64 up to 8192 vertices. The autocorrelation times are measured in units of ten sweeps of flip moves using direct integration of the estimated normalized autocorrelation function $[\tau_{\text{int}}(r^2)]$ and, alternatively, a combined binning/jackknife technique $[\tau_{\text{int}}^{\text{jack}}(r^2)]$; all error estimates are calculated via the jackknife method, cf. Appendix A.4.

scaling analysis. The results for the integrated autocorrelation time are collected in Table 3.2. Note that the cited values for $\tau_{\text{int}}(r^2)$ are given in units of ten sweeps of link-flip moves. Since for the *singular* ensemble it would be computationally very demanding to keep the ϕ^4 graph and the quadrangulation up-to-date synchronously during the flip-move process, simulations of graphs of this ensemble are very inefficient. Thus, although finite-size effects have been observed to be least there as discussed above in Section 3.1, in our simulational setup, where the graphs and not the polygonifications are the primary objects, simulations in the singular ensemble are not sensible from efficiency considerations. Therefore, we have not performed extensive simulations of graphs of this ensemble. During the simulations, the (quite expensive) measurements were taken after ten sweeps of link-flip moves. For the lattices with $N_2 = 64, \dots, 512$ vertices 50 000 measurements were taken; for the graphs with $N_2 = 1024, N_2 = 2048$ and $N_2 = 4096$ vertices we took 200 000, 300 000 and 500 000 samples, respectively. For the additional simulation with $N_2 = 8192$ vertices for the regular ensemble 100 000 samples were taken.

Considering the data presented in Table 3.2 we find good agreement between the two methods of determining the autocorrelation times. The absolute values of $\tau_{\text{int}}(r^2)$ for

the strict ensemble are clearly enhanced as compared to the results for the other two ensembles, which in turn are not strikingly different for the used sizes of the graphs. This reflects the rather large number of restrictions on the number of allowed flip moves for the strict ensemble, resulting in a quite small acceptance rate of the flip move process. In order to extract the dynamical critical exponent z_{r^2}/d_h , we fitted the functional form (3.38) to the results of Table 3.2. Figure 3.25 shows finite-size scaling plots of the autocorrelation time in the strict, regular and restricted singular ensembles and the corresponding fits of Eq. (3.38). The fits were performed using the autocorrelation times $\tau_{\text{int}}(r^2)$ estimated by direct integration of the normalized autocorrelation function; the fits to the estimates $\tau_{\text{int}}^{\text{jack}}(r^2)$ are consistent with those presented within error bars. The fit result for the strict ensemble is given by,

$$\begin{aligned} A_{r^2} &= 0.050(11), \\ z_{r^2}/d_h &= 0.597(30), \\ Q &= 0.94, \end{aligned} \tag{3.39}$$

where Q denotes the quality-of-fit parameter (see, e.g., Ref. [170]). The simulations for regular ensemble graphs give,

$$\begin{aligned} A_{r^2} &= 0.0285(53), \\ z_{r^2}/d_h &= 0.629(24), \\ Q &= 0.96, \end{aligned} \tag{3.40}$$

while the results for graphs of the restricted singular ensemble are given by,

$$\begin{aligned} A_{r^2} &= 0.0405(69), \\ z_{r^2}/d_h &= 0.585(23), \\ Q &= 0.90. \end{aligned} \tag{3.41}$$

All three fits do not include the simulation results for the graphs of sizes $N_2 = 64$ and $N_2 = 128$ in a trade-off between the attempt to make the best use of the produced simulation data and the need to keep corrections to finite-size scaling reasonably small as compared to the statistical errors. On the basis of universality arguments and the results from matrix model calculations [10, 152], we expect the exponent z_{r^2}/d_h not to depend on the considered ensemble of graphs. The given results are marginally compatible with each other with respect to the statistical errors. The remaining variation between the results is attributed to effects of corrections to finite-size scaling and give some idea about the total, statistical and systematic, precision of the estimate. Especially, a comparison of the fit results for the regular

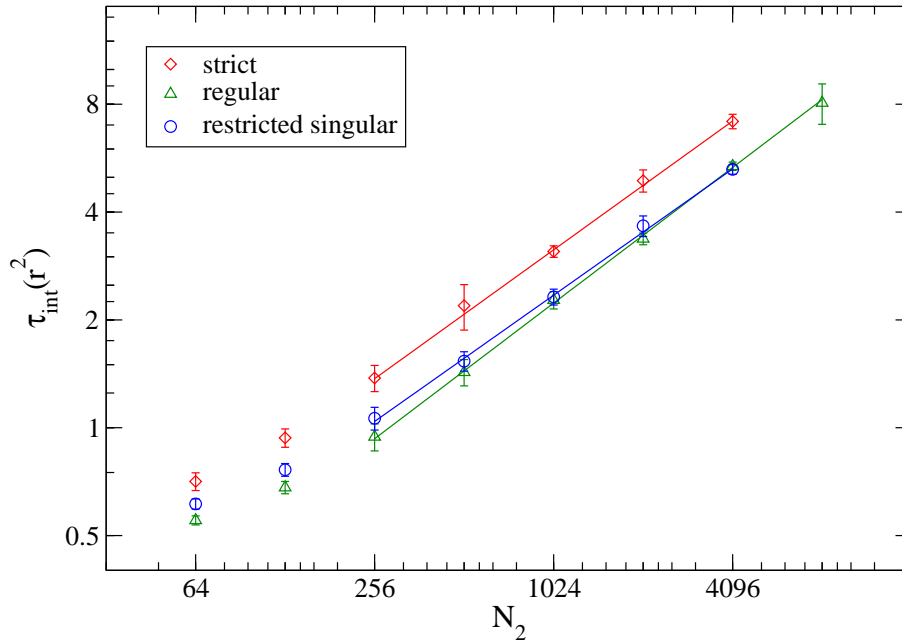


Figure 3.25: Finite-size scaling of the integrated autocorrelation times of the mean square extent of dynamical ϕ^4 graphs from a local link-flip move simulation. The autocorrelation times are given in units of ten sweeps of link-flip moves. The solid lines denote fits of the functional form (3.38) to the simulation data. The extent of the lines indicates the range of graph sizes N_2 included in the fits.

and restricted singular graphs in view of the fact that the autocorrelation times themselves do not differ much between the two ensembles, demonstrates nicely that, for a small region of graph sizes N_2 , a slight increase in amplitude can be compensated by a decrease of the exponent and vice versa. However, we do not aim at a highly precise determination of the dynamical critical behaviour of the model, but mainly want to know how the simulation parameters have to be tuned to efficiently produce an effectively uncorrelated time series of measurements. Also, considering the different graph ensembles, it is obvious that the regular and restricted singular ones are quite equally well suited for simulations from the point-of-view of autocorrelation times, at least on the given level of precision and for the considered system sizes; the dominant restrictions on flip moves for graphs of the strict ensemble, on the other hand, strongly reduce the efficiency of the considered update process. This point will be further discussed in the next section.

To provide a consistency check, we also performed simulations of dynamical ϕ^3

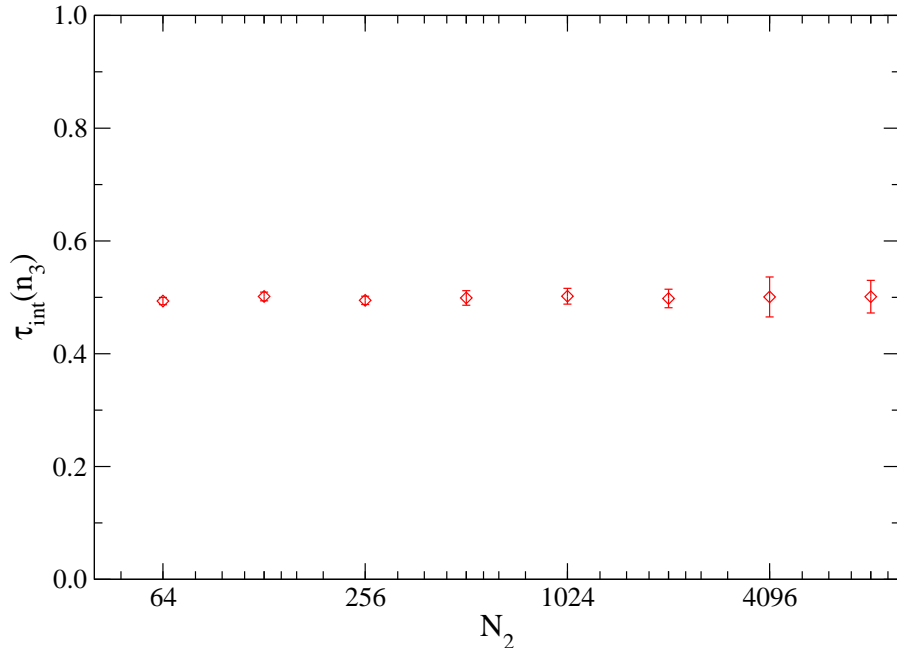


Figure 3.26: Integrated autocorrelation times $\tau_{\text{int}}(n_3)$ of the fraction n_3 of loops (faces) of length three for a MC simulation of dynamical ϕ^3 graphs of sizes between $N_2 = 64$ and 8192 vertices. Up to the present accuracy, no sign of critical slowing can be detected.

graphs, utilizing the ergodic Pachner flip-move dynamics described in Section 3.2.1, and determined the integrated autocorrelation times with the methods described above for the case of ϕ^4 graphs. Here, the starting configuration is given by a tetrahedron, blown up to the intended final graph size by successive applications of the (3, 1) insertion move. For the comparison, we restricted ourselves to simulations of the regular ensemble of ϕ^3 graphs. Again, graph sizes of $N_2 = 64, 128, 256, 512, 1024, 2048, 4096$ and 8192 vertices were considered, taking 150 000 MC samples for each system size. Fitting the expected functional form (3.38) to the estimated autocorrelation times $\tau_{\text{int}}(r^2)$, we arrive at the following fit parameters,

$$\begin{aligned}
 A_{r^2} &= 0.0238(30), \\
 z_{r^2}/d_h &= 0.635(18), \\
 Q &= 0.99,
 \end{aligned}
 \tag{3.42}$$

where, again, the results for $N_2 = 64$ and $N_2 = 128$ have been omitted, since they were too strongly affected by corrections to the leading FSS behaviour. The dynamical critical exponent z_{r^2}/d_h found is in nice agreement with the result for the

regular ensemble of ϕ^4 graphs, which gave $z_{r^2}/d_h = 0.629(24)$. This agreement is in principle expected on the basis of universality arguments, cf. Section 3.1. Note, however, that the exponent z_{r^2}/d_h is a property of the utilized graph update moves and not solely of the class of graphs considered. Thus, such agreement would not be observed if applying completely different sets of update moves to ϕ^3 and ϕ^4 graphs.

Finally, to demonstrate the large range of different relaxation modes present in the system, we also considered an autocorrelation time associated with the co-ordination number distribution, which is, in contrast to the mean square extent, a strictly local property of the graphs. In particular, we measured the autocorrelation time $\tau_{\text{int}}(n_3)$ of the fraction of loops (faces) of length three for the case of regular ϕ^3 graphs. Figure 3.26 shows the size dependence of $\tau_{\text{int}}(n_3)$ for the considered system sizes. As can be clearly seen, with the present accuracy the estimate of $\tau_{\text{int}}(n_3)$ is consistent with the minimal value $1/2$, which is a theoretical lower bound for all integrated autocorrelation times according to the definition (A.16). Thus, for this local property critical slowing down is completely absent to the achieved level of accuracy and, consequently, we conclude $z_{n_3}/d_h \approx 0$. For the case of ϕ^4 graphs we find an identical situation.

3.5.2 The baby-universe surgery method

The presence of strong autocorrelations with a rather large dynamical critical exponent¹³ z/d_h has severely hampered the conclusiveness of numerical simulations of the dynamical polygonifications model. As will be shown later in Chapter 5 these problems become even worse when coupling matter to the random graphs (see, e.g., Ref. [75]). Smaller-scale improvements can be made, e.g., by vectorized or parallelized updates (“parallel flip algorithm”) or, for the special case of pure two-dimensional quantum gravity, by exploiting exact results from the graph enumeration (“recursive sampling”), see Ref. [161]. While the corresponding problem for spin systems on regular lattices could be finally overcome by the introduction of the concept of *cluster algorithms* [168, 171], a feasible technique of similar potency could up to now not be formulated for the dynamical polygonifications model. Nevertheless, a successful push in this direction resulted in the *baby-universe surgery* al-

¹³Note that on regular lattices one usually considers z directly (and not z/d) such that, e.g., the result $z \approx 2$ for the single-spin flip dynamics of the two-dimensional Ising model would translate into $z/d \approx 1$ here.

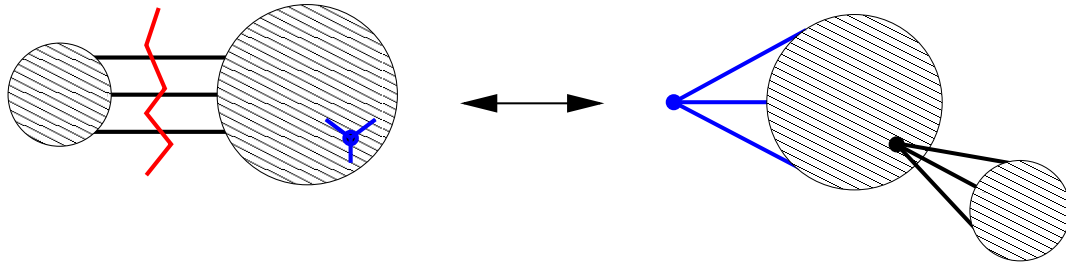


Figure 3.27: A minBU surgery step for a dynamical ϕ^3 graph. The “baby universe” is connected to the rest of the universe by three external lines (the neck). The mother universe has an additional marked vertex. After cutting the neck, the marked vertex is removed and used to connect the three external lines of the mother universe. At the old position of the marked vertex, the “baby universe” is re-connected to the main body.

gorithm [75,172], which was developed together with attempts to formulate a renormalization group transformation for the dynamical triangulations model [129,130].

The concept

It has been shown that the structure of a dynamical triangulation of the quantum gravity type is that of a self-similar tree of “baby universes” [29]. Thus, an update operating directly on this baby-universe sub-structure appears natural for the problem and, in view of its non-local character, promises an appreciable reduction of autocorrelation times. The basic idea is to cut a “baby universe” off the main universe along its neck, re-triangulate the resulting whole and glue the “baby universe” back to the main body at a different place [75]. In the most general scheme derived from the representation of Ref. [29], this transformation would have to be done for “baby universes” of arbitrary sizes and neck lengths. However, it turns out that it is computationally exceedingly demanding to identify “baby universes” with necks longer than a few links, thus destroying the potential gain in efficiency provided by such an algorithm. Therefore, one concentrates on the “baby universes” of *minimal neck length* (minBUs) [75]. For triangulations of the regular ensemble the minimal neck is given by a loop of length three, i.e., a minBU is given by a triangle that does not belong to the triangulation¹⁴. Since the simulations are done directly in

¹⁴The restricted singular and singular ensembles would allow for even smaller necks. However, we want to use the same algorithm for all three ensembles.

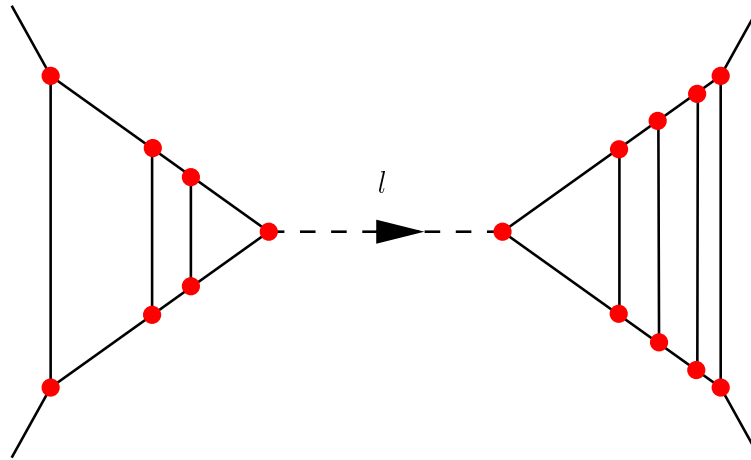


Figure 3.28: A given, oriented link of a ϕ^3 graph (dashed line) can be part of a minBU neck with the minBU lying in arrow direction (right) or opposite to it (left). The minBUs contained in each other are found by the algorithm in the order of their containment.

the graph language, we present the minBU surgery method in terms of dynamical ϕ^3 or ϕ^4 graphs. Then, a surgery step can be depicted as shown in Fig. 3.27 for the case of ϕ^3 graphs. Especially, a neck of length l corresponds to a subgraph with l external lines in the graph language. Note, that for simplicity we do not exploit an additional symmetry of the problem, i.e., the possibility to also change the vertex of the “baby universe” that connects it to the mother part. This, however, does obviously not restrict the generality of the method.

Detailed balance and implementation details

We consider first the case of dynamical triangulations and their dual ϕ^3 graphs and generalize to ϕ^4 graphs afterwards. There have been proposed (at least) two different variants of implementation of the minBU surgery algorithm. In the original paper [75] *all* necks of length three contained in a given configuration are first identified in order to choose one of them at random and perform the surgery step on it. For simulations in the language of the dual graphs, however, this technique is rather inconvenient since the identification of the necks is a computationally quite demanding task. While in the triangulation it suffices to check whether two vertices connected by a link have a common neighbour, in the ϕ^3 graph one has to traverse two neighbouring *loops* (faces) of the graph and all their respective neighbouring

loops to check for a subgraph with three external lines. Therefore, it is much more convenient to only compute the list of necks containing a given, randomly selected link of the graph as was proposed in Ref. [172]. The corresponding situation is depicted in Fig. 3.28. As a second ingredient, we have to choose a vertex in the mother universe part at random (or at least symmetric with respect to the move and its inverse) to serve as the additional marked vertex of Fig. 3.27. Since the graph is only endowed with a chiral ordering of the links around a vertex, but is not per definition considered embedded in \mathbb{R}^d , the inside and outside of a “baby universe” associated with a given neck are not *a priori* known. In other words: since the whole graph can be inverted along the neck, the labelling of the two parts separated by the neck as “baby universe” and “mother universe” can only be decided when the number of vertices (the volumes) of the two parts are known. Then, we simply *define* the “baby universe” to be the smaller part. However, if one just follows the given orientation of the chosen link l to find the volume of the part lying on the corresponding side of the neck, cf. Fig. 3.28, on average one would have to traverse half of the whole graph to decide about which part to interpret as the “baby universe”. This, obviously, would destroy any potential efficiency gain of the algorithm. There are several algorithmic tricks to overcome this difficulty. One is based on the idea of performing a *random walk* along the links of the graph starting from the randomly chosen link l and preventing the walk to touch any of the links belonging to the neck. This amounts to ignoring the distinction between “baby” and “mother universe”, which on average leads to a weaker decorrelation of the configurations between the surgery moves. Another method that does not suffer from this weakness and which will be employed here, is given by *interleaving* two breadth-first (or depth-first) searches of the graph, starting from either end of the randomly chosen link l of Fig. 3.28 and restricting both searches to their respective sides of the chosen neck¹⁵. Then, since it is known that the average minBU is very small compared to the volume of the whole graph [29], one of the searches will on average terminate after only a few steps, thus defining the smaller part of the graph, i.e., the “baby universe”. During the searches the vertices have been labelled, such that a vertex of the mother part of the graph can now be chosen at random. Note that the vertices directly adjacent to the links of the minBU neck should not be selected here such as not to produce singular configurations. Finally, a link l' of the chosen vertex is selected at random.

¹⁵We thank Z. Burda for communicating to us this idea.

After a minBU and a vertex of the mother universe have been selected in the described way, they are exchanged upon fulfilment of a detailed balance condition. Let $n(l)$ be the number of minBU necks containing the link l and $n(l')$ the corresponding number of necks after the move has been performed, i.e., the link l is located at its new position l' instead of one of the links of the marked vertex. Then, the detailed balance condition reads [172],

$$\frac{1}{n(l)}P_{\text{akz}}(l \rightarrow l') = \frac{1}{n(l')}P_{\text{akz}}(l' \rightarrow l), \quad (3.43)$$

where we symbolically denote the minBU surgery move as $l \rightarrow l'$. Thus, we choose the acceptance probability according to the Metropolis rule,

$$P_{\text{akz}}(l \rightarrow l') = \min\left(1, \frac{n(l)}{n(l')}\right). \quad (3.44)$$

Note that for the considered case of ϕ^3 graphs the counting of $n(l')$ is simplified by the fact that the decomposition of the graph into “baby universes” of neck length three is a unique transformation to a tree structure [29] and the applied neck search algorithm lists the minBUs in the order of their containment in each other, cf. Fig. 3.28. Thus, the position of the randomly chosen minBU in the list of minBUs associated with the link l gives the number of minBUs contained in the considered one. Concerning the different graph ensembles it should be noted that the minBU surgery moves do not produce singular contributions when starting from a graph of the regular ensemble, such that the *a priori* acceptance rate is one. In order to enhance the efficiency one might want to limit the size of the used minBUs from below and only consider sufficiently large “baby universes”. Since their sizes are not known in advance, however, this would be computationally more expensive than including minBUs of all sizes. Only trivial minBUs consisting of only one vertex are excluded.

Generalizing the described update scheme to the case of dynamical quadrangulations and their dual ϕ^4 graphs, a minBU is now defined for the strict and regular ensembles to be considered here as a subgraph with *four* external lines. Correspondingly, the operation of finding the necks adjacent to a given link is now $O(m^3)$ instead of $O(m^2)$ for ϕ^3 graphs, where m denotes the average co-ordination number of the polygonification. Additionally, several technical complications not present in the ϕ^3 case arise. First, a minBU surgery move on a graph of the strict ensemble can produce a double link, thus making the algorithm inapplicable for this ensemble (at

least without major changes). Triple links, on the other hand, cannot be produced, such that no additional checks are necessary for simulations in the regular ensemble, which we will hence exclusively focus on. Second, due to the presence of double links in the graphs the number of vertices adjacent to a considered neck, which would be four without multiple links, can be reduced to three or two. This is relevant for the selection of a vertex “outside” of the minBU as described above. Since this effect can be asymmetric with respect to the situations before and after the surgery move, it has to be included in the detailed balance condition, which therefore now reads

$$\frac{1}{n(l)} \frac{1}{V_{\text{out}}(l)} P_{\text{akz}}(l \rightarrow l') = \frac{1}{n(l')} \frac{1}{V_{\text{out}}(l')} P_{\text{akz}}(l' \rightarrow l), \quad (3.45)$$

where V_{out} denotes the number of vertices of the mother universe that are not directly adjacent to the considered minBU. The acceptance probability for the surgery move is therefore given by,

$$P_{\text{akz}}(l \rightarrow l') = \min \left(1, \frac{n(l)}{n(l')} \frac{V_{\text{out}}(l)}{V_{\text{out}}(l')} \right). \quad (3.46)$$

Finally, the mentioned simplification in the evaluation of $n(l')$ for the ϕ^3 case above does not apply here, since different minBUs can overlap for the case of quadrangulations or ϕ^4 graphs. Therefore, the proposed move has to be completely performed in order to evaluate $n(l')$; if the detailed balance condition (3.46) is not met, the move must be reversed to restore the original situation.

Autocorrelation times

For ergodicity reasons, the minBU surgery update has to be mixed with the local link-flip move dynamics. Since, at least for the ϕ^4 case, the baby-universe surgery moves are computationally much more expensive than the local updates, we found it an acceptable compromise to mix the local and global updates at a ratio of three to one. Then, a sweep of the new, mixed update consists of $N_2/4$ attempted surgery moves and $3N_2/4$ one- and two-link flip updates. Traversing the same steps as for the local link-flip update in Section 3.5.1, we determined the integrated autocorrelation times for the combined, “mixed” update by a finite-size scaling analysis of simulations for $N_2 = 2^6, 2^7, \dots, 2^{13}$ vertices for ϕ^3 and ϕ^4 graphs of the regular ensembles. For the ϕ^3 graphs, we took 150 000 samples each and for the ϕ^4 graphs 100 000 samples. The results for ϕ^3 and ϕ^4 graphs are compiled for comparison in Table 3.3. The corresponding FSS plot for the case of ϕ^4 graphs is shown in Fig.

N_2	ϕ^3 graphs		ϕ^4 graphs	
	$\tau_{\text{int}}(\langle r^2 \rangle)$	$\tau_{\text{int}}^{\text{jack}}(\langle r^2 \rangle)$	$\tau_{\text{int}}(\langle r^2 \rangle)$	$\tau_{\text{int}}^{\text{jack}}(\langle r^2 \rangle)$
64	0.497(15)	0.496(13)	0.506(13)	0.541(25)
128	0.510(14)	0.497(19)	0.513(13)	0.532(18)
256	0.581(14)	0.556(20)	0.593(16)	0.586(25)
512	0.742(25)	0.744(23)	0.814(28)	0.783(32)
1024	1.115(43)	1.090(43)	1.151(52)	1.144(50)
2048	1.764(73)	1.781(98)	1.896(86)	1.906(118)
4096	2.97(15)	3.27(20)	2.97(17)	2.93(19)
8192	4.76(28)	4.79(21)	4.95(29)	5.27(40)

Table 3.3: Integrated autocorrelation times of the mean square extent $\langle r^2 \rangle$ for the “mixed” link-flip and minBU surgery dynamics for ϕ^3 and ϕ^4 random graphs of the regular ensemble. The autocorrelation times are measured in units of ten sweeps of mixed moves using direct integration of the estimated normalized autocorrelation function $[\tau_{\text{int}}(\langle r^2 \rangle)]$ and, alternatively, a combined binning/jackknife technique $[\tau_{\text{int}}^{\text{jack}}(\langle r^2 \rangle)]$. For the estimation methods, see Appendix A.4.

3.29, including the data for the purely local update for comparison. Fitting the functional form (3.38) to the data, for the ϕ^4 case we find

$$\begin{aligned}
A_{\langle r^2 \rangle} &= 0.0139(22), \\
z_{\langle r^2 \rangle}/d_h &= 0.646(22), \\
Q &= 0.26,
\end{aligned} \tag{3.47}$$

while the data for ϕ^3 graphs fit best with the parameters

$$\begin{aligned}
A_{\langle r^2 \rangle} &= 0.0112(17), \\
z_{\langle r^2 \rangle}/d_h &= 0.668(21), \\
Q &= 0.49.
\end{aligned} \tag{3.48}$$

For both cases, the data points for $N_2 < 512$ have been omitted due to too strong corrections to the leading FSS behaviour. The results for both types of graphs are rather nicely compatible with each other as expected from universality arguments, since we apply the same kind of update procedure to both graph types.

Obviously, the surgery update considerably reduces the amplitude of the critical slowing down process as compared to the results (3.40) and (3.42) of the purely local update. However, somewhat surprisingly the dynamical critical exponent $z_{\langle r^2 \rangle}/d_h$ is

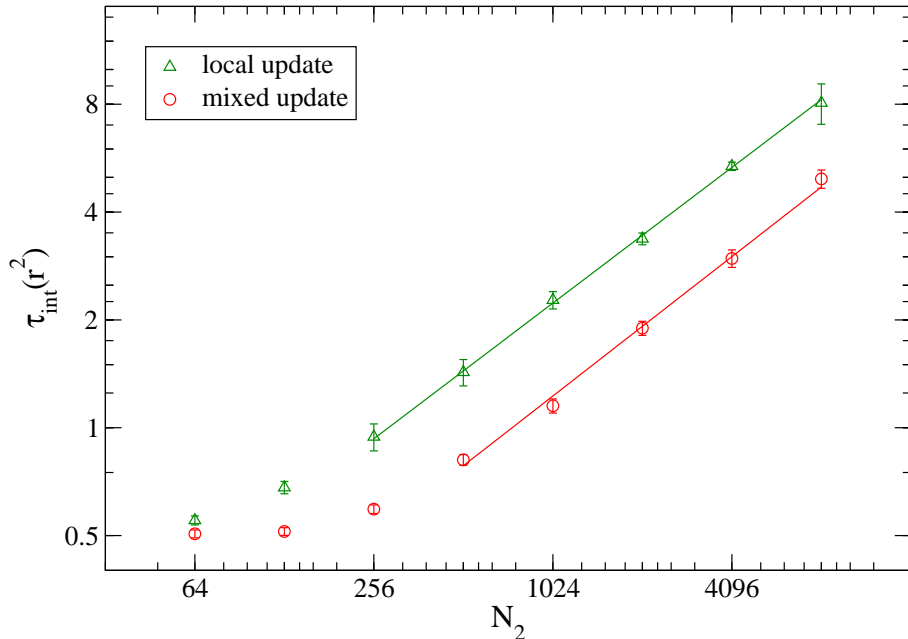


Figure 3.29: Finite-size scaling of the integrated autocorrelation times of the mean square extent of dynamical ϕ^4 graphs from a simulation applying one part of minBU surgery updates and three parts of one- and two-link flip moves (mixed update). The results from the pure link-flip dynamics of Fig. 3.25 are shown for comparison (local update). The autocorrelation times are given in units of ten sweeps of the combined update. The graphs are taken from the regular ensemble. The solid lines denote fits of the functional form (3.38) to the simulation data.

not reduced, but compatible with the value for the local algorithm within statistical errors. This might be partly an effect of the considered rather small system sizes, which could entail different correction to scaling terms for the two considered updates. We think, however, that the main reason for this disappointing performance is given by the fact that the cutting and gluing process of “baby universes” does not change very effectively the overall size of the universe, which is measured by the mean square extent $\langle r^2 \rangle$. This observation is in qualitative accordance with the results of Ref. [75] for the Polyakov string, where the authors find $z_{\langle r^2 \rangle}/d_h = 0.76(3)$ for an update of the mixed type and dynamical triangulations. As will be shown below in Chapter 5, the performance gain of the minBU surgery method is overall better for different observables and when coupling matter to the dynamical graphs. Finally, it should be noted that, of course, the integrated autocorrelation times re-

lated to the co-ordination number distribution are again compatible with a constant value of $1/2$ as was found for the case of the purely local update in Section 3.5.1.

Chapter 4

Vertex Models and Their Simulation

Ice-type or vertex models on regular lattices form one of the most general classes of models of statistical mechanics with discrete symmetry (for reviews see, e.g., Refs. [55, 56, 173]). Special cases of this class of models can be mapped onto more well-known problems such as Ising and Potts models or graph colouring problems [55]. For the case of two-dimensional lattices, a whole variety of such vertex models can be solved exactly, yielding a very rich and interesting phase diagram including various transition lines as well as critical and multi-critical points [55]. Thus, for two-dimensional vertex models one has the rare combination of a rich structure of phase transitions and an exceptional completeness of the available analytical results. In view of these appealing properties it is of obvious interest to analyze the behaviour of vertex models coupled to the random lattices occurring in the framework of dynamical polygonifications.

In this chapter we introduce the concept of vertex or ice-type models and summarize the known exact results for the case of regular lattices. Due to the encoding of the vertex-model interactions in restrictions on the allowed configurations it is non-trivial to formulate efficient algorithms for the simulation of such models. The *loop algorithm* [76], a cluster algorithm for the simulation of rather general vertex models, will be used for the vertex-model simulations of this thesis. While its implementation for ice-type models on regular lattices is well documented [174], for random lattices some special considerations have to be taken into account. After summarizing the principles and implementation details of the loop algorithm, the special necessities

of a simulation of vertex models on random graphs will be addressed.

4.1 Square-Lattice Vertex Models

4.1.1 Definition and basic properties

An *ice-type* or *vertex* model was first proposed by Slater [175] as a model for (type I) ice. It was known that ice forms a hydrogen-bonded crystal, i.e., the oxygen atoms are located on a four-valent lattice and the bonding is mediated by one hydrogen atom per bond, which has the additional property of being near one or the other end of the bond. Slater proposed that the four hydrogen atoms surrounding an oxygen atom should satisfy the *ice rule*, stating that always two of them are in the “close” position and two are in the “remote” position with respect to the considered oxygen atom. Denoting the position of the hydrogen atom by a decoration of the bond with an *arrow* pointing to the oxygen atom the hydrogen atom is closer to, this leads to the arrow configurations depicted in Fig. 4.1 when placing the oxygens on a square lattice; the other possible arrow configurations are excluded by the ice rule. This cannot, of course, be a realistic model for physical ice, which is obviously three-dimensional; some properties of ice are, however, astonishingly well described by this square-lattice model. For instance, the per-site free energy of this square-lattice ice model can be shown [176] to be $f = (\frac{4}{3})^{3/2} \approx 1.540$ in the thermodynamic limit, which is surprisingly close to the experimentally observed value for real ice of $f \approx 1.507$ [56].

In the original ice model all of the shown configurations occur with equal probability, such that the energies associated with the arrow configurations 1, . . . , 6 shown in Fig. 4.1 are all equal and can thus, by a suitable shift of the reference point, be arranged to be all zero. More generally, one assigns energies $\epsilon_1, \dots, \epsilon_6$ to the configurations, such that the Hamiltonian of the model is given by

$$\mathcal{H} = \sum_i E(v_i), \quad E(v_i) \in \{\epsilon_1, \dots, \epsilon_6\} \quad (4.1)$$

where the sum runs over all sites of the lattice and v_i denotes the configuration of vertex i of the lattice. The vertex energies give rise to the corresponding Boltzmann weights,

$$\omega_j = \exp(-\epsilon_j/k_B T), \quad (4.2)$$

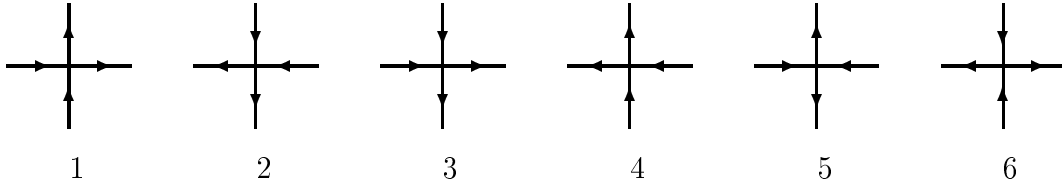


Figure 4.1: Allowed arrow configurations for the 6-vertex model on the square lattice. In the ice model the arrows symbolize the position of the hydrogen atoms on the bonds connecting the sites where the oxygen atoms are located. The allowed arrow configurations are restricted by the *ice rule*, stating that each site must have two incoming and two outgoing arrows.

and the partition function of the model is given by,

$$Z = \sum_{\{v_i\}} \exp \left[- \sum_i E(v_i)/k_B T \right]. \quad (4.3)$$

Depending on the respective choice of the vertex energies ϵ_j , this more general *6-vertex model* includes models known by other names. As mentioned before, the choice

$$\epsilon_1 = \dots = \epsilon_6 = 0 \quad (4.4)$$

corresponds to the ice model. On the other hand, taking

$$\epsilon_1 = \epsilon_2 = 0, \quad \epsilon_3 = \dots = \epsilon_6 > 0, \quad (4.5)$$

results in the so-called *KDP model* [175], which is supposed to describe the behaviour of KH_2PO_4 , a hydrogen-bonded four-valent crystal that exhibits ferroelectric order at low temperatures. Finally, setting

$$\epsilon_1 = \epsilon_2 = \epsilon_3 = \epsilon_4 > 0, \quad \epsilon_5 = \epsilon_6 = 0, \quad (4.6)$$

one arrives at the *F model* of anti-ferroelectrics [61]. In view of the vertex arrangements of Fig. 4.1 and the given energy choices it is obvious that the KDP model will have a ground state consisting entirely of the configurations 1 or 2 indicating ferroelectric order when interpreting the arrows as dipoles. On the other hand, the choice of energies of the *F* model shows that its ground state will consist of the configurations 5 and 6 and therefore is anti-ferroelectrically ordered with the arrow

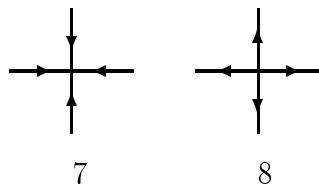


Figure 4.2: Additional vertex configurations of the 8-vertex model. These configurations form sinks and sources for the arrows and violate the ice rule. They are compatible, however, with the rule that each vertex should have an *even* number of incoming and outgoing arrows.

directions alternating between successive bonds when traversing the lattice on horizontal or vertical lines. For a general choice of the ϵ_j , symmetry considerations still impose some restriction. Namely, the fact that the model should be invariant under a reversal of all the arrows of the lattice implies that,

$$\epsilon_1 = \epsilon_2, \quad \epsilon_3 = \epsilon_4, \quad \epsilon_5 = \epsilon_6. \quad (4.7)$$

Given the interpretation of the arrows as electrical dipoles, this symmetry should be present whenever no external electrical field is applied¹. In this thesis, we will exclusively consider this zero-field model.

As will become obvious in the next section, the 6-vertex model has some pathologies when considered as a model for solid state physics, which follow from the strong constraint on the allowed vertex configurations. This observation led Sutherland [177] and Fan and Wu [178] to the proposal to relax the ice rule and replace it by the postulate that each vertex should have an *even* number of arrows going into and out of it. This, obviously, includes the configurations satisfying the ice rule, but additionally allows “sinks” (7) and “sources” (8) of arrows as depicted in Fig. 4.2. Assigning energies ϵ_7 and ϵ_8 to the newly introduced configurations, this defines the *8-vertex model* of statistical mechanics. Whenever periodic boundary conditions are imposed on the lattice, one has

$$\epsilon_7 = \epsilon_8, \quad (4.8)$$

in addition to the restrictions (4.7). To simplify notation, we introduce the variables

¹Note that the third condition, $\epsilon_5 = \epsilon_6$, is always fulfilled on a lattice with periodic boundary conditions, even if an electric field is applied.

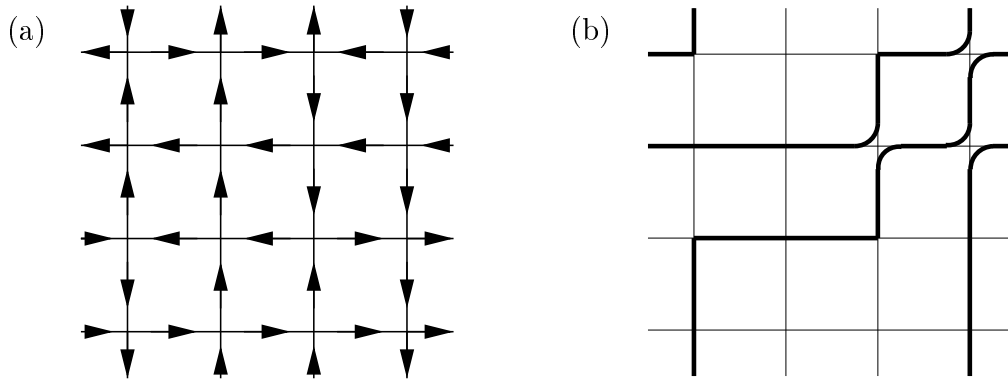


Figure 4.3: A configuration of the square-lattice 6-vertex model in the original arrow formulation (a) and its transformation to the worldline picture (b) of closed, non-intersecting lines. Periodic boundary conditions are assumed.

a, b, c, d for the vertex weights,

$$a = \omega_1 = \omega_2, \quad b = \omega_3 = \omega_4, \quad c = \omega_5 = \omega_6, \quad d = \omega_7 = \omega_8, \quad (4.9)$$

which are also used to label the vertices of type 1 and 2 (a), 3 and 4 (b) etc.

Finally, we note for future reference that the 6- and 8-vertex models have alternative representations as *worldline models*. Consider drawing a line on an edge of the square lattice whenever its arrow points down or to the left and leaving it empty otherwise. In this way a given configuration of the 6-vertex model is translated as shown in Fig. 4.3 to a number of closed, non-intersecting lines on the lattice (we assume periodic boundary conditions). For the 6-vertex model the number of present line-segments is identical for each horizontal row of vertical edges of the lattice, while for the 8-vertex model this number can vary between rows. This worldline picture is the natural representation for the quantum spin models equivalent to certain vertex models as will be described in Section 4.1.3.

4.1.2 Exact solution of the zero-field cases

The 6-vertex model

The square-lattice, zero-field 6-vertex model has been solved exactly in the thermodynamic limit by means of a transfer matrix technique by Lieb [62, 176, 179] and Sutherland [180]. As it turns out [55, 173], the analytic structure of the free energy

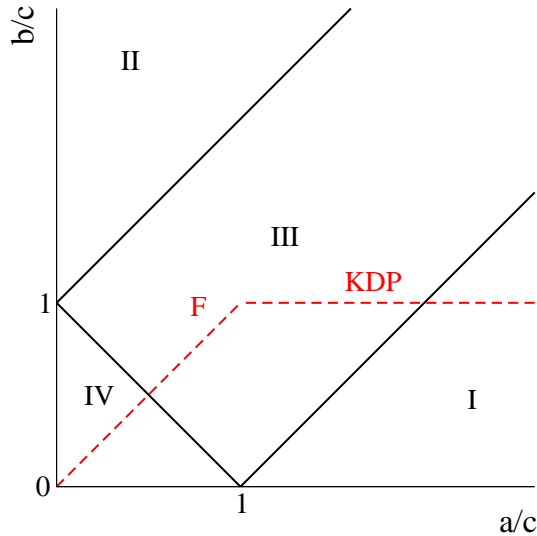


Figure 4.4: The phase diagram of the square-lattice, zero-field 6-vertex model in terms of the re-scaled weights a/c and b/c . Phase boundaries are indicated by solid lines. The phases I and II are ferroelectrically ordered, phase IV exhibits anti-ferroelectric order and phase III constitutes the disordered regime. The dashed lines do not indicate phase boundaries, but denote the parameter ranges of the KDP and F models, respectively.

is most conveniently parameterized in terms of the variable

$$\Delta = \frac{a^2 + b^2 - c^2}{2ab}, \quad (4.10)$$

such that the free energy takes a different analytic form depending on whether $\Delta < -1$, $-1 < \Delta < 1$ or $1 < \Delta$. This leads to a phase diagram of the model consisting of four distinct phases as shown in Fig. 4.4. The phases I and II are both characterized by $\Delta > 1$, thus corresponding to the same analytic form of the free energy. For phase I one has $a > b + c$, such that the configurations are dominated by the vertices 1 and 2. Therefore, at low temperatures the system orders ferroelectrically; the corresponding ground state is of the form shown in Fig. 4.5(a). Phase II is characterized by $b > a + c$, i.e., it is related to phase I by a simple exchange of vertices 1 and 2 by 3 and 4, which corresponds to a rotation of the whole lattice by $\pi/2$. Thus phase II is also a ferroelectrically ordered phase. In the intermediate case $-1 < \Delta < 1$, corresponding to phase III, the vertex weights fulfil the relation $a, b, c < (a + b + c)/2$. Since this includes the infinite temperature point $a = b = c = 1$, this region corresponds to the disordered phase. However, it can be shown [55, 173] that the correlation length is infinite everywhere in phase III,

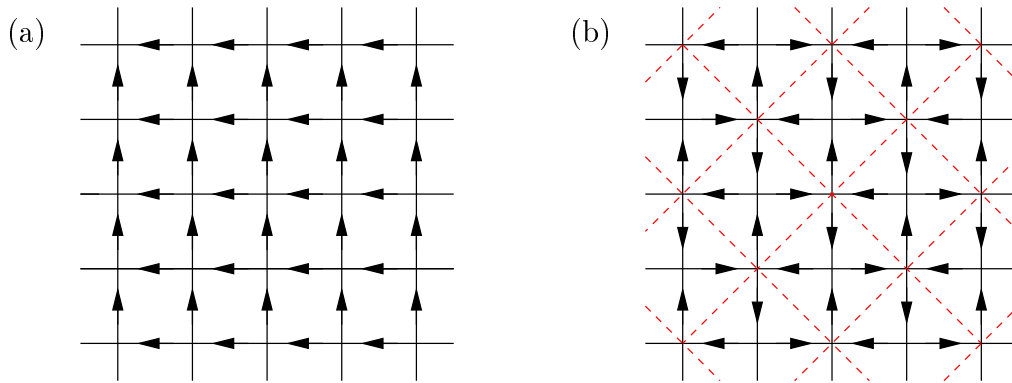


Figure 4.5: Parts of the ground-state configurations of the 6-vertex model in phases II and IV. (a) One of the two ferroelectrically ordered ground states in phase II. It consists entirely of the vertex configuration 4. (b) One of the two anti-ferroelectrically ordered ground states of phase IV. The state consists of vertices 5 and 6 at equal proportions. The dashed lines show one of the two tilted sub-lattices, which are *ferroelectrically* ordered.

i.e., correlations decay algebraically instead of exponentially. Nevertheless, there is no long-range ordering in this phase. This peculiarity can be traced back to the fact that the 6-vertex model corresponds to a *critical* surface in the phase diagram of the 8-vertex model [55]. Finally, for $\Delta < -1$ one has $c > a + b$, such that in phase IV the vertex configurations 5 and 6 dominate, leading to anti-ferroelectric order; the corresponding ground state is depicted in Fig. 4.5(b).

While the ferroelectrically ordered phases exhibit an overall polarization, which can be used as an order parameter for the corresponding transition, the anti-ferroelectric order of phase IV is accompanied by a *staggered* polarization with respect to a sub-lattice decomposition of the square lattice. That is, when decomposing the square lattice into two new square lattices tilted by $\pi/4$ against the original one as shown in Fig. 4.5(b), the anti-ferroelectric ground states correspond to a *ferroelectric* ordering of the vertices of the sub-lattices with opposite signs of the overall polarization of the sub-lattices. An order parameter for the corresponding transition can be defined by introducing overlap variables σ_i for each vertex of the lattice such that [55],

$$\sigma_i = v_i * v_i^0, \quad (4.11)$$

where v_i^0 denotes the anti-ferroelectric ground-state configuration depicted in Fig.

4.5(b) and the product “*” denotes the overlap given by

$$v * v' \equiv \sum_{k=1}^4 A_k(v)A_k(v'), \quad (4.12)$$

where k numbers the four edges around each vertex and $A_k(v)$ should be +1 or -1 depending on whether the corresponding arrow of v points out of the vertex or into it. Then, the *spontaneous staggered polarization* $\langle \sigma_i \rangle / 2 = \langle \sigma \rangle / 2$ vanishes in the disordered phase and approaches unity for low temperatures in phase IV and can thus be used as an order parameter for the anti-ferroelectric transition.

The transitions between the phases I–IV can be analyzed from the exact expression for the free energy of the model [62, 176, 179, 180]. We consider the temperature T as the external parameter to be tuned, whereas the vertex energies ϵ_j are kept fixed. Then, starting from one of the ordered, low-temperature phases I, II or IV, increasing the temperature one traces out a path in the phase diagram which always ends at the infinite-temperature point $a = b = c = 1$ in phase III, cf. Fig. 4.4. The transition temperatures can be easily inferred from the exact phase boundaries of the phase diagram Fig. 4.4. The transitions I \rightarrow III and II \rightarrow III are discontinuous or first-order phase transitions between the ferroelectrically ordered and the disordered regimes [55]. However, in the ferroelectrically ordered phases the model has the peculiarity of sticking to the ground states throughout the whole phase, i.e., also for non-zero temperatures. This is due to the fact that the simplest deformation of the ground state depicted in Fig. 4.5(a) consists of reversing the arrows of a whole *line* of bonds spanning the lattice². In the thermodynamic limit, this corresponds to an infinite amount of energy and thus does not occur within the phases I or II. On the other hand, the anti-ferroelectric transition III \rightarrow IV is also rather pathological. The singular part of the free energy density can be shown to behave as [55]

$$f_{\text{sing}} \propto \exp(-\text{const}/|t|^{\frac{1}{2}}), \quad (4.13)$$

i.e., all temperature derivatives exist and vanish exponentially as $|t| \rightarrow 0$. This corresponds to a phase transition of *infinite* order, known from the XY model as Kosterlitz-Thouless (KT) phase transition [63, 64].

²Obviously it is also possible to flip the arrows around one of the elementary plaquettes, i.e. squares. This, however, would produce vertices of the types 5 and 6, which are strongly suppressed in the ferroelectrically ordered phases at low temperatures.

The 8-vertex model

The inclusion of the vertices 7 and 8 of Fig. 4.2 allows one to make local, finite-energy deformations of the ferroelectric ground states and thus one expects less pathological behaviour from the resulting 8-vertex model. In the thermodynamical limit, it can be solved exactly by means of the method of “commuting transfer matrices” and the “star-triangle relation” [59,60]. The parameter Δ classifying the phases is now generalized to

$$\Delta = \frac{a^2 + b^2 - c^2 - d^2}{2(ab + cd)}. \quad (4.14)$$

Depending on the value of Δ , the system is confined in one of five phases [59,60]:

- I. Ferroelectric: $a > b + c + d$, $\Delta > 1$,
- II. Ferroelectric: $b > a + c + d$, $\Delta > 1$,
- III. Disordered: $a, b, c, d > (a + b + c + d)/2$, $-1 < \Delta < 1$,
- IV. Anti-ferroelectric: $c > a + b + d$, $\Delta < -1$,
- V. Anti-ferroelectric: $d > a + b + c$, $\Delta < -1$,

which can be mapped onto each other exploiting certain symmetry relations of the model [55]. In the generic case, the phase boundaries defined by the above relations correspond to second-order phase transitions. It can be shown [59,60] that for this generic case the singular part of the free energy scales in the vicinity of the phase boundaries as

$$f_{\text{sing}} \sim |t|^{\pi/\mu}, \quad (4.15)$$

where now t is a generalized reduced temperature variable and the critical value of μ is given by

$$\tan(\mu/2) = \sqrt{cd/ab}. \quad (4.16)$$

From the given scaling form of the free energy it is obvious that the critical exponents resulting from this scaling also depend on μ ; in particular, one finds [60]

$$\beta = \pi/16\mu, \quad \nu = \pi/2\mu, \quad \gamma = 7\pi/8\mu, \quad (4.17)$$

such that the critical exponents vary *continuously* with the parameter μ . Obviously, this is in contradiction with the usual notion of universality of critical exponents.

The situation can be reconciled with the expectations based on the concept of *weak universality* [181], which suggests that instead of expressing the scaling ansatz in terms of the parameter $|t|$, one should formulate scaling in terms of the correlation length ξ . This leads, very similar to the case of finite-size scaling, to an additional factor of $1/\nu$ multiplying all of the other exponents, and the renormalized exponents,

$$\beta' \equiv \beta/\nu = \frac{1}{8}, \quad \gamma' \equiv \gamma/\nu = \frac{7}{4}, \quad (4.18)$$

are constant and independent of the value of μ . At the exceptional points $\mu = \pi/n$, where n is an integer, the scaling relation (4.15) is no longer valid and must be either augmented by a logarithmic correction (n even) or is even replaced by a completely different formula (n odd). This latter case especially includes the first-order ferroelectric transitions present in the phase diagram of the 6-vertex model, which obviously must be included in the more general 8-vertex model as the limiting case $d = 0$. The special case $\mu = 0$ corresponds to the Kosterlitz-Thouless type anti-ferroelectric phase transition of the 6-vertex model. From the point of view of the 8-vertex model it is found that the disordered phase III of the *6-vertex* model corresponds to a critical surface of the 8-vertex case; this explains the divergence of the correlation length throughout this whole phase.

4.1.3 Transformations and specializations

The quite general 8-vertex model includes several interesting special cases. Additionally, it can be mapped onto a multitude of different problems of statistical mechanics and graph theory. We will only briefly summarize the most important of these correspondences. The most obvious limiting case is that of the 6-vertex model, which is obtained for $d = 0$ and in turn comprises as special cases the ice and F models, among others. The ice model itself can be mapped to a variety of counting problems, including that of dimers on the square lattice [56] and the three-colour face-colouring problem of the square lattice [55].

The 8-vertex model, on the other hand, is equivalent to a non-interacting many-fermion system for the special choice of weights [182]

$$a^2 + b^2 = c^2 + d^2, \quad (4.19)$$

which thus defines the *free-fermion model*, which is of interest since it can be solved using Pfaffians, such that one does not need the much more elaborate ansatz used

to solve the general 8-vertex model [55]. One of the most important transformations is that of the 8-vertex model in an electric field to a zero-field Ising model³ on the square lattice, including nearest-neighbour, next-nearest-neighbour and four-spin interactions [55, 182]. Especially, by means of a suitable sub-lattice decomposition, this model can be considered as the sum of two ordinary, nearest-neighbour Ising models on the sub-lattices coupled by four-spin interactions. For a certain choice of the vertex weights this coupling can be removed such that the resulting model is that of two uncoupled Ising models [56] and the partition functions are related as

$$Z_{8V} = 2Z_{\text{Ising}}. \quad (4.20)$$

Alternatively, the 8-vertex model can be mapped onto an Ising model with only two-spin interactions, which are then between nearest neighbours and next-next-nearest neighbour spins [55].

Furthermore, the 8-vertex model is equivalent to the *XYZ* chain quantum spin model with Hamiltonian

$$\mathcal{H} \equiv -\frac{1}{2} \sum_{\langle j \rangle} \mathcal{H}_{jj+1} = -\frac{1}{2} \sum_{\langle j \rangle} [J_x \sigma_j^x \sigma_{j+1}^x + J_y \sigma_j^y \sigma_{j+1}^y + J_z \sigma_j^z \sigma_{j+1}^z], \quad (4.21)$$

where the σ_j are quantum spin-1/2 operators at the sites j and $\langle j \rangle$ denotes summation over the chain assuming periodic boundary conditions. Here, “equivalence” means identity of the eigenvalues of the respective transfer matrices [177]. The transformation revealing this equivalence can be demonstrated in the *worldline representation* of the *XYZ* chain [183], which can be sketched as follows (see, e.g., Ref. [155]). Split the Hamiltonian (4.21) into commuting pieces,

$$\begin{aligned} \mathcal{H} &= \mathcal{H}_{\text{even}} + \mathcal{H}_{\text{odd}} \\ \mathcal{H}_{\text{even,odd}} &= \sum_{j: \text{even,odd}} \mathcal{H}_{jj+1}, \end{aligned} \quad (4.22)$$

and perform a Trotter-Suzuki breakup [184, 185],

$$Z = \text{Tr} e^{-\beta \mathcal{H}} = \lim_{L_t \rightarrow \infty} Z_{\text{Tr}} = \lim_{L_t \rightarrow \infty} \text{Tr} \left(e^{-\frac{\beta}{L_t} \mathcal{H}_{\text{even}}} e^{-\frac{\beta}{L_t} \mathcal{H}_{\text{odd}}} \right)^{L_t}, \quad (4.23)$$

where L_t denotes the number of (imaginary) *time slices* used in the discretisation. Inserting complete sets of σ^z eigenstates, one arrives at the worldline representation,

$$Z_{\text{Tr}} = \sum_{S_{jt}^z} W(\{S_{jt}^z\}) = \sum_{S_{jt}^z} \prod_p W_p(\{S_p\}), \quad (4.24)$$

³Note that the most general 16-vertex model on the square lattice (which has not been solved) is equivalent to two Ising models *in a magnetic field* (which has also not been solved) [56].

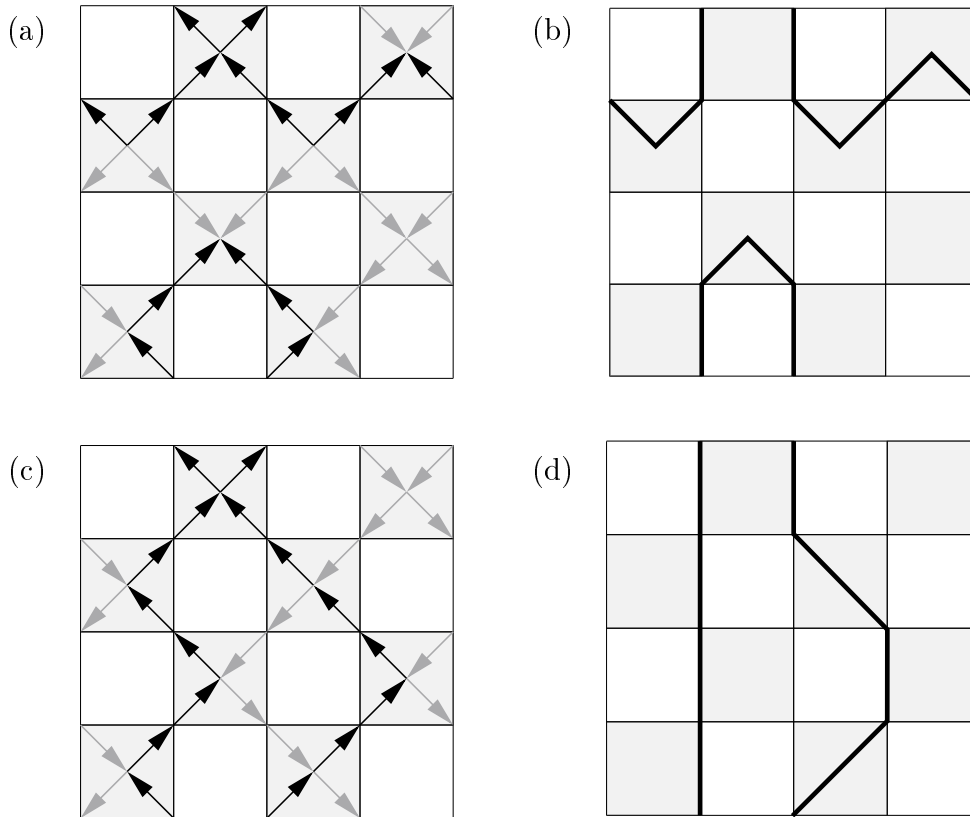


Figure 4.6: Worldline and vertex-model representations of the XYZ quantum spin chain. (a) Classical spin variables $S^z = \pm 1$ living on the corners of the shaded plaquettes and denoted by arrows pointing upward (+1) or downward (-1) in the vertical time direction. The arrow configurations correspond to those of a tilted square-lattice 8-vertex model with special boundary conditions. (b) The same configuration in the worldline representation. (c) Plaquette configuration of the Heisenberg-Ising chain corresponding to an arrow configuration of the 6-vertex model. (d) The corresponding worldlines.

which is a sum over *classical* spin variables $S_{jt}^z = \pm 1$ living on a checkerboard lattice with the original space direction $j = 1, \dots, N$ and an additional (imaginary) time direction $t = 1, \dots, L_t$, cf. Fig. 4.6(a). The configurational weights $W(\{S_{jt}^z\})$ can be broken up into weights $W_p(\{S_p\})$ associated with the elementary *plaquettes* $p = [(j, t), (j+1, t), (j, t+1), (j+1, t+1)]$ of the lattice. As it turns out [155], only the weights of plaquettes with an even number of up and down spins give non-vanishing contributions. Thus, depicting the spin values S^z by arrows pointing upwards or downwards in imaginary time direction as shown in Fig. 4.6(a), the resulting arrow

configurations on the shaded plaquettes fulfil the generalized ice-rule of the 8-vertex model⁴. On the other hand, as mentioned above, the configurations of the square-lattice vertex model can be depicted as closed, oriented, non-intersecting lines (or polygons), cf. Fig. 4.3(b); thus one arrives at the worldline representation of the XYZ quantum chain depicted⁵ in Fig. 4.6(b).

Special cases of the XYZ quantum chain are the (quantum) Heisenberg model ($J_x = J_y = J_z$), the XY model ($J_z = 0$), the XZ chain ($J_y = 0$) and the so-called Heisenberg-Ising or XXZ model ($J_x = J_y$). As it turns out, the XZ limit corresponds to the special case of the 8-vertex model equivalent to two uncoupled, nearest-neighbour Ising models, the XY model corresponds to the free-fermion model limit and the Heisenberg-Ising chain is equivalent to the 6-vertex model [55]. For the latter case, the number of corresponding worldlines is conserved in the imaginary time direction as depicted in Figs. 4.6(c) and (d).

Further transformations can be found when considering the 8-vertex model on the Kagomé lattice (which is four-valent like the square lattice). This model is also exactly solvable and has further correspondences to well-known models of statistical mechanics. Namely, it includes the triangular and honeycomb lattice nearest-neighbour Ising models, the triangular and honeycomb critical q -state Potts models and an Ising model with (only) three-spin interactions on the triangular lattice [55].

4.2 The Loop Algorithm

As mentioned above in the introduction of this chapter it is hard to formulate an efficient update for vertex models due to the strong constraints on the allowed arrow configurations. A trivial local update would be to flip the arrows around the elementary plaquettes of the lattice, e.g., the squares for the case of the square lattice. This algorithm, however, suffers from critical slowing down with the dynamical critical exponent $z \approx 2$ typical for local algorithms [174]. For the 6-vertex model one has the additional complication of a massless disordered phase, such that

⁴Note, however, that due to the tilting of the lattice the equivalent 8-vertex model acquires rather unconventional boundary conditions.

⁵Note that the way the worldlines are drawn is slightly different from the presentation of Fig. 4.3(b), since here the line segments are drawn on the links of the checkerboard lattice and not on those of the lattice formed by the vertex model arrows.

autocorrelation times are expected to be large throughout this whole region. Whenever *cluster algorithms* [168, 171, 186, 187] can be found they are usually the most efficient updates in the vicinity of continuous phase transitions. This was for the first time achieved for the ferromagnetic, nearest-neighbour Ising, Potts and $O(n)$ models [168, 171]. As could have been conjectured from the close relation of vertex models to spin models such as the Ising and Potts models, it is possible to formulate cluster algorithms for vertex models, too. The most prominent of these algorithms is given by the *loop algorithm* [76, 174, 188, 189].

4.2.1 Idea and outline

In a formal description, the basic idea of cluster algorithms is that of a transformation of the representation of the model under consideration from the “natural” state space variables such as, e.g., the spin variables of the Ising model, to an enlarged space of states, additionally comprising *graph variables*, which are usually a subgraph of the lattice under consideration and are for each configuration “compatible” with the original (e.g. spin) variables [186, 187, 190]. This is the generalized notion of a *Fortuin-Kasteleyn representation* [191]. Then, new statistical weights are chosen in the enlarged phase space in which the cluster simulation is performed. While for the Ising model the relevant graph variables are *bonds* of the lattice that are chosen to be activated or passive, for the loop algorithm the graph variables are decompositions or *breakups* of the vertices and the surrounding edges. The possible breakups for a four-valent lattice are shown in Fig. 4.7. As for the bonds in the Ising case, which can only be set between parallel spins, not every breakup is compatible with a given configuration of the vertex model.

After the graph transformation, i.e., after choosing a breakup for each vertex of the lattice, a new configuration, which is also in agreement with the chosen breakup, is achieved by a suitable flipping of the arrows on the lattice bonds. This can be done in the following way. Interpreting the vertex arrows as a discrete vector field, the ice-rule of the 6-vertex model translates to the condition of zero divergence of this field. Analogously, the generalized ice-rule of the 8-vertex model is equivalent to the statement that the corresponding vector field should have zero divergence “mod 4”. As a consequence, every configuration of the 6- or 8-vertex models can be constructed from a given reference configuration by a reversal of the arrows of

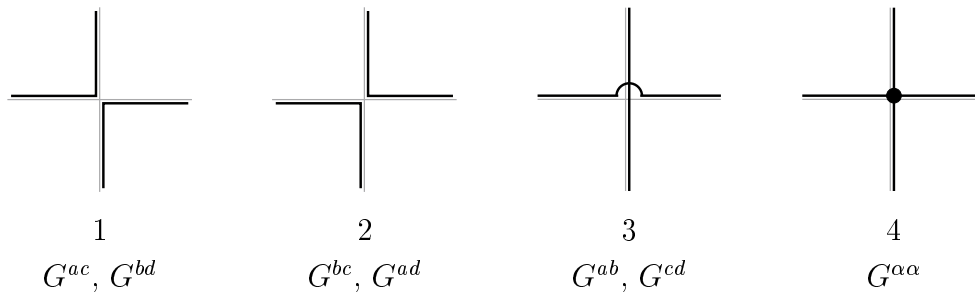


Figure 4.7: Possible vertex breakups for the 8-vertex model. The breakups $G^{\alpha\beta}$ are labelled by the vertex energies a, b, c, d , such that a symbolizes vertices 1 and 2, b vertices 3 and 4 etc. of Figs. 4.1 and 4.2. The breakup $G^{\alpha\beta}$ is possible for a vertex of type $\alpha \in \{a, b, c, d\}$ and it is taken to configuration β , if the corresponding loop is flipped. For the 6-vertex model, transitions with label d do not occur. The breakups $G^{\alpha\alpha}$ correspond to a *freezing* of the considered vertex, i.e., a flip does not change the vertex weight since all arrows are flipped together.

a number of *closed loops* on the lattice⁶, with an “almost constant” direction of the arrows along them [76]. Here, the restriction to “almost constant” takes care of the vertices 7 or 8 of the 8-vertex model, where the loops have to change their arrow direction. This set of loops is uniquely defined from the arrow configuration of the vertex model in combination with the chosen breakups of the vertices. To construct it, start to “grow” a loop at a given bond of the lattice, walking in the direction of the arrows. Each time you hit a site of the lattice, the walk continues in the direction indicated by the breakup of the corresponding vertex, i.e., it turns to the left or right for breakups 1 and 2 or it goes straight on for breakup 3 (breakup 4 will be discussed later), cf. Fig. 4.7. For vertices of the types 7 or 8 the loop changes its arrow direction at that site. Due to the (generalized) ice rule, each walk constructed in this way eventually returns to the vertex it originated from, thus closing it to a loop. Repeating this construction until each bond of the lattice has been visited, decomposes the lattice into a set of such loops. Then, the new vertex-model configuration is found by independently proposing to invert the arrow direction along each loop with a probability of, say, one half. This is completely analogous to the proposal of cluster flips in the Swendsen-Wang cluster algorithm for the Ising model [171].

⁶Note that the such defined loops are possibly self-intersecting, in contrast to the worldlines considered above.

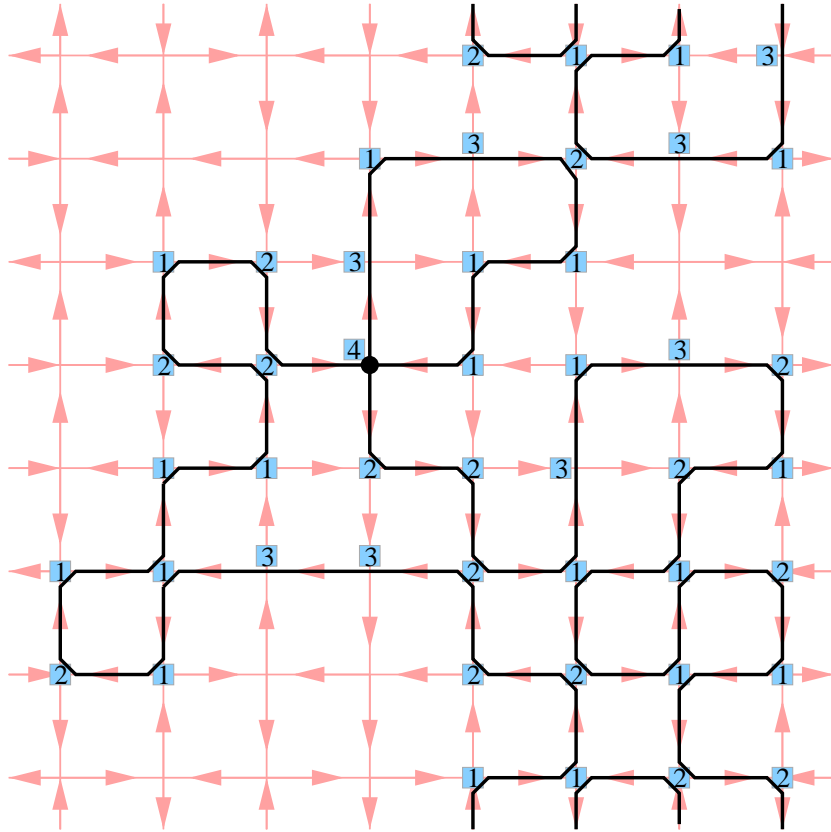


Figure 4.8: A loop cluster (black solid lines) built on top of a configuration of the 6-vertex model on a 8×8 lattice with periodic boundary conditions. The numbers 1–4 near the vertices indicate the chosen breakups according to Fig. 4.7. At the vertex with breakup 4 (black dot) two loops are glued together to form the loop cluster. For illustration purposes, the breakups are only shown along the path of the presented loop cluster.

The type-4 breakup of Fig. 4.7, also called *freezing* of a vertex, requires a different treatment. On coming across a frozen vertex, one chooses (at random) one of the breakups 1 to 3 compatible with the given vertex configuration to determine the direction to leave the vertex. After closing the loop, one has to grow a second loop starting from one of the bonds of the frozen vertex that have not yet been touched. Then, these two loops are glued together to form a *loop cluster*, i.e., one proposes to flip them together. As a consequence, the statistical weight of the frozen vertex does not change, since all four of the adjacent arrows are flipped or left unchanged. This freezing procedure corresponds to the activation of bonds in the Swendsen-Wang algorithm, which there entails that two *spins* are always flipped together. Thus,

taking the concept of freezing into account, each vertex configuration is decomposed into a set of loop clusters, which then are flipped independently with a given probability to arrive at the new vertex model configuration. Figure 4.8 shows an example of such a cluster of loops occurring in a loop algorithm simulation of the 6-vertex model.

Thus, we have the following recipe for the cluster algorithm for the 6- and 8-vertex models:

- (a) For each site of the lattice, choose one of the breakups 1–4 with suitably chosen probabilities, which solely depend on the vertex configuration at the respective site.
- (b) Decompose the vertex configuration into a set of loop clusters. To do so, choose a lattice edge at random and walk along the bonds following the arrow directions. At each site, choose the direction prescribed by the breakups determined in step (a). If freezing occurs at a site, choose one of the breakups 1–3 at random to continue the loop and (after finishing the current loop) grow another loop at the same site, which is glued to the first loop to a loop cluster. For the 8-vertex model, when hitting upon a vertex of types 7 or 8, change the orientation of the loop. Repeat this process, until all bonds are touched by a loop.
- (c) Flip each loop cluster independently with a constant probability of, e.g., one half. Here, “flipping” means reversing the direction of all the vertex arrows along the loop.
- (d) With the new vertex-model configuration, start again with the breakup step (a).

4.2.2 Choice of the breakup probabilities

In the general scheme of Refs. [186, 187, 190] the enlargement of phase space to include the breakups is expressed by the fact that the weight function of Eq. (4.3),

$$W(\mathcal{V} = \{v_i\}) = \exp\left[-\sum_i E(v_i)/k_B T\right], \quad (4.25)$$

is replaced by a generalized weight function $W(\mathcal{V}, \mathcal{G})$, such that

$$\sum_{\mathcal{G}} W(\mathcal{V}, \mathcal{G}) = W(\mathcal{V}), \quad W(\mathcal{V}, \mathcal{G}) \geq 0, \quad (4.26)$$

where $\mathcal{G} = \{G_i\}$ denotes the set of chosen vertex breakups. This results in a Fortuin-Kasteleyn type representation of the partition function (4.3),

$$Z = \sum_{\mathcal{V}} \sum_{\mathcal{G}} W(\mathcal{V}, \mathcal{G}). \quad (4.27)$$

Then, a cluster-update Monte Carlo simulation consists of the two steps of choosing the breakups with probability

$$p[\mathcal{V} \rightarrow (\mathcal{V}, \mathcal{G})] = \frac{W(\mathcal{V}, \mathcal{G})}{W(\mathcal{V})}, \quad (4.28)$$

selecting a new configuration \mathcal{V}' of the spin or vertex variables and accepting the move $\mathcal{V} \rightarrow \mathcal{V}'$, e.g., with the heat-bath probability

$$p[(\mathcal{V}, \mathcal{G}) \rightarrow (\mathcal{V}', \mathcal{G})] = \frac{W(\mathcal{V}', \mathcal{G})}{W(\mathcal{V}, \mathcal{G}) + W(\mathcal{V}', \mathcal{G})}, \quad (4.29)$$

where we have already assumed that the graph configuration is not changed by the flip, i.e., $\mathcal{G}' = \mathcal{G}$ [186]. Since the breakup process is done independently for each vertex, the generalized weight function factorizes,

$$W(\mathcal{V}, \mathcal{G}) = \prod_i w(v_i, G_i), \quad (4.30)$$

where the index i runs over all sites of the lattice⁷. In order to be able to flip the loop clusters independently, one additionally assumes that the local weights are not changed by the flip operation, i.e.,

$$w(v, G) = w(v', G). \quad (4.31)$$

Then, the cluster flip probability (4.29) becomes a constant and can be chosen to be, e.g., $p[(\mathcal{V}, \mathcal{G}) \rightarrow (\mathcal{V}', \mathcal{G})] = 1/2$. The condition (4.31) can be obviously realized by considering a fixed set of vertex breakups $G^{\alpha\beta}$, which allow exactly the transition of a vertex from type α to type β , such that the corresponding weights are given by

$$w(v, G^{\alpha\beta}) = \begin{cases} w^{\alpha\beta}, & \text{if } v \text{ is of type } \alpha, \\ 0, & \text{otherwise,} \end{cases} \quad (4.32)$$

⁷In general, one has to take an overall factor $A_{\text{global}}(\mathcal{V})$ into account here. However, for the case of zero-field vertex models, one can choose $A_{\text{global}}(\mathcal{V}) = \text{const}$ [76].

where the constants $w^{\alpha\beta} = w^{\beta\alpha}$ are taken symmetric in their indices to honour Eq. (4.31).

Suitable constants $w^{\alpha\beta}$ can always be found, see Refs. [76, 188]. However, they are not uniquely defined by the present constraints. Within the range of allowed values, an optimum can be attained guided by the principle of *minimal freezing*: it is intuitively obvious that freezing of vertices, i.e., the assignment of breakups of the type $G^{\alpha\alpha}$ of Fig. 4.7, which glues two loops together to a loop cluster to be flipped together, tends to increase the correlation between successive configurations generated by the loop algorithm. This conjecture is confirmed by numerical results [174]. Thus, minimizing $w^{\alpha\alpha}$ should result in the most efficient algorithms. We present here the optimal weights for the case of the 6-vertex model. As it turns out [188], the condition of minimal freezing gives distinct solutions for different regions of the $\{a, b, c\}$ parameter space. In fact, these regions coincide with the phases I–IV of the 6-vertex model discussed above in Section 4.1.2. Depending on the phase, the optimal weights are given in the following list [76].

(I) *Ferroelectric phase I*: Here, $a > b + c$ and the non-zero weights are

$$\begin{aligned} w^{ab} = w^{ba} &= b, \\ w^{ac} = w^{ca} &= c, \\ w^{aa} &= a - c - b, \end{aligned} \tag{4.33}$$

i.e., freezing occurs only for vertices of the types 1 and 2.

(II) *Ferroelectric phase II*: For $b > a + c$, the weights are given by interchanging indices b and c from phase I and freezing of b vertices instead of a vertices,

$$\begin{aligned} w^{ab} = w^{ba} &= c, \\ w^{ac} = w^{ca} &= b, \\ w^{bb} &= a - c - b. \end{aligned} \tag{4.34}$$

(III) *Disordered phase III*: For $a, b, c \leq (a + b + c)/2$ one can avoid freezing and has,

$$\begin{aligned} w^{ab} = w^{ba} &= (b + a - c)/2, \\ w^{ac} = w^{ca} &= (a + c - b)/2, \\ w^{bc} = w^{cb} &= (c + b - a)/2. \end{aligned} \tag{4.35}$$

(IV) *Anti-ferroelectric phase IV*: For $c > a + b$ one has,

$$\begin{aligned} w^{ac} = w^{ca} &= a, \\ w^{bc} = w^{cb} &= b, \\ w^{cc} &= c - a - b, \end{aligned} \tag{4.36}$$

such that freezing only occurs for vertices 5 and 6.

For each phase, the weights not listed above are taken to be zero in the corresponding region.

4.2.3 Practical application and tests

For the further discussion we specialize on the case of the 6-vertex model, which is of main interest in this thesis.

Ergodicity and detailed balance

The issues of ergodicity and detailed balance can be quite straightforwardly settled for the loop algorithm. Fulfilment of the detailed balance condition follows trivially from the construction of the weights from Eq. (4.28). Since, as a consequence of the (generalized) ice rule, any two vertex configurations are related to each other by a unique set of loop flips [56], ergodicity of the algorithm is obvious if all $w^{\alpha\beta}$ are chosen non-zero. For the special choices of weights presented above, where some of the breakups do not occur, one has to check explicitly that ergodicity is still guaranteed. This is in general easy to see by inspection [76]. The only region, where some problems can occur is the anti-ferroelectric phase IV. In terms of the equivalent quantum spin model in its worldline representation, the magnetization corresponds to the *number* of worldlines present as can be seen from Fig. 4.6. It can only be changed by flipping loops that wind around the lattice in temporal direction. With the given choice of weights for phase IV, however, the loops change direction at every site of the checkerboard lattice of Fig. 4.6. Thus, if the lattice has an *odd* number of rows (corresponding to a frustrated anti-ferromagnet), loops with non-trivial temporal winding numbers cannot be constructed with the given weights. In that case, one has to introduce breakups of the type G^{ab} with a finite probability and adapt the other weights correspondingly [76]. However, for the

simulations on random lattices of the topology of a sphere considered in this thesis, this “topological” problem can obviously not occur.

Implementation and test

It should be obvious from the previous discussion that the loop algorithm is with suitable adaptations in the treatment of the lattice part applicable to any four-valent graph with orientable faces, i.e., with a cyclical ordering of the links. Thus, it can be easily employed for vertex models on the ϕ^4 graphs discussed in the previous chapter. We choose a four-bit encoding of the vertex arrows in order to have an easy access to the directions of the arrows on the links as well as the total type 1–6 of the configuration of the vertex. To check the proper functioning of the algorithm, we performed simulations for the F model (cf. Eq. (4.6)) on a 4×4 square lattice with periodic boundary conditions with the same program used for the true random lattice simulations, but with no lattice-update moves employed. Deviations from the expected correct results are expected to be most prominent for such small lattice sizes. The outcomes of these simulations are compared to the exact expression for the F model on the considered lattice, found by a brute-force summation of the partition function (4.3), which can be somewhat simplified by exploiting the special symmetries of the F model. As shown in Fig. 4.9 the loop algorithm simulations with the choice of weights given above give results in perfect agreement with the exact expressions. From the condition $c = a + b$ for the boundary line between phases III and IV of the 6-vertex model, one finds the KT transition to happen at $\beta_c = 1/k_B T_c = \ln 2$, assuming $\epsilon_a = \epsilon_b = 1$ for simplicity. The location of the peaks of the specific heat and the polarizability are in qualitative agreement with this transition point.

Performance

Since the typical extent of the objects considered in a cluster algorithm coincides with the correlation length when operating at criticality, cluster algorithms promise the most substantial efficiency gain for a system in the vicinity of a continuous phase transition. The dynamical critical exponent z is usually largely reduced, and, in some cases, even compatible with an only logarithmic growth implying $z = 0$, see, e.g., Ref. [193]. A similar reduction of critical slowing down has been observed for the

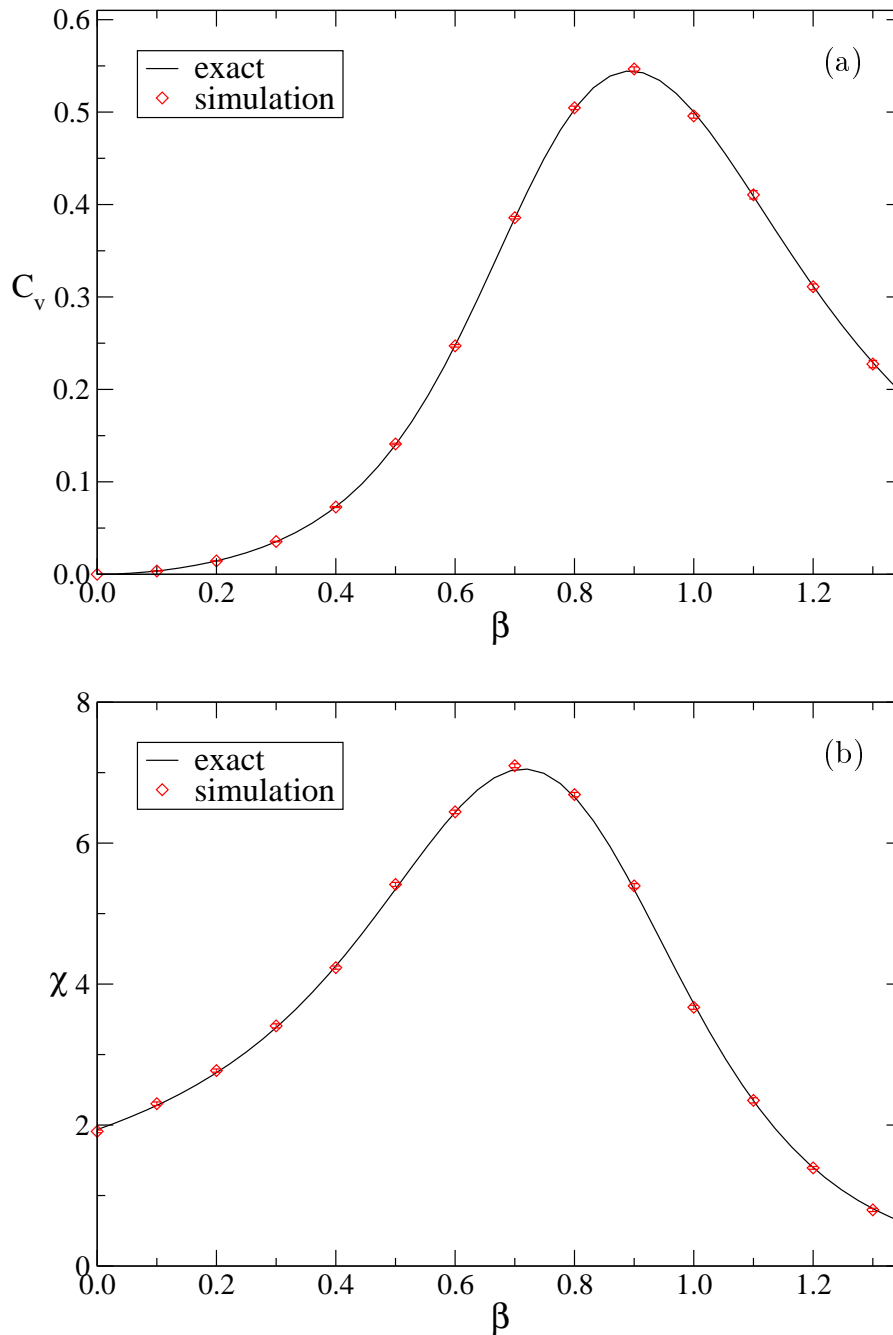


Figure 4.9: Specific heat per site (a) and the polarizability belonging to the staggered polarization of Eq. (4.11) (b) of the F model on a 4×4 square lattice with periodic boundary conditions from loop-cluster Monte Carlo simulations of 5×10^5 measurements each. The solid lines show the exact results from a brute-force summation of the partition function exploiting the symmetries of the model. The drawn error bars are mostly hidden by the plotting symbols. The F model exhibits a Kosterlitz-Thouless type phase transition at $\beta_c = \ln 2 \approx 0.693$.

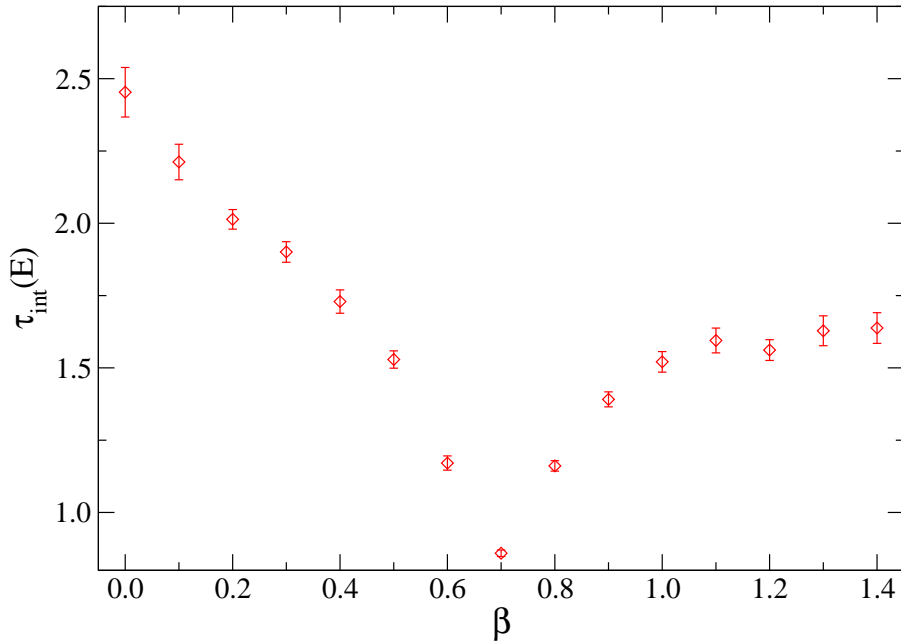


Figure 4.10: Integrated autocorrelation time of the energy E for a loop-algorithm simulation of the F model on a 4×4 square lattice with periodic boundary conditions. As typical for cluster algorithms, the performance is optimal in the critical regime (for a similar presentation for the Swendsen-Wang dynamics of the Potts model, see Ref. [192]). The autocorrelation times and the related statistical errors were estimated using the methods presented in Appendix A.4.

loop algorithm. As an example, for the F model at criticality one finds $z = 0.71(5)$ as compared to $z = 2.2(2)$ for the local algorithm flipping the arrows around the elementary plaquettes [174]. Since phase III is massless, one expects dynamical scaling to work for all $\beta < \beta_c$ and finds z to decrease with decreasing β [174]. We did not perform a detailed analysis of dynamical scaling for the loop algorithm applied to vertex models on regular lattices since we are mainly interested in the random lattice behaviour. However, to illustrate the fact that a major performance improvement for cluster algorithms as compared to local updates can only be expected in the vicinity of a critical point, in Fig. 4.10 we present the integrated autocorrelation time of the internal energy for the loop-algorithm simulation of the F model on a 4×4 lattice discussed above.

Single cluster variant

It should be noted that the loop algorithm can be easily adapted to the concept of a *single cluster* update [168], which often yields even further reductions of z and/or the corresponding scaling amplitude. This is done by just growing a single loop cluster and doing the breakups “on the fly”. However, since we finally have to mix the loop update with the (different) updates of the random graphs, it is desirable to have a fixed proportion between updates of the graph and matter parts. Therefore, we prefer to use the described multi-cluster variant. As will be demonstrated in the next chapter, the autocorrelations related to the graph dynamics are much larger than those of the vertex model, such that the minor differences between variants of the loop algorithm do not matter here.

4.3 Vertex Models on Random ϕ^4 Graphs

4.3.1 Additional symmetry

Putting a vertex model onto a *random* four-valent graph such as the quantum gravity ϕ^4 graphs discussed in the previous chapters imposes some additional restrictions on the class of vertex weights that can be sensibly considered. The ferroelectrically ordered phases I and II of the 8-vertex model and the order parameter describing the corresponding phase transition depend on the existence of a global notion of direction. The (plain, not staggered) polarization associated with the transition corresponds to the reaction of the system to an exterior electric field of constant direction. On a random graph, the notions of such a global orientation and constant direction are maldefined. The only local orientational structure available is that of the vertices and faces of the graph and their distances from each other in terms of the geodesic metric of the graph.

To demonstrate the consequences of this “loss of direction”, consider the KDP 6-vertex model coupled to planar ϕ^4 random graphs. On the square lattice this model exhibits a first-order phase transition to a ferroelectrically ordered phase consisting of vertices 1 and 2, cf. Fig. 4.4. The mechanism driving this transition is a symmetry breaking between the vertices of types a and b . The transition occurs at the point

where the vertices a attain the same weight as the sum of the other two types, i.e.,

$$1 = a = b + c = 2 \exp(-\beta_c), \quad (4.37)$$

where we have re-scaled $\epsilon_b = \epsilon_c = 1$ for simplicity; this implies $\beta_c = \ln 2$. Now, on a random graph of the described type vertices of the types a and b can obviously not be distinguished, since they are related to each other by rotations (of an angle of $\pi/2$). Since we only have a *cyclic* ordering of the links around each vertex, different rotational orientations of the vertex configurations cannot be distinguished. Thus, for an 8-vertex model coupled to quantum-gravity random ϕ^4 graphs, one has to assume that

$$a = b, \quad (4.38)$$

while the other vertex types can still be distinguished with only a cyclic ordering of the links around each vertex. For the 6-vertex model this leaves only two principally different choices of models to be sensibly considered: the F model with $\epsilon_a = \epsilon_b = 1$, $\epsilon_c = 0$ and the so-called *inverse F (IF) model* with $\epsilon_a = \epsilon_b = -1$, $\epsilon_c = 0$. The latter, however, can be shown to have no ordered phase and thus no phase transition. Since the additional disorder introduced by the random graphs can be hardly expected to make an ordered phase appear, this model is of little interest for statistical mechanics and field theory and will thus not be considered further. For the 8-vertex model one is left with a generalized F model. On the square lattice it has two anti-ferroelectric phases dominated by vertices of types c or d , respectively. The square-lattice phase diagram of this model is illustrated in Fig. 4.11.

In a computer program for the simulation of vertex models coupled to ϕ^4 graphs the rule $a = b$ can obviously be broken, since a *formal* distinction between vertices a and b is automatically made. Since, however, the dynamics of the random graphs does not respect this distinction, a ferroelectric order can impossibly occur. As a demonstration of this we present a short scan of the behaviour of a formally defined “KDP model” coupled to planar random ϕ^4 graphs. As can be seen from Fig. 4.12, the specific heat of the model exhibits a maximum for very low temperatures, mimicking the behaviour at a physical phase transition. However, this is only a consequence of the fact that the graph dynamics is subject to freezing as the temperature is lowered. Eventually, no allowed flip moves remain and, consequently, no energy changes occur, leading to a decrease of the specific heat. This mechanism obviously cannot correspond to a physical phase transition, since an allowed cyclic re-labelling of the links of some vertices of the graph corresponds to the same

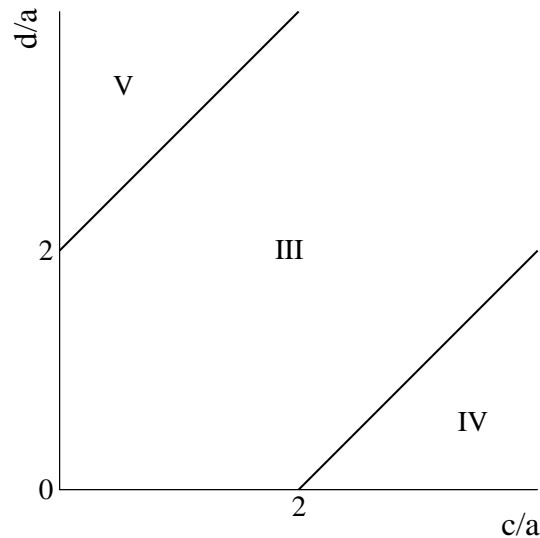


Figure 4.11: Phase diagram of the 8-vertex generalized F model on the square lattice, which is a cut of the phase diagram of the full 8-vertex model resulting from the condition $a = b$. The phases IV and V are anti-ferroelectric and vertices of types c and d , respectively, dominate. Phase III is the disordered phase.

physical situation, but would (in general) lead to an energy change since vertices of the type a are transformed into vertices of type b and vice versa, and $a \neq b$ is assumed. As a comparison, in Fig. 4.12 we plot the specific heat of the F model on the same graphs, which — as will be shown in the next chapter — exhibits a physical, continuous phase transition to an anti-ferroelectrically ordered phase.

4.3.2 The order parameter

For the square lattice an order parameter for the anti-ferroelectric transition of the F model could be defined by a suitably calculated overlap between the actual state and one of the two anti-ferroelectrically ordered ground states of the model. On a random graph, the corresponding ground states are not so easily found and, moreover, vary between different realizations of the connectivity of the graph. Thus, this notion of an order parameter cannot easily be generalized to the vertex models on random graphs.

To enable a generalization of the anti-ferroelectric order parameter to the case of random graphs, the vertex model has to be transformed to one of its numerous equivalent representations. Structurally, the anti-ferroelectrically ordered state has been

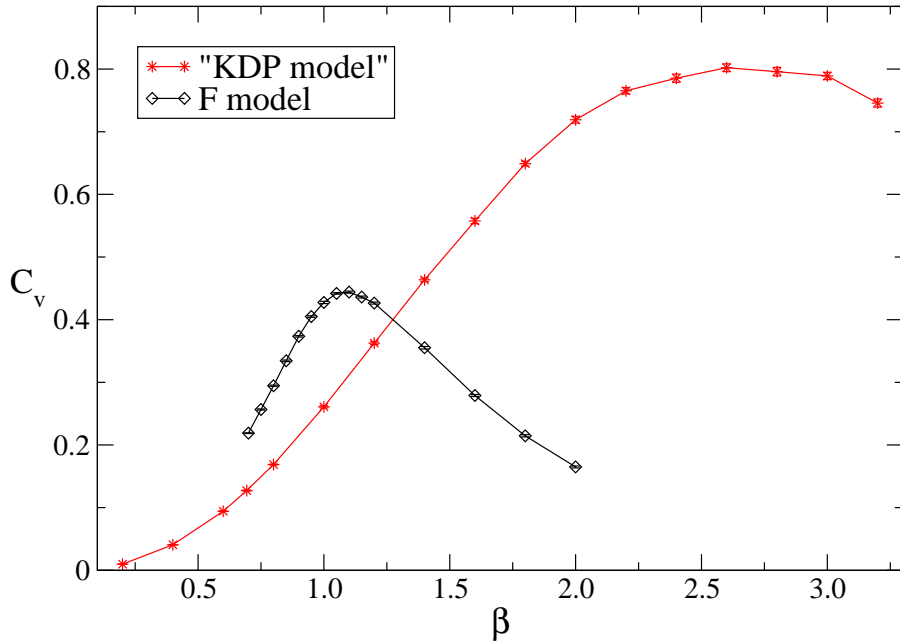


Figure 4.12: Specific heat of a formally defined “KDP model” coupled to random planar ϕ^4 graphs with labelled links and $N_2 = 256$ vertices as a function of the inverse temperature $\beta = 1/k_B T$. Its maximum for very low temperatures does not indicate a phase transition, but is merely an artefact of the labelling of the links. For comparison, the specific heat of the F model coupled to the same lattices is shown, which exhibits a physical phase transition.

described as one of ferroelectric order on two complementary sub-lattices, with the overall direction of the polarization chosen opposite to each other on the sub-lattices. A decomposition of the square lattice of this kind corresponds to a *bipartition* or *two-colouring* of its sites, cf. Fig. 4.5(b). This property of the decomposition prevents an immediate generalization to a random ϕ^4 graph, which is, in contrast to the square lattice, not necessarily bipartite. This follows from the following lemma: a graph is bipartite if and only if it has no cycles, i.e. closed paths, of an odd length. Obviously, such an odd-length cycle would not allow a labelling of the vertices met when traversing it with alternating colours. The proof of the inverse statement, namely that a graph without odd cycles is bipartite, is a bit more intricate and can be found, e.g., in Ref. [194]. However, the planar random ϕ^4 graphs considered in the previous chapter obviously include cycles of odd lengths, for example triangular faces; this can be explicitly checked by inspection of the co-ordination number dis-

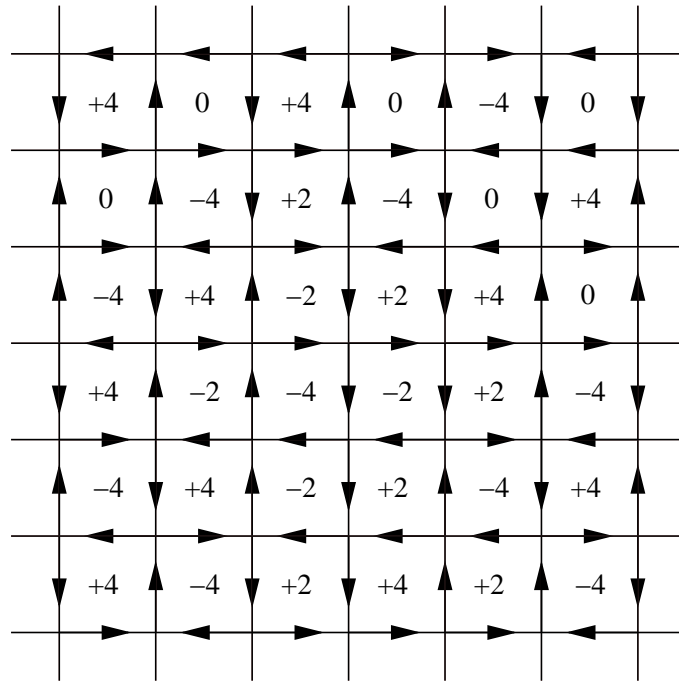


Figure 4.13: Transformation of the square-lattice 6-vertex model to a “spin” model on the dual lattice. The four links of each plaquette of the lattice are traversed counter-clockwise. The “spin” values written in the centres of the plaquettes are the sum of ± 1 around the plaquettes, where $+1$ is chosen for arrows pointing in the direction of the traversal and -1 for arrows pointing against it. Thus, the occurring “spin” values are $0, \pm 2, \pm 4$.

tributions presented in Fig. 3.20, which have non-zero entries for odd co-ordination numbers of the quadrangulations, corresponding to odd-length face cycles (loops) of the ϕ^4 graphs.

As mentioned above, when interpreting the vertex-model arrows as a discrete vector field on the lattice, the ice rule for the 6-vertex model translates to a zero-divergence condition for this field. Therefore, it is essentially characterized by its curl. We thus transform the vertex model from its interpretation as a field on the links of the original lattice to a representation of the curl of this field on the faces of the lattice or, equivalently, the sites of the dual lattice. This is done by integrating the vertex model arrows around the elementary plaquettes; by Stokes’ theorem, the result of this integral is the curl associated with the enclosed plaquette. By convention, the plaquette boundaries are traversed in a counter-clockwise orientation. Then, arrows along the direction of motion contribute $+1$ to the integral and, correspondingly,

arrows pointing against the orientation of traversal add -1 . On the square lattice the resulting “spins” on the plaquettes can assume the values $0, \pm 2, \pm 4$. This is demonstrated in Fig. 4.13. In this way, the 6-vertex model can be transformed to a sort of “spin model” on the dual of the original lattice (which is also square for the considered case). Note, however, that one still has restrictions for the “spin” values allowed between neighbouring plaquettes, which would lead to rather cumbersome interaction terms when trying to write down a Hamiltonian for this “spin” model⁸. Obviously, the mapping between both representations is not one-to-one, since there can be more than one arrow configuration compatible with a given curl around the plaquettes. As a consequence of the definition, the sum of the plaquette values inside any cycle of the lattice is equal to the integral of the arrow directions along the cycle. Especially, for a (finite) closed lattice the sum of all plaquette “spins” vanishes exactly for each configuration of the vertex model⁹.

In the new representation, the anti-ferroelectrically ordered state of the model again has a sub-lattice structure as is depicted in Fig. 4.14. However, in contrast to the sub-lattice decomposition of the original representation, now the *dual* lattice is broken down into sub-lattices, i.e., the plaquettes of the lattice are either shaded or plain, such that no two plaquettes of the same colour share a link. Then, an order parameter for the anti-ferroelectric transition can be defined as the thermal average of the sum of the plaquette “spins”, e.g., for the shaded plaquettes. Reflecting the construction of the plaquette “spins” in Fig. 4.13 it is obvious that this definition of the order parameter *exactly* coincides with the original definition of Section 4.1.2 on the level of configurations. The difference is, however, that the new definition can be easily generalized to the case of arbitrary lattices, as long as their *duals* are bipartite. This is the case for the planar random ϕ^4 graphs we are considering since any planar quadrangulation is bipartite. This can be seen from the equivalence of bipartiteness and the non-existence of odd-length cycles. The smallest cycles of such a lattice are the faces, which are quadrangles. All other cycles can be generated by gluing face cycles together to closed paths, which in each step either leaves the length

⁸Note also, that the presented transformation is vaguely similar to the transformation of the 6-vertex model to a BCSOS (body-centred solid-on-solid) model suggested by van Beijeren, see Refs. [195, 196]. The resulting models, however, are not the same. Related is also the pure loop representation of Refs. [197, 198].

⁹This constraint should be compared, e.g., to the magnetization of the Ising model, whose *thermal* average also vanishes for any finite lattice. On the level of configurations, however, non-zero values occur.

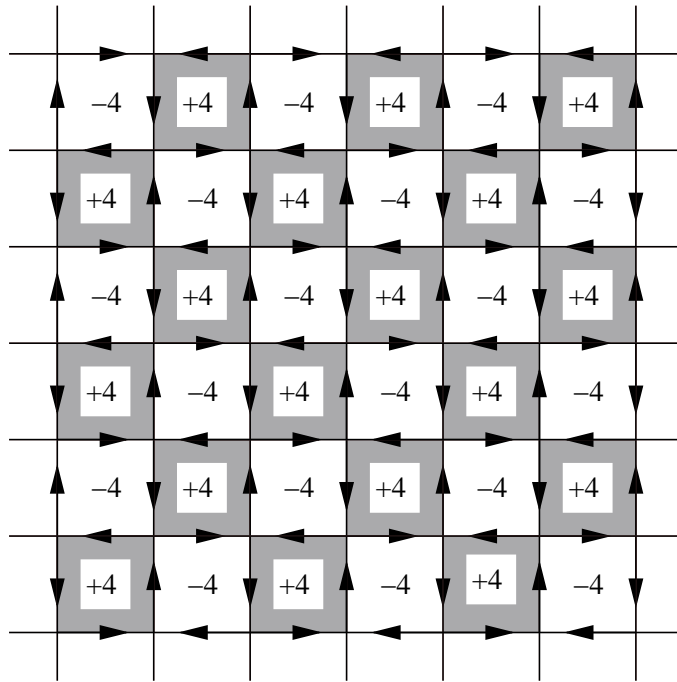


Figure 4.14: One of the two anti-ferroelectric ground states of the square-lattice F model in the “plaquette-spin” representation. The system is fully ordered on the sub-lattices of the shaded and plain plaquettes, with opposite total “magnetization” of ± 4 per plaquette. Thus, the total staggered polarization of Eq. (4.39) is ± 2 per site, the sign depending on the way ± 1 is assigned to the two colours.

of the cycle invariant or changes it by ± 2 . Thus, a planar quadrangulation has no odd-length cycles and is hence bipartite. For lattices with inequivalent cycles, i.e., with non-spherical topology, the situation is somewhat more complicated, since then a cycle winding around the lattice can have an odd length if the *lattice* has an odd length in one direction. For the vertex-model simulations we will only be concerned with planar graphs. Due to the bipartiteness of the corresponding quadrangulations, we can introduce a two-colouring of the faces (loops) of the graphs. While for the square lattice the numbers of shaded and plain plaquettes are always the same, the coloured and plain faces of the ϕ^4 random graphs not necessarily occur at equal proportions. Thus, one should take the “spins” of both types of faces into account, however “weighted” with the colour of the loops. Therefore, the configurational value of the staggered polarization of the F model on a planar ϕ^4 random graph \mathcal{G} can be defined as

$$P \equiv \frac{1}{2} \sum_{v \in V(\mathcal{G}^*)} C_v S_v, \quad (4.39)$$

where \mathcal{G}^* denotes the dual of the graph, i.e. the quadrangulation, $V(\mathcal{G}^*)$ the set of vertices of \mathcal{G}^* , $C_v = \pm 1$ the “colour” of the plaquette of \mathcal{G} corresponding to the vertex v of \mathcal{G}^* and S_v the plaquette “spin” at v . Recalling the construction of the plaquette “spins”, this can also be written in terms of the ϕ^4 graph \mathcal{G} as

$$P = \frac{1}{2} \sum_{f \in F(\mathcal{G})} \sum_{l_f \in f} C_f A(l_f), \quad (4.40)$$

where $F(\mathcal{G})$ denotes the set of faces (loops) of \mathcal{G} , l_f the links of face f , $C_f = \pm 1$ the “colour” of f and $A(l_f) = \pm 1$ the direction of the vertex-model arrow on link l_f with respect to the prescribed anti-clockwise traversal of the loops. Note that this definition coincides with the approach of counting only the shaded plaquettes for the square lattice, since now each vertex-model arrow is counted twice, which is corrected for by the additional factor of $1/2$. The thermal average $\langle P \rangle / 2$ is now taken as the order parameter of a possibly occurring anti-ferroelectric phase transition of the F model coupled to planar ϕ^4 random graphs. Note, however, that due to the overall arrow reversal symmetry of the vertex model the expectation value $\langle P \rangle$ will vanish at any temperature for a finite graph. Thus, for finite graphs we consider the modulus $\langle |P| \rangle$ instead, in complete analogy to the usual treatment of the magnetization of the Ising model.

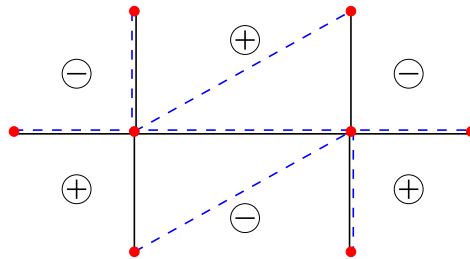
4.3.3 Implementation of the simulation scheme

Order parameter

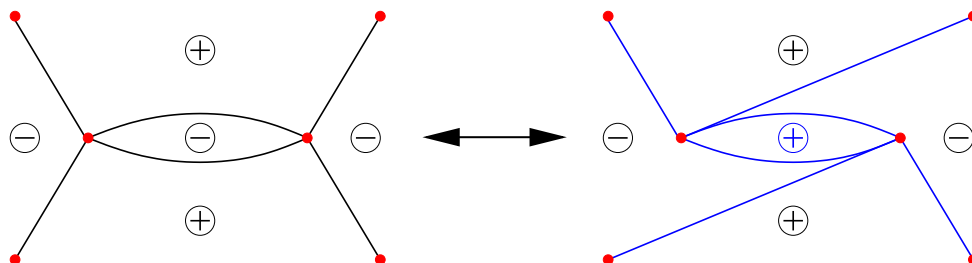
From the preceding discussion it is obvious that for the measurement of the staggered polarization of the F model on random ϕ^4 graphs one needs a two-colouring of the faces of the graph. Since in the dynamical polygonifications approach, the graphs themselves are dynamic entities, during the course of a Monte Carlo simulation such a two-colouring has to be found anew for each graph configuration observed. While in general graph colouring problems are NP hard and thus computationally practically intractable (see, e.g., Ref. [164]), finding a two-colouring of the faces of a graph whose dual is bipartite (or, equivalently, finding a two-colouring of the sites of a bipartite graph) is simple. Obviously, there are only two inequivalent ways of two-colouring such a graph. One of these ways can be found by colouring a starting face at random, colouring the neighbouring faces with the other colour and so on until all faces have been coloured. This algorithm is guaranteed to lead to a valid

two-colouring of the lattice [164]. The other colouring is found by inverting the colours of all faces. Although this algorithm is polynomial in time it is clearly still undesirable to completely re-colour the faces after each link-flip or minBU surgery move of the graph.

However, as can be easily seen, this is not really necessary. Consider one of the one-link flips for ϕ^4 graphs discussed in Section 3.2.4. Here, a proper two-colouring before the flip stays valid after the flip without changing any colours,



such that the two-colouring is invariant under the one-link flip move updates. In this and the following sketches the “ \oplus ” and “ \ominus ” symbols denote the colours of the faces adjacent to the two depicted ϕ^4 vertices. On the other hand, for a two-link flip around a double link,



the colour of the face enclosed by the double link has to be inverted. Thus, the two-link flip move is the only move capable of changing the ratio of “ \oplus ” and “ \ominus ” faces of the graph. It is obvious that in general the considered class of graphs includes graphs with varying proportions of “ \oplus ” and “ \ominus ” faces, at least for the non-strict ensembles. This exceptional property of the two-link flip provides a somewhat belated proof for the claim that the one-link flip dynamics alone is not ergodic even for the case of *singular* ϕ^4 graphs put up above in Section 3.4. Finally, the minBU surgery moves described in Section 3.5.2 do not change the adjacency properties of the faces, such that no re-colouring is necessary there. Thus, with a slight intervention for the case of the two-link flip moves, the face-two-colouring of the graphs can be easily kept

up-to-date during the graph part of the update and measurements of the staggered polarization become computationally cheap.

Graph updates in the presence of matter

The graph update moves described in the previous chapter were there discussed for the case of plain graphs, i.e., of pure quantum gravity without coupling to matter. In the presence of a decoration of the graphs with matter variables some additional considerations come into play. First of all, in all cases the change in energy of the matter part induced by a proposed flip, insertion/deletion or surgery move has to be computed and taken into account in the acceptance probability, which is, however, straightforward. For the vertex models, a flip move could in principle produce disallowed vertex configurations violating the arrow reversal symmetry. Such moves are prevented by assigning infinite energies to unwanted vertex configurations (also, e.g., to the vertices 7 and 8 for the case of the 6-vertex model), such that forbidden moves are never accepted. For the F model one checks by explicit inspection that this restriction still leaves some allowed link-flips to perform, which is maybe not self-evident.

The insertion and deletion moves used in (pseudo) grand-canonical simulations and to build up the initial graph need some different treatment. For the deletion move one has to check, whether the resulting vertex-model configuration on the reduced graph is valid for the considered vertex model. If it is not, the move has to be rejected. Otherwise, the corresponding energy change has to be taken into account for the acceptance probability. On the other hand, for the insertion moves one has some freedom in the decoration of the newly inserted links of the graph. For the 6-vertex model one can guarantee a valid vertex-model configuration after the insertion step irrespective of the initial configuration both, for the simple insertion move for the non-strict ensembles as well as for the more complicated insertion move for the strict ensemble. The recipe for the decoration is illustrated in Fig. 4.15. Again, the energy of the additional vertex configurations has to be taken into account when formulating the detailed balance condition for this type of move.

Finally, the minBU surgery moves discussed in Section 3.5.2 have to pass the additional check of whether the arrow configuration on the external lines of the minBU matches that of the marked vertex on the “mother universe” the minBU is re-connected to. For the F model, one can additionally exploit the rotational symme-

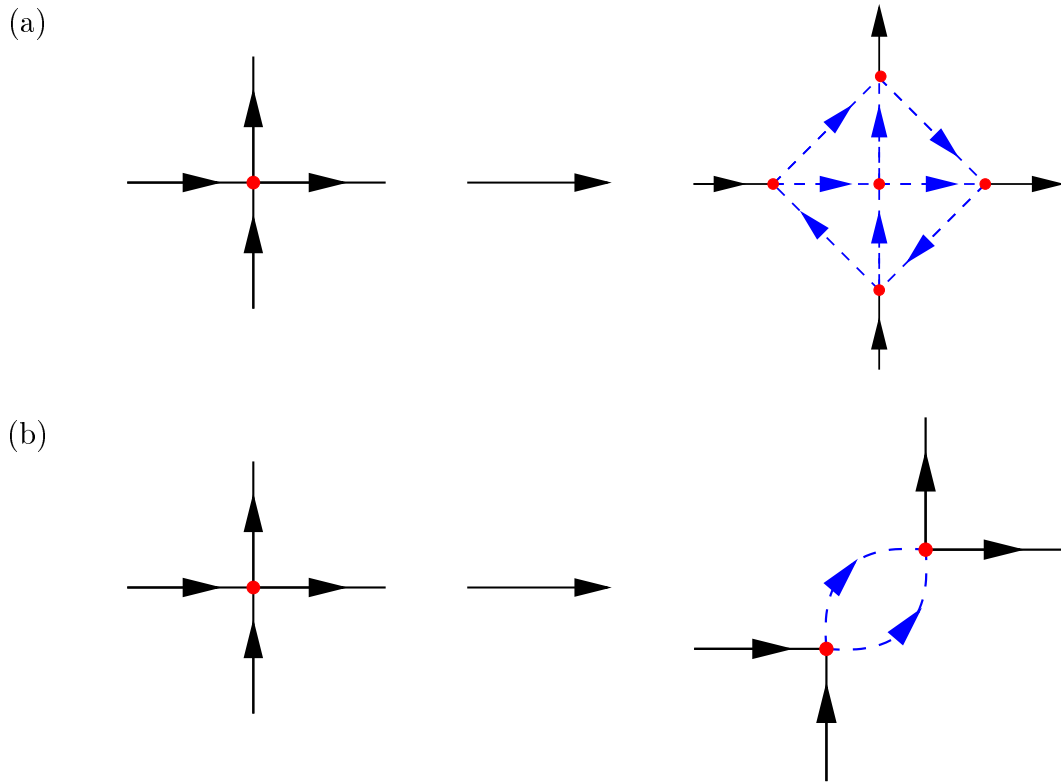


Figure 4.15: Finite-energy insertion moves for the F model coupled to planar random ϕ^4 graphs. These moves are always allowed, irrespective of the original arrow configuration, i.e., they involve a finite energy change. The dashed lines indicate the newly inserted arrows. (a) Insertion move for the strict ensemble. The arrow directions are simply copied in either of the four directions. The new “ring” is decorated consistently with arrows in a clockwise or counter-clockwise orientation. (b) Insertion move producing a double link used for the non-strict ensembles. The zero-divergence condition ensures that the double link can always be consistently decorated.

try of the vertex-model weights and check whether the minBU can be pasted at the position of the marked vertex in one of four possible rotational orientations. Note that no non-trivial change of energy is possible here; either the move is forbidden and thus rejected or it does not change the vertex-model energy and is hence always accepted. Therefore minBU surgery steps have a non-vanishing acceptance rate as the temperature goes to zero. In contrast, the (one- and two-link) flip-move dynamics freezes as $T \rightarrow 0$ for the F model, since a flip in a configuration consisting entirely of vertices of type 5 and 6 (maybe up to small frustration effects) would

always produce vertices of the types 1–4 and thus has a vanishing acceptance rate in the zero-temperature limit.

Chapter 5

The 6-Vertex Model on Random ϕ^4 Graphs

Having developed the necessary tools for Monte Carlo simulations of dynamical ϕ^4 random graphs and simulations of vertex models, an analysis of the 6-vertex model coupled to Euclidean discrete quantum gravity or, equivalently, an exploration of the influence of annealed connectivity disorder on the 6-vertex model, can be attempted. As will be discussed below, the 6-vertex model is at the heart of all integrable models of statistical mechanics in two dimensions. Transferring vertex models from the square lattice to planar ϕ^4 random graphs, they take on a similar rôle for the statistical mechanics of matter coupled to Euclidean quantum gravity. An analysis of the scaling properties of the F model on the ensemble of planar ϕ^4 graphs dual to dynamical quadrangulations provides an understanding of an important example of the marginal case of a $C = 1$ theory coupled to quantum gravity.

After a short survey of the densely meshed net of inter-relations between two-dimensional integrable models on regular and random lattices, we re-consider the square-lattice F model and the scaling properties at its Kosterlitz-Thouless transition point, mainly in order to fine-tune the needed simulational machinery, but also as an interesting problem in itself. Combining the techniques described in the previous two chapters, we perform extensive simulations of the F model coupled to random ϕ^4 graphs and analyse its behaviour in the vicinity of the Kosterlitz-Thouless transition point. Having explored the phase structure of the model, the dynamical behaviour of the simulation algorithm for the combined system of fluctuating geometry and coupled matter will be discussed. Finally, the back-reaction

of the matter variables on the fluctuating geometry, expressed in the string susceptibility exponent and the intrinsic Hausdorff dimension of the random graphs, is explored.

5.1 Analytical Results

The classification of the scaling properties of conformal field theories [199–201] coupled to the dynamical polygonifications model has received considerable interest in the past decades. The KPZ/DDK ansatz [30–32] predicts a renormalization or “dressing” of conformal weights for models with central charges $C \leq 1$, which has been confirmed by exact results from matrix model calculations in all cases treated so far, including the Ising [33–35], Potts [36–39] and $O(n)$ [40–44] models, cf. Section 2.4.

5.1.1 The case of regular lattices

Vertex models on regular lattices are closely linked with different series of integrable models, which in turn are related to an exhaustive enumeration of certain conformal field theories. In fact, it turns out that the 6-vertex model, being the critical version of the 8-vertex model, includes in suitable generalizations the critical points of all of the well-known two-dimensional lattice models of statistical mechanics. Alternatively, a common point of reference for all these critical models is given by their asymptotic equivalence to a Coulomb gas. In the following, the net of these interrelations is shortly exposed to underline the extraordinary importance of 6-vertex type of models for statistical mechanics.

SOS and minimal models

On regular lattices, the relation between lattice models, conformal field theories and integrability has been quite comprehensively explored. A particularly interesting class of conformal field theories is given by the unitary minimal series of Ref. [141], where the central charge assumes a discrete set of values labelled by an integer variable m ,

$$C = 1 - \frac{6}{m(m+1)}, \quad m = 2, 3, 4, \dots \quad (5.1)$$

A series of lattice models, which realizes each central charge of this unitary series [202] is given by the restricted solid-on-solid (RSOS) models of Andrews, Baxter and Forrester [203]. There, one assigns *height variables* h_i to the sites of a lattice, whose values are restricted to a finite set of integers, $h_i = 1, \dots, m$. Moreover, the heights of neighbouring sites of the lattice are constrained to differ by plus or minus one unit. The interactions depend of the height values at the corners of the elementary plaquettes or faces of the considered graph which are assumed to be squares, whence the RSOS models are also called interaction-round-a-face (IRF) models [55]. In Ref. [203] it was shown that these models can be asymptotically mapped onto the 8-vertex model, such that the critical RSOS models correspond to a 6-vertex model. A more abstract generalization of this class of models, the so-called ADE series of models provides an even closer correspondence between lattice systems and the conformal minimal models. These are defined as mappings from the lattice into the Dynkin diagrams of a simply-laced Lie algebra [204]. These simply-laced Lie algebras come in two discretely labelled series, A_m and D_m , and the single exceptional cases E_6 , E_7 and E_8 , see, e.g., Refs. [205, 206]. Compared to the RSOS models, the restriction of unity differences in the heights of adjacent sites is relaxed and replaced by the condition that neighbouring heights should conform to the labels of neighbouring vertices of the corresponding Dynkin diagram. The RSOS models can be shown to correspond to the A series of ADE models. Pasquier [204, 207] has shown that *each* minimal model is realized in one of the ADE models. This goes beyond the exemplary realisations of the RSOS models of Refs. [202, 203], since there are usually different realizations for a given central charge, differing in the part of the Virasoro algebra actually occurring. Thus, the ADE model classification resolves the “fine structure” of models of a given central charge.

The Coulomb gas and loop representations

Before the pioneering papers Refs. [141, 199] on the classification of critical behaviour by methods of conformal field theory, a treatment of a variety of models in two dimensions had been successfully attempted by mapping them (exactly or asymptotically) to a two-dimensional gas of interacting electric and magnetic point-like charges, i.e., the *Coulomb gas* [196], which can also be used for an exhaustive labelling of critical theories in two dimensions [208]. This scheme was pioneered by the finding of Kosterlitz and Thouless [63, 64] that the infinite-order phase transition of the two-dimensional XY or $O(2)$ model could be described by *vortex* excitations

interacting like a gas of charges. A specially tailored version of the XY model with Hamiltonian,

$$-\beta\mathcal{H} = \sum_{\langle ij \rangle} V(\theta_i - \theta_j), \quad \exp[V(\theta)] = \sum_{k=-\infty}^{\infty} \exp[-J(\theta - 2\pi k)^2], \quad (5.2)$$

introduced by Villain [209] can be mapped exactly onto a Coulomb gas. The Coulomb gas method rests on the fact that the renormalization group equations of the Coulomb gas can be formulated exactly to leading order and thus yield exact critical exponents [196]¹. The Villain model, whose critical behaviour is numerically found to coincide with that of the original XY model as expected [210,211], can be identically transformed to a model of the SOS type [212] by a duality transformation [213]. This so-called discrete Gaussian model is an *unrestricted* solid-on-solid model, i.e., with heights ranging from $-\infty$ to ∞ , and (discretised) Gaussian interactions between neighbouring heights.

An impressive series of models can be mapped onto the Coulomb gas, including the 8-vertex, Ashkin-Teller, q -state Potts and $O(n)$ vector models [196]. In all cases an intermediate step is a mapping to an SOS type model and the corresponding loop representation. The general RSOS models of Ref. [203] themselves can also be mapped onto the Coulomb gas [195]. For the F model, the equivalence with the so-called BCSOS (body-centred SOS) model has been shown by van Beijeren [214]. The corresponding transformation consists of mapping the bond arrows of the square-lattice F model to arrows on the dual lattice, turning all the arrows by a right-angle to the left. Interpreting the original arrow configuration as a divergence-free vector field, this transformation results in a curl-free vector field on the dual lattice. Thus it can be understood as the gradient of scalar height variables residing on the sites of this dual square lattice and differing by unit amounts between neighbouring sites, which decomposes the lattice into sub-lattices with only even and odd heights. This equivalence suggests that the Kosterlitz-Thouless (KT) transition point of the F model is indeed equivalent to the corresponding transition of the XY model by their common equivalence to a Coulomb gas. It should be noted that the vortices of the XY model, triggering the Kosterlitz-Thouless phase transition there, naturally correspond to the source and sink configurations 7 and 8 of the 8-vertex model and become identified in the Coulomb gas limit.

¹Note, however, that in general some exact input found by other means is needed to fix the value of the renormalized coupling.

Loop or polygon representations [215] can also be given for the discussed models, including the general RSOS model [216]. For the 6- and 8-vertex models this polygon representation coincides with the loop representation discussed in the previous chapter in the context of the loop-cluster algorithm. To mention another example, it has been shown [217] that a suitably adapted version of the $O(n)$ vector model (sometimes denoted as the $O(n)$ loop model) is identical to a model of closed polygon rings with partition function

$$Z = \sum_{\text{graphs}} K^L n^c, \quad (5.3)$$

where c is the number of present loops and L denotes their total length. The loops correspond to the contour lines of the spin clusters occurring in a high-temperature expansion. Thus, the model is equivalent to a Coulomb gas and its critical exponents can be evaluated [218]. Such loop models have attracted much attention due to their obvious relation to configurations of polymers such as protein chains etc. [219]. Note that the loops of this $O(n)$ model do not normally cover the whole lattice and, instead, the model has “dilute” and “dense” phases, whereas the loop model considered in the context of vertex models is a “fully packed” loop model [220] with the loops covering each site of the lattice. In the context of SOS type models, such loops occur as domain walls between regions of equal height.

Combining the described equivalences, the 8-vertex model is found to be the “swiss-army jackknife” of statistical mechanics. Its critical version, the 6-vertex model, can be considered as the basic element of two-dimensional critical systems and the associated conformal field theories [57, 58].

5.1.2 Vertex models coupled to quantum gravity

The KPZ/DDK formula shows that rational conformal field theories stay in the sector of minimal models on coupling them to two-dimensional Euclidean quantum gravity, the corresponding critical exponents merely being renormalized due to the presence of a fluctuating background. From the sketched various equivalences between models of statistical mechanics not all survive the transformation to random lattices. A *loop representation* in the spirit of the Coulomb gas treatment, however, has turned out to be the starting point for most of the solutions found so far. It allowed for an evaluation of critical-point properties of the ADE interaction-round-a-face models [221–223], being still related to the corresponding RSOS models, and

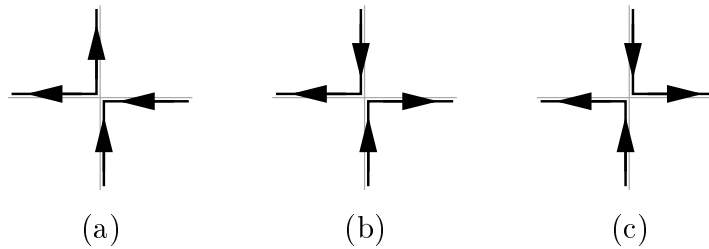


Figure 5.1: (a) Unique breakup of a vertex of type $a = b$ into upper-left and lower-right corners. (b) One of the possible breakups of a vertex of type c into upper-left and lower-right corners. (c) The other possible breakup of a vertex of type c into upper-right and lower-left corners.

a treatment of the $O(n)$ loop model [40, 41, 224].

The F model on a random lattice

The F model on a (regular or random) four-valent graph can be represented as a gas of oriented loops [55, 225]. To see this, one applies the breakup operations defined in the context of the loop algorithm in Section 4.2, restricting oneself to the “corner-type” breakups 1 and 2 of Fig. 4.7. Thus, vertices of type a and b allow exactly one breakup into corners, while vertices of type c can be broken up in both ways, cf. Fig. 5.1. As has been shown in Section 4.2, choosing such a breakup for each vertex of the graph (uniquely for vertices of types a and b and at random for vertices of type c), decomposes it into a set of fully packed, oriented loops, cf. Fig. 5.2. Conversely, summing over all possible close-packed loop arrangements and the two orientations of the loops yields all possible configurations of the F model on the considered graph. The original weights of the 6-vertex model translate into weights for the oriented loops by assigning a phase factor $\exp(i\mu\pi/2)$ to each left turn and a phase factor $\exp(-i\mu\pi/2)$ to each right turn of an oriented loop [55, 225]. Here, the coupling μ is related to the weights of the F model as²,

$$a/c = b/c = [2 \cos(\pi\mu)]^{-1}. \quad (5.4)$$

On the square (or any other regular) lattice the phase factors around each loop always sum up to a total of $\exp(\pm i\mu 2\pi)$ due to the absence of curvature. On a

²Note that, in terms of the parameter Δ of Eq. (4.10), this choice of weights covers only the range $-1 < \Delta < 1$, which corresponds to the disordered phase of the square-lattice F model.

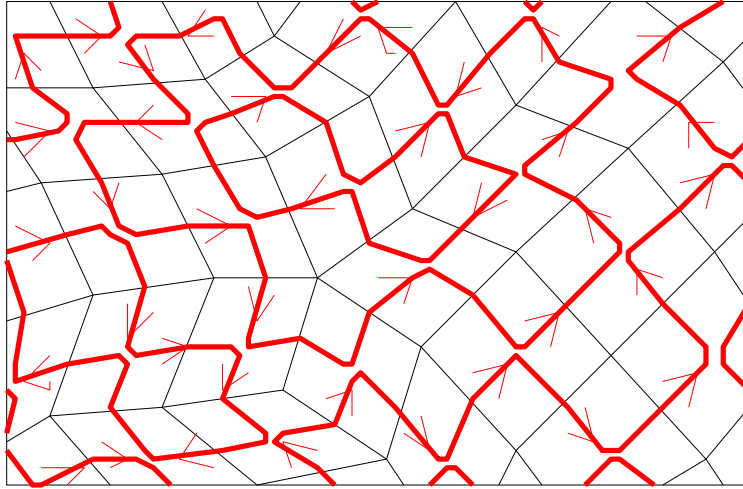


Figure 5.2: A piece of a random quadrangulation and a configuration of a fully packed gas of oriented loops on the dual ϕ^4 graph, corresponding to a configuration of the 6-vertex model. This figure is reproduced from Ref. [73].

random graph, however, a loop l in general receives a non-trivial weight $\exp[i\mu\Gamma(l)]$ with $\Gamma(l)$ denoting the integral of the geodesic curvature along the curve l , i.e.,

$$\Gamma(l) = \frac{\pi}{2} (\# \text{ left turns} - \# \text{ right turns}), \quad (5.5)$$

cf. Section 2.2.3.

This loop expansion is related to the loop representation of the $O(n)$ model mentioned above. On a regular lattice, due to the absence of curvature all loops receive the same constant fugacity $n = 2 \exp(\pm i\mu 2\pi)$ of Eq. (5.3), leading to the critical $O(n)$ model. On the considered random graphs this picture only remains valid for the limiting case $\mu = 0$, where the curvature dependence cancels. Thus, the $\mu = 0$ point of the F model on random planar ϕ^4 graphs is equivalent to the critical $O(2)$ loop model [41, 72, 226] and thus, by universality, the original XY model³. Note that this corresponds to the same critical point $a/c = b/c = 1/2$ as on the regular square lattice, which is natural since the symmetry breaking is induced by the choice of the vertex weights. The KT point itself has been considered before within the framework of the XY model [227–229] and the $O(n)$ loop models [40–44] coupled

³Note that the loops occurring in the expansion of the $O(n)$ model are not in general close packed on the lattice as are the loops of the presented loop expansion of the F model. However, the critical $O(2)$ model lies at the boundary of the dense phase of the $O(n)$ model, where loops are close packed [224].

to dynamical polygonifications. Also within the framework of ADE models considered in Refs. [221, 222] the symmetric 6-vertex model is naturally included and some exact results were given at criticality. Finally, it should be noted that the critical F model coupled to the random graphs is equivalent to the critical point of a free massless boson compactified on a circle and coupled to quantum gravity [226].

The matrix model solution

An exact solution of the F model coupled to planar random ϕ^4 graphs in its formulation as a matrix model has been found independently by P. Zinn-Justin [72] and I. Kostov [73]. As was first noted by Ginsparg [124] the model can be formulated as the perturbative expansion of the matrix integral

$$W(a, c, N) = \int d\phi d\phi^\dagger \exp \left[-N \text{Tr} \left(\phi\phi^\dagger - a\phi^2\phi^{\dagger 2} - \frac{c}{2}(\phi\phi^\dagger)^2 \right) \right], \quad (5.6)$$

such that the partition function of the F model on planar graphs is the leading term of the $1/N$ expansion of

$$Z(a, c, N) = \ln \frac{W(a, c, N)}{W(0, 0, N)}, \quad (5.7)$$

cf. Eq. (2.94). Here, in contrast to the Hermitian matrix models considered in Section 2.3.4 above, ϕ is taken to be a general $N \times N$ complex matrix, thus endowing the links of the ϕ^4 graphs represented by the propagators $\langle \text{Tr} \phi\phi^\dagger \rangle$ with a sense of direction, which in turn can be interpreted as the decoration of the graph edges with the arrows of a vertex model, see also Refs. [128, 230]. The pairing of two “heads” ϕ and two “tails” ϕ^\dagger at each vertex in the matrix model potential ensures that the generated configurations satisfy the ice rule.

Introducing an additional auxiliary Hermitian matrix, the resulting matrix model can be interpreted as a deformation of the $O(2)$ loop matrix model and the integration over the complex ϕ matrices can be performed [73]. Employing the usual saddle point technique, the planar $N \rightarrow \infty$ limit of the model can be solved. What is found is that for each value of the coupling μ of Eq. (5.4) the model has a critical point⁴ with central charge $C = 1$. In terms of the vertex model coupling a these

⁴Note that, as mentioned above, real values of μ only cover the parameter range of the disordered phase of the square-lattice F model. Thus, also the square-lattice model is critical for all μ .

critical points are parameterized as [72],

$$a_{\text{crit}} = \frac{1}{32} \frac{\sin(\pi\mu/2)}{\pi\mu/2} \frac{1}{\cos^3(\pi\mu/2)}. \quad (5.8)$$

Note that in contrast to the regular lattice model, where only the ratio $a/c = b/c$ had physical significance, the couplings $a = b$ and c of the F model can be varied independently here, since a takes on the rôle of the cosmological constant, i.e., the fugacity controlling the cost of adding a new site to the graph. Exploring the vicinity of this critical point, it is found that the string susceptibility exponent $\gamma_s = 0$ for all μ , leading to only logarithmic divergences of the free energy [72, 73]. This behaviour is indeed expected from the $C \rightarrow 1$ limit of the KPZ/DDK prediction Eq. (2.137). The spectral density of the matrix integral has a singularity with an exponent $(1 - \mu)/(1 + \mu)$ varying continuously along the critical line, which leads to an also continuously varying exponent for the scaling of the typical length of loops on the worldsheet, which is a generally considered observable within the loop model scheme [41, 73, 224]. Finally, the *vortex operators*, which correspond to the deformation of the 6-vertex model to an 8-vertex model by insertion of sinks and sources, i.e., vertices of the types 7 and 8, are found to have dimension $1 - \mu$ [73].

Thus, the general phase structure of the F model coupled to planar random ϕ^4 graphs in the grand-canonical ensemble of a varying number of vertices has been found in Refs. [72, 73]. The existence of a Kosterlitz-Thouless type phase transition at $\mu = 0$ was obvious beforehand from the equivalence to the $O(2)$ loop model at this point. Details of the behaviour of matter-related observables in the vicinity of this point, such as the scaling of the staggered anti-ferroelectric polarizability, however, could naturally not be extracted from the matrix model ansatz.

Further vertex models

From the given interpretation of the matrix model (5.6) it is obvious that a complex matrix model with potential,

$$V(\phi, \phi^\dagger; a, c, d) = \frac{1}{2} \phi \phi^\dagger - a \phi^2 \phi^{\dagger 2} - \frac{c}{2} (\phi \phi^\dagger)^2 - \frac{d}{4} (\phi^4 + \phi^{\dagger 4}), \quad (5.9)$$

introduces the source and sink configurations 7 and 8 and thus describes an *8-vertex model* coupled to random ϕ^4 graphs. For the special choice of weights $c = d$, this matrix model, written as a two-matrix model of real matrices, can be solved by a

character expansion method [231]. As expected, the model is found to have a critical point as it crosses the parameter space of the 6-vertex model at $d = 0$, implying $c = 0$, which corresponds to the point $\mu = 1/2$ of the above parameterization (5.4) of the F model. Along its critical line the model exhibits central charge $C = 0$ behaviour with $\gamma_s = -1/2$, the only exception being its critical point, where it has central charge $C = 1$ and, correspondingly, a string susceptibility exponent $\gamma_s = 0$.

Varying the potential of the complex matrix integral, one can easily construct matrix model formulations of further vertex models, including matrix models on three-valent ϕ^3 graphs [128, 230]. In the limit $N \rightarrow 1$, the matrices become replaced by scalar variables and one describes generic, “thin” random graphs without a defined topology. The corresponding scalar integrals can be generally solved by a saddle-point calculation. For the vertex models on thin ϕ^3 and ϕ^4 graphs, a clever choice of the parameters of a simple linear transformation of the matrices maps the models onto known (and solved) problems such as Ising and Potts models in the mean-field limit [128]. For planar, “fat” ϕ^3 and ϕ^4 graphs, while a general solution is lacking, it is still possible to formulate well-known solved two-matrix models, especially the Ising model, as special cases of vertex models [128]. Also, the solution of a so-called *bond vertex model* for the ϕ^3 case, where the links of the graph do not carry arrows but are rather occupied or unoccupied, could be found by transformation to an Ising model in a field [230].

5.2 The Anti-Ferroelectric Phase Transition

Obviously, the infinite-order phase transition to an anti-ferroelectrically ordered phase predicted to occur at the particular choice of weights $a/c = b/c = 1/2$ of the F model coupled to planar random ϕ^4 graphs is the main point of interest in analyzing this model. The scaling and finite-size scaling theories associated with such a phase transition of the Kosterlitz-Thouless type are quite different from those at finite-order phase transitions and will thus be reviewed shortly. Even though the KT point of the F model is known to be equivalent to the critical point of the XY model, the two models do not exhibit completely identical scaling behaviour due to differences in the relevant observables. Since we will find a numerical scaling analysis of the KT point of the F model on *random lattices* extremely difficult due to the combined effect of the logarithmic corrections associated with every $C = 1$ theory and the smallness of the accessible effective linear extensions of the lattices

resulting from their large Hausdorff dimension, the machinery of analysis is tested and refined for the case of the F model on the *square lattice*, where at least the second correction effect is absent.

5.2.1 Scaling at an infinite order phase transition

Essential singularities and the XY model

Even though a transition of infinite order was found by Lieb [56, 62] in the phase diagram of the F model before Kosterlitz and Thouless formulated their famous theory for the phase transition of the two-dimensional XY model [63, 64], the occurrence of essential singularities at a phase transition point is invariably linked to the latter two names⁵. As a consequence of a theorem by Mermin, Wagner and Hohenberg [233, 234], the two-dimensional XY model cannot develop an ordered phase with a non-vanishing value of a locally defined order parameter for non-zero temperature. Instead, the transition is described as the binding or unbinding of *vortex pairs* superimposed on an effective spin-wave behaviour of the low-temperature phase. Above the critical temperature, spin-spin correlations decay exponentially,

$$G(r) \sim e^{-r/\xi(T)}, \quad T > T_c, \quad (5.10)$$

while below T_c long-range correlations are encountered,

$$G(r) \sim r^{-\eta(T)}, \quad T \leq T_c, \quad (5.11)$$

such that the correlation length $\xi(T) = \infty$ for all $T \leq T_c$ and the massless low-temperature phase corresponds to a critical line terminating in the critical point T_c [63, 64, 235]. The critical exponent η varies continuously along this critical line. Approaching the critical point T_c from above, the correlation length diverges *exponentially* instead of *algebraically* as for a usual continuous phase transition⁶,

$$\xi(T) \sim \exp(a/t^\rho), \quad t > 0, \quad (5.12)$$

⁵It should be noted that the notion of topological excitations triggering the phase transition of the XY model was introduced before the works of Kosterlitz and Thouless by Berezinskii [232].

⁶For the KT point of the square-lattice F model it can be shown that in fact all temperature derivatives of the free energy exist and are continuous across the transition point [55].

where $t = (T - T_c)/T_c$ and⁷ $\rho = 1/2$. The behaviour of further observables at the transition point can be conveniently expressed in terms of this singularity of the correlation length. In particular, the magnetic susceptibility diverges as

$$\chi(T) \sim \xi^{\gamma/\nu} = \xi^{2-\eta_c}, \quad T > T_c, \quad (5.13)$$

where $\eta_c \equiv \eta(T_c) = 1/4$. The specific heat, on the other hand, is only very weakly singular, behaving as

$$C_v \sim \xi^{-2}. \quad (5.14)$$

Finite-size scaling

Finite-size scaling (FSS) analyses of the KT transition of the XY model are hampered by the occurring essential singularities and the presence of a critical phase. As a consequence of the latter, magnetic observables such as the susceptibility do not exhibit maxima in the vicinity of the critical point, which otherwise could be used for an estimation of the transition temperature from finite systems. As will be shown below, the situation is different for the KT point of the F model, where the analogue of the magnetic susceptibility, the staggered anti-ferroelectric polarizability, shows a maximum for finite lattices. Nevertheless, the general arguments for finite-size shifting and rounding remain valid, such that suitably defined pseudo-critical points $T^*(L)$ for systems with linear extent L scale to the critical point T_c as [236]

$$[T^*(L) - T_c]/T_c \sim (\ln L)^{-1/\rho}, \quad (5.15)$$

cf. Eq. (5.12). Sufficiently close to the critical point the growth of the correlation length becomes limited by the linear extent L of the system and, correspondingly, ξ can be replaced by L to yield the finite-size scaling law

$$\chi(L, T_c) \sim L^{\gamma/\nu} = L^{2-\eta_c}, \quad (5.16)$$

which for $\eta_c = 1/4$ predicts a rather strong divergence. On finite lattices, the specific heat is found to exhibit a smooth peak, which is however considerably shifted away from the critical point into the high-temperature phase and does not scale as the lattice size is increased [236]. Thus, with the main strengths of FSS being

⁷Note that the exponent ρ is often called ν . However, to underline the fact that this exponent, albeit being related to the singular behaviour of the correlation length like ν for an ordinary phase transition, does not describe a power-law singularity, we prefer to use a different symbol.

not exploitable for the KT phase transition, the focus of numerical analyses of the XY and related models has been on *thermal* scaling, see, e.g., Refs. [210, 237–239]. In addition, renormalization group analyses predict *logarithmic corrections* to the leading scaling behaviour [240, 241], as expected for a $C = 1$ theory, which have been found exceptionally hard to reproduce numerically due to the presence of higher order corrections of comparable magnitude (for the accessible lattice sizes) [211].

5.2.2 The square-lattice F model

As mentioned above, an analysis of the square-lattice F model is put in front of the investigation of the random graph problem to allow for a detailed comparison and to calibrate the needed numerical machinery. To begin, we present some specific exact results and conjectures for the square-lattice F model, which have not yet been reported in Section 4.1.2 above.

Analytical results

We assume a parameterization of the F model coupling parameters, which involves a temperature variable and thus sticks more closely to the language of statistical mechanics than to that of field theory. It thus differs from the parameterization (5.4) used in the context of the matrix model solution, which only covers the critical disordered phase of the F model. Assuming $\epsilon_a = \epsilon_b = 1$ in Eq. (4.6), we have

$$a = b = e^{-\beta}, \quad c = 1, \quad (5.17)$$

where $\beta = 1/k_B T$, such that the KT point occurs for $\beta_c = \ln 2$. From Lieb's exact solution of the square-lattice F model [62], the correlation length and the free energy are expected to exhibit the essential singularities found for the XY model, cf. Section 4.1.2. Additionally, the exact solution provides the amplitudes and correction terms. In the thermodynamic limit, one finds [55]

$$\begin{aligned} \xi^{-1}(\lambda) &\sim 4 \exp(-\pi^2/2\lambda), \\ f_{\text{sing}}(\lambda) &\sim 4k_B T_c \exp(-\pi^2/\lambda), \end{aligned} \quad (5.18)$$

where λ is related to the reduced coupling Δ of Eq. (4.10) as $\Delta = -\cosh \lambda$, which covers the anti-ferroelectrically ordered phase $\Delta < -1$ for real values of λ . In general, the coupling λ is related to the coupling μ defined in (5.4) as $\lambda = 2\pi i\mu$. As

the critical point is approached from the low-temperature side, λ behaves as $\lambda \sim t^{1/2}$ to leading order⁸, i.e., $\rho = 1/2$ as for the XY model. Here, f_{sing} denotes the singular part of the free energy per site. The specific heat diverges as ξ^{-2} as expected. For later reference, we also note the critical values of the internal energy U and specific heat C_v , which are given by [56]

$$\begin{aligned} U(T_c) &= 1/3, \\ C_v(T_c) &= 28(\ln 2)^2/45. \end{aligned} \tag{5.19}$$

Concerning properties related to the order parameter, the situation for the F model is somewhat different from that of the XY model. The order parameter defined in Eq. (4.11) for the square lattice resp. in Eqs. (4.39) or (4.40) for general (including random) lattices, is non-vanishing for finite temperatures in the ordered phase⁹. Thus, the corresponding staggered anti-ferroelectric polarizability,

$$\chi = N_2^{-1}(\langle P_0^2 \rangle - \langle |P_0| \rangle^2), \tag{5.20}$$

where N_2 as usual denotes the number of vertices of the considered graph, shows a clear peak in the vicinity of the critical point for finite lattices. However, in the limit $N_2 \rightarrow \infty$ the polarizability diverges throughout the whole high-temperature phase, which is critical as mentioned in Section 4.1.2. Note that compared to the XY model the rôles of high- and low-temperature phases are exchanged in this respect, as expected from duality [213]. Although the F model has not been solved in a staggered electric field for general temperatures, the spontaneous staggered polarization is known exactly for all temperatures [242],

$$P_0(\lambda) = \left[\prod_{n=1}^{\infty} \tanh(n\lambda) \right]^2, \tag{5.21}$$

which in the vicinity of the critical point scales as

$$P_0(\lambda) \sim \lambda^{-1} \exp(-\pi^2/4\lambda). \tag{5.22}$$

⁸Note that the deviation t from the critical point is defined in terms of the weights a , b and c instead of the temperature T in Ref. [55]. For small t , however, both definitions asymptotically coincide.

⁹Note that the Mermin-Wagner-Hohenberg theorem [233, 234] does not apply to the F model with its discrete symmetry.

Assuming the Widom-Fisher scaling relation $\alpha + 2\beta + \gamma = 2$ to be valid¹⁰, from Eqs. (5.18) and (5.22) Baxter conjectured the following scaling of the zero-field staggered polarizability [242],

$$\chi(\lambda) \sim \lambda^{-2} \exp(\pi^2/2\lambda) \sim (\ln \xi)^2 \xi, \quad (5.23)$$

which implies $\gamma/\nu = 2 - \eta_c = 1$. The apparent discrepancy with the XY model results should not be interpreted as an indication of differing universality classes of the models (which are equivalent at their critical points), but reflects the fact that the F model staggered polarizability is not equivalent to the magnetic susceptibility of the XY model. Since the whole high-temperature phase is critical, scaling of the polarizability is expected throughout this phase. In fact, the F model in a staggered field can be solved exactly at the point $a/c = 1/\sqrt{2}$ (corresponding to $\Delta = 0$ or $\lambda = i\pi/2$), where its parameter space crosses that of the free-fermion model, cf. Eq. (4.19) [243]. At this point, a logarithmic divergence of the polarizability is found, implying $2 - \eta = 0$, such that, obviously, the divergence of χ becomes weaker within the critical phase, in contrast to the XY model, where η is found to decrease from its critical value $\eta_c = 1/4$ when moving further into the critical phase, see, e.g., [237].

Monte Carlo analysis

In contrast to the exactly solvable Ising model in two dimensions, which has served as a playground and reference point for the Monte Carlo method right from its first beginnings (see, e.g., Ref. [155]), the exactly solved 6-vertex model has received considerably less attention as far as numerical work is concerned. The only Monte Carlo analyses of the square-lattice F model we found are reported in Refs. [244, 245] in the context of the equivalence of the F model to the BCSOS surface model, whose roughening transition corresponds to the KT point of the F model¹¹.

To calibrate our set of simulation and analysis tools, we performed simulations of the square-lattice F model and investigated the scaling behaviour of the specific heat and

¹⁰Although the KT transition is characterized by essential singularities and thus the conventional critical exponents are meaningless, one can re-define them by considering scaling as a function of the correlation length ξ instead of the reduced temperature t , cf. Section 4.1.2. The exponents α , β and γ used here and in the following should be understood in that sense. The exponent ρ , however, has its special meaning defined by (5.12).

¹¹Note that in contrast to the “static” F model considered here, various dynamic extensions of the 6-vertex model have been extensively explored as models of surface growth, see, e.g., Ref. [246].

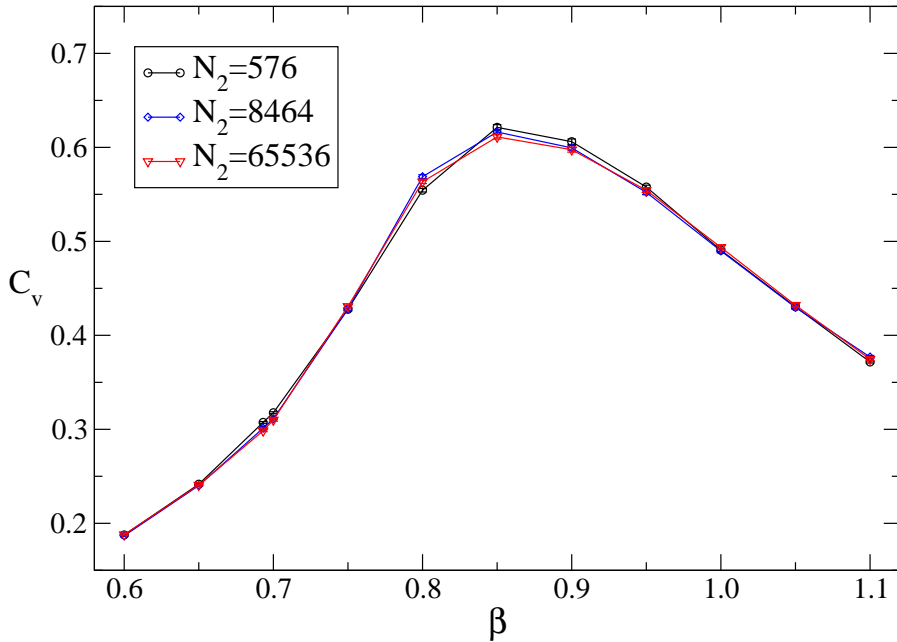


Figure 5.3: Non-scaling of the specific heat C_v of the square-lattice F model from Monte Carlo simulations. The square lattice is considered wrapped around a torus. From the simulated lattice sizes ranging from $N_2 = 16^2 = 256$ up to $N_2 = 256^2 = 65\,536$ sites, only three are shown for the sake of clearness of the diagram.

the staggered anti-ferroelectric polarization and polarizability. The focus was laid on the influence of different correction terms as well as the considered lattice sizes on the fit results, such as to develop an intuition for the analysis of the random graph case, guided by the available exact results for the much simpler square-lattice model. Simulations were performed for square lattices with periodic boundary conditions using the same simulation program as later on for the random graph systems (but with the graph flip and surgery moves omitted) to ensure maximal comparability between the regular and random graph results. Since the loop algorithm is found to be very efficient in eliminating the critical slowing down at the F model KT point [174,188], measurements were taken after each multi-cluster loop-update step. Lattice sizes up to $N_2 = 1024^2 \approx 10^6$ sites were simulated, which is by far larger than the accessible sizes for the random graph case, taking between 1×10^5 and 2×10^5 measurements.

$N_{2,\min}$	β_c	A_β	Q
256	0.73822(48)	1.419(25)	0.00
576	0.73270(59)	1.813(35)	0.00
1024	0.73033(74)	2.007(50)	0.00
2116	0.72635(110)	2.365(89)	0.46
4096	0.72409(172)	2.581(154)	0.88
8464	0.72322(261)	2.667(249)	0.78
16 384	0.72077(463)	2.923(469)	0.79

Table 5.1: Parameters of least-squares fits of the functional form (5.24) to the simulation estimates for the peak locations of the staggered polarizability of the square-lattice F model. From the set of simulated lattice sizes from $N_2 = 256$ to $N_2 = 65\,536$ sites, the smallest sizes are successively excluded from the fits, which are performed for the data points between $N_2 = N_{2,\min}$ and $N_2 = 65\,536$. Q denotes the quality-of-fit parameter, see Ref. [170].

Non-scaling of the specific heat

The specific heat of the square-lattice F model exhibits a broad peak shifted away from the critical point into the low-temperature phase [56]¹². The essential singularity predicted by Eq. (5.14) cannot in general be resolved, since it is covered by the presence of non-singular background terms. Thus, a *non-scaling* of the broad specific-heat peaks (together with a scaling of the susceptibility or polarizability to be considered below) is commonly taken as a good indicator for a phase transition to be of the KT type [236]. Indeed, this is what is found from the simulation data as is shown in Fig. 5.3. Neither does the width of the peaks shrink nor do their heights scale as the lattice size is increased. In fact, for the broad range of lattice sizes from $N_2 = 16^2 = 256$ up to $N_2 = 256^2 = 65\,536$ sites, all data almost collapse onto a single curve with only small deviations for the smallest lattices.

The critical coupling

To determine the critical coupling, we exploit the fact that the maxima of the staggered polarizability for finite lattices should be shifted away from the critical point

¹²Note that the specific heat of the 2D XY model exhibits a peak in the *high-temperature* phase, as expected from duality.

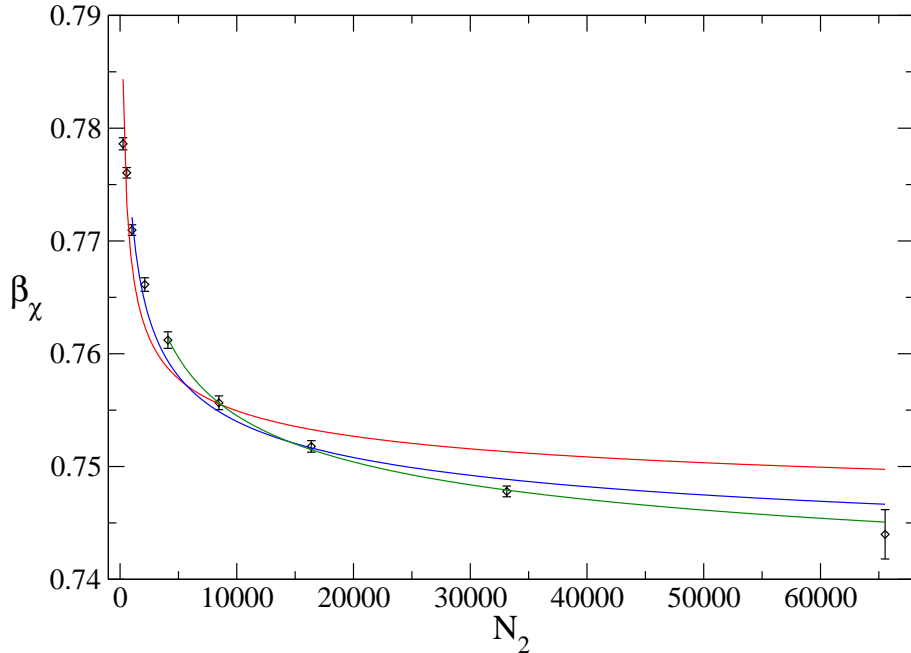


Figure 5.4: Peak positions of the staggered anti-ferroelectric polarizability of the square-lattice F model from MC simulations, as a function of the number of sites N_2 of the considered lattices. The solid lines show fits of the functional form (5.24) to the data, the range of the fits indicating the window of lattice sizes included in the fit.

according to the scaling relation Eq. (5.15). The peak locations were determined from simulations at nearby couplings β by means of the reweighting technique, cf. Appendix A.5. Transforming the scaling ansatz (5.15) to the coupling β instead of the temperature T , we have to first order,

$$\beta_\chi(N_2) = \beta_c + A_\beta (\ln N_2)^{-2}, \quad (5.24)$$

where scaling is formulated in terms of the number of sites N_2 of the lattice, anticipating the notation of the random graph case, and $\beta_\chi(N_2)$ denotes the location of the maximum of the staggered polarizability χ for a $\sqrt{N_2} \times \sqrt{N_2}$ square lattice. The determined peak locations of the polarizability together with several fits of the functional form (5.24) to the data, omitting more and more of the smaller lattice results, are shown in Fig. 5.4. The corresponding fit parameters are compiled in Table 5.1. Apparently, the presented curves fit the data rather poorly, at least for the smaller lattice sizes. Compared to the exact transition point $\beta_c = \ln 2$, the estimates are clearly too large, dropping only very slowly as points from the small- N_2

(a)	$N_{2,\min}$	β_c	A_β	$1/\tilde{\rho}$	Q
	256	-155.34	156.21	0.00033	0.00
	576	-17.033	17.92	0.0032	0.82
	1024	-14.42	15.31	0.0038	0.72
	2116	0.63(21)	0.357(33)	0.48(82)	0.96
	4096	0.69(11)	0.481(835)	0.88(157)	0.91

(b)	$N_{2,\min}$	β_c	A_β	B_β	Q
	256	0.6957(25)	13.8(7)	-2.64(2)	0.51
	576	0.7020(42)	11.7(14)	-2.56(5)	0.88
	1024	0.6974(64)	13.4(22)	-2.63(8)	0.93
	2116	0.7050(117)	10.4(44)	-2.47(31)	0.97

Table 5.2: (a) Parameters of non-linear fits of the functional form (5.25) to the simulation estimates for the peak locations of the staggered polarizability of the square-lattice F model. For small $N_{2,\min}$ the fit routine gives huge or even undefined error estimates, which are thus omitted. (b) Parameters of fits with log-log correction term of the functional form (5.26) to the simulation estimates for the peak locations of the staggered polarizability.

side of the list are successively omitted. Thus, the expected logarithmic corrections to the leading scaling behaviour (5.24) have to be taken into account to yield reliable results. Note that this effect here occurs for rather large lattices, where for a *finite-order* continuous phase transition the presence of corrections would not be much of an issue for the determination of the leading scaling behaviour. The linear extents of the lattices considered here are in fact much larger than the sizes accessible for the random graph case to be discussed below.

Since for the polarizability an exact, closed-form expression is not available even for the square-lattice model, corrections cannot be taken into account with their exact form. Instead, an effective description will have to be employed. One possible ansatz is to relax the constraint on the exponent of the logarithm of Eq. (5.24), introducing as an additional fit parameter an exponent $\tilde{\rho}$ as

$$\beta_\chi(N_2) = \beta_c + A_\beta (\ln N_2)^{-1/\tilde{\rho}}, \quad (5.25)$$

resulting in an effective exponent $\tilde{\rho} \neq \rho = 1/2$, incorporating the present correction terms in a phenomenological way. This approach yields very unstable results, since

to a wide extent an increase in the amplitude A_β can be compensated by an increase of the effective exponent $\tilde{\rho}$ and vice versa, cf. Table 5.2(a). Only for the two largest starting sizes $N_{2,\min}$ a sensible result is obtained. A different choice of correction term yields much more reliable results, namely a log-log correction of the form

$$\beta_\chi(N_2) = \beta_c + A_\beta(\ln N_2)^{-2} \left[1 + B_\beta \frac{\ln \ln N_2}{\ln N_2} \right], \quad (5.26)$$

which has the advantage of still being a linear fit, thus promising much more stable fit results. This is indeed the case, as can be seen from Table 5.2(b) and Fig. 5.5. This choice of functional form is somewhat *ad hoc*; however, similar corrections have been observed for the case of the XY Villain model [211, 240, 241]. In principle, one would at least want to admit the log-log correction term to have an additional, variable exponent. However, we find the data not precise enough to reliably fit to them a non-linear function with more than two independent parameters. Using thus the ansatz (5.26) and taking, e.g., the result with $N_{2,\min} = 1024$, our estimate for the critical coupling is $\beta_c = 0.6974(64)$, in good agreement with the exact answer $\beta_c = \ln 2 \approx 0.693$.

FSS of the polarizability

From Baxter's conjecture (5.23) for the scaling of the staggered anti-ferroelectric polarizability of the square-lattice F model one deduces the following critical-point finite-size scaling behaviour of χ ,

$$\chi(N_2, \beta_c) \sim N_2^{\gamma/d\nu} (\ln N_2)^2, \quad (5.27)$$

where d denotes the dimensionality of the lattice and, from Eq. (5.23), $\gamma/d\nu = 1/2$. Taking only the leading term into account, i.e. fitting the form

$$\chi(N_2, \beta_c) = A_\chi N_2^{\gamma/d\nu}, \quad (5.28)$$

to the simulation data, again a very slow drift from slightly too large values for $\gamma/d\nu$ towards the correct result is observed, just as for the case of the peak positions. Figure 5.6 shows the simulation results for the critical polarizability together with a fit of the functional form (5.28) to the data, resulting in an estimate $\gamma/d\nu = 0.53892(85)$, which is clearly too large. Here, the results from lattice sizes between $N_2 = 64^2$ and $N_2 = 1024^2$ sites have been taken into account. Thus, again, corrections to scaling have to be taken into account, even though the lattice sizes have now been increased

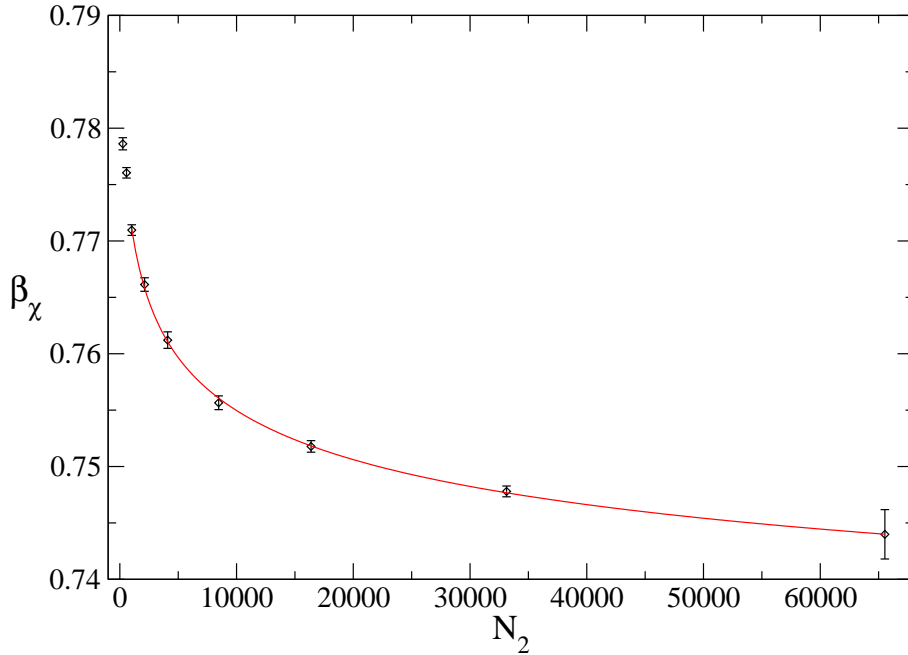


Figure 5.5: Peak positions of the staggered anti-ferroelectric polarizability of the square-lattice F model from MC simulations, as a function of the number of sites N_2 of the considered lattices. The solid line shows a fit of the log-log correction form (5.26) to the data, where the range of included lattice sizes was taken to be $N_2 = 1024, \dots, 65\,536$.

up to $N_2 \approx 10^6$ sites. Fitting to the exact form given in Eq. (5.27), we find poor fit results with exponents $\gamma/d\nu$ around 0.3 and quality-of-fit parameters Q vanishing to machine precision. However, letting the correction exponent vary, i.e., fitting the functional form

$$\chi(N_2, \beta_c) = A_\chi N_2^{\gamma/d\nu} (\ln N_2)^\omega, \quad (5.29)$$

with an additional heuristic fit parameter ω yields stable and good-quality fit results. Fitting the range $N_2 = 24^2, \dots, 1024^2$ to (5.29), we find the following fit parameters,

$$\begin{aligned} A_\chi &= 1.27(06), \\ \gamma/d\nu &= 0.5083(45), \\ \omega &= 0.32(04), \\ Q &= 0.78, \end{aligned} \quad (5.30)$$

in reasonable agreement with the exact result $\gamma/d\nu = 1/2$.

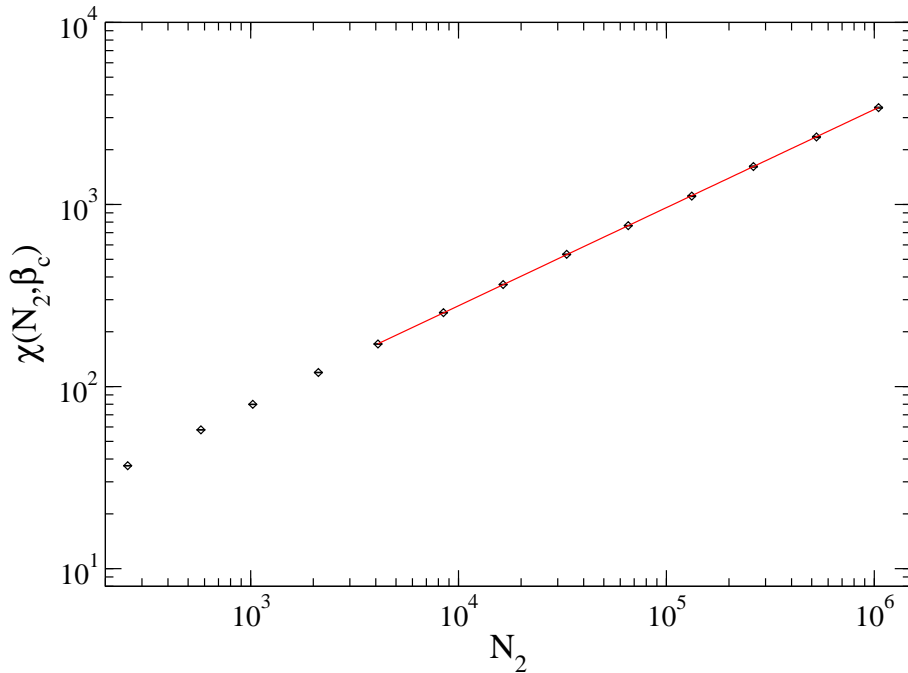


Figure 5.6: Finite-size scaling of the critical staggered polarizability χ of the square-lattice F model for lattice sizes from $N_2 = 16^2$ up to $N_2 = 1024^2$ in a log-log plot. The solid line shows a least-squares, power-law fit of the functional form (5.28) to the data.

FSS of the spontaneous polarization

The scaling form (5.22) of the spontaneous staggered polarization translates into FSS as

$$P_0(N_2, \beta_c) \sim N_2^{-\beta/d\nu} \ln N_2, \quad (5.31)$$

where $\beta/d\nu = 1/4$ from Eq. (5.22). As for the previously discussed observables, a simple fit to the leading term,

$$P_0(N_2, \beta_c) = A_{P_0} N_2^{-\beta/d\nu}, \quad (5.32)$$

yields exponents $\beta/d\nu$ approaching the expected value logarithmically slow on successively omitting data points from the small- N_2 side of the list. For instance, for the range $N_2 = 92^2, \dots, 1024^2$ we find $\beta/d\nu = 0.23290(98)$, which is still far from the exact value in terms of the quoted statistical error. On the other hand, including the logarithmic correction term of (5.31) as it stands, leads to estimates for $\beta/d\nu$ even farther away from the true answer, with values around 0.3 and standard error

around 10^{-3} . Again taking higher-order corrections into account via an effective correction exponent ω as

$$P_0(N_2, \beta_c) = A_{P_0} N_2^{-\beta/d\nu} (\ln N_2)^\omega, \quad (5.33)$$

leads to stable fits and a satisfactory agreement with the exact result for the considered lattice sizes, the parameter estimates being

$$\begin{aligned} A_{P_0} &= 2.002(78), \\ \beta/d\nu &= 0.2436(38), \\ \omega &= 0.109(33), \\ Q &= 0.14, \end{aligned} \quad (5.34)$$

where lattice sizes from $N_2 = 24^2$ to $N_2 = 1024^2$ were included.

Thermal scaling

The discussed FSS of the critical polarization and polarizability is independent of the value of the critical exponent ρ . Thus, to directly verify the exponential type of the observed divergences and to estimate the parameter ρ , one has to consider *thermal* instead of finite-size scaling. Figure 5.7 shows an overview of the thermal behaviour of the staggered polarizability for different lattice sizes. The clear scaling of χ for the high-temperature region $\beta < \beta_c = \ln 2$ indicates the presence of a critical phase. In contrast, for the low-temperature phase to the right of the peaks, the polarizability curves essentially collapse and only start to diverge as the correlation length reaches the linear extent of the considered lattice. Therefore, a thermal scaling analysis must be performed in the low-temperature vicinity of the critical point, the behaviour in the high-temperature phase being completely governed by finite-size effects.

Here, we do not consider the scaling of the correlation length itself, since for the case of random lattices to be discussed below it is a non-trivial and not completely resolved question, how to reliably determine connected correlation functions (and thus the correlation length) in an ordered phase [247]. Instead, we consider the thermal scaling of the staggered polarizability for a single lattice size of $N_2 = 256^2 = 65\,536$ sites. Simulations were performed for a closely spaced series of temperatures in the low-temperature vicinity of the critical point. From the scaling conjecture (5.22), we expect the following scaling relation,

$$\ln \chi(\beta) \sim A_\chi + B_\chi (\beta - \beta_c)^{-\rho} + C_\chi \ln(\beta - \beta_c), \quad (5.35)$$

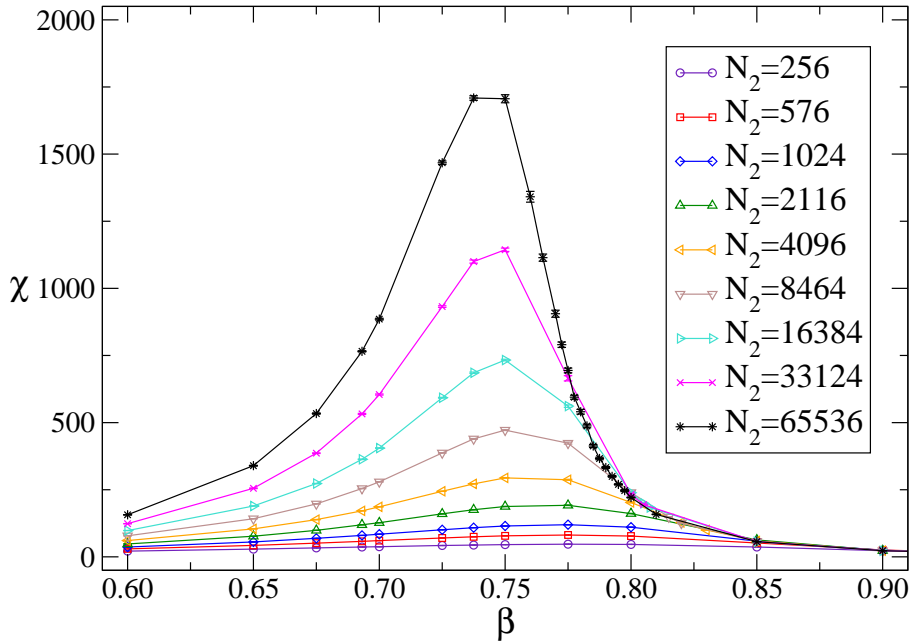


Figure 5.7: Scaling of the polarizability peaks of the square-lattice F model from Monte Carlo simulations. The lines simply connect the data points and are drawn for illustrative purposes. The curves show a clear scaling of the polarizability in the critical high-temperature phase (to left of the peaks), whereas in the low-temperature limit $\beta \rightarrow \infty$ the curves collapse, only diverging as the correlation lengths reach the respective linear extents of the lattices when approaching the critical point.

which should be valid as $\beta \rightarrow \beta_c^+$ in the thermodynamic limit $N_2 \rightarrow \infty$. Note that this relation is essentially independent of the value of the critical exponent γ , which only enters the amplitude A_χ . The window of validity of (5.35) for the thermal scaling of χ for a finite lattice is limited for small deviations $\beta - \beta_c$ by finite-size effects and for large deviations $\beta - \beta_c$ by higher-order corrections to scaling. Ideally, one would want to monitor the effect of the finite lattice size by comparing the value of the correlation length ξ at a given $\beta > \beta_c$ with the linear extent L of the lattice and ensuring the ratio ξ/L not to exceed a given threshold, say $1/15$ [210]. However, since we do not want to consider correlation lengths in view of the more complicated random graph problem, the onset of finite-size effects is estimated by the beginning of the rounding of the exponential increase of χ as β_c is approached. Furthermore, with the given accuracy of our data we find it impossible to reliably fit the five-parameter family of functions (5.35) to the data. Thus, we first drop

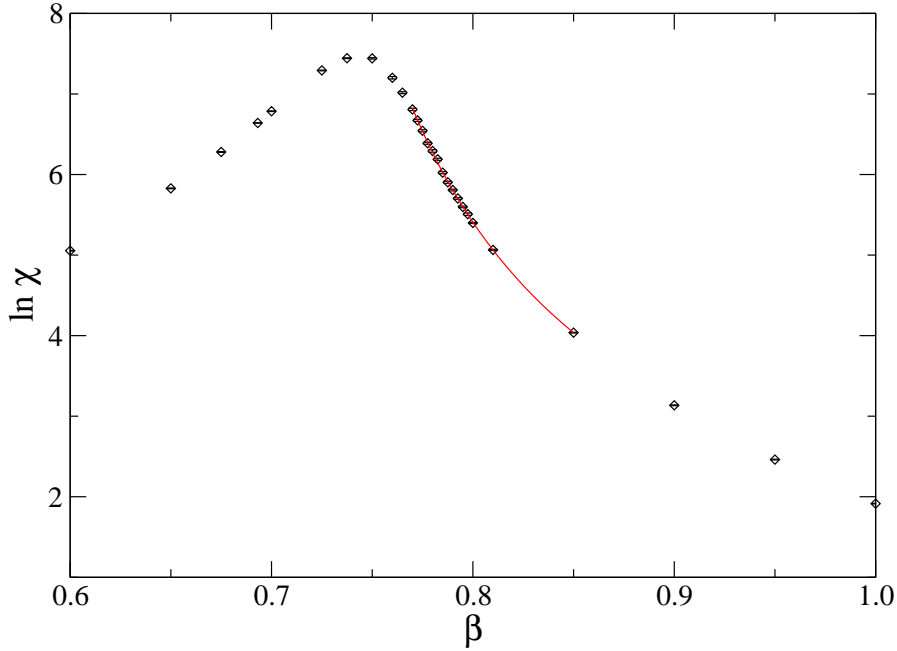


Figure 5.8: Thermal scaling of the polarizability of the square-lattice F model on a $N_2 = 256^2 = 65\,536$ lattice. The solid line shows a fit of the functional form (5.35) to the data, where the parameters $C_\chi = 0$ and $\beta_c = \ln 2$ were kept fixed. The extent of the curve indicates the window of data points included in the fit.

the logarithmic correction term, i.e., we enforce $C_\chi = 0$. The resulting non-linear four-parameter fit yields $\beta_c = 0.56(24)$ and $\rho = -2.4(33)$, which is consistent with the exact result, but obviously not very useful. Thus, we additionally either fix the critical coupling β_c at its exact value $\beta_c = \ln 2$ and determine ρ from the fit, or we fix $\rho = 1/2$ and determine β_c . The simulation results together with a fit with β_c fixed are shown in Fig. 5.8. The fit parameters are,

$$\begin{aligned}
 A_\chi &= -2.18(39), \\
 B_\chi &= 2.37(27), \\
 \rho &= 0.519(27), \\
 Q &= 0.12,
 \end{aligned}
 \tag{5.36}$$

indicating good agreement with the expected result $\rho = 1/2$. The other type of fit,

i.e., with $\rho = 1/2$ fixed, yields,

$$\begin{aligned} A_\chi &= -2.38(13), \\ B_\chi &= 2.531(67), \\ \beta_c &= 0.6944(19), \\ Q &= 0.12, \end{aligned} \tag{5.37}$$

for the same set of simulation points, which should be compared to $\beta_c = \ln 2 \approx 0.693$.

5.2.3 The F model on planar ϕ^4 random graphs

While it is already rather non-trivial to resolve the Kosterlitz-Thouless nature of the phase transition of the *square-lattice* F model via MC simulations due to the presence of logarithmic correction terms, an analysis of the F model on planar random ϕ^4 graphs is additionally complicated by the strongly reduced linear extents of the lattices resulting from their large fractal dimension. We performed simulations of the combined system exclusively for lattices of spherical topology, i.e., planar graphs, of sizes up to $N_2 = 65\,536$ sites. The graph geometry is being updated with the combined (one- and two-) link-flip and minBU surgery dynamics described in Chapter 3 and the loop algorithm of Section 4.2 is applied for the vertex model part. Unless otherwise stated, all simulations were performed for the *regular* ensemble of ϕ^4 graphs. A profiling analysis of the execution times of the simulation program shows that more than half of the total run time is spent for finding the minimal necks of the minBU surgery part. This procedure is much more time consuming, if the problem is formulated in terms of the ϕ^4 graphs, as it is when considering the dynamical quadrangulations. The simulations were performed partly on the Cray T3E 1200 of the “John von Neumann-Institute for Computing” (NIC) in Juelich (ca. 12 000 CPU hours) and on the heterogeneous cluster of i386 PC’s of the Institute for Theoretical Physics of the University of Leipzig (ca. 50 000 CPU hours) as well as its 40 Athlon MP1800+ cluster computer “Hagrid” (ca. 60 000 CPU hours).

The specific heat

As for the case of the square-lattice F model, for the random graph case we find no signal of a scaling of the specific heat. Instead, it exhibits a broad peak in the low-temperature phase, which is found to be independent from the lattice size up

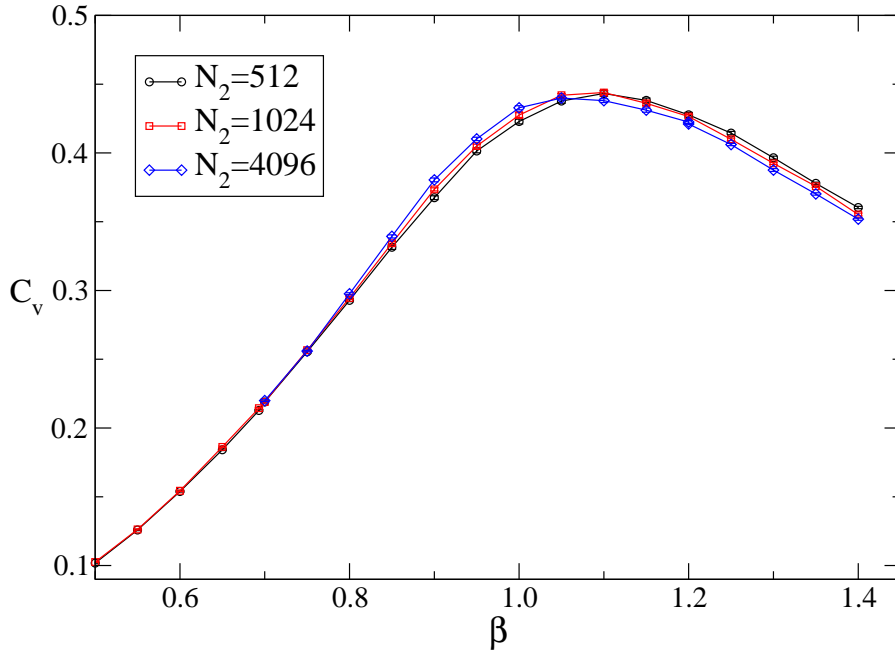


Figure 5.9: Non-scaling of the specific heat of the F model coupled to planar random ϕ^4 graphs. The solid curves are line sections connecting the data points and are drawn for illustrative purposes only. Note the much stronger shift of the peak positions towards lower temperatures as compared to the square-lattice F model of Fig. 5.3.

to small finite-size corrections, cf. Fig. 5.9. Comparing Figs. 5.3 and 5.9, note that this peak appears for much lower temperatures around $\beta_{C_v} \approx 1.2$ for the ϕ^4 random graphs as compared to $\beta_{C_v} \approx 0.85$ for the square-lattice model. This behaviour of the specific heat is commonly considered as a first good indicator for the presence of an infinite-order phase transition [236].

Location of the critical point

As for the square-lattice model, we determine the location of the KT point from the scaling of the maxima of the staggered anti-ferroelectric polarizability, now defined from the generalized polarization of Eqs. (4.39) or (4.40). Again, the peak locations are expected to scale logarithmically to the true critical point; to leading order we have,

$$\beta_\chi(N_2) = \beta_c + A_\beta (\ln N_2)^{-1/\rho}, \quad (5.38)$$

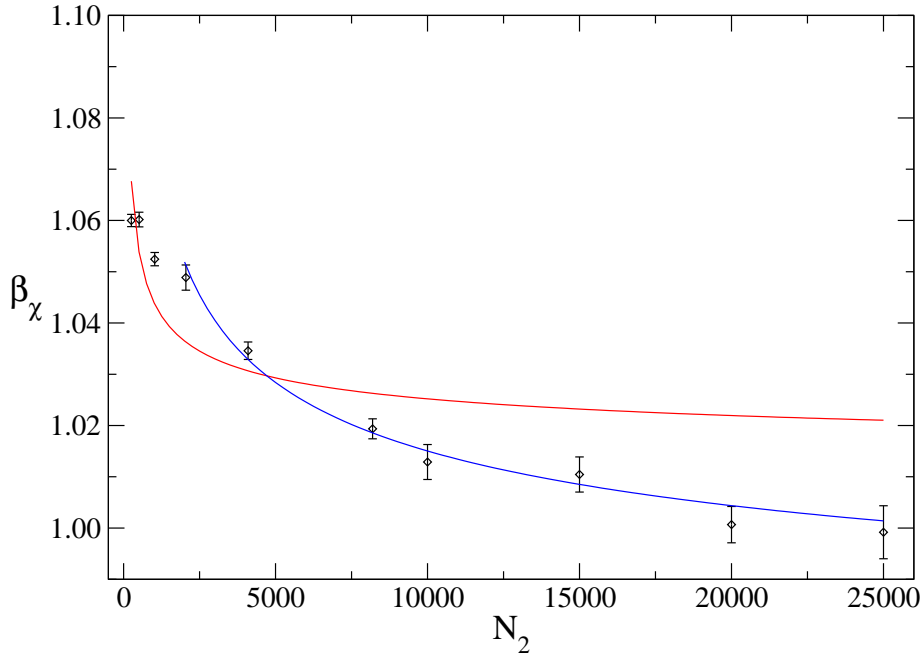


Figure 5.10: Scaling of the peak locations of the polarizability of the F model on planar ϕ^4 random graphs from MC simulations. The solid lines show fits of the simple analytic form (5.38) to the simulation data, where $\rho = 1/2$ was kept fixed. The ranges of the curves indicate the windows of included graph sizes N_2 .

cf. Eq. (5.24). For the determination of the peak positions we made use of the temperature-reweighting technique described in Appendix A.5. Note that the quoted errors do not cover the potential bias induced by the reweighting procedure. We performed simulations for graph sizes between $N_2 = 256$ and $N_2 = 25\,000$ sites, taking some 10^6 measurements after the systems had been equilibrated. Measurements were taken after every tenth sweep of the combined link-flip and minBU surgery dynamics, confining the graphs to the *regular* ensemble of Section 3.1. All statistical errors were determined by the combined binning/jackknife techniques described in Appendix A.3.

Figure 5.10 shows the FSS of the peak locations resulting from the simulations. Comparing to the corresponding presentation for the square-lattice model, Fig. 5.4, we first note that the accessible part of the scaling regime is strongly shifted towards lower temperatures, being rather far away from the conjectured critical coupling $\beta_c = \ln 2 \approx 0.693$. We start with fits of the simple form Eq. (5.38) without including any correction terms. Additionally, we assume $\rho = 1/2$ here as in the square-lattice

$N_{2,\min}$	β_c	A_β	Q
256	1.0011(18)	2.049(77)	0.00
512	0.9810(24)	3.28(13)	0.00
1024	0.9676(32)	4.22(19)	0.00
2048	0.9361(59)	6.69(44)	0.53
4096	0.9265(84)	7.49(66)	0.82

Table 5.3: Parameters of fits of the analytic form (5.38) to the simulation data for the peak locations of the staggered anti-ferroelectric polarizability of the F model on random ϕ^4 graphs. The exponent ρ was kept fixed at the value $\rho = 1/2$ for the fits. Here, $N_{2,\min}$ denotes the minimum graph size included in the fit.

case, which has to be justified *a posteriori* by the thermal scaling analysis. Within this scheme, the influence of correction terms is taken into account by successively omitting lattice sizes from the small- N_2 side. As can be seen from the fits of this type presented in Fig. 5.10 and the corresponding fit parameters listed in Table 5.3, this ansatz does not lead to good fits when the small lattices are included. The fit with $N_{2,\min} = 2048$ yields a reasonable fit quality, resulting in an estimate of $\beta_c = 0.9361(59)$ for the critical coupling. However, in analogy with the square-lattice case and guided by the matrix model conjecture, we interpret the slowly decreasing values of β_c as more and more of the small- N_2 graphs sizes are excluded from the fit as an indicator of a bad fit form for the considered graph sizes and conclude that the resulting estimate for β_c is still clearly too large. Thus, we revert to fits including effective correction terms.

Adding the exponent ρ to the fit parameters amounts to a fit with an effective exponent $\tilde{\rho}$ as in Eq. (5.25), i.e.,

$$\beta_\chi(N_2) = \beta_c + A_\beta (\ln N_2)^{-1/\tilde{\rho}}, \quad (5.39)$$

The parameters resulting from the corresponding non-linear three-parameter fits are listed in Table 5.4(a) as a function of the minimum included graph size $N_{2,\min}$. Obviously, the available accuracy of the data hardly allows such a non-linear fit, which yields rather non-sensical results for small values of $N_{2,\min}$. Additionally, we find that the fit results for small $N_{2,\min}$ partly depend on the choice of the starting values for the fit parameters, i.e., that the fit routine gets stuck in local minima of the χ^2 distribution. Thus, at least the results for small $N_{2,\min}$ cannot be taken seriously. Only for the choices $N_{2,\min} = 2048$ and $N_{2,\min} = 4096$ the fits yield

(a)

$N_{2,\min}$	β_c	A_β	$1/\tilde{\rho}$	Q
256	-0.4	1.6	0.06	0.00
512	-0.4	1.7	0.08	0.00
1024	-0.2	1.6	0.1	0.00
2048	0.3(40)	1.2(30)	0.3(15)	0.76
4096	0.83(58)	1.7(62)	1.0(31)	0.69

(b)

$N_{2,\min}$	β_c	A_β	B_β	Q
256	0.856(11)	42.6(27)	-2.737(10)	0.13
512	0.823(18)	49.3(53)	-2.774(22)	0.17
1024	0.758(33)	70.6(104)	-2.862(28)	0.63
2048	0.834(65)	42.9(229)	-2.659(414)	0.80

Table 5.4: (a) Parameter results of least-squares fits of the functional form (5.39) for the FSS of the peak locations of the staggered polarizability of the F model on ϕ^4 random graphs to the simulation data. $\tilde{\rho}$ denotes an effective exponent and $N_{2,\min}$ symbolizes the minimum graph size included in the fits. (b) Parameter results of linear three-parameter fits of the form (5.40) to the simulation data with more and more of the small- N_2 data points omitted.

reasonable parameters, which are in principle in agreement with the expected value $\beta_c = \ln 2$ for the critical coupling, but are endowed with statistical errors which are far too large for the estimate to be of much practical use. As in the square-lattice case, the result for the exponent $\tilde{\rho}$ cannot be taken as a serious estimate for ρ , since it incorporates correction terms in an effective way.

Since for the square-lattice case we found a linear fit incorporating an additive log-log correction of the form

$$\beta_\chi(N_2) = \beta_c + A_\beta (\ln N_2)^{-2} \left[1 + B_\beta \frac{\ln \ln N_2}{\ln N_2} \right] \quad (5.40)$$

to be the best of the considered descriptions for the available finite-size data (and a corresponding correction is found for the KT phase transition of the XY model on regular lattices [211, 240, 241]), we also consider this fit for the random graph data. This functional form fits the data rather well already for small values of $N_{2,\min}$, as can be seen from the collection of fit parameters in Table 5.4(b). Nevertheless, the fits still show some inherent instability as can be seen from the result for $N_{2,\min} = 1024$, where obviously a slightly different local minimum of the χ^2 distribution is favoured

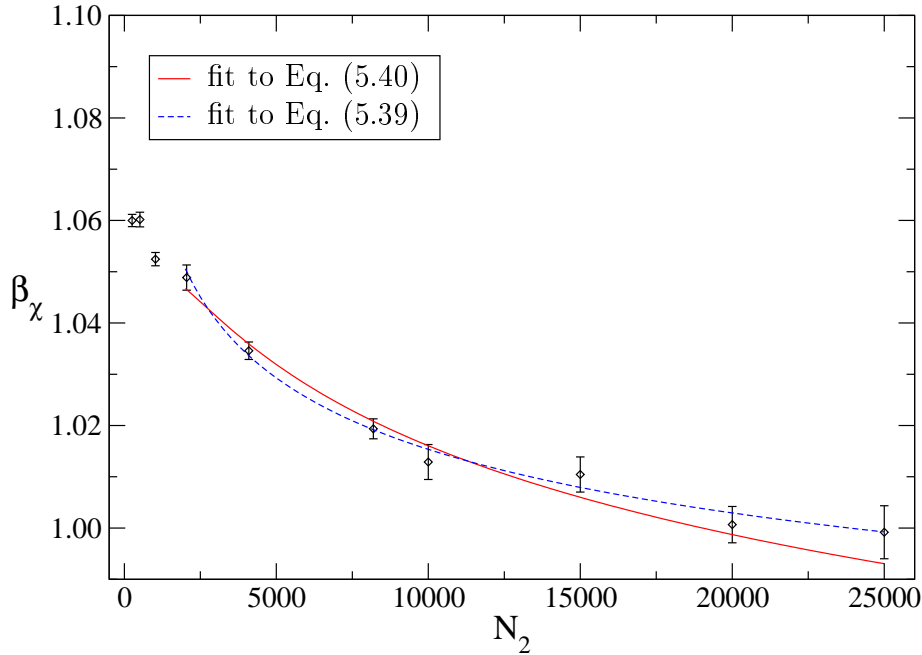


Figure 5.11: Fits of the functional forms (5.40) resp. (5.39) with the constant fixed to $\beta_c = \ln 2 \approx 0.693$ to the simulation data for the peak locations of the staggered polarizability of the random graph F model.

over the minimum obtained for the other values of $N_{2,\min}$. However, the critical coupling β_c estimated for, e.g., the $N_{2,\min} = 2048$ case is still noticeably larger than the expected value of $\beta_c = \ln 2$. Nevertheless, it can be considered still marginally consistent with the conjectured value, the deviation being about 2.2 times the quoted standard error of the estimate. On the other hand, if we *fix* the critical coupling at the expected value $\ln 2$, reducing the number of fit parameters to two, we still get a proper fit result of reasonable quality Q , the parameters being,

$$\begin{aligned} A_\beta &= 92.51(167), \\ B_\beta &= -2.920(19), \\ Q &= 0.27, \end{aligned} \tag{5.41}$$

where $N_{2,\min} = 2048$ was chosen. This fit is shown in Fig. 5.11 to convince the reader of our opinion that the simulation data are well compatible with the expected asymptotic behaviour, the accuracy of the data and, especially, the reachable graph sizes just being not sufficient to properly resolve the finite-size approach to criticality. It should be noted that also the other type of fits presented here still yield good quality-of-fits when fixing the parameter β_c at $\ln 2$. For example, a fit of the form

(5.39) to the data with $N_{2,\min} = 2048$ gives,

$$\begin{aligned} A_\beta &= 1.071(81), \\ 1/\tilde{\rho} &= 0.541(35), \\ Q &= 0.84. \end{aligned} \tag{5.42}$$

The corresponding curve is also shown in Fig. 5.11.

Universality of the critical coupling

One might be tempted to suspect that the observed rather large distances of the finite-size positions of the polarizability maxima from the expected value $\beta_c = \ln 2 \approx 0.693$ are due to the fact that we use graphs of the *regular* ensemble, whereas the matrix model calculations of Refs. [72, 73] naturally concern graphs of the *singular* ensemble. Indeed, quite generally one does not expect the critical coupling of a model of statistical mechanics to be *universal*. Instead, one finds that the location of the transition points of problems such as percolation, Potts or $O(n)$ models depends on the type (e.g., the valency) of the considered lattice. Similarly, for the Ising model coupled to dynamical polygonifications or the dual graphs, the location of the observed third-order phase transition depends on whether one considers spins located on the vertices of triangulations, quadrangulations, ϕ^3 or ϕ^4 graphs [34, 49, 74]¹³. Additionally, depending on the considered ensemble of graphs with respect to the inclusion or exclusion of certain types of singular contributions as defined in Section 3.1, one arrives at different values for the critical coupling [34, 35, 152, 248]. However, the situation is quite different for the case of the F model coupled to random lattices. As has been mentioned above in Section 5.1.2, in the matrix model description of the problem, Eq. (5.6), the matrix potential becomes equivalent to that of the $O(2)$ model in the limit $\mu = 0$ [73]; according to Eqs. (5.4) and (5.17), this limit corresponds to the choice $a/c = b/c = 1/2$ or $\beta_c = \ln 2$. Thus, renormalizing the matrix model for restricted singular or regular ϕ^4 graphs merely changes the critical point a_{crit} of Eq. (5.8), which takes on the rôle of the cosmological constant in the grand-canonical ensemble. But the KT point still occurs for the ratio $a/c = b/c = 1/2$ of coupling constants¹⁴. This universality aspect is maybe

¹³However, it is found that the location of the critical point does *not* depend on the topology of the lattices [146].

¹⁴This universality can already be expected from the fact that the location of the critical point is the same for the square-lattice and random ϕ^4 graph models.

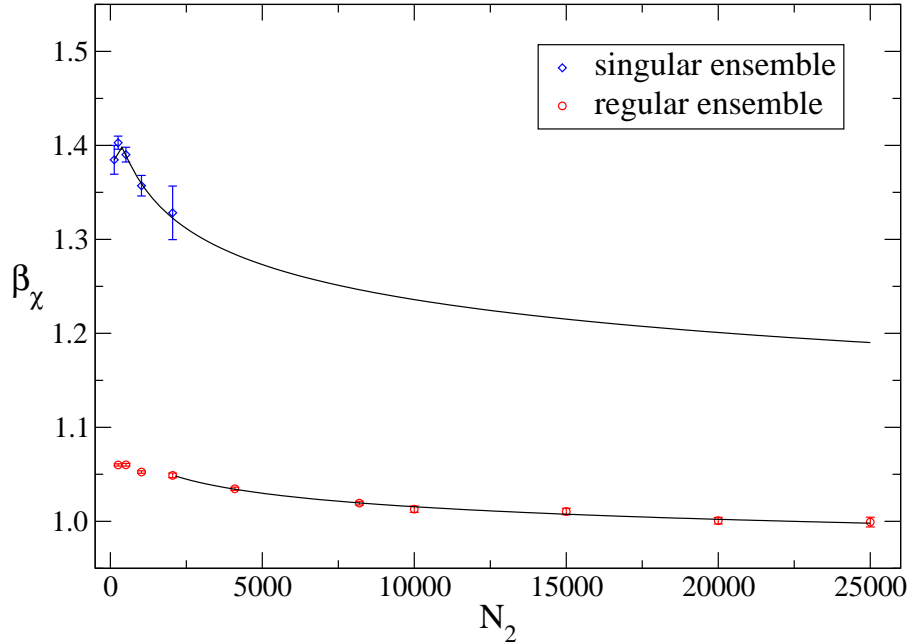


Figure 5.12: Finite-size approach of the peak locations of the staggered polarizability of the F model on ϕ^4 random graphs of the singular and regular ensembles. The solid lines show fits of the functional form (5.40) to the data. The lower limits in N_2 of the curves are identical to the choice of $N_{2,\min}$ for the fits.

most strikingly demonstrated by the loop representations of the F and $O(2)$ models as described in Section 5.1.2: the loop expansion of the F model assigns curvature dependent weights $\exp[i\mu\Gamma(l)]$ to the loops on the ϕ^4 graphs; for $\mu = 0$, the curvature dependence disappears and one is left with the loop weights of the $O(2)$ model. Obviously, the structure of this construction does not depend on the detailed type of the considered graphs, i.e., whether they do or do not contain singular contributions such as self-energy and tadpole terms. Thus, the correspondence of the $\mu = 0$ point of the F model and the KT point is not influenced by lattice details, hence endowing the critical coupling $\beta_c = \ln 2$ with an universality aspect.

We have not performed extensive simulations of graphs of the singular ensemble to demonstrate this behaviour numerically. This is due to the fact that our implementation of the simulation scheme for the case of singular graphs is rather inefficient since it does not incorporate the minBU surgery moves and, additionally, the “on-line” updating of the dual lattice information used for the other ensembles cannot be easily adapted to the case of singular graphs since it would entail a separate

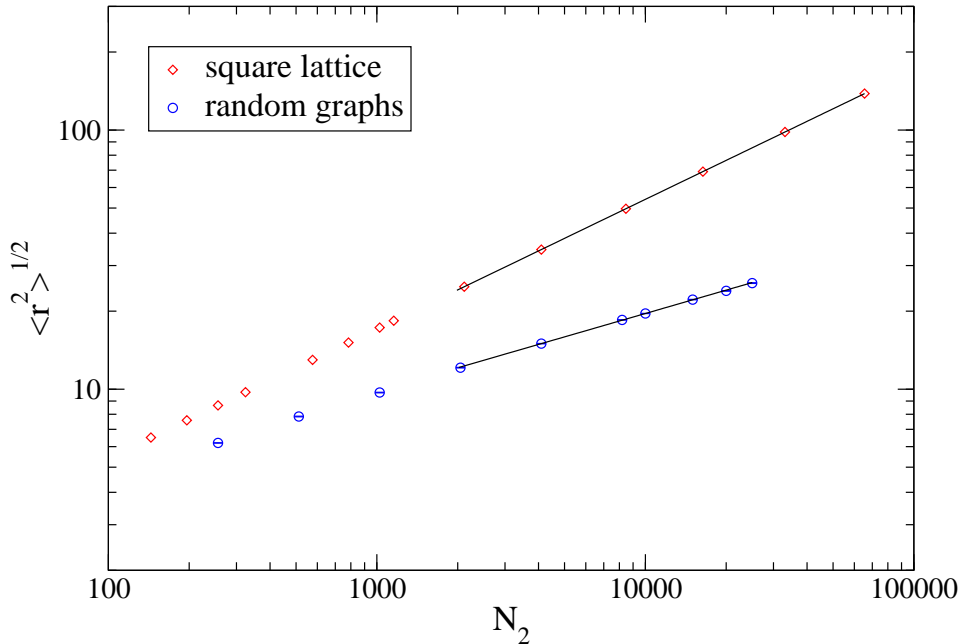


Figure 5.13: FSS of the square-root $\sqrt{\langle r^2 \rangle}$ of the mean square extent of the square-lattice on a torus and planar ϕ^4 random graphs at the peak positions of the polarizability of the coupled F model. The solid lines show fits of the simple power-law form $\sqrt{\langle r^2 \rangle} \sim N_2^{1/d_h}$ to the data. The range of the curves indicates the lattice sizes included in the fit.

treatment of numerous special cases; thus, the dual lattice has to be constructed anew for each measurement cycle. Hence, simulations for graphs of the singular ensemble are by orders of magnitude less efficient for the considered graph sizes than simulations of the other graph ensembles. Nevertheless, we performed some simulations for smaller graph sizes and analyzed the FSS of the peak locations of the staggered polarizability just as for the the case of regular graphs. The corresponding FSS data are shown in Fig. 5.12 together with the results for regular graphs. A fit of the log-log form Eq. (5.40) to the data including all five points from $N_2 = 128$ to $N_2 = 2048$ yields the following parameters,

$$\begin{aligned}
 \beta_c &= 0.76(19), \\
 A_\beta &= 114.9(364), \\
 B_\beta &= -2.676(22), \\
 Q &= 0.95,
 \end{aligned}
 \tag{5.43}$$

in agreement with the expectations. Note that from Fig. 5.12 the finite-size correc-

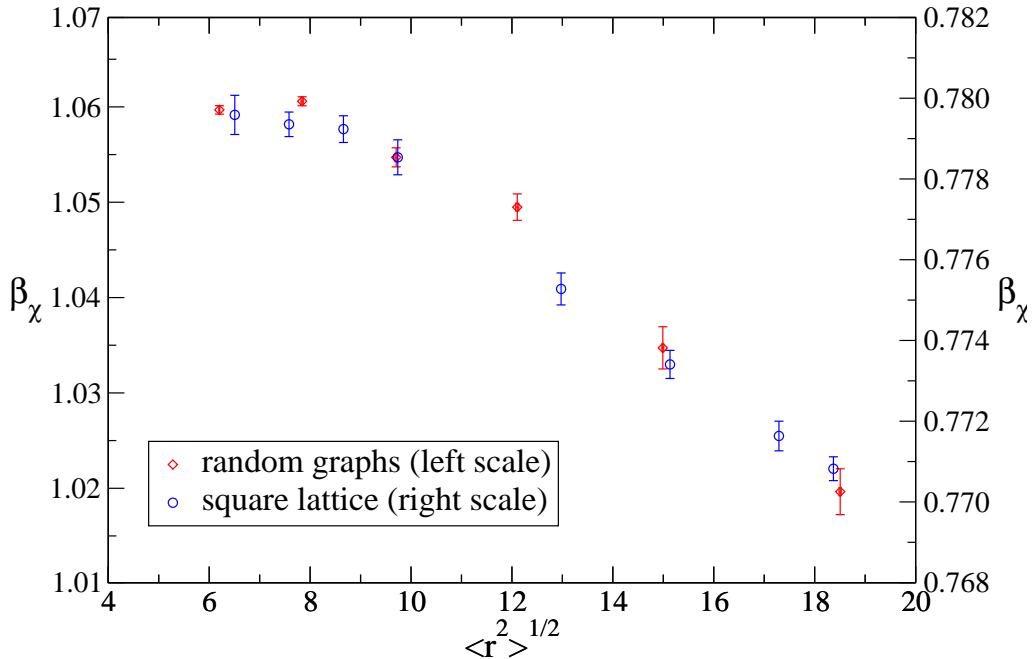


Figure 5.14: Collapse of the FSS approach of the scaling of the peak locations of the staggered anti-ferroelectric polarizability of the F model on random ϕ^4 graphs (left scale) and on the square lattice (right scale).

tions for the singular graph case are much larger than those for the regular graph model. This is in contrast to previous observations for the case of the Potts model coupled to random triangulations [50] and the resulting common belief that the inclusion of singular graph contributions reduces FSS effects, at least for the considered small lattice sizes. Exploratory simulations for the other graph ensembles defined in Section 3.1 imply that the polarizability peak locations occur in the order $\beta_\chi(\text{strict}) \leq \beta_\chi(\text{regular}) \leq \beta_\chi(\text{restricted singular}) \leq \beta_\chi(\text{singular})$, at least for small graph sizes.

As has been previously mentioned, the reason for the observed very slow approach to the expected asymptotic behaviour lies in the double effect of the presence of logarithmic corrections to scaling and the small linear extent of the highly fractal lattices. In principle it should be possible to resolve the resulting scaling corrections by including higher-order correction terms in the fit ansätze. However, it must be admitted that, refraining from any artificial “good-will” tinkering with the fit parameters, the accuracy of the present data is not sufficient for reliable multi-parameter, possibly non-linear fits. The strength of this combined effect is nicely

demonstrated numerically by the fact that the fits to the FSS of the polarizability peak locations with β_c fixed to its true value $\beta_c = \ln 2$ shown in Fig. 5.11 come as close as $\beta_\chi(N_2) = 0.7$ to the critical value only for graph sizes $N_2 \approx 10^{50}$ for the form (5.40) or even $N_2 \approx 10^{5000}$ for the form (5.39). Instead of figuring out more elaborate fits, we try to disentangle the two correction effects by a comparison to the square-lattice model, where only the logarithmic corrections are present, but the considered lattices are not fractal. For this purpose, we plot the polarizability peak locations as a function of the square-root of the mean square extent of the considered lattices as defined by Eq. (3.37), which is the relevant measure for the linear extent of the graphs. The mean extents $\sqrt{\langle r^2 \rangle}$ scale very differently for the two types of considered lattices as can be seen from Fig. 5.13. Here, the values for the square lattices are exact up to machine precision. From the simple scaling ansatz

$$\langle r^2 \rangle \sim N_2^{1/2d_h}, \quad (5.44)$$

without considering any correction terms for the random graph case, we find $d_h = 2.000(20)$ for the square lattice, the deviation stemming from discretisation effects for the smallest lattices. For the case of ϕ^4 random graphs the fit yields $d_h = 3.336(11)$. Note, however, that the result for d_h is slowly increasing as more and more of the small- N_2 lattices are excluded and we expect the true value of the Hausdorff dimension to be somewhat larger, see Refs. [115, 249, 250] and Section 5.4.3 below. From Fig. 5.13 one reads off that, in order to obtain results for the F model at comparable linear extents of the square and random lattices, one has to consider rather small volumes for the square-lattice case. For the comparison we use $L \times L$ square lattices with edge lengths L chosen such that the resulting mean square extent comes as close as possible to the $\langle r^2 \rangle$ values for the ϕ^4 random graphs of volumes between $N_2 = 256$ up to $N_2 = 8192$, increasing in powers of two.

In Fig. 5.14 we present a comparison of the FSS approach of the peak locations of the polarizability for the ϕ^4 graph and square-lattice models plotted as a function of the linear extent $\sqrt{\langle r^2 \rangle}$ of the lattices. Here, the abscissae of the plot have been scaled such as to account for the difference in the overall correction amplitude, but *assuming the same value $\ln 2$ for the offset*. From the two simulation points near $\sqrt{\langle r^2 \rangle} \approx 10$ we find the ratio of the correction amplitudes as¹⁵

$$A_\beta = \frac{\beta_\chi^{\text{rl}}(N_2 = 1024) - \ln 2}{\beta_\chi^{\text{sl}}(N_2 = 324) - \ln 2} \approx 4.23, \quad (5.45)$$

¹⁵These two simulation points have been chosen since there the difference in $\sqrt{\langle r^2 \rangle}$ between the square and random lattices is minimal within the set of considered lattice sizes.

where β_χ^{rl} denotes the peak position for the random ϕ^4 graph model and β_χ^{sl} the value for the square-lattice case. The thus achieved collapse of the FSS data is obvious from Fig. 5.14. Consequently, we come to the clear conclusion that the larger deviations of the peak locations for random graphs are simply due to an about four times larger overall amplitude of the correction terms as compared to the square-lattice model, the details of the FSS approach being otherwise surprisingly similar between the two considered lattice types. Especially, the fact that for the ϕ^4 graph case the asymptotic value $\beta_c = \ln 2$ cannot be clearly resolved by the considered fits to the data is an obvious consequence of the comparative smallness of the accessible lattice sizes in terms of their effective linear extents $\sqrt{\langle r^2 \rangle}$. To underline this finding, we performed fits of the simple form (5.38) to the data for both types of lattices (there are not enough data points for fits with correction terms), including sizes starting from the points near $\sqrt{\langle r^2 \rangle} \approx 10$, which result in estimates $\beta_c = 0.7554(18)$ for the square lattice resp. $\beta_c = 0.9416(89)$ for the random graphs. In terms of the quoted statistical errors these are obviously both far away from the asymptotic result. The deviation from $\beta_c = \ln 2$ is, however, just about four times larger for the random graph case than for the square-lattice model, in agreement with the previous discussion of the scaling collapse of Fig. 5.14.

Critical energy and specific heat

We note in passing that for the largest lattice we have simulated, i.e., for $N_2 = 65\,536$, at $\beta = \beta_c = \ln 2$ we find the following values of the internal energy and specific heat per site,

$$\begin{aligned} U(\beta = \ln 2) &= 0.333355(11), \\ C_v(\beta = \ln 2) &= 0.2137(12). \end{aligned} \tag{5.46}$$

Comparing these results to the values (5.19) found analytically for the square-lattice F model, we see that $U(\beta = \ln 2)$ is very close to the value $1/3$ found for the square lattice, whereas $C_v(\beta = \ln 2)$ is far away from the square-lattice result $28(\ln 2)^2/45 \approx 0.2989$. On the basis of these results, we conjecture that the critical value of the internal energy of the F model is not affected by the coupling to random graphs, while the critical specific heat is. Thus, as one would expect, the critical distribution of vertex energies naturally changes its shape on moving from the square-lattice to the random graph model, but, curiously, its mean is not shifted by this procedure. Interestingly, this situation seems to be specific to the critical point $\beta_c = \ln 2$ of the model, whereas for other inverse temperatures the square-lattice and random graph

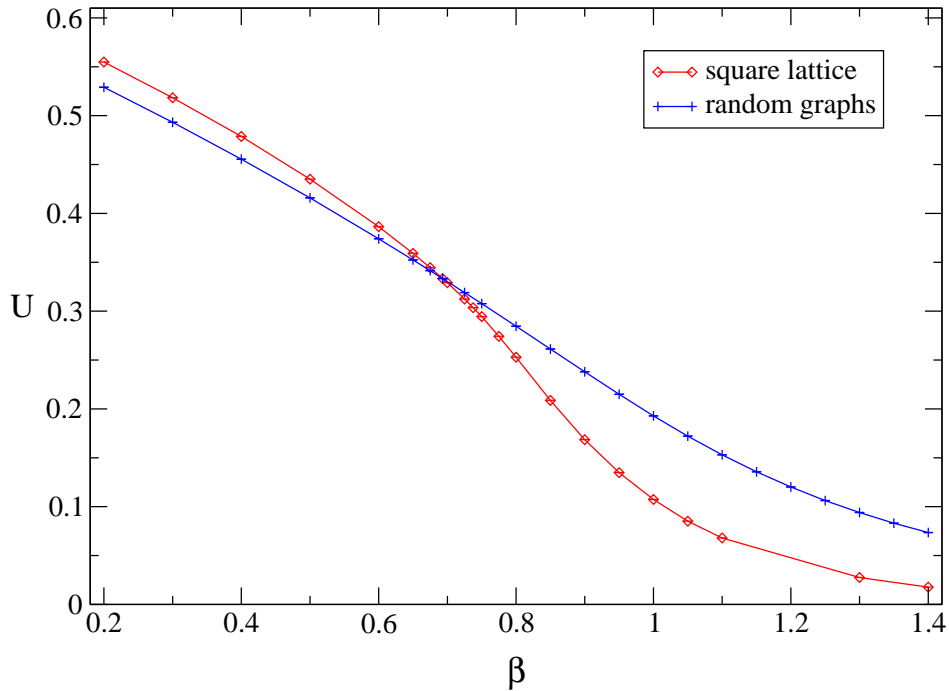


Figure 5.15: Temperature dependence of the internal energy U of the square-lattice and random ϕ^4 graph F models. Simulations have been performed for a $N_2 = 46^2 = 2116$ square lattice and random graphs with $N_2 = 2048$ sites. The lines drawn only connect the data points.

energies diverge, see Fig. 5.15. This probably indicates the presence of an additional symmetry common to the critical square-lattice and random graph models.

FSS of the polarizability

On coupling the vertex model to quantum gravity we expect a renormalization of the critical exponents as prescribed by the KPZ/DDK framework described in Section 2.4. The work of KPZ/DDK [30–32] considers conformal minimal models with $C < 1$ coupled to the Liouville field, however it should also marginally apply to the limiting case $C = 1$ of the model considered here. As described above in Section 2.4, the critical exponents of the random graph model can be found from the KPZ formula in terms of the *conformal weights* of the scaling operators of the theory. To find the usual critical exponents from the weights, one *assumes* that the well-known scaling

relations stay valid (see, e.g., Refs. [46, 140]) and thus arrives at,

$$\begin{aligned}
 \alpha &= \frac{1 - 2\Delta_\epsilon}{1 - \Delta_\epsilon}, \\
 \beta &= \frac{\Delta_P}{1 - \Delta_\epsilon}, \\
 \gamma &= \frac{1 - 2\Delta_P}{1 - \Delta_\epsilon}, \\
 d_h\nu &= \frac{1}{1 - \Delta_\epsilon}, \\
 2 - \eta &= (1 - 2\Delta_P)d_h.
 \end{aligned} \tag{5.47}$$

Here, Δ_ϵ denotes the weight of the energy operator and Δ_P symbolizes the weight of the scaling operator corresponding to the spontaneous staggered polarization P_0 , which here takes on the rôle of the magnetization operator σ of magnetic models. As before, d_h is the internal Hausdorff dimension of the random graphs. For the special case of an infinite-order phase transition considered here, the usual exponents written above are not well-defined in the sense of describing power-law singularities, as has been mentioned above. Especially, the energy operator does not carry a conformal weight Δ_ϵ in the usual sense. However, the corresponding finite-size scaling exponents, i.e.,

$$\begin{aligned}
 \beta/d_h\nu &= \Delta_P, \\
 \gamma/d_h\nu &= 1 - 2\Delta_P,
 \end{aligned} \tag{5.48}$$

have a well-defined meaning in the sense of Eqs. (5.27) and (5.31). Note that we cannot solve for β/ν resp. γ/ν since the Hausdorff dimension of the graphs in the presence of the vertex model is not known *a priori*. From the exponents $\beta/d_h\nu = 1/4$ and $\gamma/d_h\nu = 1/2$ cited above for the square-lattice F model, we find the corresponding anti-ferroelectric “spin” operator to have conformal weight

$$\Delta_P = 1/4, \tag{5.49}$$

leading to the intended critical exponents $\beta/d_h\nu = 1/4$ and $\gamma/d_h\nu = 1/2$ via Eq. (5.48). Note that the weight $\Delta_P = 1/4$ is different from the weight $\Delta_\sigma = 1/16$ found for the magnetization of the critical XY model in two dimensions, see e.g. Ref. [201]. For the present limiting case of conformal charge $C = 1$, the KPZ formula (2.140) reduces to the simple relation

$$\tilde{\Delta} = \sqrt{\Delta}, \tag{5.50}$$

such that one has $\tilde{\Delta}_P = 1/2$ and the dressed critical exponents become

$$\begin{aligned}\widetilde{\beta/d_h\nu} &= \tilde{\Delta}_P = 1/2, \\ \widetilde{\gamma/d_h\nu} &= 1 - 2\tilde{\Delta}_P = 0,\end{aligned}\tag{5.51}$$

implying a merely logarithmic singularity of the staggered polarizability¹⁶. Note, that the dimension $x_P = 2\Delta_P = 1/2$ does *not* appear in the list of scaling dimensions of the primary operators of the Coulomb gas, which are given by [58, 196, 201, 251]

$$x_{e,m} = \frac{1}{2} \left(\frac{e^2}{R^2} + R^2 m^2 \right), \quad e, m = \pm 1, \pm 2, \dots,\tag{5.52}$$

where R denotes the compactification radius and is given by $R = 1/2$ for the square-lattice F model [73], in contrast to $R = 2$ for the two-dimensional XY model [201] (the lowest present vortex operator has $m = \pm 4$, see below). This fact, however, should not be taken too seriously, since it has been observed that the identification of operators of the Gaussian line of fixed points (i.e., the Coulomb gas) and of the corresponding 8-vertex model (resp. its critical version, the 6-vertex model) is a rather delicate task, which cannot be reduced to reading off the dimensions from Eq. (5.52) [252–255]. As far as the application of the KPZ formula for the prediction of the “dressed” exponents is concerned, one should additionally keep in mind that, although the Coulomb gas picture in principle survives the transformation to a random graph model, one has always the possibility of additional differences between the regular and random graph models with respect to the spectrum of operators actually *realized* (i.e., having non-vanishing amplitude)¹⁷. One rather obvious difference between both models is that for the square-lattice case the lowest vortex (or magnetic) operator with non-vanishing amplitude is that with vorticity $m = \pm 4$, corresponding to an insertion of a vertex of type 7 resp. 8. On a random graph, vortices with smaller vorticity can be realized due to the irregularity of the faces [73]. However, this is not important for the considered case of the F model, since there the fugacity of all vortices is strictly zero ($d = 0$).

For a numerical check of the exponents conjectured by the KPZ formula, there are the two principal possibilities of considering the FSS of the staggered polarizability at its maxima for the finite graphs *or* at the fixed asymptotic transition coupling $\beta_c = \ln 2$. While in the asymptotic regime both approaches are expected to lead to

¹⁶In the following we will drop the tilde ($\tilde{}$) from the dressed exponents to improve readability.

¹⁷Note that there are even different opinions about whether the KPZ scheme should be applied at all for the case of the XY model coupled to random lattices, see Refs. [45, 256].

(a)	$N_{2,\min}$	A_χ	$\gamma/d_h\nu$	Q
	256	0.9110(41)	0.7255(7)	0.00
	512	1.0582(78)	0.7048(11)	0.00
	1024	1.238(16)	0.6853(17)	0.00
	2048	1.581(44)	0.6575(32)	0.00
	4096	1.864(87)	0.6395(52)	0.15

(b)	$N_{2,\min}$	A_χ	$\gamma/d_h\nu$	ω	Q
	256	0.1975(97)	0.4749(81)	1.698(55)	0.00
	512	0.116(14)	0.406(16)	2.22(12)	0.00
	1024	0.039(12)	0.281(37)	3.24(30)	0.24
	2048	0.047(37)	0.301(79)	3.07(68)	0.16

Table 5.5: Results of fits of the functional form (5.53) to the simulation data for the peak values of the staggered polarizability of the F model on random ϕ^4 graphs. (a) Fits with the effective correction exponent fixed at $\omega = 0$, i.e., fits without correction term. (b) Fits including ω as an additional fit parameter.

identical results, this is not at all obvious in the presence of large, not completely controlled correction effects for the accessible graph sizes. In both cases, we start from an FSS form including a leading effective correction term as in the square-lattice case, namely,

$$\chi(N_2) = A_\chi N_2^{\gamma/d_h\nu} (\ln N_2)^\omega, \quad (5.53)$$

where $\chi(N_2)$ is taken to be either the peak value as a function of β or the value at $\beta = \beta_c = \ln 2$. We consider the peak value case first, taking the simulation results for the graph sizes quoted in the previous section for the determination of the critical coupling, i.e., $N_2 = 256, \dots, 25000$. Omitting the correction term, i.e., forcing $\omega = 0$, and trying to control the effect of corrections to scaling by successively omitting data points from the small- N_2 side, results in quite poor fits with an exponent estimate $\gamma/d_h\nu \approx 0.7$ steadily decreasing with increasing lower cut-off $N_{2,\min}$, cf. Table 5.5(a). Allowing the effective correction exponent ω to vary, the resulting leading exponent estimate $\gamma/d_h\nu$ is considerably reduced, still showing a tendency to decline as $N_{2,\min}$ increased, cf. Table 5.5(b). However, the fit quality is still not very good and the resulting exponent estimate for, e.g., $N_{2,\min} = 2048$, $\gamma/d_h\nu = 0.301(79)$ is not consistent in terms of the statistical error with the purely logarithmic singularity expected from the KPZ/DDK prediction. Figure 5.16 shows

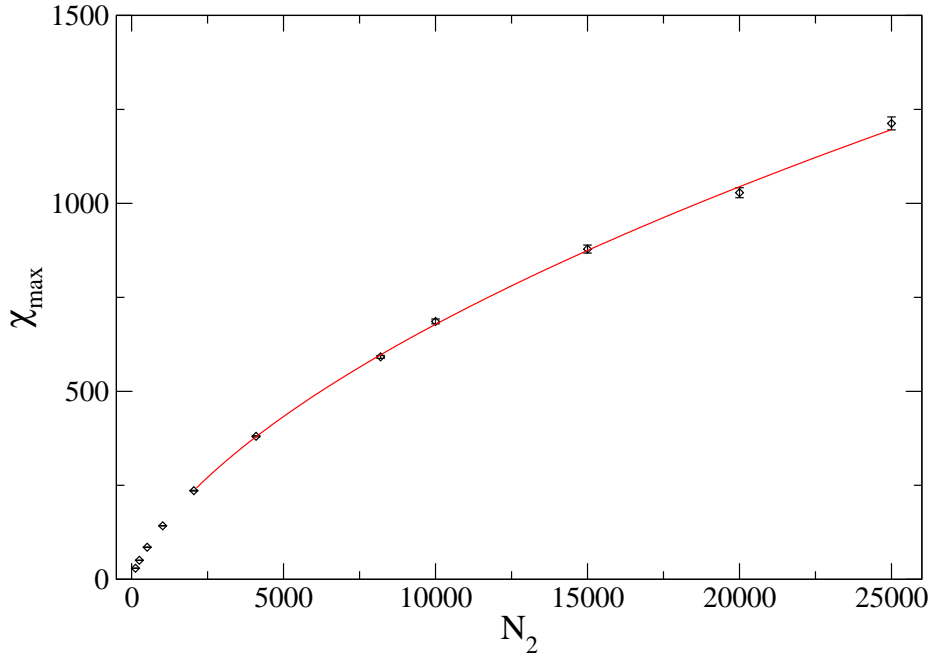


Figure 5.16: FSS of the peak values of the staggered polarizability of the random-graph F model together with a fit to the functional form (5.53) including the points with $N_2 \geq N_{2,\min} = 2048$.

the simulation data for the peak heights together with this last fit.

For the data at fixed coupling $\beta_c = \ln 2$ simulations up to slightly larger graph sizes could be performed since no reweighting analysis is necessary there. Hence, results are available for graph sizes between $N_2 = 256$ and $N_2 = 32\,768$ sites, increasing by powers of two. Again, the functional form (5.53) is fit to the resulting finite-size data for the polarizability at $\beta = \ln 2$. For the constrained fits with $\omega = 0$ we do not find a quality-of-fit of at least 10^{-2} for $N_{2,\min}$ up to 4096 and thus do not consider this form further. The parameters of fits including the logarithmic term are collected in Table 5.6. Note that the fact that the data scale at all cannot in itself be taken as an indirect justification of the claim that $\beta_c = \ln 2$ is the critical coupling since, as mentioned several times, the whole high-temperature phase of the model is critical and thus shows scaling behaviour. As is obvious from Table 5.6, the functional form including a logarithmic correction fits the data rather well already for quite small values of $N_{2,\min}$, leading to exponent estimates $\gamma/d_h\nu$ at least marginally compatible with the conjecture $\gamma/d_h\nu = 0$ in terms of the quoted statistical errors. In fact, if we *assume* a purely logarithmic increase of $\chi(N_2)$, i.e., if we fix $\gamma/d_h\nu = 0$, the data

$N_{2,\min}$	A_χ	$\gamma/d_h\nu$	ω	Q
256	0.491(19)	0.0194(55)	2.117(40)	0.66
512	0.543(42)	0.0304(91)	2.026(72)	0.91
1024	0.569(75)	0.035(14)	1.98(12)	0.85

Table 5.6: Parameters resulting from fits of the functional form (5.53) to the simulation data for the staggered polarizability at $\beta = \beta_c = \ln 2$ of the random-graph F model as a function of the minimum graph size $N_{2,\min}$ included in the fit.

yield good-quality fits for $N_{2,\min} \gtrsim 512$; for $N_{2,\min} = 2048$ the parameters of this purely logarithmic fit are

$$\begin{aligned}
 A_\chi &= 0.3960(96), \\
 \omega &= 2.295(11), \\
 Q &= 0.39.
 \end{aligned}
 \tag{5.54}$$

The simulation data at $\beta = \ln 2$ together with this last fit are shown in Fig. 5.17. Note that for the peak height data discussed before, such a purely logarithmic fit is *not* possible with acceptable values of Q . To enable a somewhat better judgement of the observed discrepancy between the scaling at the peak maxima and at the asymptotic critical coupling for the random graph model, we shortly consider the same two lines for the *square-lattice* model, using a range of lattice sizes comparable to that of the random graph case in terms of the effective linear extents as it has been discussed in the previous section. Fitting the functional form (5.6) to these two data sets, we find $\gamma/d_h\nu = 0.475(46)$ for the scaling at $\beta = \ln 2$ also considered above, but an estimate of $\gamma/d_h\nu = 0.598(36)$ from the scaling of the peak values of χ . Thus, also for the square-lattice model, the scaling of the peak values yields an exponent estimate lying off the expected result ($\gamma/d_h\nu = 1/2$ in this case), while fits at the critical coupling are in good agreement with the expectations. However, this effect is much less pronounced for the regular-lattice model and, in fact, at the given level of accuracy at the verge of statistical significance. This observation, on the other hand, fits well into the general picture drawn in the context of the scaling of the polarizability peak positions above, implying a general enhancement of correction amplitudes on moving from the regular lattice to the random-graph model.

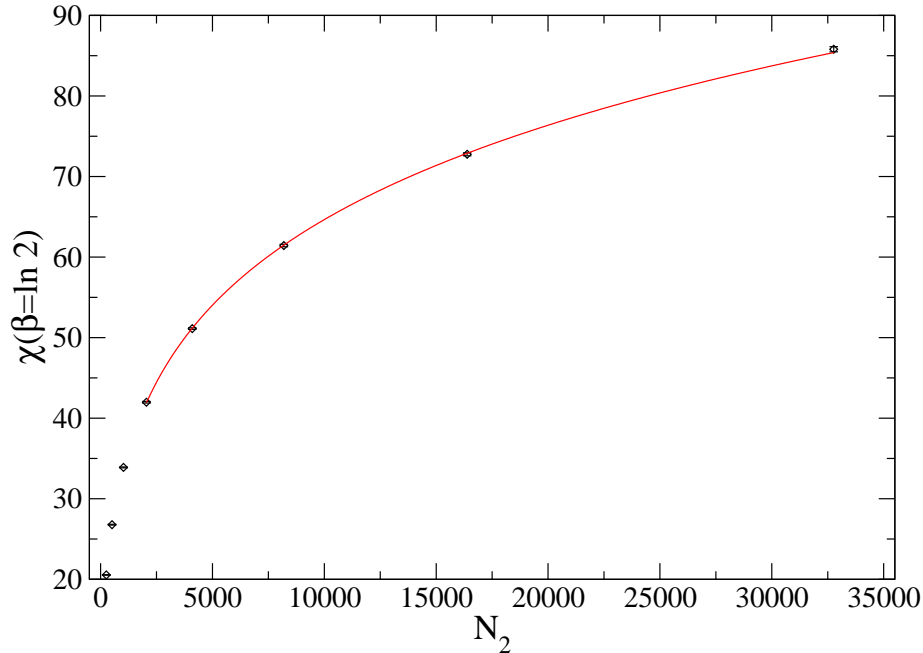


Figure 5.17: Finite-size simulation data of the polarizability of the F model on random ϕ^4 graphs at the asymptotic critical coupling $\beta_c = \ln 2$. The solid curve shows a fit of the form (5.53) to the data, where $\gamma/d_h\nu = 0$ was kept fixed.

FSS of the spontaneous polarization

For the scaling of the spontaneous polarization the situation is found to be very similar to the above discussed case of the polarizability. Hence, we do not present the results in such detail as for the latter observable. We assume the same FSS form as in the square-lattice case, i.e.,

$$P_0(N_2) = A_{P_0} N_2^{-\beta/d_h\nu} (\ln N_2)^\omega, \quad (5.55)$$

where, again, $P_0(N_2)$ is taken to be either the value at the peak position of the polarizability or, alternatively, the result at the asymptotic critical coupling $\beta_c = \ln 2$. Fits without the logarithmic correction term show unacceptable quality throughout the whole region of choices of the cut-off $N_{2,\min}$ and are thus not explicitly presented here. Table 5.7(a) shows the parameters resulting from fits of the functional form (5.55) to the spontaneous polarization at the peak positions of the polarizability. For all choices of $N_{2,\min}$ shown in Table 5.7(a) the quality-of-fit parameter Q assumes values below 10^{-2} . This, however, seems not to be due to a principally bad choice

(a)	$N_{2,\min}$	A_{P_0}	$\beta/d_h\nu$	ω	Q
	256	1.031(17)	0.1378(24)	0.468(17)	0.00
	512	0.850(32)	0.1615(4)	0.653(37)	0.00
	1024	0.681(58)	0.1855(96)	0.853(78)	0.00
	2048	2.15(42)	0.076(20)	0.12(17)	0.00
	4096	1.46(109)	0.064(40)	0.23(37)	0.00

(b)	$N_{2,\min}$	A_{P_0}	$\beta/d_h\nu$	ω	Q
	256	1.583(35)	0.4633(30)	0.726(22)	0.74
	512	1.658(68)	0.4581(50)	0.684(39)	0.91
	1024	1.58(11)	0.4633(79)	0.728(64)	0.98
	2048	1.48(23)	0.469(15)	0.779(134)	1.00

Table 5.7: Parameters resulting from fits of the form (5.55) to the finite-graph spontaneous polarization at (a) the peak position of the staggered polarizability and (b) the infinite-volume critical coupling $\beta_c = \ln 2$.

of the functional form of the fit, but rather is the effect of one or two outliers, which are rather far away from the fitted curve in terms of their statistical error. Apart from pure chance, a plausible explanation for this finding is the presence of systematic reweighting errors (bias) which are much more important for the spontaneous polarization than they were for the polarizability due to the much smaller statistical errors. The situation is illustrated by the plot of such a fit in Fig. 5.18. As far as the results for the exponent $\beta/d_h\nu$ are concerned, as a function of $N_{2,\min}$ we observe two regions corresponding to two different local minima of the χ^2 distribution; the jump between both minima occurs for $N_{2,\min} = 2048$, cf. Table 5.7(a). At least for the minimum corresponding to the smaller values of $N_{2,\min}$, the results for $\beta/d_h\nu$ are slowly increasing as a function of $N_{2,\min}$, but are still far away from the value $\beta/d_h\nu = 1/2$ conjectured within the KPZ/DDK framework discussed above. Again, an analysis of the FSS of the spontaneous polarization at the polarizability peak positions for the square-lattice model reveals a similar behaviour for comparable graph sizes in terms of the effective linear extent, however with the size of the deviations from the expected result being much smaller.

Table 5.7(b) shows the parameters resulting from least-squares fits of Eq. (5.55) to the simulation data at the fixed coupling $\beta = \beta_c = \ln 2$. The overall quality of the fits is much better than for the data at the polarizability peak locations discussed

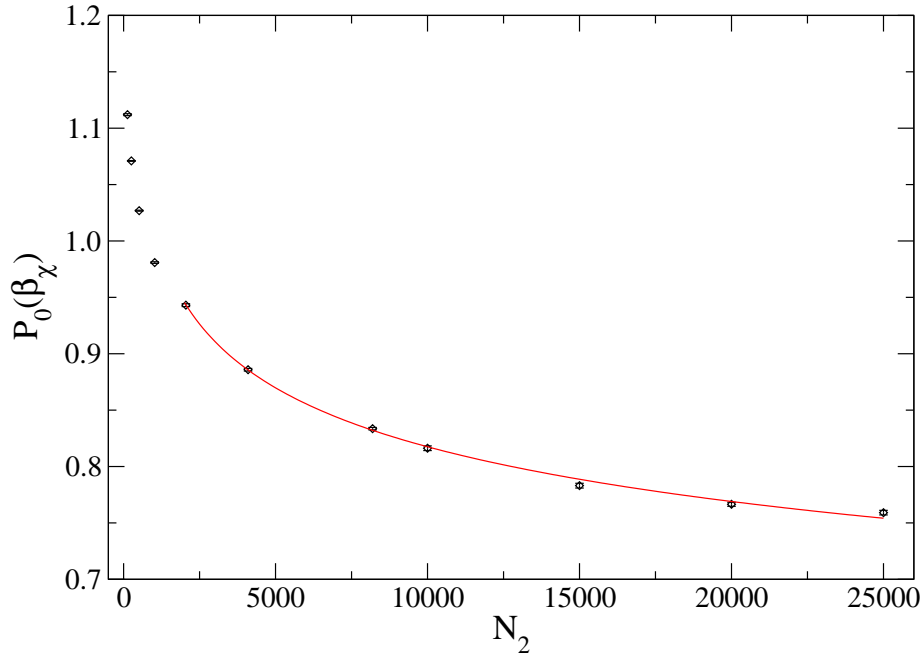


Figure 5.18: Scaling of the finite-size spontaneous polarization of the random-graph F model at the peak locations $\beta_\chi(N_2)$ of the polarizability. The curve shows a fit of the functional form (5.55) to the data, including all graph sizes starting from $N_{2,\min} = 2048$.

before. This is at least partially due to the fact that for the results at fixed coupling no bias effects induced by a reweighting procedure are present since the simulations were performed directly at $\beta = \ln 2$. We do not observe a clear overall drift of the exponent estimate $\beta/d_h\nu$ resulting from the fits as a function of the cut-off $N_{2,\min}$ and the quality-of-fit is found to be exceptionally high already for small values of $N_{2,\min}$, cf. Table 5.7(b). Figure 5.19 shows the simulation data at $\beta = \ln 2$ together with the fit corresponding to $N_{2,\min} = 2048$. The fits yield values for $\beta/d_h\nu$ close to the expected result $\beta/d_h\nu = 1/2$. The result for $N_{2,\min} = 2048$ is consistent with the KPZ/DDK conjecture within about two times the quoted standard deviation.

Thermal scaling

In order to extract information about the critical exponent ρ and possibly to find additional evidence for the location of the critical point, we try to perform a thermal scaling analysis and consider the dependence of the staggered anti-ferroelectric

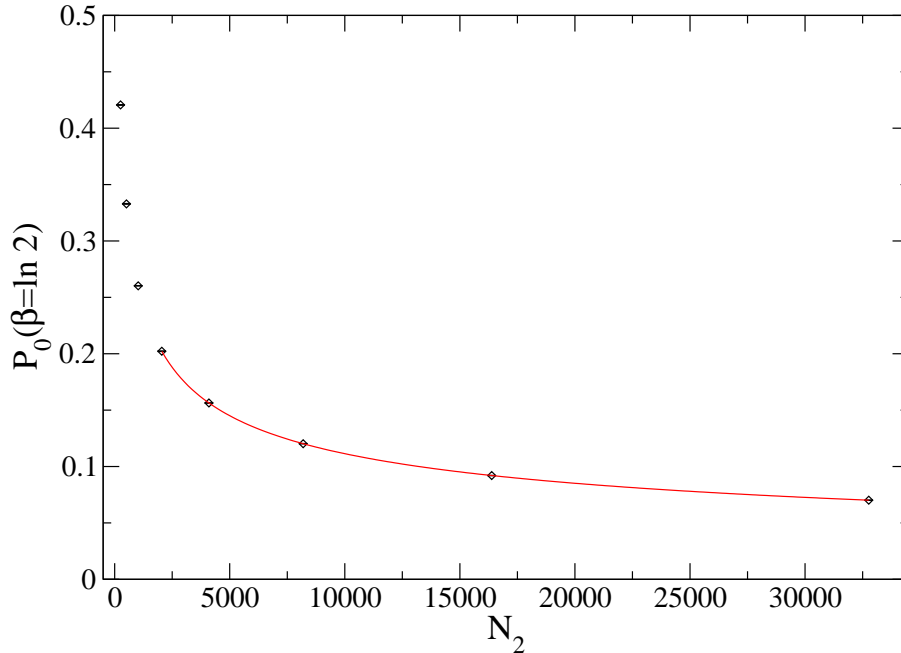


Figure 5.19: Scaling of the spontaneous polarization of the F model on ϕ^4 random graphs at the asymptotic critical coupling $\beta_c = \ln 2$ and a fit of the functional form (5.55) to the data, including graph sizes starting from $N_{2,\min} = 2048$ (solid curve).

polarizability on the inverse temperature β in the vicinity of the critical point. Since the high-temperature phase of the F model coupled to ϕ^4 random graphs is expected to be critical as for the case of the square-lattice F model, such a scaling analysis has to be performed on the low-temperature side of the polarizability peak. Figure 5.20 shows a survey of the thermal and FSS scaling properties of the staggered polarizability of the random graph F model. As for the square-lattice model (cf. Fig. 5.7), we find scaling throughout the high-temperature phase to the left of the peaks. However, the contrast of a non-scaling polarizability in the low-temperature phase cannot be demonstrated here as easily as for the regular lattice model. Due to the exponential slowing down of the link-flip and minBU surgery dynamics of the ϕ^4 graphs above β_c to be discussed in Section 5.3 below, simulations cannot proceed arbitrarily deep into the ordered phase. Comparing the regions to the right of the peaks of Figs. 5.7 and 5.20, we see that the finite-size effects in the low-temperature phase are extremely strong for the random graph model, much stronger than for the square-lattice case. Thus, up to the inverse temperature $\beta = 1.4$ shown in Fig. 5.20, there is no sign of a convergence of the curves for different lattice sizes as it is

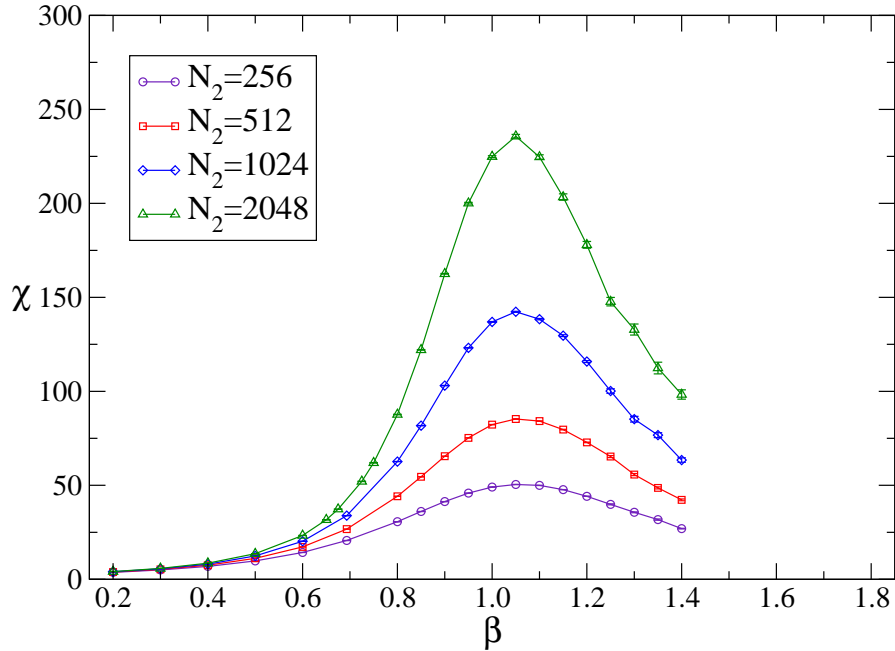


Figure 5.20: Scaling of the polarizability peaks of the F model on planar ϕ^4 random graphs from Monte Carlo simulations. The lines are drawn for illustrative purposes only.

already found for $\beta \approx 0.8$ in Fig. 5.7. This effect is, again, attributed to the relative smallness of the linear extents of the random graphs as compared to those of the square lattice.

The requirements of a proper thermal scaling analysis of the polarizability resulting from these observations are almost impossible to fulfil: one has to keep enough distance from the critical point for the linear extent of the graph to be large compared to the correlation length of the matter part to keep finite-size effects under control and, on the other hand, one should not proceed too deep into the ordered phase such as not to leave the thermal scaling region in the vicinity of the critical point. Thus, one would have to go to huge graph sizes to get rid of these constraints to a practically acceptable extent. Nevertheless, we attempt a thermal scaling analysis of the polarizability from simulations of graphs of size $N_2 = 30\,000$ with inverse temperatures ranging from $\beta = 0.9$ up to $\beta = 1.6$ taking about 800 000 measurements at each β . The expected scaling form is given by Eq. (5.35), i.e.,

$$\ln \chi(\beta) \sim A_\chi + B_\chi(\beta - \beta_c)^{-\rho}, \quad (5.56)$$

which should hold for $\beta \rightarrow \beta_c^+$ as $N_2 \rightarrow \infty$ and where logarithmic corrections have already been omitted. We find it impossible to reliably fit all four of the parameters involved in Eq. (5.56) to the available data. Varying the starting values we find a multitude of local minima of the χ^2 distribution, such that virtually any result can be “found” for β_c and ρ in this way. Fixing one or the other of both parameters at the expected values $\beta_c = \ln 2$ resp. $\rho = 1/2$, the fits become more stable. The dependency on the range of included values of β is found to be rather small and for $\beta \geq 1.25$ we arrive at the following fit parameters,

$$\begin{aligned} A_\chi &= -101(4662), \\ B_\chi &= 106(4662), \\ \rho &= 0.02(103), \\ Q &= 0.03, \end{aligned} \tag{5.57}$$

for β_c fixed at $\ln 2$ resp.

$$\begin{aligned} A_\chi &= -86(1083), \\ B_\chi &= 324(5744), \\ \beta_c &= -11(147), \\ Q &= 0.04, \end{aligned} \tag{5.58}$$

with ρ fixed at $1/2$. Obviously both fits are not very useful, such that we are finally forced to fix both parameters at their expected values to find,

$$\begin{aligned} A_\chi &= 0.91(41), \\ B_\chi &= 4.20(33), \\ Q &= 0.03. \end{aligned} \tag{5.59}$$

This fit is shown in Fig. 5.21 together with the simulation data. Thus, the best we can conclude about the thermal scaling behaviour of the polarizability of the F model coupled to ϕ^4 random graphs is that there is no obvious contradiction with the expectations concerning the parameters β_c and ρ . However, in view of the fact that already for the regular lattice model thermal scaling fits were not at all easily possible, this finding is probably not a too astonishing one.

Long-range order

To complete the picture, we try to visualize graphically how the anti-ferroelectric order parameter, i.e., the staggered polarization, changes on passing from the disordered high-temperature to the ordered low-temperature phase. For this purpose

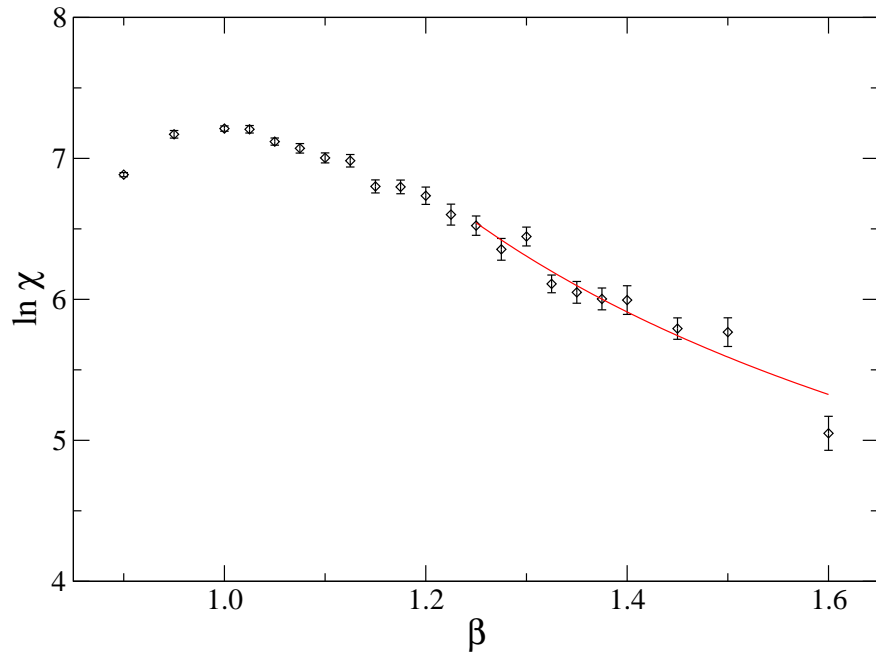


Figure 5.21: Thermal scaling of the polarizability of the random graph F model for graphs with $N_2 = 30\,000$ sites. The curve shows a fit of the function (5.56) to the data, where $\beta_c = \ln 2$ and $\rho = 1/2$ have been kept fixed.

we use the graph embedding and 3D visualization scheme described in Appendix B, which yields 3D computer graphics of an embedding of the dynamical polygonifications into three-dimensional Euclidean space without edge crossings. For the case of ϕ^4 graphs and the corresponding quadrangulations considered here, the square faces are divided into two triangular parts for technical reasons. To visualize the local value of the order parameter we use the “plaquette spin” representation defined in Section 4.3.2, where to each face of the ϕ^4 graph a scalar variable is attributed, which represents the integral over the arrow directions around the face with respect to the reference direction defined by the two-colouring of the faces of the graph. In the language of polygonifications this corresponds to scalar “spin” variables residing on the *sites* of the quadrangulation. These variables we symbolize with colours, positive “spins” being drawn in red and negative “spins” in blue. The faces of the quadrangulations are filled with colour gradients interpolating between the colours of the quadrangulation sites. In this way a smooth impression of the local behaviour of the order parameter can be created.

Figures 5.22 and 5.23 show the outcome of such a visualization attempt starting

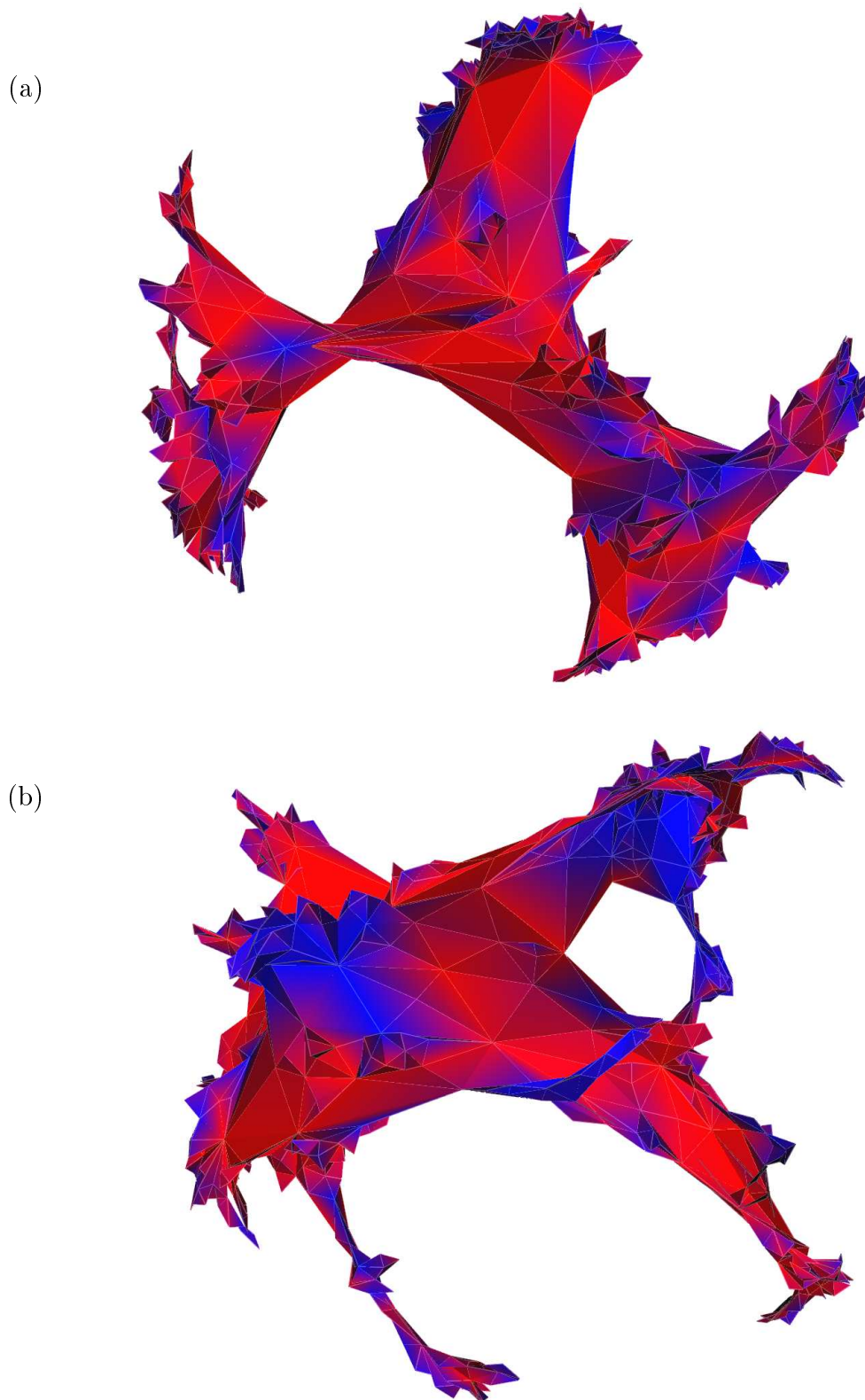


Figure 5.22: Configuration snapshots of the F model coupled to ϕ^4 random graphs at $\beta = 0.4$ (a) and $\beta = 0.75$ (b). Depicted is the dual quadrangulation with each square face divided into two triangles. Red and blue regions denote positive and negative values of the “plaquette spins” defined in Section 4.3.2.

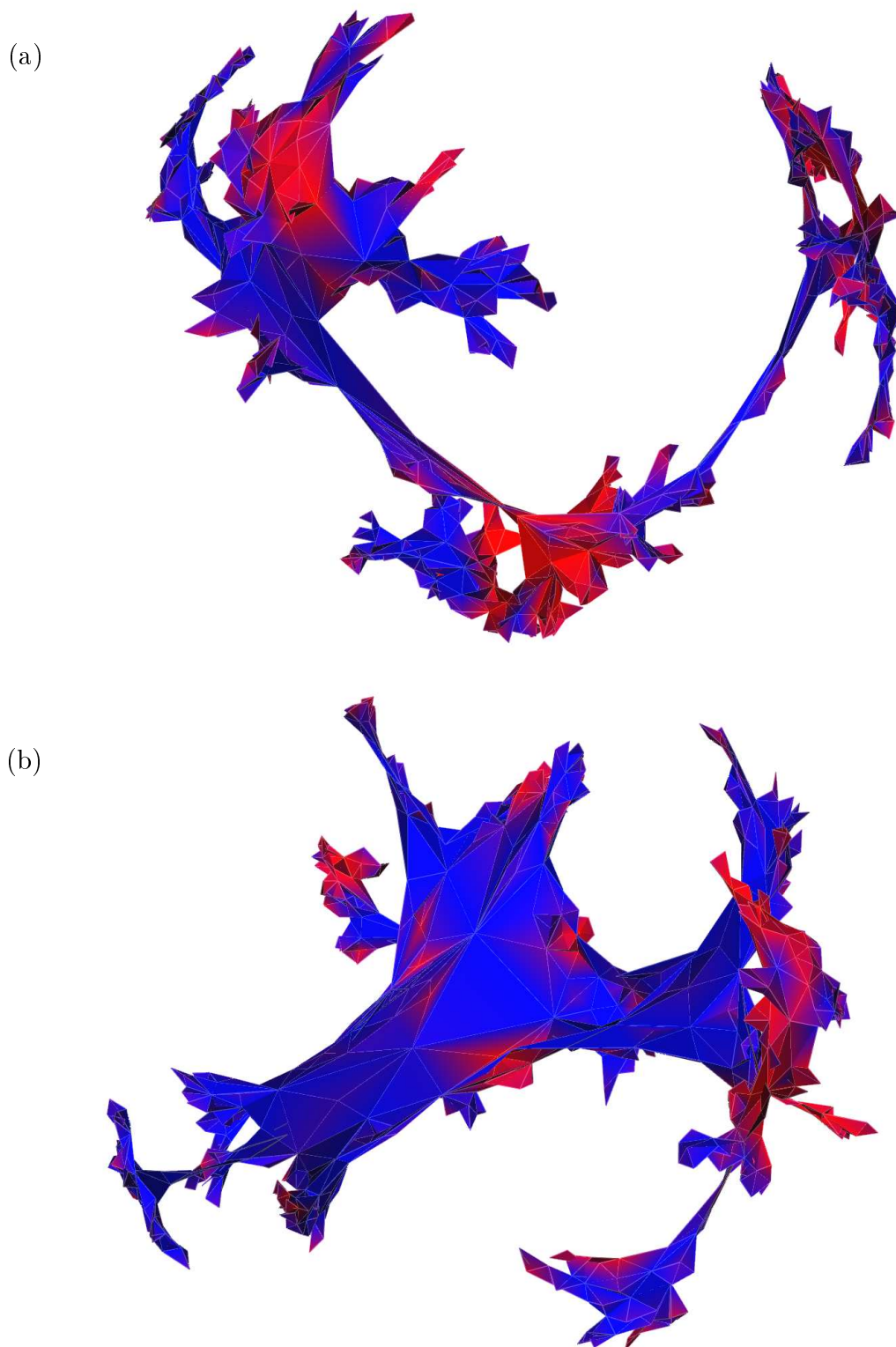


Figure 5.23: Configuration snapshots of the F model coupled to ϕ^4 random graphs at $\beta = 0.8$ (a) and $\beta = 0.9$ (b). Depicted is the dual quadrangulation with each square face divided into two triangles. Red and blue regions denote positive and negative values of the “plaquette spins” defined in Section 4.3.2.

from ϕ^4 graphs with $N_2 = 1000$ sites. Figure 5.22 shows configuration snapshots of the high-temperature phase and the vicinity of the critical point $\beta_c = \ln 2$, whereas Fig. 5.23 represents configurations for inverse temperatures, which in the thermodynamic limit belong to the low-temperature phase. Obviously, as the temperature is decreased from the high-temperature phase, the snapshots show the expected ordering behaviour with patches of equal “spin” orientations of all sizes around the critical point and a clear long-range ordering in the low-temperature phase. Note that the presented snapshots also give a good impression of the overall variation of the extent and fractal structure of the graphs during the link-flip and surgery updating process, which to most of the extent visible from Figs. 5.22 and 5.23 is independent from the variation of the inverse temperature β and would be seen for different snapshots at the same temperature in quite the same way.

5.3 Dynamical Scaling and Autocorrelation Times

The dynamical behaviour of the graph-update dynamics for the case of pure Euclidean quantum gravity has been studied in Section 3.5. For the two cases of the purely local (one- and two) link-flip update and the combined dynamics of link-flip and minBU surgery moves the dynamical critical exponents $z_{\langle r^2 \rangle} / d_h$ belonging to the integrated autocorrelation time of the mean square extent have been determined. Coupling a spin model to the dynamical graphs introduces an additional type of updates related to the matter variables (i.e., the loop algorithm for the case of the vertex model). Since both types of variables fluctuate on the same time scale (annealed disorder), the coupling of the geometry and matter subsystems naturally induces changes in the dynamical behaviour of both kinds of observables, those related to geometry (such as the mean square extent) and those referring to the matter degrees of freedom (such as the energy and polarization of the vertex model).

In this section, dynamical scaling analyses will be presented for the purely local and the combined link-flip/surgery updating schemes at the asymptotic critical coupling $\beta_c = \ln 2$ of the model. An analysis of the behaviour at the pseudo-critical points of systems of finite size is not easily possible since the reweighting scheme does not properly transform the autocorrelations of the involved time series. This is obvious from the fact that these temporal correlations are not themselves described by the Boltzmann distribution of the model, which only covers the static, equilibrium properties of the system. Additionally, some attention will be paid to the dynamical

behaviour of the considered updates beyond the KT point in the high- and low-temperature phases.

5.3.1 Local update

As has been mentioned above in Section 3.5, the mean square extent of the random graphs is generically found to constitute the slowest mode of relaxation of the geometric sector of the theory. Thus, for the geometric part we again concentrate on this observable, defined as described in Section 3.5.1. Among the observables of the coupled F model we consider the internal energy of Eq. (4.1) and the staggered anti-ferroelectric polarization defined by (4.39) resp. (4.40). For the determination of the dynamical critical exponent $z_{\mathcal{O}}/d_h \equiv z_{\text{int},\mathcal{O}}/d_h$ of the observable \mathcal{O} the following functional form is fitted to the the finite-size results,

$$\tau_{\text{int}}(\mathcal{O}) = A_{\mathcal{O}} N_2^{z_{\mathcal{O}}/d_h}, \quad (5.60)$$

i.e., no correction terms are taken into account in this exploratory study. From the usual universality arguments, the exponents $z_{\mathcal{O}}/d_h$ are not expected to depend on the ensemble of graphs considered. On the other hand, in contrast to the case of dynamical exponents associated to the *exponential* autocorrelation times, $z_{\mathcal{O}}/d_h$ in general can depend on the considered observable \mathcal{O} [169]. As for the case of the pure polygonifications model, local (one- and two-) link-flip simulations were performed for graph sizes N_2 between 64 and 4096 sites, where the number of measurements was increased with N_2 , ranging between 50 000 and 300 000 samples. As for all simulations of random graph models presented in this thesis, measurements were taken every ten sweeps of the respective graph update under consideration. The loop-cluster update of the vertex model part, on the other hand, was performed only once per measurement, since the dynamics of the loop-cluster update is found to be much faster than that of the graph-related updates.

Table 5.8 shows the integrated autocorrelation times $\tau_{\text{int}}(r^2)$ corresponding to the mean square extent of graphs of the strict, regular and restricted singular ensembles coupled to the F model. The simulations were performed at the asymptotic critical coupling $\beta_c = \ln 2$. Simulations for the singular ensemble have not been performed due to the computational inefficiency of the update for this ensemble, which has been mentioned several times. As for the case of pure dynamical polygonifications analyzed in Section 3.5.1, we find clearly larger autocorrelation times for graphs of

N_2	strict	regular	restr. sing.
64	3.78(76)	2.03(56)	2.96(64)
128	6.40(135)	4.32(120)	4.44(60)
256	8.86(59)	6.34(87)	7.51(75)
512	14.6(17)	10.3(11)	12.04(90)
1024	24.8(34)	17.7(16)	18.0(11)
2048	38.8(64)	27.6(34)	29.5(39)
4096	58.7(73)	47.6(61)	44.8(56)

Table 5.8: Critical integrated autocorrelation times $\tau_{\text{int}}(r^2)$ of the mean square extent $\langle r^2 \rangle$ for the local link-flip dynamics of planar random ϕ^4 graphs of the strict, regular and restricted singular ensembles coupled to the F model. The autocorrelation times are given in units of ten sweeps of flip moves. They were evaluated using the direct integration method for the normalized autocorrelation function described in Appendix A.4. The results from the combined binning/jackknife technique agree with those quoted within the estimated statistical errors.

the strict ensemble than for graphs of the other two ensembles, but no dramatic difference between the regular and restricted singular cases. Also, independent from the considered ensemble, coupling the vertex model to the random graphs strongly increases the autocorrelations between successive measurements of the mean square extent, indicating a strong reaction of the coupled matter back onto the graph geometry, cf. Table 3.2 and Fig. 5.24. On the configuration level, these enlargement of autocorrelation times can be traced back to the ice-rule restriction of the vertex model, which leads to a strong reduction of the flip-move acceptance rate. Figure 5.25 shows FSS plots of the autocorrelation times of the mean square extent for the strict, regular and restricted singular ensembles. For the fits of the power-law form (5.60) to the data, the graph sizes $N_2 = 64$ and $N_2 = 128$ were omitted since there clear deviations from linearity can be recognized from the logarithmic plots of Fig. 5.25. For graphs of the *strict* ensemble we find,

$$\begin{aligned}
 A_{r^2} &= 0.194(56), \\
 z_{r^2}/d_h &= 0.691(45), \\
 Q &= 0.95.
 \end{aligned}
 \tag{5.61}$$

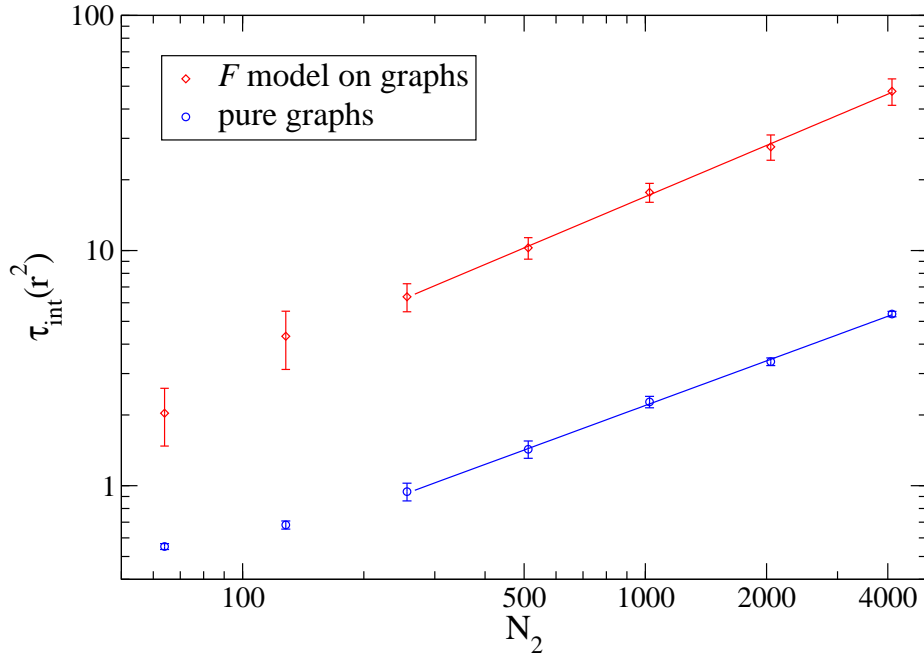


Figure 5.24: Comparison of the critical integrated autocorrelation times $\tau_{\text{int}}(r^2)$ of (one- and two-) link-flip simulations of pure ϕ^4 random graphs of the regular ensemble and the same graphs coupled to the F model. The times are given in units of ten sweeps of link flips. The lines show fits of the functional form (5.60) to the data.

The case of *regular* graphs yields the following fit parameters,

$$\begin{aligned} A_{r^2} &= 0.114(46), \\ z_{r^2}/d_h &= 0.724(58), \\ Q &= 0.98, \end{aligned} \tag{5.62}$$

whereas for the *restricted singular* ensemble of graphs we arrive at

$$\begin{aligned} A_{r^2} &= 0.218(73), \\ z_{r^2}/d_h &= 0.640(50), \\ Q &= 0.97. \end{aligned} \tag{5.63}$$

Obviously, the dynamical critical exponents found for the different graph ensembles are statistically consistent with each other as expected from universality, cf. Section 3.5. Comparing these results to the fit parameters found in Section 3.5.1 for the pure polygonifications model, we find an overall increase of z_{r^2}/d_h from $z_{r^2}/d_h \approx 0.6$

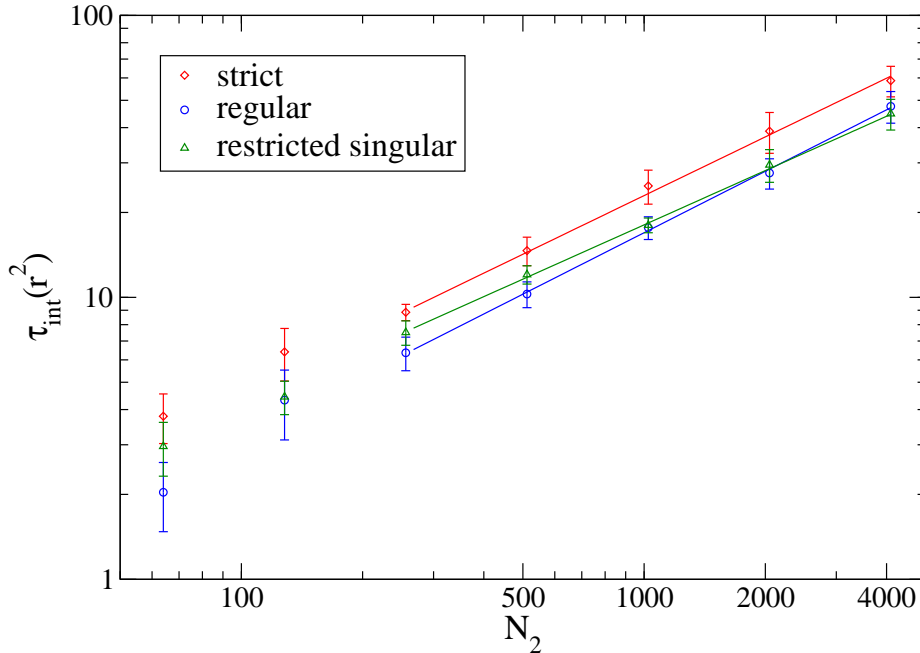


Figure 5.25: Critical integrated autocorrelation times $\tau_{\text{int}}(r^2)$ of the mean square extent of local (one- and two-) link-flip simulations of ϕ^4 random graphs of the strict, regular and restricted singular ensembles coupled to the F model. The autocorrelation times are given in units of ten sweeps of link flips. The solid lines show fits of the power-law form (5.60) to the data.

to $z_{r^2}/d_h \approx 0.7$, reflecting the effect of the ice-rule restriction of the vertex model on the link-flip graph dynamics.

As far as the autocorrelations of the matter-related observables are concerned, we find almost no size dependence of $\tau_{\text{int}}(E)$, i.e., the integrated autocorrelation time associated with the internal energy of the vertex model. This is illustrated in Fig. 5.26, which also shows that the values for $\tau_{\text{int}}(E)$ are only very slightly above the theoretical minimum of $1/2$, cf. Eq. (A.16). The same effect has been observed for simulations of the F model on the square lattice via the loop algorithm and other cluster algorithms, cf. Refs. [174, 257]. There, this effect is attributed to the sub-lattice structure of the anti-ferroelectric model. For the square lattice, one can easily define sub-lattice energies associated with the vertex configurations on the two square sub-lattices. These are found to exhibit temporal correlations for different considered updates, however with a strong *anti*-correlation between the two sub-lattice energies induced by the ice-rule constraint [174, 257]. Thus, for the total

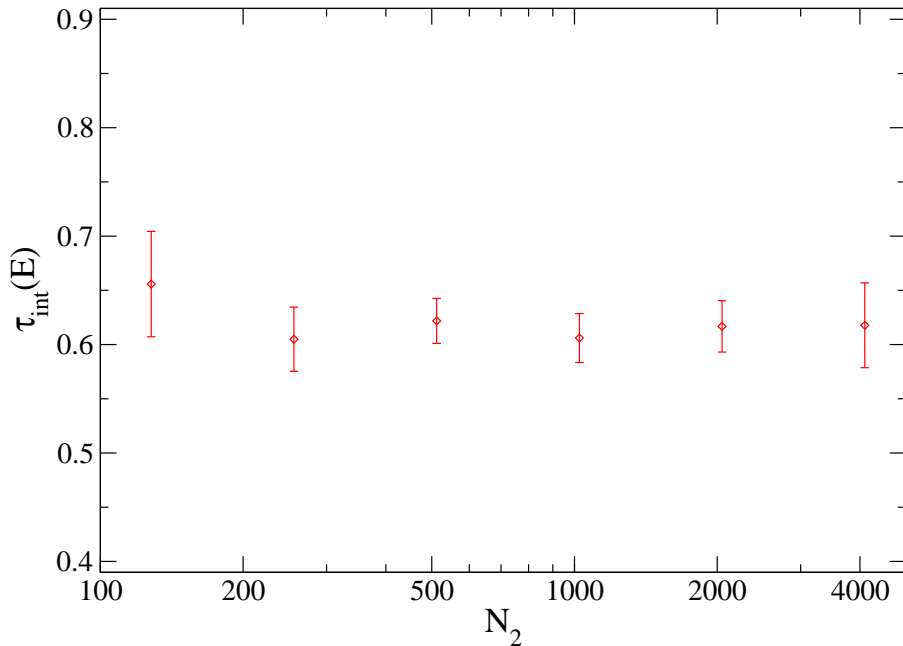


Figure 5.26: FSS plot of the critical integrated autocorrelation times $\tau_{\text{int}}(E)$ of the internal energy of local link-flip simulations of ϕ^4 random graphs of the regular ensemble coupled to the F model. The autocorrelation times are given in units of ten sweeps of link flips.

energy significant temporal correlations are expected to show up only for extremely large lattices. For the case of ϕ^4 random graphs, on the other hand, sub-lattice energies cannot be easily defined since the graphs are not bipartite (although their duals are). Hence, we do not further consider the energy-related observables here, but concentrate on the spontaneous staggered polarization P_0 . Figure 5.27 depicts the FSS of the integrated autocorrelation times $\tau_{\text{int}}(P_0)$ at $\beta = \beta_c = \ln 2$ for graphs of the strict, regular and restricted singular ensembles. Fits of the power-law form (5.60) to the finite-size data yield the following parameters,

$$\begin{aligned}
 A_{P_0} &= 0.295(54), \\
 z_{P_0}/d_h &= 0.190(28), \\
 Q &= 0.86,
 \end{aligned}
 \tag{5.64}$$

for graphs of the *strict ensemble*,

$$\begin{aligned}
 A_{P_0} &= 0.320(58), \\
 z_{P_0}/d_h &= 0.155(27), \\
 Q &= 0.88,
 \end{aligned}
 \tag{5.65}$$

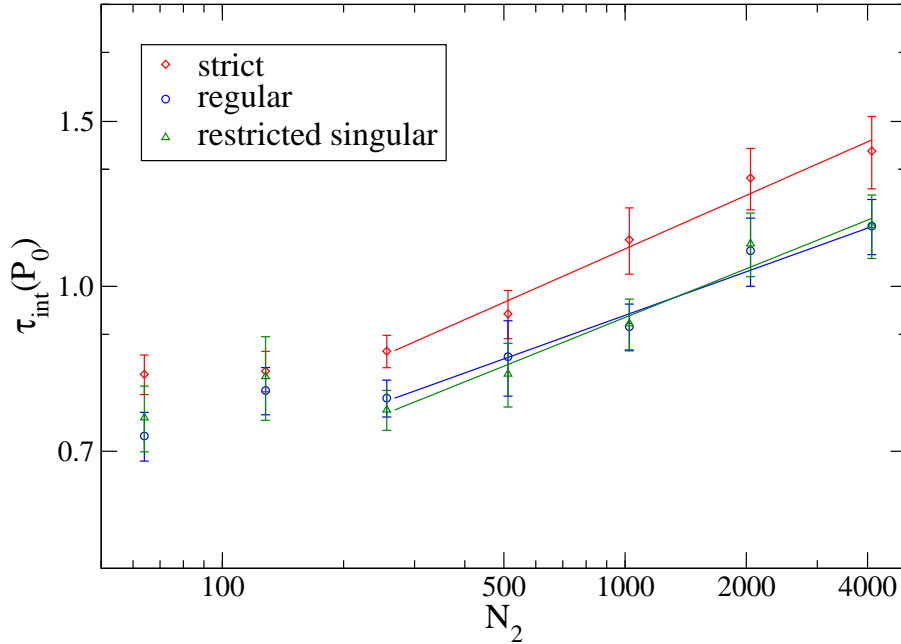


Figure 5.27: Finite-size scaling of the critical integrated autocorrelation times of the spontaneous staggered polarization of the F model on planar ϕ^4 random graphs of the strict, regular and restricted singular ensembles from MC simulations with the local link-flip dynamics. The solid lines show power-law fits according to Eq. (5.60) to the data.

for the case of the *regular* ensemble and

$$\begin{aligned}
 A_{P_0} &= 0.281(55), \\
 z_{P_0}/d_h &= 0.173(29), \\
 Q &= 0.85,
 \end{aligned}
 \tag{5.66}$$

for simulations in the *restricted singular* ensemble. Here, the points corresponding to $N_2 = 64$ and $N_2 = 128$ have been omitted from the fits to accommodate for their apparent deviation from linearity (in the log-log plot). Again, the estimates of z_{P_0}/d_h are consistent between the different graph ensembles, the remaining deviations indicating the size of the corrections to the leading scaling behaviour. Comparing z_{P_0}/d_h to the exponent z_{r^2}/d_h found for the mean square extent, however, we find a large disagreement of the dynamical exponents associated with both types of variables, which is, however, not unexpected for dynamical critical exponents defined from *integrated* autocorrelation times, see the discussion above in Section 3.5.1.

An overview of autocorrelation times off the critical point is given in Fig. 5.28, where a temperature scan of $\tau_{\text{int}}(r^2)$, $\tau_{\text{int}}(E)$ and $\tau_{\text{int}}(P_0)$ is shown for the case of regular graphs. For all of the high-temperature regime $\beta < \beta_c = \ln 2$ we expect scaling since the corresponding phase is critical. The absolute values of the autocorrelation times of the matter-related observables, however, decrease largely as one moves further into the disordered phase, such that for the practical purposes considered here autocorrelations become less and less important in this regime. For $\beta > \ln 2$, on the other hand, we find a systematic increase of autocorrelation times of differing intensity. The autocorrelations of the mean square extent increase only quite slowly (albeit starting from a high level) and $\tau_{\text{int}}(E)$ starts to significantly exceed its trivial value $\approx 1/2$ as β is increased above β_c . On the other hand, $\tau_{\text{int}}(P_0)$ explodes exponentially above $\beta = \ln 2$ (mind the logarithmic scale of the abscissa in Fig. 5.28). This reflects the ergodicity breaking of the dynamics between the two antiferroelectrically ordered states in the low-temperature phase of the model. Once again, on the configuration level it is obvious how the dynamical properties of the vertex model part act back onto the graph dynamics: to the extent that vertices of types a and b disappear from the configurations due to the suppression of their Boltzmann weights as β is increased above β_c , the acceptance rate of the link-flip moves is reduced, thus slowing down the relaxation of, e.g., the mean square extent. In fact, it is easy to see that the acceptance rate of the link-flip moves vanishes as $\beta \rightarrow 0$.

5.3.2 Surgery update

The combined link-flip and minBU surgery dynamics utilized for the main part of the F model simulations has only been implemented for the case of the *regular* ensemble of ϕ^4 graphs, cf. Section 3.5.2. For all simulations presented, link-flip and surgery updates were mixed at a ratio of three to one, such that a sweep now denotes $N_2/4$ attempted surgery moves and $3N_2/4$ one- and two-link flip updates. Again, loop-cluster updates of the vertex model part were performed only once per measurement due to the much higher efficiency of this cluster update as compared to the graph update. For the determination of autocorrelation times, simulations at $\beta = \beta_c = \ln 2$ were performed for graphs between $N_2 = 64$ and $N_2 = 8192$ sites, taking between 50 000 and 300 000 measurements after equilibration and increasing the length of the time series with the number of sites. As for the local update, the

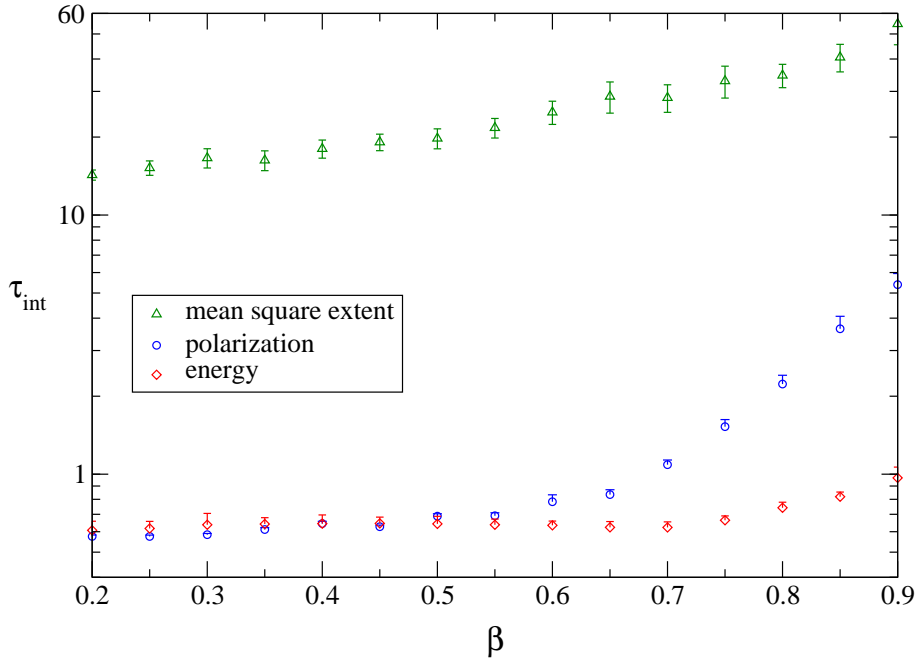


Figure 5.28: Temperature scan of the integrated autocorrelation times of the internal energy, the spontaneous staggered polarization and the mean square extent of link-flip simulations of the F model on ϕ^4 random graphs of the regular ensemble. The presented data correspond to graphs with $N_2 = 2048$ sites. Note the logarithmic scale of the abscissa.

simple power-law form (5.60) was fitted to the finite-size data in order to extract the dynamical critical exponents.

Figure 5.29 shows the autocorrelation times for the mean square extent of the graphs as compared to the results for the purely local link-flip update. From the power-law fit (5.60) to the data, again omitting the results for $N_2 = 64$ and $N_2 = 128$, we find the parameters

$$\begin{aligned}
 A_{r^2} &= 0.0097(24), \\
 z_{r^2}/d_h &= 0.863(33), \\
 Q &= 0.86.
 \end{aligned}
 \tag{5.67}$$

Thus, in agreement with the case of pure graphs considered in Section 3.5.2, compared to the purely local update we find a considerable reduction in the overall size of autocorrelations and thus the scaling amplitude, but *no* reduction of the dynamical critical exponent z_{r^2}/d_h . Instead, the exponent found for the global update marginally agrees with that found for the local update above, with a tendency to

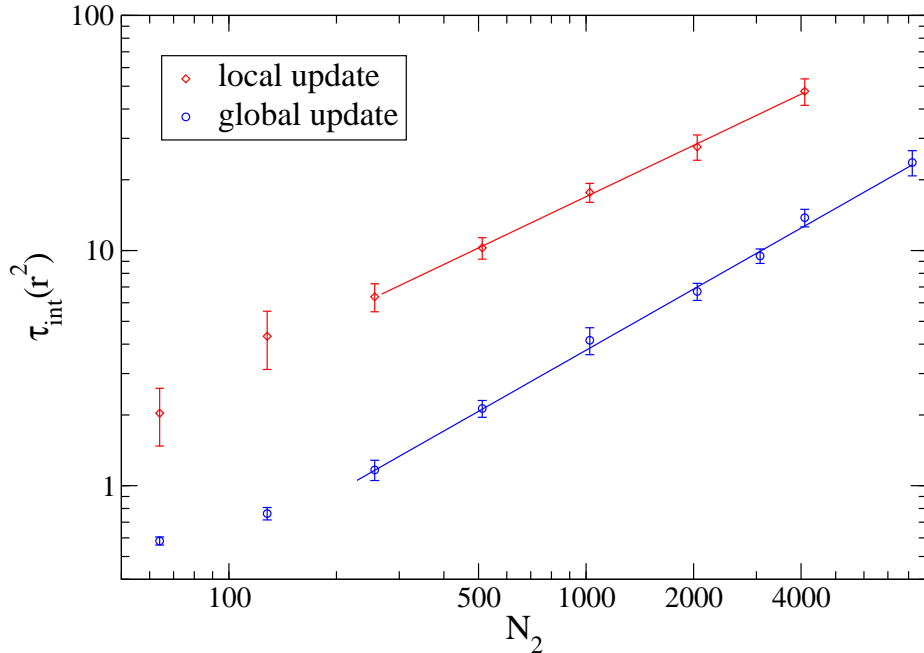


Figure 5.29: Autocorrelation times $\tau_{\text{int}}(r^2)$ at $\beta = \ln 2$ of the mean square extent of ϕ^4 random graphs coupled to the F model resulting from simulations utilizing the combined, “global” link-flip and surgery move dynamics. The results for the purely local link-flip update are shown for comparison. The lines show fits of the power-law Eq. (5.60) to the data. The times are given in units of ten sweeps of graph updates.

be even larger. This last fact, however, only hints at the size of the present systematic errors (i.e., corrections to scaling), since obviously the additional application of surgery moves can asymptotically only decrease the value of z/d_h or leave it constant. As a rule of thumb for the considered graph sizes, at $\beta_c = \ln 2$ the combined link-flip and surgery update reduces the autocorrelation time of the mean square extent to about a fifth of the value for the purely local update¹⁸.

Considering the matter-related observables, the energy is again found to lack any sign of critical slowing down at $\beta = \ln 2$. The integrated autocorrelation times of the spontaneous polarization are collected in Table 5.9 in comparison to those of the local update simulations for the case of regular graphs. This comparison is additionally illustrated by the FSS plot of Fig. 5.30. The power-law fit (5.60) applied

¹⁸Note, however, that the local link-flip dynamics is about three times faster than the combined “global” update in terms of computer time.

N_2	local	global
64	0.692(41)	0.605(14)
128	0.774(45)	0.631(15)
256	0.760(34)	0.652(23)
512	0.841(77)	0.666(17)
1024	0.905(52)	0.687(22)
2048	1.091(91)	0.762(36)
4096	1.160(78)	0.901(47)
8192		1.050(58)

Table 5.9: Integrated autocorrelation times of the spontaneous staggered polarization of the random graph F model from “local” simulations (link-flip moves only) and from “global” simulations (combined link-flip and surgery move dynamics) at $\beta = \beta_c = \ln 2$. The times are given in units of ten sweeps of link-flip or combined link-flip/surgery moves. Both types of simulations were restricted to the regular ensemble of graphs.

to the range $N_2 = 512, \dots, 8192$ yields the following fit parameters,

$$\begin{aligned}
 A_{P_0} &= 0.249(31), \\
 z_{P_0}/d_h &= 0.153(17), \\
 Q &= 0.27.
 \end{aligned}
 \tag{5.68}$$

Again comparing to the result for the purely local dynamics discussed in the previous section, we find no significant change of the dynamical critical exponent. In fact, the measured autocorrelation times at $\beta = \ln 2$ are still so close to the lower bound of $1/2$ that even in the amplitude no differences between the two updates can be detected¹⁹. However, considering the exponential increase of $\tau_{\text{int}}(P_0)$ above $\beta = \ln 2$, we find an appreciable reduction of autocorrelations by the application of the combined link-flip and surgery update, cf. Fig. 5.31. For the shown example of $N_2 = 4096$, the autocorrelation times for the purely local update are about four times larger than those for the combined, global dynamics. This is of some importance since, as has been discussed above in Section 5.2.3, most of the FSS analysis of the static critical behaviour had to be performed in the region $\beta > \ln 2$ where the finite-size peaks of the staggered polarizability are located. For the mean square extent above β_c a similar situation is found.

¹⁹Recall the fact that all autocorrelation times have been measured in units of ten sweeps of update moves.

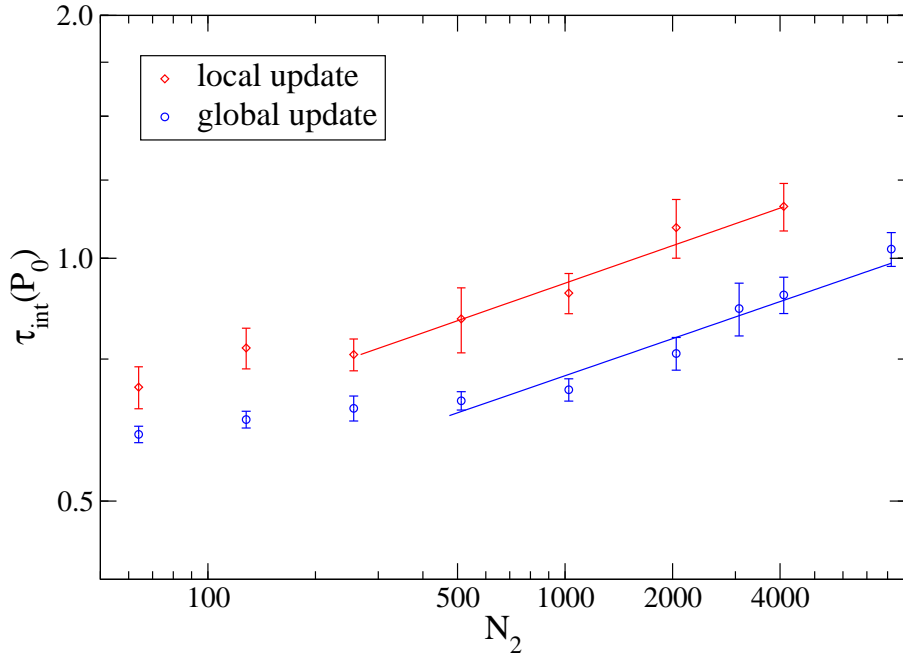


Figure 5.30: Comparison of the FSS of the critical integrated autocorrelation times of the spontaneous polarization of the random graph F model from local update and global update simulations. The solid lines denote fits of the form (5.60) to the data.

5.4 Geometrical Properties

The annealed nature of disorder applied to the vertex model via its placement onto dynamical ϕ^4 random graphs induces a back-reaction of the matter variables onto the underlying geometry and thus a possible change in the (local and global) geometrical properties of the graphs. Since the general mechanism of matter back-reaction onto the graphs is the tendency to minimize interfaces between pure-phase regions of the matter variables, a “strong” coupling between matter and graph variables is only expected if the combined system of spin model and underlying geometry is critical, i.e., when clusters of ordered configurations exist on all length scales. Thus, one expects the universal graph properties such as the graph-related critical exponents to remain at the values of pure Euclidean quantum gravity, unless the coupled matter system has a diverging correlation length, see, e.g., Ref. [258].

From the graph properties discussed in Chapters 2 and 3, we consider the coordination number distribution as a typical local property as well as the string

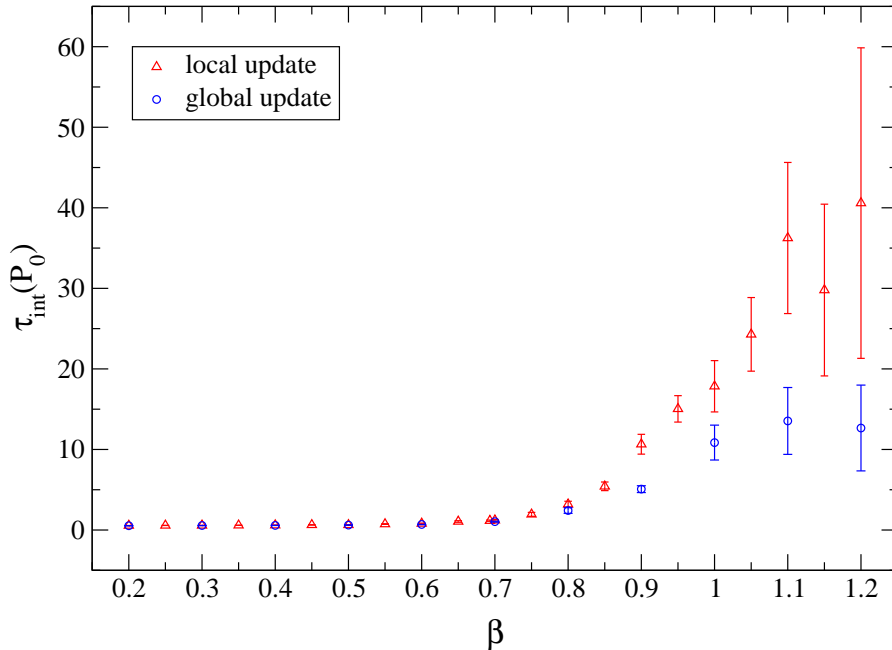


Figure 5.31: Temperature dependence of the integrated autocorrelation times of the spontaneous staggered polarization of the random graph F model from simulations utilizing the link-flip only (“local”) and the combined link-flip and surgery move (“global”) update. The data points correspond to a graph size of $N_2 = 4096$ sites.

susceptibility exponent describing the tendency of the area of the graphs to diverge in the grand-canonical ensemble and the fractal or Hausdorff dimension as global geometrical properties. As for the analysis of the KT transition in Section 5.2.3 above, we return to exclusively using graphs of the regular ensemble.

5.4.1 The co-ordination number distribution

The distribution of ring lengths of the random graphs or, equivalently, the co-ordination number distribution of the dual polygonifications has been rather extensively studied for the case of pure Euclidean quantum gravity in Chapter 3. When coupling matter to the graphs, it is obvious that the back-reactions of the matter variables on the graphs in principle are able to alter this local graph characteristic. Especially, for the case of the vertex model considered here, the ice-rule forbids certain link-flip update moves and thus potentially changes the distribution $P_{N_2}(q)$ of co-ordination numbers. Note that the ice-rule restriction of the vertex

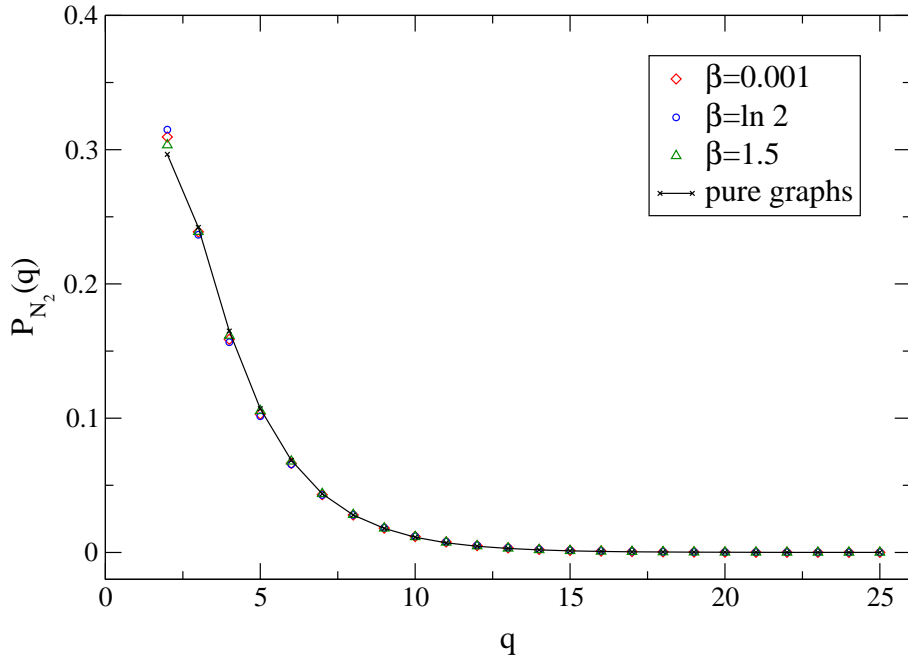


Figure 5.32: Co-ordination number distribution of ϕ^4 random graphs (resp. the dual quadrangulations) with $N_2 = 512$ sites coupled to the F model from MC simulations. The error bars are of the size of the plotting symbols. The solid curve shows the distribution for pure ϕ^4 random graphs of the same size.

model leads to a coupling between matter variables and geometry which is quite different from that of, say, an Ising model placed on random graphs. While for the latter case the energy differences of the spin model configurations become irrelevant in the infinite-temperature limit $\beta \rightarrow 0$, thus leading to a complete decoupling of spin and graph variables, the forbidden configurations of the F model correspond to contributions of *infinite* energy such that even in the limit $\beta \rightarrow 0$ there is a back-reaction of the vertex model configurations on the underlying graphs. To put it differently, the matter back-reaction is of *entropic* instead of energetic nature for the case of the vertex model.

Figure 5.32 shows the distribution of co-ordination numbers for ϕ^4 random graphs of the regular ensemble and with $N_2 = 512$ sites coupled to the F model at the three different inverse temperatures $\beta = 0.001$, $\beta = \ln 2$ and $\beta = 1.5$. Obviously, on the scale of the whole distribution $P_{N_2}(q)$ no dramatic differences between the temperature extremes can be distinguished and all three distributions look very similar to the case of pure ϕ^4 random graphs of the same size also shown in Fig.

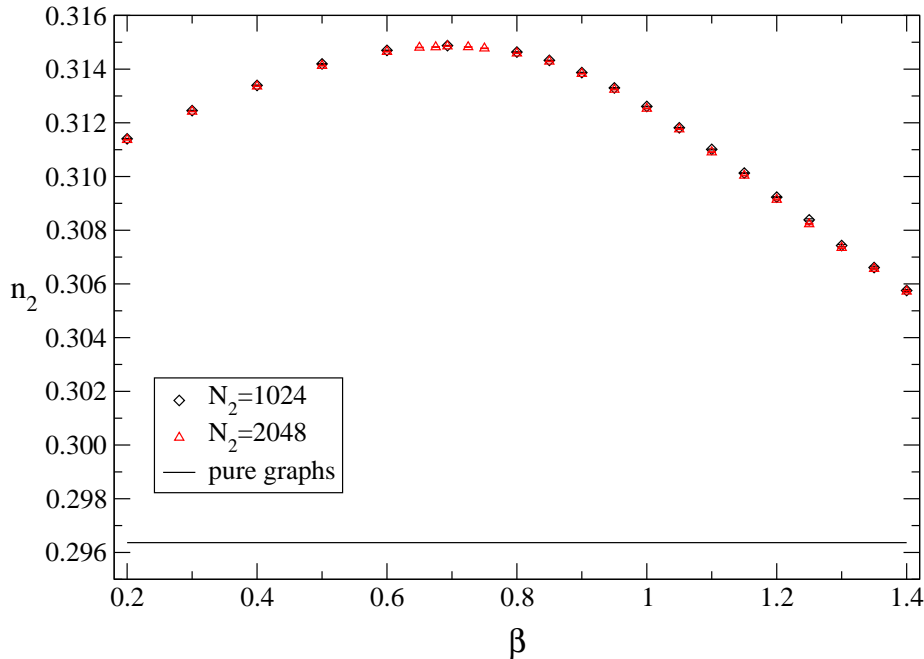


Figure 5.33: Fraction n_2 of loops (faces) of length two of planar ϕ^4 random graphs with a coupled F model as a function of the inverse temperature β . The drawn error bars are mostly covered by the size of the symbols. The solid line shows the value of n_2 for the case of pure ϕ^4 random graphs of the regular ensemble and with $N_2 = 2048$ sites.

5.32. As it turns out, however, the distribution of co-ordination numbers can be determined very precisely from the simulations. Thus, concentrating on a single point of the distribution, namely the fraction of quadrangulation sites with co-ordination number two or, equivalently, the fraction n_2 of length-two loops of the ϕ^4 graphs, which already has been considered in Chapter 3, a clear variation with the inverse temperature β can be resolved, cf. Fig. 5.33. Also, in terms of the quoted statistical errors, which are of the order of 10^{-5} for the measurements of n_2 , the pure graph result of $n_2 = 0.296365(32)$ is very far away from the whole of the shown variation of the F model case. We find a pronounced peak of n_2 around $\beta \approx 0.7$ with only rather small variations with the size of the considered graph. A similar peak of the fraction of *three-loops* for different spin models coupled to dynamical *triangulations* has been observed before, see Refs. [45, 46, 259]. Since the co-ordination number distribution is normalized and (for the regular ensemble) monotonous, such an increase of n_2 is necessarily accompanied by a decrease of the

N_2	β_{n_2}	$n_2(\beta_{n_2})$
256	0.6941(27)	0.3151620(81)
512	0.6904(25)	0.3149714(76)
1024	0.6961(55)	0.3148749(93)
2048	0.6926(46)	0.3148528(68)
4096	0.6894(54)	0.3148274(68)

Table 5.10: Maxima of the fraction of loops of length two of ϕ^4 graphs coupled to the F model as a function of the inverse simulation temperature β for different sizes of the graphs.

probability to find very large loops in the graph. The latter, on the other hand, typically occur in the vicinity of bottlenecks connecting “baby universes” to the main body of the graph. Thus, at criticality one would expect slightly less “baby universes” to occur, thereby resulting in a dominance of more compact configurations of the graphs. However, if this effect is indeed present, it is too small to be detected by measurements of the mean square extent of the graphs, which are much less precise than measurements of the co-ordination number distribution, see Fig. 5.40 below.

Since, as has been mentioned above, a pronounced back-reaction of the matter variables onto the underlying graphs is only expected at criticality, we interpret the location of the observed peak of $n_2(\beta)$ as a pseudo-critical point β_{n_2} which should scale²⁰ to the asymptotic critical coupling $\beta_c = \ln 2$. As before, the precise location of the maxima can be determined from the simulation data via the reweighting technique described in Appendix A.5. This has been done for the data from simulations of graphs of sizes between $N_2 = 256$ and $N_2 = 4096$ sites with time series of lengths between 8×10^5 and 4×10^6 measurements. The results of this analysis are compiled in Table 5.10. As is additionally illustrated in Fig. 5.34, we find only very small changes of this peak position on variation of the size of the graphs, such that within the present statistical errors β_{n_2} can be considered constant. Thus, we do not perform a finite-size fit to the data of the peak locations, but instead quote the result from the largest considered lattice as an estimate for the asymptotic critical

²⁰Note, however, that this is in contrast to the interpretation of Refs. [45, 46, 259] for the corresponding peak of n_3 in the triangulation model, which was that it should stay away from the critical point even in the thermodynamic limit.

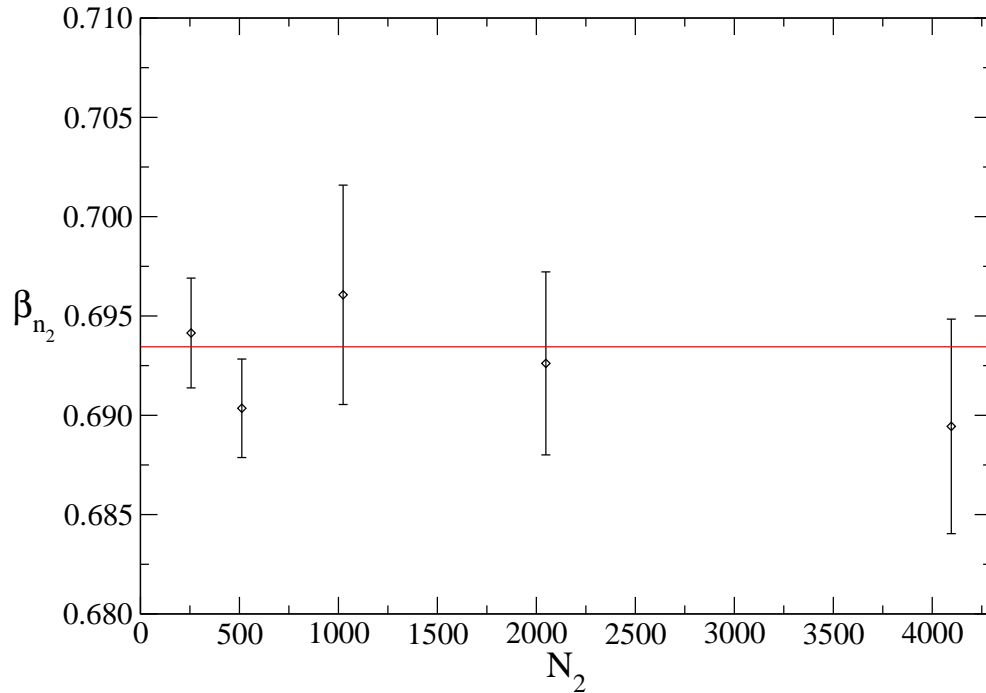


Figure 5.34: Inverse pseudo-critical temperatures β_{n_2} defined by the maximum of the fraction n_2 of loops of length two of ϕ^4 random graphs coupled to the F model as a function of the graph size N_2 . The solid line shows the error-weighted mean of the estimates, which is $\bar{\beta}_{n_2} = 0.6934(20)$.

coupling, namely

$$\beta_{n_2} = 0.6894(54), \quad (5.69)$$

resulting from the simulations for $N_2 = 4096$. This is in nice agreement with the expected value of $\beta_c = \ln 2 \approx 0.693$ and almost two orders of magnitude more precise than the results found above from the scaling of the polarizability peak locations. From simulations of Potts models, it has been argued in Ref. [46] that the maximum value $n_2(\beta_{n_2})$ of the fraction of two-loops itself (resp. the maximum value of the fraction of three-loops for the dynamical triangulations model considered there) could be a universal property which only depends on the central charge of the matter coupled to the lattices. An analysis of the XY model coupled to dynamical triangulations by the same authors [45], however, showed a clear discrepancy to this conjecture.

5.4.2 The string susceptibility exponent

In the grand-canonical ensemble of the dynamical polygonifications model the string susceptibility exponent γ_s governs the leading singularity of the partition function $Z(\mu)$ via²¹

$$Z(\mu) \sim (\mu - \mu_0)^{2-\gamma_s}, \quad (5.70)$$

cf. Eqs. (2.59) and (2.60). Thus, a direct measurement of γ_s requires computationally demanding simulations with a varying number of polygons or graph vertices. Additionally, since (as for all the graph properties) a shift of γ_s due to the presence of some matter variables coupled to the polygonifications model can only be expected at criticality, a numerical setup for the detection of such a change needs to tune two coupling constants, namely μ and β , to criticality. Due to the combination of these two problems a reliable estimation of γ_s from grand-canonical MC simulations has proved difficult, see e.g. [109, 110].

The method

As it turns out, the string susceptibility exponent is related to the baby-universe structure of the dynamical polygonifications [29]. This observation can be turned into a method for the determination of γ_s from simulations at a fixed number of polygons or graph vertices [258]. The distribution of volumes B contained in the minBUs of the dynamical polygonifications model can be expressed in terms of the canonical partition function of the model in the following way; for simplicity, we start with the case of dynamical triangulations. Consider the situation of a minBU of volume B connected to the “mother universe” of volume $N_2 - B$ via its neck of length three. This whole triangulation can be imagined as constructed in the following way: take two “universes” of volumes $B + 1$ and $N_2 - B + 1$ with one triangle marked on each “universe”, remove the marked triangles and glue both parts together to give the triangulation discussed before. Thus, the total number of such configurations is given by the following product of partition functions,

$$3 \mathcal{Z}'(B + 1) \mathcal{Z}'(N_2 - B + 1), \quad (5.71)$$

where the factor of three accounts for the three possible ways to glue both parts together along the omitted triangles and $\mathcal{Z}'(B)$ denotes the canonical partition func-

²¹Since we always consider planar graphs here, γ_s corresponds to the genus zero exponent γ_s^0 of Chapter 2.

tion of dynamical triangulations with B triangles and one marked triangle, i.e.,

$$\mathcal{Z}'(B) = B\mathcal{Z}(B), \quad (5.72)$$

where $\mathcal{Z}(B)$ denotes the usual canonical partition function of Section 2.3.3. Now, the average number $\langle n_{N_2}(B) \rangle$ of minBUs of volume B for triangulations of volume N_2 is given by the absolute number (5.71), normalized by the total partition function $\mathcal{Z}(N_2)$,

$$\langle n_{N_2}(B) \rangle \propto \frac{3}{\mathcal{Z}(N_2)} (B+1)\mathcal{Z}(B+1) (N_2 - B + 1)\mathcal{Z}(N_2 - B + 1). \quad (5.73)$$

From Eq. (2.81) the canonical partition function to leading order scales as

$$\mathcal{Z}(N_2) \sim e^{\mu N_2} N_2^{\gamma_s - 3}. \quad (5.74)$$

Inserting this expression into Eq. (5.73) the leading exponential part cancels and we arrive at,

$$\begin{aligned} \langle n_{N_2}(B) \rangle &\sim \frac{(B+1)^{\gamma_s - 2} (N_2 - B + 1)^{\gamma_s - 2}}{N_2^{\gamma_s - 2}} \\ &\sim N_2^{2 - \gamma_s} [B(N_2 - B)]^{\gamma_s - 2}, \end{aligned} \quad (5.75)$$

where from (5.74) one has to demand that $B \gg 1$ and $N_2 - B \gg 1$ for this relation to be valid. A very similar argument can be given for “baby universes” with larger (than minimal) neck length [29]. For the case of minBUs of the dynamical quadrangulations model the argument is obviously unchanged apart from the replacement $3 \rightarrow 4$ in Eq. (5.71). Also, it can be shown that the same relation should hold for the case of $C < 1$ conformal matter coupled to the polygonifications or dual graphs with γ_s then denoting the corresponding dressed string susceptibility exponent [29]. For the limiting case $C = 1$, on the other hand, it is argued in Ref. [29] that the distribution of minBUs should acquire logarithmic corrections and look like,

$$\langle n_{N_2}(B) \rangle \sim N_2^{2 - \gamma_s} [B(N_2 - B)]^{\gamma_s - 2} [\ln B \ln(N_2 - B)]^\kappa, \quad (5.76)$$

with $\kappa = -2$.

An estimate $\bar{n}_{N_2(B)}$ for the volume distribution of minBUs of the dynamical polygonifications model can be easily found numerically from a decomposition of the graphs into “baby universes”. When the minBU surgery algorithm described in Section 3.5.2 is applied, such an estimate can even be produced as a simple by-product

of the updating scheme, since there the relevant information has to be gathered anyway for the update process. Then, an estimate for γ_s can be found from a fit of the conjectured functional form (5.75), resp. (5.76) for the $C = 1$ case, to the estimated distribution $\bar{n}_{N_2(B)}$ [258]. In order to honour the constraints $B \gg 1$ and $N_2 - B \gg 1$ of Eqs. (5.75) and (5.76) one has to introduce cut-offs B_{\min} and B_{\max} , such that only data with $B_{\min} \leq B \leq B_{\max}$ are included in the fit. Here, the choice of the lower cut-off B_{\min} is found to be much more important for the outcome of the fit than the choice of B_{\max} . As a consequence of this observation we use the following recipe for the determination of the cut-offs: as a rule of thumb, we choose $B_{\max} = N_2/8$, which has turned out to be a good choice for most situations. With B_{\max} fixed, the lower cut-off B_{\min} is steadily increased from $B_{\min} \approx 0$, monitoring the effect of those increases on the resulting fit parameters, especially the estimated string susceptibility exponent γ_s . Finally, with the resulting value of B_{\min} fixed, a second adaption of B_{\max} is attempted, usually changing B_{\max} by factors of two resp. one half. Additionally, the quality-of-fit parameter Q is utilized as a further indicator of whether neglected corrections to scaling are important for the considered window of minBU volumes B . As far as corrections to the leading scaling behaviour are concerned, it is speculated in Ref. [258] that a good effective description of the leading correction term results from the replacement

$$B^{\gamma_s-2} \rightarrow B^{\gamma_s-2} \left(1 + \frac{D_{\gamma_s}}{B} + O(1/B^2) \right). \quad (5.77)$$

Hence, the actual fits were performed to the functional form

$$\ln \bar{n}_{N_2}(B) = A_{\gamma_s} + (\gamma_s - 2) \ln [B(N_2 - B)] + \frac{D_{\gamma_s}}{B}, \quad (5.78)$$

for $C < 1$, resp. to the form

$$\ln \bar{n}_{N_2}(B) = A_{\gamma_s} + (\gamma_s - 2) \ln [B(N_2 - B)] + \kappa \ln [\ln B \ln (N_2 - B)] + \frac{D_{\gamma_s}}{B}, \quad (5.79)$$

for the limiting case of $C = 1$. Here, the dependency on the total volume N_2 has been condensed into the constant A_{γ_s} . Note that both of these fits are linear and the number of data points is of the order of 10^3 for the lattice sizes we have considered, such that a fit with four independent parameters is not utterly unrealistic. In Eq. (5.79) we keep κ as a free parameter since its presumable value $\kappa = -2$ is only a conjecture and, additionally, further corrections to scaling can be covered in an effective way by letting κ vary.

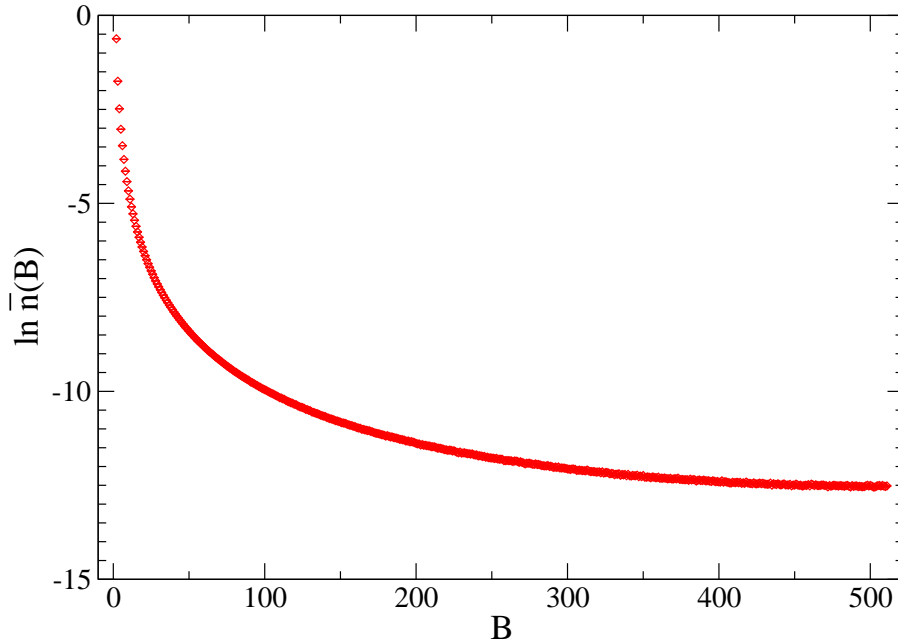


Figure 5.35: Distribution $\ln \bar{n}_{N_2}(B)$ of minBUs of the dynamical quadrangulations model with $N_2 = 1024$ quadrangles. Note the precision down to a probability of 10^{-12} .

Results for pure ϕ^4 graphs

For the case of pure dynamical triangulations and planar topology the string susceptibility exponent is exactly known to be $\gamma_s = -1/2$, cf. Section 2.3.3. In order to check the correct functioning of the described analytical machinery and to explicitly check for the expected universality of γ_s with respect to the change from triangulations to quadrangulations, we performed simulations for pure ϕ^4 random graphs and measured the distribution $n_{N_2}(B)$ of minBUs. Since the measurements are taken as a by-product of the minBU surgery update, a large number of events is built up rather automatically. As can be seen from the presentation of the measured distribution for graphs with $N_2 = 1024$ sites of Fig. 5.35, this results in high-precision results even down to the very improbable events of minBU volumes around $B \approx N_2/2$. Table 5.11 shows the gradual decrease of the estimated γ_s as the lower cut-off B_{\min} is increased to accommodate for higher corrections to scaling. Note that the quoted error estimates, being the usual error estimates resulting from a least-squares fit routine, cannot be taken seriously since they do not account for

B_{\min}	γ_s	Q
0	-0.24879(11)	0.00
10	-0.43439(64)	0.00
20	-0.4613(18)	0.45
30	-0.4722(37)	0.72
40	-0.4722(72)	0.62
50	-0.463(13)	0.58
60	-0.474(25)	0.79

Table 5.11: Influence of the choice of the lower cut-off B_{\min} on the string susceptibility exponent estimate resulting from fits of the functional form (5.78) to the measured minBU distribution $\bar{n}_{N_2}(B)$ for *pure* ϕ^4 random graphs of size $N_2 = 1024$. The upper cut-off has been chosen to be $B_{\max} = 128$. Note that the given error estimates do not fully reflect the statistical fluctuation due to the correlation between the individual points of the distribution B_{\min} .

the apparent correlations of the points of $\bar{n}_{N_2}(B)$ for different sizes B of the minBUs. These correlations generically lead to an underestimation of variances. The drift of γ_s as a function of B_{\min} shown in Table 5.35 is found to become small against the apparent statistical fluctuations between different choices of the cut-off for $B_{\min} \approx 60$, which then was chosen as the final lower cut-off for the graph size $N_2 = 1024$. The authors of Ref. [258] have proposed to additionally extrapolate the results $\gamma_s(B_{\min})$ with an *ad hoc* exponential ansatz towards $B \rightarrow \infty$. Apart from the fact that it is in general arguable, whether one should try extrapolations of noisy data, in the present situation we find the combination of wrongly estimated errors from the fits to $\bar{n}_{N_2}(B)$ and the apparent strong correlations of successive values of $\gamma_s(B_{\min})$ as well as the lack of justified assumptions of the functional form of the approach of $\gamma_s(B_{\min})$ towards γ_s sufficient arguments to refrain from using such additional fits.

We note that statistically reliable error estimates for γ_s could be found when taking into account the full covariance matrix of the individual entries of $\bar{n}_{N_2}(B)$. This, however, in practice would be a huge matrix and one could hardly take enough MC samples to reliably estimate each of its entries. Instead, we revert to a more tractable jackknifing technique: first the upper and lower cut-offs in B are determined as described using the full estimate $\bar{n}_{N_2}(B)$. Then, of the order of ten jackknife blocks are built from the times series the estimate $\bar{n}_{N_2}(B)$ is based on and fits with the same constant cut-offs are performed for each block to yield jackknife-block estimates of

N_2	B_{\min}	B_{\max}	A_{γ_s}	γ_s	D_{γ_s}	Q
1024	60	128	18.36(49)	-0.474(40)	-2.9(30)	0.79
2048	70	256	20.34(14)	-0.495(10)	-3.8(12)	0.56
4096	70	512	22.030(90)	-0.4915(63)	-3.78(74)	0.05
8192	100	1024	23.853(72)	-0.4977(47)	-4.80(87)	0.04

Table 5.12: Parameters of fits of the functional form (5.78) to the simulation data for the distribution $\bar{n}_{N_2}(B)$ of minBUs for pure ϕ^4 random graphs. The parameter error estimates were found by jackknifing over the whole fit procedure, keeping the cut-offs B_{\min} and B_{\max} fixed. Note that the small values of the quality-of-fit parameter Q for the two largest graph sizes are simply an effect of the under-estimation of errors resulting from the cross-correlations in $\bar{n}_{N_2}(B)$.

γ_s and the other fit parameters. Using the formulas of Appendix A.3, then reliable error estimates for the fit parameters can be given. For the pure gravity case we have performed simulations for graphs of sizes $N_2 = 1024$ up to $N_2 = 8192$ increasing by factors of two, taking about $10^9 \times N_2$ minBUs into account for each graph size. Table 5.12 collects the resulting estimates of γ_s together with the remaining fit parameters for the different graph sizes. As far as finite-size effects with respect to N_2 are concerned, we conclude that the estimates for γ_s for $N_2 \geq 2048$ are compatible with each other and, consequently, effects of finite N_2 can be neglected at the given level of accuracy. Thus, as our best estimate of γ_s we quote the result for $N_2 = 8192$, which is $\gamma_s = -0.4977(47)$. Obviously, this is in very good agreement with the exact result $\gamma_s = -1/2$.

Results for the F model case

For the case of the F model coupled to ϕ^4 random graphs we expect a variation of the string susceptibility exponent γ_s with the inverse temperature β of the F model. Since the whole high-temperature phase is critical, in the thermodynamic limit γ_s should vanish for all $\beta \leq \beta_c = \ln 2$, whereas in the non-critical ordered phase the exponent should stick to the pure quantum gravity value of $\gamma_s = -1/2$. To get an impression of the temperature dependence of γ_s we measured the distribution $\bar{n}_{N_2}(B)$ of minBUs over an inverse temperature range of $0.2 \leq \beta \leq 1.3$ for graphs of size $N_2 = 2048$ and performed fits of the functional form (5.78) to the data to extract γ_s . The lower and upper cut-offs B_{\min} resp. B_{\max} were adapted according

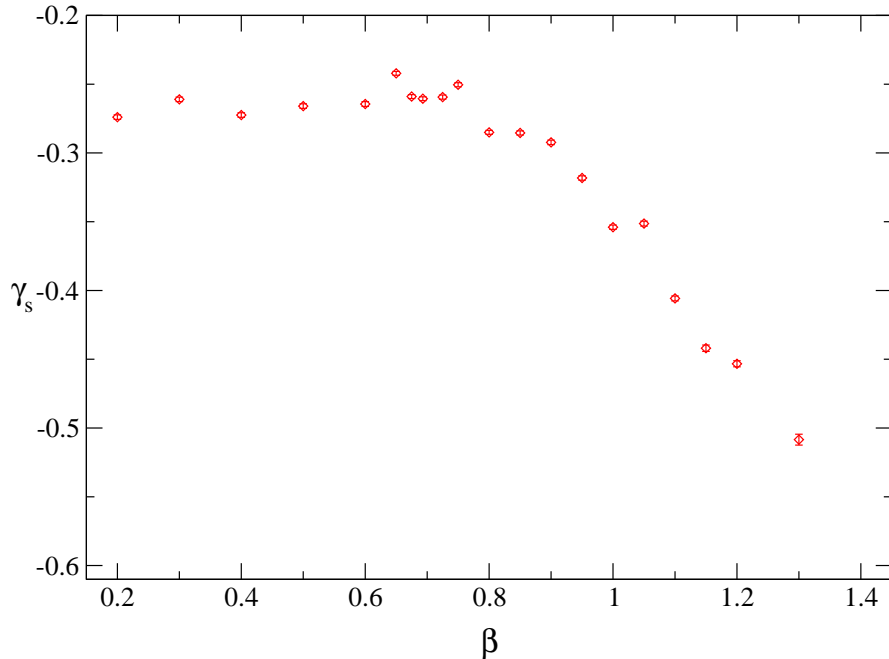


Figure 5.36: Estimates of the string susceptibility exponent γ_s from fits of the functional form (5.78) to the measured distribution $\bar{n}_{N_2}(B)$ of minBUs for ϕ^4 random graphs of size $N_2 = 2048$ coupled to the F model as a function of the inverse temperature β . As is explained in the main text, the displayed error bars do not represent the full statistical error.

to the procedure described above for the case of pure dynamical ϕ^4 graphs. The resulting estimates for γ_s presented in Fig. 5.36 show a plateau value of $\gamma_s \approx -0.25$ within the critical phase $\beta \leq \ln 2$ and a slow drop down to $\gamma_s \approx -0.5$ at $\beta = 1.3$ in the low-temperature phase. Note that the error bars displayed in Fig. 5.36 are those resulting from the fit procedure itself and are thus not representing the full statistical variation due to the above mentioned cross-correlations between the values of $\bar{n}_{N_2}(B)$ at different B . As shall be shown below, the fact that γ_s is found to be still considerably smaller than zero in the high-temperature phase is due to a finite-size effect. In principle, this could be reduced by performing fits of the form (5.79) including the logarithmic corrections expected at central charge $C = 1$. For the quite small graph size of $N_2 = 2048$, however, this type of (four parameter) fit is in general found to be too unstable to yield reliable results.

More precise estimates for γ_s are found from a finite-size scaling study of three series of simulations, one at the critical point $\beta_c = \ln 2$, one in the critical high-temperature

N_2	B_{\min}	B_{\max}	A_{γ_s}	γ_s	D_{γ_s}
2048	70	256	20.48(23)	-0.496(18)	-5.9(18)
4098	70	256	22.48(34)	-0.515(25)	-8.2(26)
8192	100	512	23.75(51)	-0.482(35)	-5.9(41)
16 384	100	2048	25.39(27)	-0.478(17)	-3.5(31)

Table 5.13: Parameters of fits of the form (5.78) to the distribution of minBUs of ϕ^4 random graphs coupled to the F model at $\beta = 1.4$. Larger graphs could not be properly relaxed due to the exponential slowing down of the MC dynamics found in the low-temperature phase.

phase at $\beta = 0.2$ and one deep in the ordered phase at $\beta = 1.4$, using ϕ^4 graphs of the regular ensemble. For the latter case, the exponential slowing down of the combined link-flip and surgery dynamics of the graphs reported in Section 5.3 limited the maximum accessible graph size to $N_2 = 16\,384$, while for the simulations at the critical point and in the high-temperature phase graphs with up to $N_2 = 65\,536$ sites were considered. The fit results at $\beta = 1.4$ are collected in Table 5.13. Obviously, within the present accuracy of the data no relevant finite-size effects are visible, all results being compatible with the conjectured value of $\gamma_s = -1/2$. Thus, as our final estimate for $\beta = 1.4$ we report the value found for $N_2 = 16\,384$,

$$\begin{aligned}
 A_{\gamma_s} &= 25.39(27), \\
 \gamma_s &= -0.478(17), \\
 D_{\gamma_s} &= -3.5(31), \\
 Q &= 1.00,
 \end{aligned}
 \tag{5.80}$$

where $B_{\min} = 100$ and $B_{\max} = 2048$ have been used. For the quoted statistical error estimates the jackknifing procedure described above for pure dynamical ϕ^4 graphs has been used, thus taking full account of the present fluctuations.

At the critical point $\beta_c = \ln 2$ fits of the form (5.78) without logarithmic corrections show considerable finite-size effects, cf. Table 5.14(a). For the largest graph size considered, the thus found estimate $\gamma_s = -0.2075(17)$ is still far away from the expected result $\gamma_s = 0$. Taking the logarithmic corrections into account, these results can be considerably improved. The parameters of fits of the corresponding functional form (5.79) are collected in Table 5.14(b). The relatively large statistical errors of the estimates for the smaller graph sizes are explained by the fact that the fits show a competition of two distinct local minima of the χ^2 distribution, such that for some

(a)	N_2	B_{\min}	B_{\max}	A_{γ_s}	γ_s	D_{γ_s}
	2048	80	256	17.80(17)	-0.259(13)	1.1(15)
	4098	100	512	19.25(13)	-0.2498(92)	2.0(13)
	8192	140	1024	20.70(23)	-0.2426(15)	4.1(32)
	16 384	150	2048	21.87(17)	-0.2193(10)	10.7(25)
	32 786	170	4096	23.525(59)	-0.2263(34)	9.9(15)
	65 536	180	8192	24.73(30)	-0.2075(17)	15.6(53)

(b)	N_2	B_{\min}	B_{\max}	A_{γ_s}	γ_s	κ	D_{γ_s}
	2048	60	256	19.7(37)	-0.06(41)	-1.2(24)	-5.5(116)
	4098	65	512	22.3(13)	0.04(13)	-1.81(81)	-9.4(45)
	8192	90	1024	23.6(19)	-0.01(19)	-1.6(12)	-9.7(73)
	16 384	100	2048	25.7(15)	0.05(13)	-1.97(89)	-10.9(69)
	32 768	110	4096	27.08(93)	0.013(70)	-1.80(50)	-12.6(47)
	65 536	120	4096	27.5(14)	-0.05(12)	-1.27(82)	-6.9(71)

Table 5.14: Parameters of fits to the distribution $\bar{n}_{N_2}(B)$ of minBUs for ϕ^4 random graphs coupled to the F model at $\beta = \beta_c = \ln 2$. (a) Fits to the functional form (5.78), i.e., without inclusion of logarithmic corrections expected for $C = 1$. (b) Fits to the form (5.79) including logarithmic corrections.

of the jackknife blocks the fit yields $\gamma_s \approx -0.2$. This effect, however, vanishes for the larger graphs. Apart from this finding, no relevant finite-size dependence of the estimate γ_s could be detected. The occurring values for the “correction exponent” κ are not too far away from and indeed statistically compatible with the conjectured (however not exactly known) value of $\kappa = -2$. Since for the case of $N_2 = 65\,536$ only a much shorter time series than for the smaller graph sizes was recorded, we present as our final estimate of the critical value of γ_s the result at $N_2 = 32\,768$,

$$\begin{aligned}
A_{\gamma_s} &= 27.08(93), \\
\gamma_s &= -0.013(70), \\
\kappa &= -1.80(50), \\
D_{\gamma_s} &= -12.6(47), \\
Q &= 1.00,
\end{aligned} \tag{5.81}$$

where the cut-offs have been chosen at $B_{\min} = 110$ and $B_{\max} = 4096$.

Finally, in the high-temperature phase at $\beta = 0.2$ the simulation results behave very

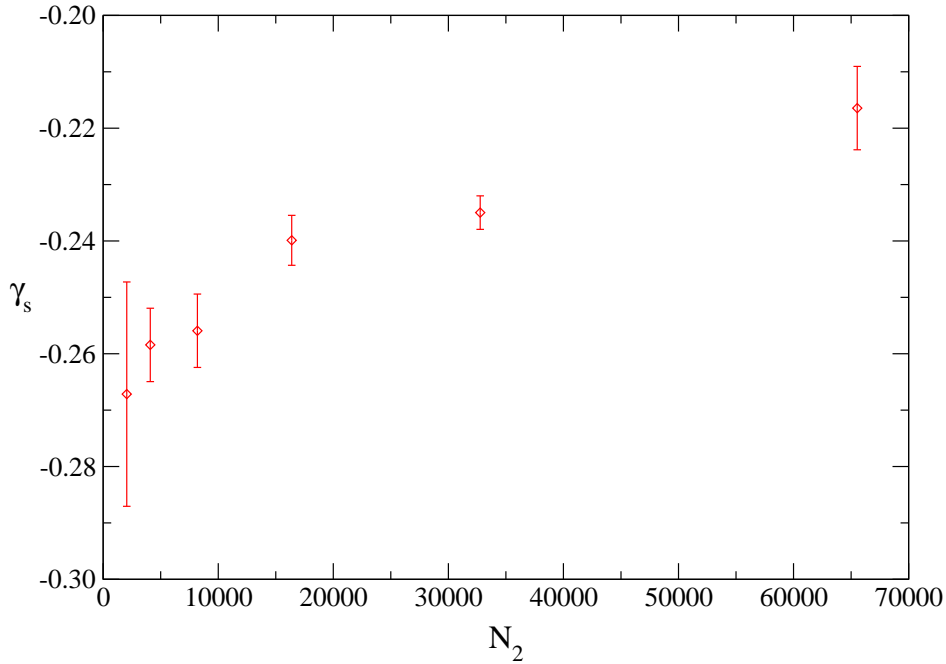


Figure 5.37: Estimates of γ_s from fits to the functional form (5.78), i.e., without the inclusion of logarithmic corrections expected at $C = 1$, for the random graph F model at $\beta = 0.2$ as a function of the graph size N_2 . The statistical errors were evaluated using the jackknife technique described in the main text.

similarly to the critical point case. When applying fits of the form (5.78) without logarithmic corrections, considerable finite-size effects are found, the resulting exponent estimates γ_s only very slowly approaching the expected value of $\gamma_s = 0$. This situation is depicted in the FSS plot of Fig. 5.37. On the other hand, the estimates resulting from fits of the form (5.79) to the data are compatible with $\gamma_s = 0$ for the larger of the considered graph sizes. For graphs of sizes up to $N_2 = 4096$ the “other” minimum of the χ^2 distribution wins against the “true” minimum relevant for the larger graphs. We report here the estimate resulting from graphs of size $N_2 = 32\,768$:

$$\begin{aligned}
 A_{\gamma_s} &= 26.25(79), \\
 \gamma_s &= -0.041(73), \\
 \kappa &= -1.38(47), \\
 D_{\gamma_s} &= -8.1(30), \\
 Q &= 0.05,
 \end{aligned} \tag{5.82}$$

with cut-offs $B_{\min} = 100$ and $B_{\max} = 2048$.²² To complete the picture, it should be mentioned that the functional form (5.79) does *not* fit the data in the low-temperature phase at $\beta = 1.4$ well and does not give estimates of γ_s compatible with $\gamma_s = 0$.

5.4.3 The Hausdorff dimension

The non-trivial (internal) Hausdorff dimension d_h of the lattices of the dynamical polygonifications model, defined by the relations of Section 2.3.5, is one of its most striking features. Apart from the present physical implications, this fact results in a quite inconvenient obstacle for the numerical analysis of the model, namely the comparable smallness of the effective linear extent of the graphs at a given total volume N_2 as compared to flat lattices.

As matter variables are coupled to the dynamical graphs, the strong coupling between graph and matter variables at criticality could lead to a change of the fractal dimensionality of the lattices. In a phenomenological picture, such a strong coupling of matter and geometry should set in as soon as the intrinsic length scale of the graphs or polygonifications, usually defined as their mean square extent, becomes comparable to the correlation length of the matter system. For conformal minimal matter, there has been quite some debate about how d_h should depend on the central charge C of the coupled matter system, see, e.g., Refs. [51, 116, 166, 172, 249, 250]. For $C = 0$ the result $d_h = 4$ is exactly known [26–28] as has been mentioned in Chapter 2. On the other hand, the branched polymer model [109] describing the $C \rightarrow \infty$ limit [53] yields $d_h = 2$ (see, e.g., Ref. [119]), cf. the discussion of Section 2.4. For the intermediate region $0 < C \leq 1$ two differing conjectures have been made for d_h , cf. Eqs. (2.142) and (2.143). All numerical investigations up to now, on the other hand, are consistent with a constant $d_h = 4$ for $0 < C \leq 1$ [51, 144, 172, 250]. Naturally, the limiting case $C = 1$ also considered here is of special interest for the investigation of the transition to the branched polymer regime $C \gg 1$.

Numerically, it has proved exceptionally difficult to extract the Hausdorff dimensions from the statistics of the numerically accessible graph sizes, see, e.g., Refs. [22, 161,

²²Note that due to the present correlations, as has been mentioned above, the quoted values of the quality-of-fit parameter cannot be really taken seriously as far as their absolute values are concerned. However, they still serve a helpful purpose in comparing the quality of different fits to the same data.

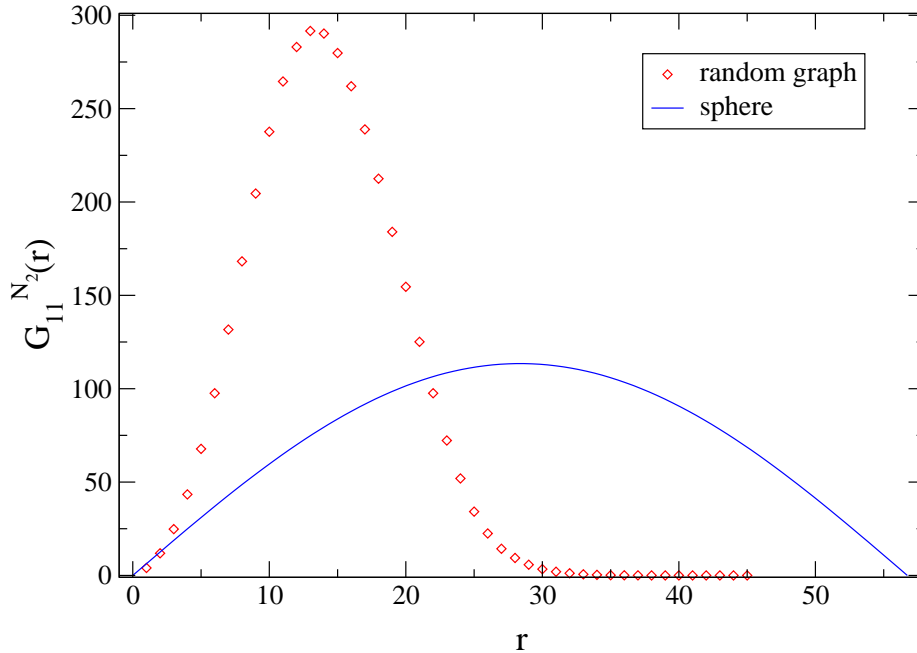


Figure 5.38: Measured geometrical two-point function $G_{11}^{N_2}(r)$ for pure ϕ^4 random graphs of the regular ensemble with $N_2 = 4096$ sites. For comparison, we also show the two-point function of a perfect sphere of the same size, i.e., the function $G_{11}^{N_2}(r) = N_0/(2\sqrt{N_0/4\pi}) \sin(r/\sqrt{N_0/4\pi})$ with $N_0 = 4098$.

172]. Before the exact result $d_h = 4$ for the case of pure Euclidean quantum gravity had been found, an analysis of very large, recursively constructed pure dynamical triangulations even implied an only logarithmic growth of the mean square extent with the area of the mesh, corresponding to the limit $d_h \rightarrow \infty$ [161]. Only in the last several years, the development and application of suitable FSS techniques allowed for a more successful and precise determination of d_h [166, 249, 250].

Scaling and the two-point function

Information about the fractal structure of the graphs or polygonifications is encoded in the loop-loop correlator or geometrical two-point function of the lattices. It can be defined in terms of different geometrical entities, i.e., the vertices or faces of the polygonifications or the dual graphs and employing different notions of geodesic distance of these geometrical entities as discussed above in Sections 2.2.3 and 2.3.5. The asymptotic, large-volume behaviour of the two-point functions should not depend

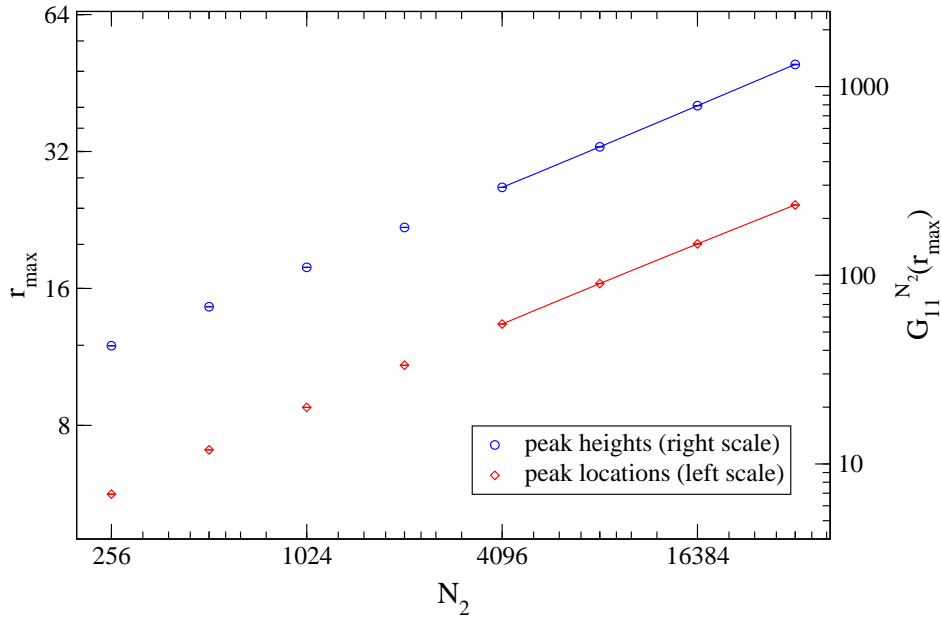


Figure 5.39: FSS plots of the peak locations r_{\max} (left scale) and peak heights $G_{11}^{N_2}(r_{\max})$ (right scale) of the two-point function of pure dynamical ϕ^4 random graphs as a function of the number of sites N_2 . The solid lines show fits of the functional form (5.89) to the data. The extent of the lines indicates the range of N_2 included in the fits.

on these microscopical details of its definition (apart from trivial re-scalings). Here, as in Section 3.5.1 above, we define the geometrical two-point function $G_{11}^{N_2}(r)$ as the average number of vertices of the polygonifications at a distance r from a marked vertex, where “distance” denotes the minimal number of links one has to traverse to connect both vertices. In terms of the dual graphs considered here, $G_{11}^{N_2}(r)$ denotes the number of loops or faces of the graphs at a distance r from a marked face, with the distance measured in dual links.

Since the intrinsic length of the model scales as N_2^{1/d_h} by definition of the intrinsic Hausdorff dimension d_h , from the usual FSS arguments one can make the following scaling ansatz (see, e.g., Ref. [166]),

$$G_{11}^{N_2}(r) \sim N_2^\alpha F(r/N_2^{1/d_h}), \quad (5.83)$$

i.e., $G_{11}^{N_2}(r)$ is a generalized homogeneous function and one can define a scaling function $F(x)$ of the single scaling variable $x = rN_2^{-1/d_h}$ and a critical exponent α .

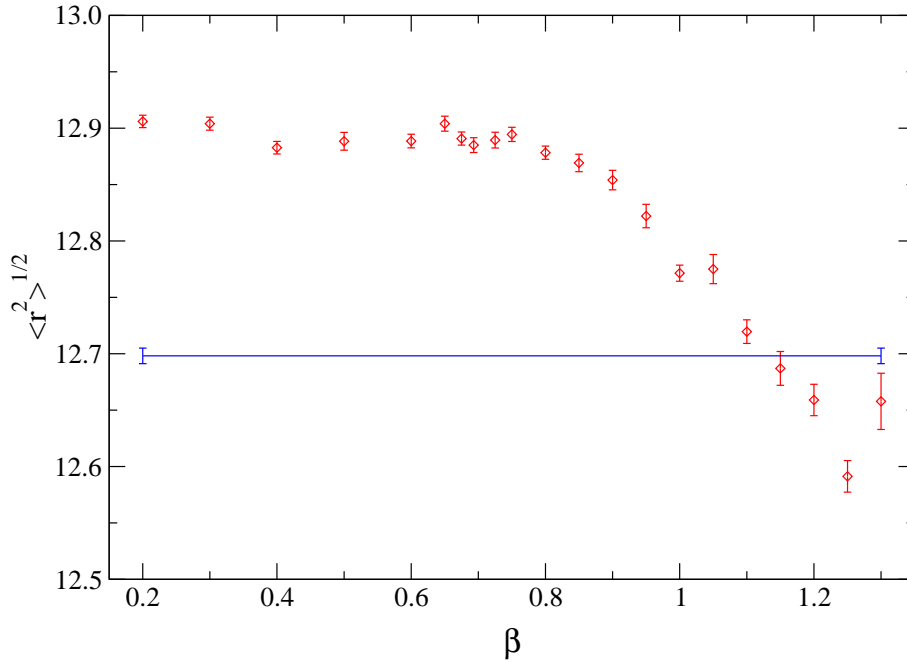


Figure 5.40: Mean extent $\sqrt{\langle r^2 \rangle}$ of regular ϕ^4 random graphs coupled to the F model as a function of the inverse temperature β . The considered graphs have $N_2 = 2048$ sites. The horizontal line indicates the mean square extent of pure ϕ^4 random graphs of the same size.

As a simple calculation shows, due to the obvious constraint

$$N_2 = \sum_r G_{11}^{N_2}(r), \quad (5.84)$$

resp. its continuous analogue with the sum replaced by an integral, the exponent α is not independent, but simply related to d_h as $\alpha = 1 - 1/d_h$. As it has turned out, for practical purposes the scaling variable has to be *shifted* to yield reliable results, see, e.g., Refs. [116, 247, 249]. The necessity of such a shift can be most easily seen by a phenomenological scaling discussion of the mean extent defined by

$$\langle r \rangle_{N_2} = \frac{1}{N_2} \sum_r r G_{11}^{N_2}(r) \sim F_0 N_2^{1/d_h}, \quad (5.85)$$

with $F_0 = \sum_r F(r)$. As usual in FSS theory, one expects analytical corrections to this leading behaviour, i.e. correction terms containing negative integral powers of the linear length scale L of the considered lattice. For the random lattices considered

$N_{2,\min}$	A_r	a	d_h	Q
256	1.4476(93)	1.063(23)	3.6347(76)	0.00
512	1.501(13)	1.219(35)	3.675(10)	0.05
1024	1.535(21)	1.326(63)	3.700(16)	0.15
2048	1.549(33)	1.37(11)	3.709(24)	0.09
4096	1.669(61)	1.78(20)	3.789(41)	0.98

Table 5.15: Parameters of fits of the functional form (5.89) to the peak locations r_{\max} of the geometrical two-point function of random ϕ^4 graphs coupled to the F model at $\beta = 0.2$ as a function of the minimum included graph size $N_{2,\min}$.

here, the mean extent $\langle r \rangle$ itself takes on the rôle of L , such that one can write [249]

$$\frac{\langle r \rangle_{N_2}}{N_2^{1/d_h}} \sim F_0 + \frac{a}{N_2^{1/d_h}} + \frac{b}{N_2^{2/d_h}} + \dots \quad (5.86)$$

Combining the terms proportional to $1/N_2^{1/d_h}$ on both sides, one arrives at

$$\langle r + a \rangle_{N_2} \sim F_0 N_2^{1/d_h} + O\left(\frac{1}{N_2^{2/d_h}}\right), \quad (5.87)$$

Thus, to incorporate first-order corrections to scaling, the ansatz (5.83) is replaced by

$$G_{11}^{N_2}(r) \sim N_2^\alpha F[(r + a)/N_2^{1/d_h}], \quad (5.88)$$

i.e., the scaling variable is now defined to be $x = (r + a)/N_2^{1/d_h}$. Although one can give physically more profound arguments speaking in favour of the inclusion of such a shift parameter, see Ref. [247], we will restrict ourselves to the phenomenological explanation given above.

Scaling of the maxima

A typical form of the measured two-point function $G_{11}^{N_2}(r)$ for pure dynamical ϕ^4 graphs of size $N_2 = 4096$ is shown in Fig. 5.38. It exhibits a pronounced peak and declines exponentially for $r \rightarrow \infty$. The two-point function of a sphere also shown in Fig. 5.38 illustrates the comparably small linear extent of the random lattice as compared to a regular geometry. From the scaling ansatz (5.88) one infers the following leading scaling behaviour of the position and height of the maxima of the

peak locations					
β	$N_{2,\min}$	A_r	a	d_h	Q
0.2	4096	1.669(61)	1.78(20)	3.789(41)	0.98
$\ln 2$	4096	1.641(79)	1.73(26)	3.769(53)	0.25
1.4	2048	1.611(84)	1.53(25)	3.754(60)	0.21

peak heights					
β	$N_{2,\min}$	A_n	B_n	d_h	Q
0.2	4096	0.740(44)	6.7(36)	3.446(68)	0.76
$\ln 2$	4096	0.753(63)	6.2(51)	3.426(92)	0.55
1.4	2048	0.567(84)	12.7(60)	3.94(23)	0.55

Table 5.16: Parameters of fits of the form (5.89) to the data for the peak locations and heights of the geometrical two-point function $G_{11}^{N_2}(r)$ of dynamical ϕ^4 graphs coupled to the F model at the inverse temperatures $\beta = 0.2$, $\beta = \ln 2$ and $\beta = 1.4$. For $\beta = 0.2$ and $\beta = \ln 2$ graph sizes between $N_{2,\min}$ and $N_2 = 65\,536$ were included in the fits; for $\beta = 1.4$ the maximum graph size was $N_2 = 32\,768$.

two-point function $G_{11}^{N_2}(r)$,

$$\begin{aligned} r_{\max} + a &= A_r N_2^{1/d_h}, \\ G_{11}^{N_2}(r_{\max}) &= A_n N_2^{1-1/d_h} + B_n. \end{aligned} \quad (5.89)$$

Since the location and height of these maxima can be determined numerically from simulation data, these relations can be used to estimate the intrinsic Hausdorff dimension d_h of the lattices. A technical difficulty is given by the fact that r can only take on integer values for the discrete graphs considered. This problem is circumvented by a smoothing out of the vicinity of the maximum by a fit of a finite-order polynomial to $G_{11}^{N_2}(r)$ around its maximum. For practical purposes, we find a fourth-order polynomial sufficient for this fit. The position and height of the maxima are then taken to be the corresponding properties of the fitted polynomial. To arrive at reliable error estimates for the position and height estimates, the simulation data for $G_{11}^{N_2}(r)$ are combined into jackknife blocks to which the fitting procedure is applied separately, with a subsequent application of the jackknife variance estimator to the set of thus determined jackknife block estimates of the peak positions and heights, cf. Appendix A.3. The fits themselves are done with equal weights given to the points of $G_{11}^{N_2}(r)$ around the maximum included in the fit. This choice of weights is found appropriate since only a very small number of between five and

peak locations						
β	$N_{2,\min}$	A_r	B_r	a	d_h	Q
0.2	2048	2.34(43)	9.2(39)	5.5(21)	4.13(20)	0.86
$\ln 2$	2048	1.96(39)	5.6(43)	3.7(20)	3.93(21)	0.11
1.4	1024	2.18(49)	6.0(37)	4.4(22)	4.07(26)	0.44

Table 5.17: Parameters of fits of the form (5.92) to the peak locations of the two-point functions of ϕ^4 random graphs coupled to the F model at different inverse temperatures β . The maximum graph size was $N_2 = 65\,536$ for $\beta \leq \ln 2$ resp. $N_2 = 32\,768$ for $\beta = 1.4$.

fifteen adjacent points around the maximum are included in the fit, whose individual statistical errors are found to be almost identical. Thus, one arrives at estimates for the peak locations r_{\max} and heights $G_{11}^{N_2}(r_{\max})$ as a function of the graph size N_2 , to which then the functional forms of Eq. (5.89) are fitted.

Figure 5.39 shows FSS plots of the peak locations and heights for the case of pure dynamical ϕ^4 random graphs and the corresponding fits of (5.89) to the data. As usual, we tried to account for the effect of neglected scaling corrections by successively dropping data points from the small- N_2 side. We find the value of d_h to steadily increase on omitting more and more points. The fits of Fig. 5.39 include the lattice sizes $N_2 = 4096$ up to $N_2 = 32\,768$ with the following final fit parameters,

$$\begin{aligned}
 A_r &= 1.705(42), \\
 a &= 1.84(14), \\
 d_h &= 3.803(28), \\
 Q &= 0.22,
 \end{aligned}
 \tag{5.90}$$

for the peak locations and,

$$\begin{aligned}
 A_n &= 0.606(27), \\
 B_n &= 12.0(26), \\
 d_h &= 3.814(63), \\
 Q &= 0.44,
 \end{aligned}
 \tag{5.91}$$

for the peak heights. Thus, in terms of the statistical errors both estimates are still quite far away from the exact result $d_h = 4$ for the pure gravity case, which is, however, in agreement with previous attempts to determine d_h with similar methods, see e.g. Ref. [166]. It should be noted, on the other hand, that the results are already

much improved by the introduction of the shift parameter a ; enforcing $a = 0$, the fit to the peak locations yields $d_h = 3.4313(20)$. We note that by varying the definition of the two-point function one can probably reduce the amount of finite-size corrections, but we will not attempt to do this here [166]. Instead, in view of the success of introducing a first-order scaling correction via the shift parameter a , we add the next analytic correction term to the fit, i.e., for the peak locations we make the ansatz

$$r_{\max} + a = A_r N_2^{1/d_h} + B_r N_2^{-1/d_h}, \quad (5.92)$$

which, again, is found to improve the estimate for d_h considerably. Including graphs with $N_2 = 512$ up to $N_2 = 32\,768$ sites, we find the following fit parameters,

$$\begin{aligned} A_r &= 2.007(77), \\ B_r &= 4.50(61), \\ a &= 3.55(35), \\ d_h &= 3.964(42), \\ Q &= 0.24, \end{aligned} \quad (5.93)$$

which gives now good agreement with $d_h = 4$ at the price of an increased statistical error.

For random ϕ^4 graphs coupled to the F model, we find a small dependence of the mean square extent on the inverse temperature β of the coupled F model and also a slight shift of $\sqrt{\langle r^2 \rangle}$ as compared to the case of pure ϕ^4 random graphs, cf. Fig. 5.40. Thus, it is at least not impossible for the Hausdorff dimension d_h to be temperature dependent, too. We performed the same analysis as described above for the case of pure dynamical graphs for three specific inverse temperatures of the F model, namely $\beta = 0.2$, $\beta = \ln 2$ and $\beta = 1.4$, covering the critical high-temperature phase, the critical point and the non-critical low-temperature phase, respectively. Simulations were performed for graphs of sizes between $N_2 = 256$ and $N_2 = 65\,536$ for $\beta = 0.2$ and $\beta = \ln 2$ resp. between $N_2 = 256$ and $N_2 = 32\,768$ for $\beta = 1.4$. The results for d_h from fits of the functional form (5.89) to the data steadily increase on omitting more and more points from the small- N_2 side. This is exemplified for the case of the peak locations of the $\beta = 0.2$ data in Table 5.15. A similar situation is found for the scaling of the peak heights and the data at the other simulated couplings β . The final results from fits of the form (5.89) to the data are collected in Table 5.16. Obviously, the estimates of d_h extracted from the scaling of the peak locations are significantly smaller than $d_h = 4$ in terms of the statistical errors,

$N_{2,\min}$	$A_{\langle r \rangle}$	a	d_h	Q
256	1.601(41)	1.49(11)	3.657(30)	0.01
512	1.592(54)	1.47(15)	3.651(39)	0.00
1024	1.85(10)	2.23(28)	3.821(66)	0.30
2048	2.14(21)	3.08(59)	3.99(12)	0.81

Table 5.18: Parameters of fits of the form (5.94) with $B_{\langle r \rangle} = 0$ to the simulation estimates for the mean extent $\langle r \rangle$ of pure ϕ^4 random graphs as a function of the cut-off $N_{2,\min}$. Graphs with up to $N_2 = 32\,768$ sites were included in the fits.

however in good agreement with the results found from the same fits to the data for pure ϕ^4 random graphs. The estimates of d_h resulting from the scaling of the peak heights, on the other hand, are much lower than they were for the case of pure ϕ^4 graphs. The rather different result for $\beta = 1.4$ as compared to the other inverse temperatures again indicates the presence of competing local minima of the χ^2 distribution — an effect which is always rather likely to occur in non-linear fitting procedures.

As for the pure gravity model, we try to improve on the found estimates for d_h by including the next sub-leading correction term into the fits to the peak locations of the two-point function, using the fit ansatz (5.92). With this type of fit we find no significant dependency of the results on the lower cut-off $N_{2,\min}$ in the graph sizes. The parameters of fits of this form are shown in Table 5.17. The resulting estimates of d_h are compatible within statistical errors with $d_h = 4$, such that from this data we have no reason to suspect that d_h differs from its pure gravity value $d_h = 4$ for any inverse temperature β of the F model.

Scaling of the mean extent

As an alternative to the scaling of the maxima of the two-point function, one can also consider the behaviour of *mean* properties of the distribution $G_{11}^{N_2}(r)$, especially the scaling of the mean extent (5.85). Taking the next sub-leading analytic correction term into account, we make the scaling ansatz

$$\langle r + a \rangle_{N_2} = A_{\langle r \rangle} N_2^{1/d_h} + B_{\langle r \rangle} N_2^{-1/d_h}. \quad (5.94)$$

Estimates for $\langle r \rangle$ can be easily found from the simulation data for $G_{11}^{N_2}(r)$ together with statistical error estimates evaluated by a jackknife blocking of the time se-

(a)	$N_{2,\min}$	a_{opt}	\bar{d}_h	χ^2/dof
	256	1.47(41)	3.67(11)	2.5
	512	1.57(63)	3.69(16)	3.0
	1024	2.22(49)	3.83(11)	0.7
	2048	2.97(100)	3.97(21)	0.1

(b)	$N_{2,\min}$	a_{opt}	\bar{d}_h	χ^2/dof
	256	1.46(10)	3.657(28)	2.3
	512	1.52(14)	3.672(37)	2.7
	1024	2.20(23)	3.818(55)	0.7
	2048	2.98(60)	3.97(12)	0.1

Table 5.19: Estimates of the shift a and the internal Hausdorff dimension d_h from the adaption method proposed by the authors of Ref. [249]. (a) Estimates resulting from the original prescription of Ref. [249]. (b) Results from the same method, however with the average (5.98) replaced by (5.100) and error estimates evaluated by a jackknife technique. In the adaption process graph sizes from $N_2 = N_{2,\min}$ up to $N_2 = 32\,768$ sites were included.

ries. Setting $B_{\langle r \rangle} = 0$ first and adapting the lower cut-off $N_{2,\min}$ of the graph sizes successively as before, for the case of pure dynamical ϕ^4 graphs we find the estimates listed in Table 5.18. As for the results from the scaling of the peaks of the two-point function, the resulting estimates of d_h are significantly too small in terms of the statistical errors with an obvious tendency to increase as more and more of the points from the small- N_2 side are omitted. On the other hand, including the correction term of Eq. (5.94) largely reduces the dependency on the cut-off $N_{2,\min}$. For $N_{2,\min} = 256$ we find the following fit parameters,

$$\begin{aligned}
 A_{\langle r \rangle} &= 2.01(27), \\
 B_{\langle r \rangle} &= 3.1(18), \\
 a &= 3.3(11), \\
 d_h &= 3.90(15), \\
 Q &= 0.01,
 \end{aligned}
 \tag{5.95}$$

with an estimate of d_h in nice agreement with $d_h = 4$. Obviously, in view of the results already found without inclusion of the correction term, the use of this additional correction is more questionable here than it was for the scaling of the peak locations above. Also, the fits become very unstable as less points are included;

β	$N_{2,\min}$	$A_{\langle r \rangle}$	a	d_h	Q
0.2	4096	1.54(20)	1.60(74)	3.57(12)	0.04
$\ln 2$	4096	1.23(19)	0.50(80)	3.35(14)	0.84
1.4	2048	1.95(33)	2.67(94)	3.89(21)	0.31

Table 5.20: Parameters of fits of the functional form (5.94) with $B_{\langle r \rangle} = 0$ to the mean extents of ϕ^4 random graphs coupled to the F model at inverse temperatures $\beta = 0.2$, $\beta = \ln 2$ and $\beta = 1.4$. The fits for $\beta = 0.2$ and $\beta = \ln 2$ include graph sizes up to $N_2 = 65\,536$ sites, whereas the fit at $\beta = 1.4$ includes graphs up to $N_2 = 32\,768$ sites.

this explains the use of the cut-off $N_{2,\min} = 256$ above, although the quality-of-fit is rather poor.

The authors of Ref. [249] have proposed a different and less conventional method to extract a and d_h from data of the mean extent, which they claim to be especially well suited for obtaining high-precision results. They consider the following combination,

$$R_{a,N_2}(d_h) \equiv \frac{\langle r + a \rangle_{N_2}}{N_2^{1/d_h}}, \quad (5.96)$$

and evaluate it for a series of simulations for different graph sizes N_2 . Then, for a given a and for each pair (N_2^i, N_2^j) they define $d_h^{ij}(a)$ such that $R_{a,N_2^i}(d_h^{ij}) = R_{a,N_2^j}(d_h^{ij})$, i.e.,

$$d_h^{ij}(a) = \frac{\ln N_2^i - \ln N_2^j}{\ln(\langle r \rangle_{N_2^i} + a) - \ln(\langle r \rangle_{N_2^j} + a)}, \quad (5.97)$$

where we have used that $\langle r + a \rangle_{N_2} = \langle r \rangle_{N_2} + a$. By a binning technique, an error estimate $\sigma(d_h^{ij})$ is evaluated and the estimates $d_h^{ij}(a)$ are averaged over all pairs (N_2^i, N_2^j) of volumes,

$$\bar{d}_h(a) = \frac{1}{\#\text{pairs}} \sum_{i < j} d_h^{ij}(a). \quad (5.98)$$

Then, the optimal choice a_{opt} of the shift is found by minimizing

$$\chi^2(a) = \sum_{i < j} \frac{[d_h^{ij}(a) - \bar{d}_h(a)]^2}{\sigma^2[d_h^{ij}(a)]}, \quad (5.99)$$

being accompanied by an optimal estimate $\bar{d}_h(a_{\text{opt}})$. The authors of Ref. [249] suggest to estimate the statistical error of this final estimate by considering the variation of (a, \bar{d}_h) in an interval of a around a_{opt} defined by $\chi^2(a) < \min[1, 2\chi^2(a_{\text{opt}})]$.

β	$N_{2,\min}$	$A_{\langle r \rangle}$	$B_{\langle r \rangle}$	a	d_h	Q
0.2	512	2.58(48)	11.4(33)	7.0(22)	4.08(21)	0.10
$\ln 2$	512	1.37(22)	0.4(29)	1.1(12)	3.45(14)	0.41
1.4	512	2.6(10)	9.1(58)	6.2(42)	4.15(47)	0.29

Table 5.21: Parameters of fits of the form (5.94) including the correction term to the mean extent of dynamical ϕ^4 graphs coupled to the F model at different inverse temperatures β .

We implemented this whole procedure to compare its outcomes to the results of the fits to Eq. (5.94); the resulting estimates for a and d_h are compiled in Table 5.19(a). First of all, we find the *ad hoc* assumption for the estimation of the errors of (a, \bar{d}_h) not adequate. We apply a second-order jackknifing technique as described in Appendix A.3 to be able to give error estimates for $d_h^{ij}(a)$ as well as the final estimate (a, \bar{d}_h) and find error estimates largely differing from that resulting from the rule $\chi^2(a) < \min[1, 2\chi^2(a_{\text{opt}})]$. For the set of simulations considered, the jackknife estimated errors are about three to four times smaller than those estimated by the rule for $\chi^2(a)$; however, for the simulations of the F model coupled to the random graphs we also find situations where the jackknife errors are up to ten times larger than the errors estimated from χ^2 . As far as the estimate of d_h itself is concerned, we find indeed slightly increased values as compared to the fit method, cf. the data compiled in Table 5.19(a). However, this increase can be traced back to the fact that the individual estimates $d_h^{ij}(a)$ all receive the same weight in the average (5.98), irrespective of their precision. This gives an extra weight to the results for larger graphs, which cannot be justified on statistical grounds. If, instead, we replace the average (5.98) by the variance-weighted average

$$\bar{d}_h(a) = \frac{\sum_{i < j} d_h^{ij}(a) / \sigma^2[d_h^{ij}(a)]}{\sum_{i < j} 1 / \sigma^2[d_h^{ij}(a)]}, \quad (5.100)$$

the resulting estimates for d_h and a are statistically equivalent to those found from the fits to (5.94), cf. the parameters listed in Table 5.19(b). Thus, we do not find any special benefits of this computationally rather demanding method as compared to a plain fit to (5.94) with $B_{\langle r \rangle} = 0$ and hence do not present further detailed results for this method.

For the case of the F model coupled to the ϕ^4 random graphs we proceeded as before, again using simulation data for $\beta = 0.2$, $\beta = \ln 2$ and $\beta = 1.4$. The results

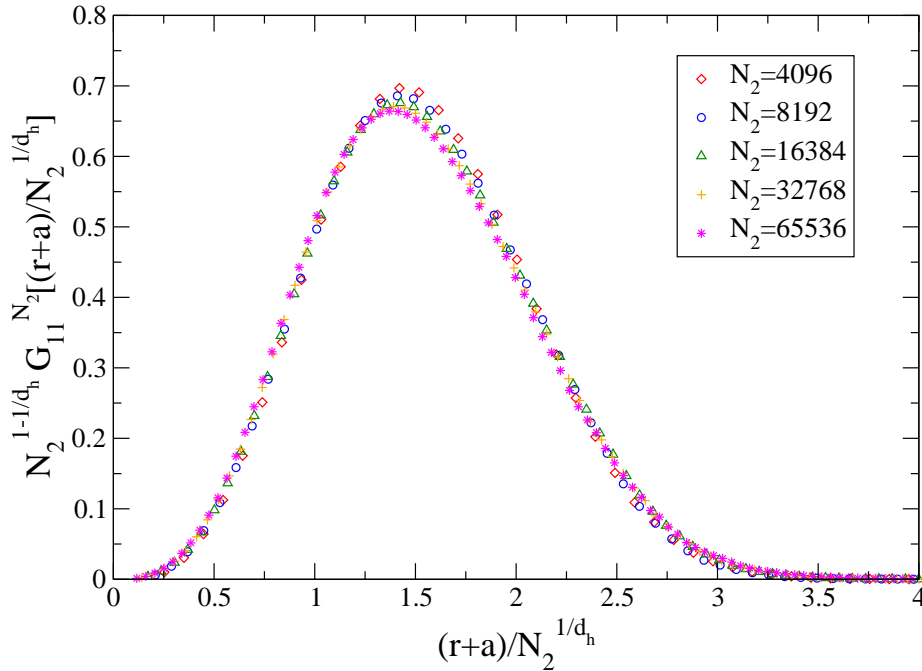


Figure 5.41: Collapse of the two-point functions $G_{11}^{N_2}(r)$ of ϕ^4 graphs coupled to the F model at $\beta = 0.2$, re-scaled according to Eq. (5.88) with $d_h = 3.57$ and $a = 1.60$.

from fits of the mean extent $\langle r \rangle_{N_2}$ to the form (5.94) with $B_{\langle r \rangle} = 0$ show very much the same behaviour as the results from the scaling of the maxima of the two-point function, with estimates of d_h clearly below $d_h = 4$ and slowly increasing as more and more points from the small- N_2 side are omitted from the fits. In Table 5.20 we only show the final estimates with $N_{2,\min}$ already adapted. The outcomes of the method of Ref. [249] described above, with the average (5.98) replaced by (5.100) and the $\chi^2(a)$ rule replaced by a jackknife error estimate, are again very close to the fit results. Only occasionally it gives a result being marginally different in terms of the statistical errors; we interpret this as different local minima of the corresponding χ^2 distribution being found by different methods resp. from different starting values. Including the correction term of (5.94), i.e., relaxing the constraint $B_{\langle r \rangle} = 0$, on the other hand, yields estimates consistent with $d_h = 4$ for $\beta = 0.2$ and $\beta = 1.4$, however with rather large statistical errors, cf. the parameters collected in Table 5.21. Note that, as mentioned before, the results for $\beta = 1.4$ are in general less precise than those for the other two inverse temperatures, which is due to the exponential slowing down of the combined link-flip and surgery dynamics in the low-temperature phase, cf. Section 5.3. The fit for $\beta = \ln 2$ settles down at a completely different minimum of

the χ^2 distribution, yielding a non-sensical result for d_h , which is almost unchanged as compared to the outcome of the corresponding fit without correction term. This underlines the fact that the complexity of the chosen fit is at least at the verge of being too large for the available data. Nevertheless, combining the data for d_h from the presented methods and including the comparison to the pure gravity case, we find no reason to assume that d_h differs from $d_h = 4$ for the case of the F model coupled to ϕ^4 random graphs.

Finally, we note that the parameters a and d_h determined from the fits discussed above lead to a nice scaling collapse of the two-point functions $G_{11}^{N_2}(r)$ when re-scaled according to the scaling ansatz of Eq. (5.88). Figure 5.41 shows this collapse of distributions for the case of $\beta = 0.2$ and the choice of parameters listed in Table 5.20, i.e., $d_h = 3.57(12)$ and $a = 1.60(74)$. The visible deviations around the distribution peaks indicate the presence of higher-order corrections not incorporated into the scaling ansatz (5.88).

Chapter 6

Conclusions and Outlook

In this thesis, we have reported the results of large scale Monte Carlo simulations of the F model of statistical mechanics coupled to planar ϕ^4 quantum gravity graphs. This system is of significance as a model of annealed connectivity disorder applied to a prototypic spin model of statistical mechanics *and* as a realization of a conformal field theory with central charge $C = 1$ coupled to discrete Euclidean quantum gravity in two dimensions.

For the case of dynamical triangulations or, equivalently, “fat” ϕ^3 random graphs, a set of ergodic update moves for simulations in the canonical and grand-canonical ensembles is given by the Pachner or (k, l) moves of Ref. [156]. For simulations of dynamical quadrangulations and the dual ϕ^4 random graphs a flip move for canonical simulations was proposed in Refs. [49, 74]. To this flip move we add suitable generalizations of the insertion and deletion moves for triangulations to the quadrangulation model. According to the extent of singular contributions in the polygonifications or dual graphs (such as self-energies and tadpoles), we distinguish different graph ensembles, which we label as *strict*, *regular*, *restricted singular* and *singular*; although the original ergodicity proof of Ref. [156] for the Pachner moves for the triangulation model considered *combinatorial* triangulations corresponding to the *regular* ensemble of our classification, this proof can be easily extended to the other ensembles considered here. Comparing the simulation results for ϕ^4 graphs to exact results from the graph counting via matrix models, we find the “one-link flip” of Refs. [49, 74] to be sufficient to ensure ergodicity for canonical simulations at a fixed number of graph vertices for the case of the *strict* ensemble, which forbids the occurrence of any multiple links in the graphs. For the other three ensembles,

however, this update can be shown to be *not* ergodic. Introducing a second type of flip move, which we call “two-link flip”, the visible effects of ergodicity breaking for the regular, restricted singular and singular ensembles disappear, and we conclude that the combination of one- and two-link flip is ergodic for all of the considered ensembles for simulations of ϕ^4 graphs at a fixed number of graph vertices. On the other hand, for simulations in the grand-canonical ensemble of a varying number of graph vertices, the additional two-link flip move it found to be not necessary.

We attempt to formulate exact expressions for the co-ordination number distribution of the polygonifications or, equivalently, the distribution of loop lengths of the dual graphs in the spirit of a proposal put forth in Ref. [21]. This is found to be possible for the regular and restricted singular ensembles of the triangulation model. For singular triangulations and the quadrangulation model this approach fails due to a change in the symmetry factors associated to the graphs induced by the occurrence of multiple links. The values of the co-ordination number distribution for small co-ordination numbers are shown to be related to ratios of canonical partition functions; these ratios can be determined exactly for finite sizes of the polygonifications or graphs and all of the considered ensembles of the triangulation and quadrangulation models. Setting up a grand-canonical simulation scheme with non-Boltzmann weights which we call “pseudo grand-canonical simulations”, these partition function ratios are estimated numerically. Alternatively, they can be measured by considering suitable observables in canonical simulations of a fixed number of polygons resp. graph vertices. With the help of these tools, very sensitive comparisons between exact and simulation results can be performed.

A scaling analysis of the integrated autocorrelation times of the mean square extent of pure ϕ^3 and ϕ^4 random graphs shows that the considered canonical link-flip dynamics as a local update suffers from critical slowing down which affects only global properties of the graphs, whereas local characteristics such as the co-ordination number distribution are not concerned. To improve the dynamical performance of the simulations, the minBU surgery algorithm proposed in Ref. [75] is adapted for simulations of quadrangulations and ϕ^4 graphs. A dynamical scaling analysis of an algorithm combined from local link-flip and non-local minBU surgery steps shows a considerable reduction of autocorrelation times of non-local observables, however *no* reduction of the dynamical critical exponents z/d_h , which is in contrast to previous claims [75, 172]. Additionally, the performance of the algorithm for ϕ^4 graphs is hampered by the higher computational cost of the search for minBU necks for the

case of quadrangulations as compared to the triangulation model.

For simulations of the 6-vertex model coupled to ϕ^4 random graphs, we adapt the loop algorithm of Ref. [76] to the needs of random lattices. Due to the lack of a global sense of direction on the random graphs, the definition of the staggered anti-ferroelectric polarization as an order parameter of the Kosterlitz-Thouless phase transition of the F model cannot be trivially transferred to the random graph model. However, since the dynamical quadrangulations considered are bipartite lattices, a two-colouring of the quadrangulations together with a “plaquette spin” representation of the vertex model allows for a generalization of the order parameter to the random graph model, which coincides exactly on the configuration level with the conventional definition when applied to the square-lattice model.

In view of the lack of numerical work on square-lattice vertex models and to calibrate the applied simulational and analytical machinery, a finite-size and thermal scaling analysis of the square-lattice F model is performed. Although the Kosterlitz-Thouless point of the model is known to be equivalent to the critical point of the two-dimensional XY model, observables related to the order parameters of both models show different scaling behaviour. Additionally, due to duality, the high- and low-temperature phases of both models appear exchanged with respect to each other. The scaling analysis is found to be considerably complicated by the nature of the infinite-order phase transition as well as the presence of logarithmic corrections expected for a critical point of central charge $C = 1$. Nevertheless, we find good agreement between the simulation results and the exact solution of Lieb for the zero-field model [62] as well as further results and conjectures of Baxter [242] for the observables related to the staggered anti-ferroelectric polarization.

For the F model coupled to planar ϕ^4 random graphs, we performed large-scale simulations and a finite-size scaling analysis guided by the results for the square-lattice case. In addition to the present logarithmic corrections, the finite-size scaling analysis is hampered by the large fractal dimension of the random graphs, which leads to very small effective linear extents at a given volume as compared to the square lattice. Thus, finite-size effects are found to be very strong. The apparent non-scaling of the specific heat together with a clear divergence of the staggered anti-ferroelectric polarizability are taken as indicators for the presence of an infinite-order phase transition of the Kosterlitz-Thouless type. The results of Refs. [72, 73] and further symmetry arguments imply that the critical coupling of the random graph model is identical to that of the square lattice. However, we find the peaks

of the polarizability for the numerically accessible graph sizes to be shifted very far into the low-temperature phase as compared to the asymptotic critical coupling. Thus, finite-size scaling fits to the shifts of the polarizability peaks are at best in marginal agreement with the conjectured value of the asymptotic critical coupling. A comparison of the peak positions re-scaled according to the mean linear extents of the lattices between the random graph and square-lattice models, however, shows that the finite-size approaches of both models are indeed very similar, but with larger correction amplitudes for the random graph model. Thus, the identity of the critical couplings between both models can be made very plausible numerically. A cursory comparison of the scaling behaviour of the model for different ensembles regarding the inclusion of singular contributions in the graphs reveals that corrections to scaling *increase* as more and more singular contributions are included. This is in contrast to the behaviour of the pure polygonifications model found here and by other authors [50]. As far as the critical exponents related to the order parameter are concerned, a finite-size scaling analysis of the values of the spontaneous polarization and the polarizability at the asymptotic critical coupling yields critical indices in agreement with the predictions from the KPZ formula. An attempted *thermal* scaling analysis of the polarizability around its peak remains inconclusive due to the huge size of present finite-size corrections. This, however, was to be expected in view of the problems already encountered in the analysis of the square-lattice model (and, similarly, the difficulties in the analysis of the two-dimensional XY model encountered by many authors before) and the additional complication of the much smaller linear extents accessible for the random graph model as compared to models on regular lattices. As before for the square-lattice model, we find signs of scaling throughout the whole high-temperature region of the model, indicating a critical phase. As a curiosity, we report the finding of a critical internal energy of the model, which is identical between the square-lattice and random graph cases.

A dynamical scaling analysis of the combined Monte Carlo update of graph-related and matter-related moves at the asymptotic critical point of the model reveals increased autocorrelation times for the global, graph-related properties, exemplified by the mean square extent, for the local link-flip as well as the global minBU surgery dynamics as compared to the pure polygonifications model. Although the global, minBU surgery algorithm is found to perform overall better than the pure local link-flip dynamics, as for the pure graph model we find no change in the corresponding dynamical critical exponents. This identically applies to the behaviour of matter-

related observables such as the spontaneous polarization. On proceeding into the ordered phase, however, the gain of using the minBU update is found to increase, since the link-flip dynamics is there found to be subject to “freezing” induced by the ice-rule constraint of the vertex model, leading to vanishing acceptance rates for the link flips there.

Several aspects of the back-reaction of the matter variables onto the properties of the ϕ^4 random graphs are analyzed as a function of temperature. The distribution of co-ordination numbers of the quadrangulations can be determined very accurately. The fraction of quadrangulation sites of co-ordination number two is found to be sharply peaked around the asymptotic critical coupling, thus defining a pseudo-critical point which determines the infinite-volume critical coupling quite accurately and in good agreement with the analytical predictions. A scaling analysis of the distribution of “baby universes” of the graphs in the spirit of Refs. [29, 258] allows to extract the string susceptibility exponent of the model. It is found to coincide with the value $\gamma_s = 0$ expected for a $C = 1$ theory throughout the critical high temperature phase. The pure-gravity value $\gamma_s = -1/2$ is found in the non-critical low-temperature phase. Exploiting finite-size scaling relations, we analyze the geometrical two-point function of the graphs and extract the fractal Hausdorff dimension. We find it to be consistent with the pure gravity value $d_h = 4$ for all temperatures of the coupled vertex model. Determining all these graph properties also for the case of pure ϕ^4 random graphs, we find agreement with the results previously found for the dynamical triangulations model, thus confirming the expected universality of the dynamical polygonifications model with respect to the form of the polygons.

Using an adaptive algorithm and a 3D computer graphics package, the lattices of the dynamical polygonifications model can be visualized by an embedding into three-dimensional Euclidean space. For the pure gravity model, this yields a valuable impression of the fractal structure of the lattices as well as a visualization of the large variation of the graph properties in the considered ensembles. For the vertex model coupled to random graphs, it provides helpful snapshots revealing the interaction between the matter variables and the underlying geometry as the system passes from the disordered to the ordered phase.

From the point of view of statistical mechanics an obvious generalization of the considered model is given by the generalized 8-vertex type F model discussed in Section 4.3, which — on the square lattice — exhibits two different ordered phases and a rich phase diagram. This model has been considered in a matrix model

formulation in Ref. [231] and a special, one-dimensional slice of the parameter space could be solved analytically. The general phase diagram of this model coupled to ϕ^4 random graphs, however, is as yet unknown. From the quantum gravity point of view, a very promising application of the coupling of vertex models to random graphs could be given in an alternative formulation of discrete Lorentzian quantum gravity proposed in Ref. [230]. There, the arrows of the vertex model on links connecting neighbouring sites allow to distinguish between space-like and time-like edges (ϕ^3 case) or, alternatively, forward and backward light cones (ϕ^4 case) and thus provide a Lorentzian signature of the configurations in the spirit of spin network evolution [260]. This approach could lead to a formulation of discrete Lorentzian quantum gravity starting out with less initial assumptions than the formulation of Ambjørn *et al.* [12, 85, 86, 261].

Appendix A

Methods of Simulation and Data Analysis

A.1 The Monte Carlo Process

A.1.1 Simple sampling

The Monte Carlo (MC) method is a general technique for the statistical evaluation of (typically) high-dimensional integrals. Consider, e.g., a thermal average of an observable A for a system of statistical mechanics,

$$\langle A \rangle = \frac{1}{Z} \sum_{\{\mathbf{s}_i\}} A(\{\mathbf{s}_i\}) \exp[-\beta \mathcal{H}(\{\mathbf{s}_i\})], \quad (\text{A.1})$$

where $\mathcal{S} \equiv \{\mathbf{s}_i\}$ denotes the state-space variables (e.g., spin degrees of freedom), \mathcal{H} is the Hamiltonian of the model and Z denotes the partition function. Here, the sum symbolizes either an integral for systems with continuous degrees of freedom or a true summation for discrete variables. The number N of variables \mathbf{s}_i , e.g. the number of spins of a lattice model, is typically huge and, eventually, a consideration of the thermodynamic limit $N \rightarrow \infty$ is intended. For the vast majority of the cases, the integral (A.1) cannot be performed analytically, such that one has to revert to a numerical integration (or other approximation methods). Unlike for low-dimensional integrals, however, a numerical integration using a regular (e.g. hyper-cubic) grid of evaluation points in the phase space \mathcal{S} is not very well suited. The standard rationale for this failure rests on the observation that the fraction of

interior points of a regular grid vanishes as the grid dimension N tends to infinity (see, e.g., Ref. [153]). That is, in this limit all points are located on the boundary of the considered phase-space region, which is a surface of vanishing N -dimensional volume. To guarantee a proper convergence of the numerical integration one needs a more sensible, e.g. uniform, distribution of evaluation points. This can be achieved by choosing phase-space points *at random* instead of regularly leading to a statistical or *Monte Carlo* evaluation of the integral (A.1).

In this scheme, a time sequence of integration points $\mathcal{S}(t)$, i.e. a realization of a discrete stochastic process, is chosen according to some probability density¹ $P_{\text{sim}}(\mathcal{S})$ and an estimate of $\langle A \rangle$ is then given by

$$\bar{A} = \frac{\sum_t A[\mathcal{S}(t)] P_{\text{eq}}[\mathcal{S}(t)] / P_{\text{sim}}[\mathcal{S}(t)]}{\sum_t P_{\text{eq}}[\mathcal{S}(t)] / P_{\text{sim}}[\mathcal{S}(t)]}, \quad (\text{A.2})$$

where $P_{\text{eq}}(\mathcal{S})$ denotes the integration measure of the integral (A.1), i.e., the Boltzmann equilibrium distribution of statistical mechanics,

$$P_{\text{eq}}(\mathcal{S}) = \frac{1}{Z} \exp[-\beta \mathcal{H}(\mathcal{S})]. \quad (\text{A.3})$$

Choosing a uniform distribution $P_{\text{sim}}(\mathcal{S})$ of evaluation points results in the so-called *simple sampling* MC scheme. Then, successive integration points $\mathcal{S}(t)$ can be chosen completely independent of each other, corresponding to a true random sampling. This is a sensible procedure for cases where the Boltzmann factors in Eq. (A.1) are constant, such that all regions of phase space contribute equally to the integral, i.e., when β tends to zero or the temperature to infinity. Typically, however, this is not the case and, instead, the Boltzmann factors give large weight to a comparably small region of the state space. This largely unequal distribution of “importance” over the phase space should then be taken into account when choosing the integration points, leading to the *importance sampling* MC method.

A.1.2 Importance sampling

Obviously, the optimal probability density $P_{\text{sim}}(\mathcal{S})$ for the choice of integration points is the integration measure of Eq. (A.1) itself, i.e., the case $P_{\text{sim}}(\mathcal{S}) = P_{\text{eq}}(\mathcal{S})$.

¹For systems with discrete phase-space variables the densities have to be replaced by simple probabilities.

If this choice of integration points can be achieved, every region of phase space receives attention exactly according to its importance for the integral (A.1) and the estimate (A.2) reduces to a simple arithmetic time-series average,

$$\bar{A} = \frac{1}{T} \sum_{t=1}^T A[\mathcal{S}(t)], \quad (\text{A.4})$$

where T denotes the length of the time series. In order to realize this goal, a discrete Markov process (or Markov chain) $\mathcal{S}(t)$ is utilized. There, the transition or conditional probabilities are independent of all but the last predecessor states,

$$P_{\text{sim}}[\mathcal{S}(t+1)|\mathcal{S}(t), \dots, \mathcal{S}(1)] = P_{\text{sim}}[\mathcal{S}(t+1)|\mathcal{S}(t)], \quad (\text{A.5})$$

i.e., at each time the choice of the next integration point $\mathcal{S}(t+1)$ depends only on the current state $\mathcal{S}(t)$ of the system. Additionally, one requires the Markov chain to be homogeneous, i.e., the transition probability $W(\mathcal{S} \rightarrow \mathcal{S}') \equiv P_{\text{sim}}[(\mathcal{S}', t+1)|(\mathcal{S}, t)]$ should not depend on t . It can be easily shown (see, e.g., Ref. [262]) from this Markov property and the normalization of probability densities that the probabilities of the chain have to fulfil the so-called *Master equation*,

$$P_{\text{sim}}(\mathcal{S}, t+1) - P_{\text{sim}}(\mathcal{S}, t) = \sum_{\mathcal{S}'} [P_{\text{sim}}(\mathcal{S}', t)W(\mathcal{S}' \rightarrow \mathcal{S}) - P_{\text{sim}}(\mathcal{S}, t)W(\mathcal{S} \rightarrow \mathcal{S}')], \quad (\text{A.6})$$

which is simply a continuity equation for the conserved quantity $P_{\text{sim}}(\mathcal{S})$; on the rhs of Eq. (A.6) the first term denotes the amount of probability entering the state \mathcal{S} and the second term the amount of probability leaving \mathcal{S} in the time step $t \rightarrow t+1$. Thus, a sufficient, though not necessary, condition for the Boltzmann distribution to be a stationary probability density $P(\mathcal{S}, t) = P(\mathcal{S})$ of the chain is given by the postulate of *detailed balance* for the transition probabilities W ,

$$W(\mathcal{S} \rightarrow \mathcal{S}')P_{\text{eq}}(\mathcal{S}) = W(\mathcal{S}' \rightarrow \mathcal{S})P_{\text{eq}}(\mathcal{S}'). \quad (\text{A.7})$$

To guarantee not only stationarity of the Boltzmann distribution, but the *convergence* of P_{sim} to P_{eq} , is more intricate. However, this convergence can be proved under the additional condition of *ergodicity* of the Markov chain. For a finite number of states, ergodicity means that with a finite probability the chain will adopt any of these states after a finite number of steps, irrespective of the initial conditions. For an infinite number of discrete states or a continuum of states this notion has to be suitably generalized. For the case of a finite number of states, the convergence

property is known as Markov's ergodicity theorem [262]. A recent compilation of proofs of the convergence of the MC process can be found in Ref. [263].

Therefore, an importance sampling Monte Carlo simulation scheme satisfying the conditions of detailed balance and ergodicity is guaranteed to converge to the Boltzmann distribution and thermal averages are given by the simple time-series average (A.4). While ergodicity is a property of the set of considered *update moves* $\mathcal{S} \rightarrow \mathcal{S}'$ (such as, e.g., single spin flips for a spin model), which have to be ensured to connect any two states of the system within a finite number of steps (at least for the case of a finite number of states), detailed balance is a condition to be fulfilled by the chosen transition probabilities $W(\mathcal{S} \rightarrow \mathcal{S}')$. The most commonly adopted choice is given by the Metropolis formula [264],

$$W(\mathcal{S} \rightarrow \mathcal{S}') = \min \{1, \exp(-\beta[\mathcal{H}(\mathcal{S}') - \mathcal{H}(\mathcal{S})])\}, \quad (\text{A.8})$$

which satisfies Eq. (A.7) as can be easily checked.

A.2 Autocorrelations and Dynamical Scaling

The Markovian nature of the stochastic process involved in the importance sampling Monte Carlo scheme entails the fact that subsequent system states generated in the chain are not statistically independent. The degree of correlation between subsequent realizations of a random variable A at times s and t is measured by the connected, *unnormalized autocorrelation function*

$$C_A(s, t) \equiv \langle A_s A_t \rangle - \langle A_s \rangle \langle A_t \rangle, \quad t \geq s. \quad (\text{A.9})$$

The stationarity of the process implies translation invariance $\langle A_s \rangle = \langle A_t \rangle \equiv \langle A \rangle$ and $\langle A_s A_t \rangle = \langle A_0 A_{t-s} \rangle$, so that we can consider $C_A(t) \equiv C_A(0, t)$. One can also define the *normalized autocorrelation function* of A ,

$$\rho_A(t) \equiv C_A(t)/C_A(0), \quad (\text{A.10})$$

such that $\rho_A(0) = 1$ and $\lim_{t \rightarrow \infty} \rho_A(t) = 0$. The autocorrelation function is generically expected to decline exponentially, i.e.

$$C_A(t) \sim C_A(0)e^{-t/\tau(A)}, \quad (\text{A.11})$$

which defines the exponential *autocorrelation time* $\tau(A)$ which is specific to the considered process (i.e., MC dynamics) and the random variable (i.e., observable) A . Obviously, $C_A(0)$ is identical to the variance $\sigma^2(A)$ of A . In general the dynamics of a Monte Carlo process will be characterized by a *set* of different correlation times $\tau_0 \geq \dots \geq \tau_n$, where, potentially, $n \rightarrow \infty$. By *the* exponential correlation length $\tau(A)$ of an observable A we refer to the largest correlation length $\tau_0(A)$ present with non-vanishing amplitude in the dynamic spectrum of A , i.e. [169]

$$\tau_0(A) = \limsup_{t \rightarrow \infty} \frac{t}{-\ln \rho_A(t)} \quad (\text{A.12})$$

Note, however, that due to the possibility of a very small amplitude of the leading exponential, this correlation length could be suppressed as compared to the non-leading terms even for long, but finite time series.

The degree of dependence in *time* of successive states of a Markov chain generated by local moves (like single spin flips in a lattice spin model) is obviously linked to the strength of correlations of the system's degrees of freedom in *space*, i.e., the autocorrelation times are expected to grow with the spatial correlation length ξ . In the vicinity of a critical point, where clusters of pure phase states of all sizes constitute the typical configurations, autocorrelation times (in units of lattice sweeps) are observed to grow algebraically (*critical slowing down*),

$$\tau \propto \min(\xi, L)^z, \quad (\text{A.13})$$

where the *dynamical critical exponent* z is now on the basis of universality arguments expected to be independent of the observable under consideration. In a simplified dynamical model for a general local algorithm, the information about a local excitation within a pure phase region is assumed to travel diffusively, thus implying a random-walk exponent of $z = 2$. In real-world models, however, z like static critical exponents takes on a non-trivial value, which is for local dynamics close to but different from $z = 2$.

The precision of a time-series average $\bar{A} = (\sum_t A_t)/N$ from a Monte Carlo simulation is maximal for uncorrelated measurements A_t ; here, N denotes the length of the time series. The variance of the mean $\sigma^2(\bar{A}) \equiv \langle \bar{A}^2 \rangle - \langle \bar{A} \rangle^2$ for the case of correlated measurements is given by

$$\sigma^2(\bar{A}) = \frac{1}{N^2} \sum_{s,t=1}^N C_A(s,t) = \frac{2C_A(0)}{N} \left[\frac{1}{2} + \sum_{t=1}^{N-1} \rho_A(t) \left(1 - \frac{t}{N} \right) \right]. \quad (\text{A.14})$$

Abbreviating the factor in square brackets as $\tilde{\tau}_{\text{int},N}(A)$, this expression can be rearranged with $C_A(0) = \sigma^2(A)$ to give

$$\sigma^2(\bar{A}) = \frac{\sigma^2(A)}{N/2\tilde{\tau}_{\text{int},N}(A)} \approx \frac{\sigma^2(A)}{N/2\tilde{\tau}_{\text{int},\infty}(A)}, \quad N \gg 1. \quad (\text{A.15})$$

For historical and technical reasons (stemming from spectral analysis, cf. Ref. [265]), the *integrated autocorrelation time* is not defined as $\tilde{\tau}_{\text{int},\infty}(A)$, but omitting the factor $(1 - t/N)$ as

$$\tau_{\text{int}}(A) \equiv \tau_{\text{int},\infty}(A) \equiv \frac{1}{2} + \sum_{t=1}^{\infty} \rho_A(t), \quad (\text{A.16})$$

which, for an exponentially decaying autocorrelation function $\rho(t)$ only differs by an exponentially small amount from $\tilde{\tau}_{\text{int},\infty}(A)$, such that, for practical purposes, both definitions are equivalent. Thus, if we define,

$$N_{\text{eff}} = \frac{N}{2\tau_{\text{int}}(A)}, \quad (\text{A.17})$$

the variance still vanishes inversely linear with the number of measurements, but with N replaced by the effective number of *independent* measurements N_{eff} .

The relation between the exponential and integrated autocorrelation times, $\tau_0(A)$ and $\tau_{\text{int}}(A)$, is obvious for the purely exponential form of $\rho_A(t)$ of Eq. (A.11); then, we have

$$\tau_{\text{int}}(A) = \frac{1}{2} \left(\frac{1 + e^{-1/\tau_0(A)}}{1 - e^{-1/\tau_0(A)}} \right) \approx \tau_0(A). \quad (\text{A.18})$$

For a spectrum of $\rho_A(t)$ containing higher order excitations $\tau_i(A)$, $i > 0$, one can show that Eq. (A.18) has to be replaced by [266]

$$\tau_{\text{int}}(A) \leq \tau_0(A). \quad (\text{A.19})$$

Also, then, one can ask, whether the dynamical critical exponents of Eq. (A.13) associated with the two types of autocorrelation times coincide. This is not generally the case; instead from Eq. (A.19) it is obvious that

$$z_{\text{int}} \leq z_0, \quad (\text{A.20})$$

and cases where $z_{\text{int}} < z_0$ have been observed [267].

A.3 Binning and the Jackknife

A.3.1 The binning technique

As discussed in Appendix A.2 above, the fact that the importance sampling method utilizes a stochastic Markov process for the generation of the Monte Carlo integration points, entails autocorrelations between successive configurations of the system. As far as the analysis of the resulting time series A_t of observable measurements is concerned, these autocorrelations are rather unpleasant, since the statistical analysis of time series is much simpler for uncorrelated data, see, e.g., Refs. [265, 268]. For instance, to evaluate the variance of the mean value \bar{A} of an autocorrelated time series, according to Eq. (A.15) one has to estimate the *integrated autocorrelation time* $\tau_{\text{int}}(A)$ first, which is not completely straightforward and computationally quite expensive, cf. Appendix A.4. Apart from that, advanced analysis tools such as the “jackknife” method to be described below can only be applied to a set of “iid” (identically and independently distributed) random variables. The blocking process discussed in the following re-arranges the simulation data in a way such as to generate an effectively uncorrelated time series, thus alleviating the above-mentioned problems.

The *binning* approach exploits the observation that the combination of neighbouring entries of the time series of length N to sub-averages,

$$A'_t = \frac{1}{2}(A_{2t-1} + A_{2t}), \quad N' = \frac{N}{2}, \quad (\text{A.21})$$

results in a less correlated new time series A'_t of (smaller) length N' as long as the correlations of the original time series decay fast enough. This has some important consequences for the estimation of the variance of the mean from the transformed time series. Obviously, the mean value \bar{A} and its variance $\sigma^2(\bar{A})$ are not affected by this transformation. However, the variance $\sigma^2(A) = C_A(0)$ of a single measurement transforms as [269],

$$\sigma^2(A') = \frac{1}{2}[C_A(0) + C_A(1)], \quad (\text{A.22})$$

where $C_A(t)$ denotes the autocorrelation function of A defined by Eq. (A.9). That is, a part of the autocorrelations, namely the one-step-distance part $C_A(1)$, is being incorporated into the variance $\sigma^2(A')$ of the transformed variable A' . Now, from Eq. (A.14) it is obvious that $C_A(0)/N$ is a lower bound of the variance $\sigma^2(\bar{A})$ and for

the transformed variables one finds,

$$\sigma^2(\bar{A}) = \sigma^2(\bar{A}') \geq \frac{C'_A(0)}{N'} = \frac{C_A(0)}{N} + \frac{C_A(1)}{N}, \quad (\text{A.23})$$

such that the sequence $C_A^{(k)}(0)/N^{(k)}$ resulting from k successive applications of the binning transformation (A.21) is bounded and monotonous as long as the autocorrelation function $C_A(t)$ decays faster than $1/t$ [269]. Thus, the sequence $C_A^{(k)}(0)/N^{(k)}$ is convergent, and its fixed point value $C_A^*(0)/N^*$ is the variance $\sigma^2(\bar{A})$ of the mean. On the other hand, from Eq. (A.14) this implies that the higher order autocorrelations $C_A^*(t)/N^*$, $t > 0$ vanish at this fixed point. Therefore, the fixed point time series is uncorrelated and for the estimate of the variance of its mean, the naïve formula can be employed [268],

$$\sigma^2(\bar{A}) = \sigma^2(\bar{A}^*) = \left\langle \frac{1}{N^* - 1} \hat{C}_A^*(0) \right\rangle \equiv \left\langle \frac{1}{N^*(N^* - 1)} \sum_{t=1}^{N^*} (A_t^* - \bar{A}^*)^2 \right\rangle. \quad (\text{A.24})$$

In practice, the estimates $\hat{C}_A^{(k)}(0)/(N^{(k)} - 1)$ are evaluated after each application of the binning transformation. According to the preceding discussion, they are expected to grow monotonously and to settle down on the plateau value $\hat{C}_A^*(0)/(N^* - 1)$ as soon as “enough” binning transformations have been performed. While in theory this requires infinitely many of such transformations, in practice it suffices to do this $k = \kappa \log_2 \tau_{\text{int}}(A)$ times with a factor κ of the order of 10^1 to shift the effect of autocorrelations below the noise of the statistical fluctuations. This is due to the fact that for the usual Monte Carlo dynamics autocorrelations in fact decline exponentially and not only algebraically, cf. Appendix A.2 above.

A.3.2 Jackknife bias and variance estimates

In this section we consider a Monte Carlo time series A_t which is uncorrelated, i.e., which either comes from a simple sampling MC simulation or is already the result of a re-blocking of the original time series via the binning scheme of the previous section. The length n of the time series then corresponds to the number of blocks used in the binning transformation. The analysis of stationary, uncorrelated time series can be generally described as the estimation of some parameter $f(F)$ of the underlying probability density $F(A)$ of the random variable (observable) A by consideration of the sampled density $\hat{F} = [\sum_t \delta(A - A_t)]/n$. The two main issues related to this estimation are the question of its *bias*, i.e. how far on average the

estimate is from the expected value, and the need to determine the *accuracy* of the estimate in terms of the present statistical fluctuations. For reviews of the jackknife and other resampling schemes see Refs. [270, 271].

Bias reduction

The *bias* of the estimate $f(\hat{F})$ of the parameter $f(F)$ is given by

$$\text{BIAS} \equiv \langle f(\hat{F}) \rangle - f(F). \quad (\text{A.25})$$

For the parameters f commonly considered in MC simulations, the bias depends analytically on the length n of the time series, so one can expand²

$$\langle f(\hat{F}) \rangle = f(F) + \frac{a_1}{n} + \frac{a_2}{n^2} + \dots \quad (\text{A.26})$$

For time series analyses of MC data, the parameter f will most often be a function of the expectation value $\langle A \rangle$, i.e. $f(F) = f(\langle A \rangle)$, and the estimate is given by replacing the expectation by the mean, i.e. $\hat{f} \equiv f(\hat{F}) = f(\bar{A})$. We will discuss this case here, the generalization to more general situations being straightforward. Obviously, the identity $f(\langle A \rangle) = \langle A \rangle$ can be estimated without bias by $f(\bar{A}) = \bar{A}$. For non-linear functions f , however, in general a bias will occur that, to first order, vanishes as $1/n$ for large lengths n of the time series. Denoting the expectation value $\langle f(\bar{A}) \rangle$ from a time series of length n as E_n , from Eq. (A.26) one reads off that, to first order in $1/n$,

$$\frac{E_n - E_\infty}{E_{n-1} - E_n} = \frac{1/n}{1/(n-1) - 1/n}, \quad (\text{A.27})$$

such that the true expectation value $E_\infty = f(\langle A \rangle)$ can be estimated by

$$E_\infty = nE_n - (n-1)E_{n-1}. \quad (\text{A.28})$$

Thus, if one can construct an estimate for the expectation values E_{n-1} for time series of length $n-1$ from the original series of length n , a bias-reduced estimator for $E_\infty = f(\langle A \rangle)$ can be easily found. The simple trick on which the *jackknife resampling scheme* is based, is the observation that n time series of length $n-1$ can be constructed from a series of length n by *omitting* in each series a single measurement A_s . That is, one considers the jackknife empirical densities

$$\hat{F}_{(s)}(A) \equiv \frac{1}{n-1} \sum_{t \neq s} \delta(A - A_t), \quad s = 1, \dots, N. \quad (\text{A.29})$$

²Note, that in contrast to many of the textbook formulae of statistics we do not have to assume a Gaussian distribution here.

From the corresponding jackknife block averages,

$$\bar{A}_{(s)} = \frac{1}{n-1} \sum_{t \neq s} A_t, \quad (\text{A.30})$$

jackknife estimates for the expectation value E_{n-1} and their average are given by

$$\begin{aligned} \hat{f}_{(s)} &= f(\bar{A}_{(s)}), \\ \hat{f}_{(\cdot)} &= \frac{1}{n} \sum_{s=1}^n \hat{f}_{(s)}. \end{aligned} \quad (\text{A.31})$$

From Eq. (A.28) the jackknife bias-reduced estimator of $f(\langle A \rangle)$ is therefore given by

$$\tilde{f} = n\hat{f} - (n-1)\hat{f}_{(\cdot)}, \quad (\text{A.32})$$

and, correspondingly, the jackknife or *Quenouille estimator of bias* is given by [270],

$$\widehat{\text{BIAS}}(\hat{f}) = (n-1)(\hat{f}_{(\cdot)} - \hat{f}). \quad (\text{A.33})$$

From the expansion (A.26) it is obvious that the improved estimator \tilde{f} now merely has a bias proportional to $1/n^2$ instead of $1/n$. In principle, this process of bias reduction can be iterated to also remove higher-order bias contributions. It should be clear, however, that the variance of \tilde{f} will in general be larger than that of the original estimator \hat{f} . Thus, a reduction of bias is paid for by an increase in statistical fluctuations. Therefore, a (further) reduction of bias is only sensible if the bias is (at least) of the same order of magnitude as the variance of the considered observable.

Variance estimation

A quantification of the statistical accuracy of a parameter estimation is given by its variance. While, again, an estimation of this parameter is straightforward for the trivial case $\hat{f} = f(\bar{A}) = \bar{A}$, where an unbiased estimate of variance is given by

$$\hat{\sigma}^2(\bar{A}) = \frac{1}{n(n-1)} \sum_{t=1}^n (A_t - \bar{A})^2, \quad (\text{A.34})$$

for non-linear functions $f(\bar{A})$ an unbiased variance estimate can in general not be constructed. This problem is often solved by the application of well-known error propagation formulae [170]. These assume a Gaussian distribution of the observable \bar{A} , which is approximately the case for long enough time series thanks to the central

limit theorem. However, there is no simple way to quantify the systematical error entailed by this approximation. Furthermore, the analytic form of the function f is needed for the error propagation, which is not always known, for example when f denotes the operation of finding the location of the maximum of the specific heat as a function of temperature found by a reweighting analysis of a time series of energy measurements.

A brute-force ansatz for the evaluation of variances of parameter estimates would be to perform k independent MC simulations of length n/k each and to evaluate the desired parameter estimates \hat{f}_i , $i = 1, \dots, k$. Then the analogue of the naïve variance estimate (A.34) can be applied to this set of time series,

$$\hat{\sigma}^2(\hat{f}) = \frac{1}{k(k-1)} \sum_{i=1}^k (\hat{f}_i - \bar{\hat{f}})^2, \quad (\text{A.35})$$

with a bias of at most $O(k/n)$ and a variance of $O(1/k)$. In contrast, applying (A.34) directly on the level of the measurements of a single time series would result in a bias which is $O(1)$. Eq. (A.35) corresponds to the plain blocking or binning scheme presented in the previous section applied to an uncorrelated time series. However, one can improve on this and find an estimator with bias and variance $O(1/n)$ using the jackknifing idea. Interpreting the jackknife blocks of Eq. (A.31) as the outcomes of n simulations with time series of length $n-1$ one can write down an estimate of the type (A.35). This, however, would neglect the large but trivial correlations between these n series, which differ only by one measurement each. Yet, as it turns out [270], the effect of these correlations is simply an under-estimation of the variance by a factor of $1/(n-1)^2$, which can be easily amended. Therefore, the *jackknife estimate of variance* of \hat{f} is given by

$$\widehat{\text{VAR}}(\hat{f}) = \frac{n-1}{n} \sum_{s=1}^n [\hat{f}_{(s)} - \hat{f}_{(\cdot)}]^2, \quad (\text{A.36})$$

with a bias which is $O(1/n)$. The fact that the effect of the correlations between the jackknife blocks can simply be corrected for by a multiplication with $(n-1)^2$ can be easily checked for the trivial case of $\hat{f} = \bar{A}$. For more general parameter estimates, one has to assume certain analyticity properties of the parameters f as a function of n [270]. In general, it can be shown [270] that the jackknife variance estimate is conservative in the following sense,

$$\left\langle \frac{n}{n-1} \widehat{\text{VAR}}(\hat{f}) \right\rangle \geq \sigma_{n-1}^2(\hat{f}), \quad (\text{A.37})$$

where $\sigma_{n-1}^2(\hat{f})$ denotes the true variance of the estimate \hat{f} from time series of length $n - 1$.

Finally, it should be noted that the jackknife bias reduction and variance estimation techniques can be combined to assess the variance of the bias-reduced estimates \tilde{f} of Eq. (A.32). For this purpose, the jackknife blocking scheme has to be iterated to second order, leading to a matrix of jackknife blocks of length $n - 2$. The corresponding formulae are given in Ref. [272].

A.4 Estimation of Autocorrelation Times

Given a realisation of the time series A_t of length N the autocorrelation function Eq. (A.9) can be estimated as

$$\hat{C}_A(t) = \frac{1}{N-t} \sum_{s=1}^{N-t} (A_s - \bar{A})(A_{s+t} - \bar{A}), \quad (\text{A.38})$$

where

$$\bar{A} = \frac{1}{N} \sum_{t=1}^N A_t. \quad (\text{A.39})$$

However, the estimate Eq. (A.38) is not unbiased; in fact, it can be shown [268] that its bias is approximately given by $-\sigma^2(A)\tau_{\text{int}}(A)/N$, so that it is still asymptotically unbiased for $N \gg \tau_{\text{int}}(A)$, which is anyway a necessary condition for reliable and accurate parameter estimates from finite-length time series. Alternatively, $C_A(t)$ can be estimated by

$$\hat{C}_A(t) = \frac{1}{N-t} \sum_{s=1}^{N-t} A_s A_{s+t} - \bar{A}^2, \quad (\text{A.40})$$

which is also not unbiased due to the bias of the second term. For time series with, e.g., $N \gtrsim 10\,000 \tau_{\text{int}}$, typically occurring in Monte Carlo simulations, the two estimates (A.38) and (A.40) are nearly indistinguishable. The second estimate Eq. (A.40) is computationally somewhat more convenient since the estimate \bar{A} can be computed within the same loop as the estimate for $\langle A_s A_{s+t} \rangle$. From this, the normalized autocorrelation function can be estimated by

$$\hat{\rho}_A(t) = \hat{C}_A(t)/\hat{C}_A(0), \quad (\text{A.41})$$

which is also a biased estimate; for the rather long times series needed for the estimation of autocorrelation times, however, this bias can be rather safely neglected.

An estimate of the exponential autocorrelation time $\tau_0(A)$ follows from a three-parameter fit of $\hat{C}_A(t)$ to the functional form

$$\hat{C}_A(t) = \hat{C}_A(0) \exp(-t/\hat{\tau}_0(A)) + \text{const}, \quad (\text{A.42})$$

where the additive constant should be included to account for the statistical uncertainty in the estimation of the disconnected part $\langle A \rangle^2$ [273]. An alternative set of estimates that eliminate variance and bias connected to the additive and multiplicative constants is given by [274]

$$\hat{\tau}_0(A; t) = \Delta \left[\ln \frac{\hat{C}_A(t) - \hat{C}_A(t - \Delta)}{\hat{C}_A(t + \Delta) - \hat{C}_A(t)} \right]^{-1}, \quad (\text{A.43})$$

where the free parameter Δ can be used to tune the signal-noise ratio to an optimum. For a final estimate of $\tau_0(A)$ an average over different distances t in Eq. (A.43) should be performed, taking the covariances of the estimates $\hat{\tau}_0(A; t)$ for different offsets t into account [274].

Of more interest also for the analysis of static behaviour of model systems is the integrated autocorrelation time $\tau_{\text{int}}(A)$. Unfortunately, the obvious estimator,

$$\hat{\tau}_{\text{int},N}(A) = \frac{1}{2} + \sum_{t=1}^{N-1} \hat{\rho}_A(t), \quad (\text{A.44})$$

which would also be used to approximately estimate $\tau_{\text{int}}(A) \equiv \tau_{\text{int},\infty}(A)$, is very badly-behaved statistically. Since the number of data points used for the estimate $\hat{\rho}_A(t)$ of Eq. (A.41) decreases with the distance t as $(N - t)$, the estimate $\hat{\rho}_A(t)$ becomes very noisy for large separations t . These variances of $\hat{\rho}_A(t)$ sum up to a total variance of $\hat{\tau}_{\text{int},N}(A)$ of Eq. (A.44) that does not vanish with $N \rightarrow \infty$ [265], thus destroying the reliability of the estimate $\tau_{\text{int}}(A)$. To circumvent this problem, one introduces a cut-off $M < N - 1$ in the distances t , i.e.,

$$\hat{\tau}_{\text{int},M}(A) = \frac{1}{2} + \sum_{t=1}^M \hat{\rho}_A(t), \quad (\text{A.45})$$

which, on the other hand, introduces an additional bias. Since an increase of M increases the variance of $\hat{\tau}_{\text{int},M}(A)$, but reduces the bias, the choice of M is a tradeoff between bias and variance. In practice, a self-consistent determination of the cut-off turns out to be useful [169], i.e. M is successively increased to the point where

$$M \approx \kappa \hat{\tau}_{\text{int},M}(A). \quad (\text{A.46})$$

For the usual lengths of time series in Monte Carlo simulations of $N > 10\,000$ τ_{int} , a cut-off parameter of $\kappa \approx 6$ turns out to be a sensible choice [210]. The variance of the estimate $\hat{\tau}_{\text{int},M}(A)$ can be approximately found from straightforward but tedious calculations [169, 265, 268] for $\tau_{\text{int}} \ll M \ll N$ to be

$$\sigma^2 [\hat{\tau}_{\text{int},M}(A)] \approx \frac{2(2M+1)}{N} \tau_{\text{int}}^2(A). \quad (\text{A.47})$$

A more accurate determination of the estimator variance can be constructed with the jackknife technique, cf. Appendix A.3. Define jackknife block estimates for n blocks of the autocorrelation function as

$$\hat{C}_A^{(\alpha)}(t) \equiv \frac{1}{N} \frac{n}{n-2} \sum_{s \in \mathcal{T}_\alpha} A_s A_{s+t} - \left(\frac{1}{N} \frac{n}{n-2} \sum_{s \in \mathcal{T}_\alpha} A_s \right)^2, \quad t < N/n \quad (\text{A.48})$$

where $\alpha = 1, \dots, n$ and

$$\mathcal{T}_\alpha \equiv \{0 < i \leq (\alpha-1)N/n\} \cup \{\alpha N/n < i \leq (n-1)N/n\}, \quad i \in \mathbb{N}. \quad (\text{A.49})$$

Then, from the resulting jackknife block estimates of $\tau_{\text{int}}(A)$,

$$\begin{aligned} \hat{\tau}_{\text{int},M}^{(\alpha)}(A) &\equiv \frac{1}{2} + \sum_{t=1}^M \hat{C}_A^{(\alpha)}(t) / \hat{C}_A^{(\alpha)}(0), \\ \hat{\tau}_{\text{int},M}^{(\cdot)}(A) &\equiv \frac{1}{n} \sum_{\alpha=1}^n \hat{\tau}_{\text{int},M}^{(\alpha)}(A), \end{aligned} \quad (\text{A.50})$$

the jackknife estimate of variance for $\hat{\tau}_{\text{int},M}(A)$, $M < N/n$, is given by

$$\widehat{\text{VAR}}[\hat{\tau}_{\text{int},M}(A)] = \frac{n-1}{n} \sum_{\alpha=1}^n \left[\hat{\tau}_{\text{int},M}^{(\alpha)}(A) - \hat{\tau}_{\text{int},M}^{(\cdot)}(A) \right]^2. \quad (\text{A.51})$$

An alternative estimate of $\tau_{\text{int}}(A)$ can be found from Eq. (A.15),

$$\tau_{\text{int},n}(A) \approx \frac{1}{2} \frac{\sigma^2(\bar{A})}{\sigma^2(A)/N}, \quad (\text{A.52})$$

where the “ \approx ” accounts for the difference between $\tau_{\text{int},n}(A)$ and the factor in square brackets of Eq. (A.14) that is negligible for all practical purposes. Considering the usual n -block jackknife estimate of the variance of \bar{A} ,

$$\widehat{\text{VAR}}_n(\bar{A}) \equiv \frac{n-1}{n} \sum_{s=1}^n [A_{(s)} - A_{(\cdot)}]^2, \quad (\text{A.53})$$

a jackknife estimate of the integrated autocorrelation time is given by

$$\hat{\tau}_{\text{int},n}(A) \equiv \frac{1}{2} \widehat{\text{VAR}}_n(\bar{A}) / \widehat{\text{VAR}}_N(\bar{A}), \quad (\text{A.54})$$

where, as usual, n has to be chosen such that the jackknife blocks are approximately independent statistically; this is commonly achieved by monitoring the value of $\widehat{\text{VAR}}_n(\bar{A})$ on increasing n , until a plateau value is reached. An estimate for the variance of $\hat{\tau}_{\text{int},n}(A)$ can be found from iterating the jackknife procedure to second order, i.e., in the usual notation,

$$\widehat{\text{VAR}}_n(\widehat{\text{VAR}}_n(\bar{A})) = \frac{n-1}{n} \sum_{s=1}^n [\widehat{\text{VAR}}_{n-1}^{(s)}(\bar{A}) - \widehat{\text{VAR}}_{n-1}^{(\cdot)}(\bar{A})]^2, \quad (\text{A.55})$$

such that

$$\hat{\sigma}^2[\hat{\tau}_{\text{int},n}(\bar{A})] \equiv \frac{1}{4} \frac{\widehat{\text{VAR}}_n(\widehat{\text{VAR}}_n(A))}{\widehat{\text{VAR}}_N^2(\bar{A})}, \quad (\text{A.56})$$

where the variance of $\widehat{\text{VAR}}_N(\bar{A})$ has been neglected due to its suppression by $\tau_{\text{int}}(A)/N$ compared to the variance of $\widehat{\text{VAR}}_n(\bar{A})$.

A.5 Histogram Reweighting

As it has been described in Section A.1, a single importance-sampling Monte Carlo simulation yields statistically exact information about thermal averages of a system of statistical mechanics only at a single point of the coupling parameter space. For simplicity, we restrict ourselves to the case of the (inverse) temperature β as the only present coupling. Implicitly, however, the gathered data contains temperature independent information about the system. Within the importance sampling scheme, the probability density of the system energies at the inverse temperature β_0 ,

$$p_{\beta_0}(E) = \frac{1}{Z_{\beta_0}} \Omega(E) e^{-\beta_0 E}, \quad (\text{A.57})$$

is sampled by the normalized energy histogram $\hat{H}_{\beta_0}(E)$, i.e., $\langle \hat{H}_{\beta_0}(E) \rangle = p_{\beta_0}(E)$. Here, $\Omega(E)$ denotes the density of energy states of the system. Since the temperature dependence of $p_{\beta_0}(E)$ is explicit, i.e., the non-trivial term $\Omega(E)$ does not depend on β_0 , one has the following basic relation,

$$p_{\beta}(E) = W_{\beta-\beta_0}(E) p_{\beta_0}(E) \equiv \frac{\exp[-(\beta - \beta_0)E]}{\sum_E p_{\beta_0}(E) \exp[-(\beta - \beta_0)E]} p_{\beta_0}(E), \quad (\text{A.58})$$

which is the starting point for the *reweighting* procedure in the importance sampling scheme [275, 276]. Thus, obtaining information about the system at the coupling β from a simulation at β_0 amounts to the application of the *reweighting factors* $W_{\beta-\beta_0}(E)$. Therefore, from the estimate $\hat{H}_{\beta_0}(E)$, the distribution at a different inverse temperature β can be evaluated as

$$\hat{H}_\beta(E) = \hat{W}_{\beta-\beta_0}(E) \hat{H}_{\beta_0}(E) \equiv \frac{\exp[-(\beta - \beta_0)E]}{\sum_E \hat{H}_{\beta_0}(E) \exp[-(\beta - \beta_0)E]} \hat{H}_{\beta_0}(E). \quad (\text{A.59})$$

Consequently, estimates of expectation values of temperature dependent observables $A(E)$ at β are given by

$$\hat{A}_\beta = \sum_E \hat{H}_\beta(E) A(E). \quad (\text{A.60})$$

In terms of the time series (E_t, A_t) of energy and observable measurements at β_0 , this can be written as

$$\hat{A}_\beta = \sum_t \hat{W}_{\beta-\beta_0}(t) A_t \equiv \sum_t \frac{\exp[-(\beta - \beta_0)E_t]}{\sum_t \exp[-(\beta - \beta_0)E_t]} A_t. \quad (\text{A.61})$$

For the reweighting of observables A , whose value for a given system configuration is not uniquely defined by the configurational energy (such as, e.g., the magnetization), one has to construct micro-canonical (fixed-energy) averages $\langle A \rangle_E$, which then can be treated as the observables $A(E)$ above.

While the given relations are statistically exact for arbitrary choices of β , in practice the quality of the estimates strongly depends on the separation $\beta - \beta_0$. Since in the importance sampling process events are sampled only in the vicinity of the rather narrow peak(s) of the energy histogram, whose positions strongly depend on the inverse temperature β , for too large separations $\beta - \beta_0$ the histogram $\hat{H}_{\beta_0}(E)$ eventually contains no entries for the region of E receiving large weights from the reweighting factors $\hat{W}_{\beta-\beta_0}(E)$. The reliability of the reweighting process for a given inverse temperature β is conveniently assured by monitoring the *overlap* $\mathcal{O}_E(\beta - \beta_0)$ of the corresponding energy histograms at the couplings β_0 and β , i.e.,

$$\mathcal{O}_E(\beta - \beta_0) = \sum_E \min[\hat{H}_{\beta_0}(E), \hat{H}_\beta(E)] = \sum_t \min[1/T, \hat{W}_{\beta-\beta_0}(t)], \quad (\text{A.62})$$

where T denotes the length of the time series. For the reweighting to work reliably, the overlap should exceed a certain threshold, say $2/3$. Thus, reweighting is mostly useful in the vicinity of critical points, where the corresponding energy distributions are rather broad, ensuring a non-trivial size $|\beta - \beta_0|$ of the region where reweighting

works reliably. Note that suitably evaluated statistical errors of the reweighted estimates do *not* (or only partially) reflect the error stemming from a lack of overlap of the relevant histograms, since the (undefined) relative variance of energy bins with no entries is usually assumed to be zero. For the reweighting of observables related to the magnetization, it is sometimes convenient to also consider the overlap $\mathcal{O}_M(\beta - \beta_0)$ of the magnetization histograms, which can be easily defined in terms of the two-dimensional histogram $\hat{H}(E, M)$. Note that in general an absolute threshold for the overlap can not guarantee reliability of the reweighting process, since observables can be defined to use more and more data from the far wings of the energy (or magnetization) distributions by including terms with large-order moments $\langle E^k \rangle$ or $\langle M^k \rangle$, $k \gg 1$. In addition to the fluctuations, the reweighting process entails a *bias* of the reweighted estimates, which also results from missing histogram entries and vanishes as $1/T$ with the length of the time series.

Appendix B

Graph Embedding and Visualization

In contrast to embedded string and lattice random surface models, the dynamical triangulations (or, more generally, dynamical polygonifications) model as defined in Chapter 2 describes abstract graphs without any reference to an embedding space. Obviously, this is what one would expect from a discretised theory of quantum gravity, which should be formulated entirely in terms of intrinsic variables such as the intrinsic metric tensor. However, for practical purposes and, especially, for the visualization of the resulting abstract surfaces, the possibility of an embedding of the two-dimensional graphs into three-dimensional Euclidean space is highly desirable. In connection with suitable software for three-dimensional visualization such as the OpenGL API [277], an embedding allows for quite decorative and, more importantly, physically very instructive representations of graphs of the considered ensembles. For the pure gravity model, the corresponding representation provides a visualization of the fractal structure of the graphs, being described as that of a self-similar tree of baby universes [29]. Furthermore, encoding discrete matter variables coupled to the vertices or faces of the graphs by a suitable colouring of these entities, the interactions between space-time and matter can be directly “observed”. Especially, the influence of the tendency of (partially) ordered spin models to minimize the boundaries between pure-phase regions on the branching properties of the baby universe tree is directly visible, see also Section 2.4.

For visualization purposes, one should concentrate on the polygonifications, since the *faces* are planar there (the types of polygons being restricted to triangles or

squares). Thus, when considering ϕ^3 or ϕ^4 graphs, they should be transformed to the dual triangulations resp. quadrangulations. Additionally, the square faces of the quadrangulations are divided into two triangles for the visualization with the OpenGL package. Since the faces of the polygonifications are assumed to be equilateral, the embedding problem is in principle a combinatorial one: the number of equilateral polygons meeting at a given vertex (i.e., its co-ordination number) determines the configuration of such a “dome” or “trough” of polygons uniquely up to a finite number of discrete transformations. Thus, for any finite, planar polygonification there are only a finite number of representations satisfying the constraint of equilaterality, which could be successively tested to find an embedding without edge intersections. Practically, however, we find this not very convenient since the number of possible configurations still grows exponentially with the number of graph vertices. Thus, instead, we revert to an adaptive embedding algorithm.

Although the considered graphs are planar and can thus be drawn in the plane, this is obviously impossible if the equilaterality constraint should be observed at the same time. Also, the fractal structure is much better visible for a spherical representation. Hence, the embedding procedure is split into three sub-steps:

1. Find a *planar* embedding of the triangulation or quadrangulation, i.e., draw it in the plane ensuring that no two edges intersect.
2. Project this embedding stereographically onto the unit sphere.
3. Approximately satisfy the equilaterality constraint by the simulation of a generalized spring embedder.

The problem of planarity testing and the construction of plane embeddings of planar graphs has received much attention in algorithmic theory and several efficient, but mostly quite complex, solutions have been put forward. For the first time, it has been shown by Tarjan *et al.* [278] (see also Refs. [164, 279]) that planarity of a graph can be tested in $O(V + E)$ time, where V denotes the number of vertices and E the number of edges of the graph. We use this algorithm, which produces a valid planar embedding in the course of the test (for a planar graph). However, it does not pay any attention to the length of the edges, which are thus arbitrarily adapted to eliminate edge crossings. In the second step, the resulting plane embedding is stereographically projected onto a sphere, i.e., from the co-ordinates (x, y) in the

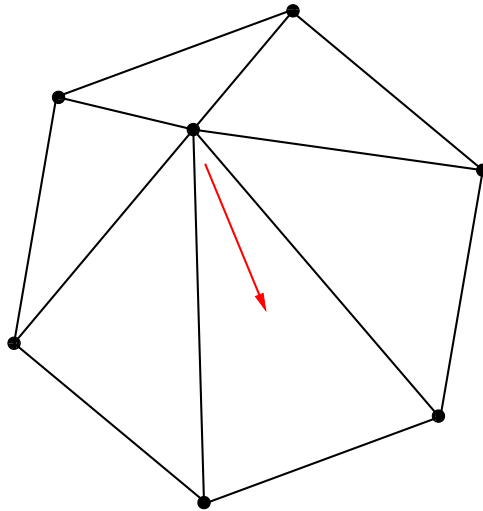


Figure B.1: Force trying to unify the lengths of the edges adjacent to a single vertex of a dynamical triangulation.

plane, co-ordinates (x', y', z') on the unit sphere are found as

$$\begin{aligned} (x', y', z') &= (x/r^2, y/r^2, 1/2 - 1/r^2), \\ r^2 &= 1 + x^2 + y^2. \end{aligned} \tag{B.1}$$

This transformation has the advantage of not producing any edge intersections since the mapping preserves angles. Finally, to bring the postulate of equal edge lengths into play, a generalized spring embedder is iteratively solved, i.e., we assume two-body forces (“springs”) between the vertices of the polygonification embedded on the sphere trying to unify the edge lengths,

$$\mathbf{F}_{ij} = F_0 \frac{|\mathbf{r}_{ij}| - r_0}{r_0} \frac{\mathbf{r}_{ij}}{|\mathbf{r}_{ij}|}, \tag{B.2}$$

where \mathbf{r}_{ij} denotes the difference vector between vertices i and j , r_0 is the desired common edge length and F_0 denotes the force strength, i.e., a free parameter to be adjusted. These forces are iteratively evaluated until the system has relaxed into a steady state, adjusting the time steps such as to prevent edge and face intersections from occurring. Additionally, a second type of interactions is assumed, which moves a single vertex with respect to all its neighbours, trying to unify the lengths of the involved edges, cf. Fig. B.1. Both types of forces are applied alternately, until the system has converged into a steady state.

Note that this combined algorithm cannot *guarantee* the absence of edge or face intersections for the final embedding. However, a suitable adaption of the inherent parameters ensures this with only a few local exceptions. Furthermore, full equality of edge lengths is not achieved, but the overall structure of the resulting graphs is clearly resolved, as can be seen from the corresponding figures presented in the main text.

Bibliography

- [1] N. Seiberg and E. Witten, “String theory and noncommutative geometry,” JHEP **9909**, 032 (1999).
- [2] D. Weingarten, “Euclidean quantum gravity on a lattice,” Nucl. Phys. B **210**, 229 (1982).
- [3] J. Ambjørn, B. Durhuus, and J. Fröhlich, “Diseases of triangulated random surface models, and possible cures,” Nucl. Phys. B **257**, 433 (1985).
- [4] F. David, “Planar diagrams, two-dimensional lattice gravity and surface models,” Nucl. Phys. B **257**, 45 (1985).
- [5] V. A. Kazakov, I. Kostov, and A. A. Migdal, “Critical properties of randomly triangulated planar random surfaces,” Phys. Lett. B **157**, 295 (1985).
- [6] P. di Francesco, P. Ginsparg, and J. Zinn-Justin, “2D gravity and random matrices,” Phys. Rept. **254**, 1 (1993).
- [7] J. Ambjørn, J. Jurkiewicz, and Y. Watabiki, “Dynamical triangulations, a gateway to quantum gravity?,” J. Math. Phys. **36**, 6299 (1995).
- [8] J. Ambjørn, “Quantization of geometry,” In *Fluctuating Geometries in Statistical Mechanics and Field Theory*, F. David, P. Ginsparg, and J. Zinn-Justin, eds., 1994 Les Houches Summer School, Session XLII (North-Holland, Amsterdam, 1996).
- [9] D. A. Johnston, “Gravity and random surfaces on the lattice — A review,” Nucl. Phys. B (Proc. Suppl.) **53**, 43 (1996).
- [10] J. Ambjørn, B. Durhuus, and T. Jonsson, *Quantum Geometry — A Statistical Field Theory Approach* (Cambridge University Press, Cambridge, 1997).

- [11] Z. Burda, “Lattice models of random geometries,” *Act. Phys. Polon. B* **29**, 573 (1998).
- [12] J. Ambjørn, J. Jurkiewicz, and R. Loll, “Lorentzian and Euclidean quantum gravity — Analytical and numerical results,” preprint hep-th/0001124 (unpublished).
- [13] W. P. Thurston, “Three-dimensional geometry and topology,” Math. Sci. Research Inst., Berkeley (1991).
- [14] J. Ambjørn, M. Carfora, and A. Marzuoli, *The Geometry of Dynamical Triangulations* (Springer, Berlin, 1997).
- [15] W. T. Tutte, “A census of planar triangulations,” *Can. J. Math.* **14**, 21 (1962).
- [16] E. Brézin, C. Itzykson, G. Parisi, and J.-B. Zuber, “Planar diagrams,” *Comm. Math. Phys.* **59**, 35 (1978).
- [17] M. L. Mehta, “A method of integration over matrix variables,” *Comm. Math. Phys.* **79**, 327 (1981).
- [18] M. L. Mehta, *Random Matrices*, 2nd ed. (Academic Press, San Diego, 1996).
- [19] G. 't Hooft, “A planar diagram theory for the strong interactions,” *Nucl. Phys. B* **72**, 461 (1974).
- [20] V. A. Kazakov, “Bilocal regularization of models of random surfaces,” *Phys. Lett. B* **150**, 282 (1985).
- [21] D. V. Boulatov, V. A. Kazakov, I. K. Kostov, and A. A. Migdal, “Analytical and numerical study of a model of dynamically triangulated random surfaces,” *Nucl. Phys. B* **275**, 641 (1986).
- [22] A. Billoire and F. David, “Scaling properties of randomly triangulated planar random surfaces: a numerical study,” *Nucl. Phys. B* **275**, 617 (1986).
- [23] P. Ginsparg and G. Moore, “Lectures on 2D gravity and 2D string theory,” Lectures given June 11–19, 1992 at TASI summer school, Boulder, CO, preprint hep-th/9304011.

- [24] F. David, “Simplicial quantum gravity and random lattices,” Lectures given July 5 – August 1, 1992 at Les Houches summer school, Session LVII, preprint hep-th/9303127.
- [25] J. Ambjørn, L. Chekhov, C. F. Kristjansen, and Y. Makeenko, “Matrix model calculations beyond the spherical limit,” Nucl. Phys. B **404**, 127 (1993).
- [26] H. Kawai, N. Kawamoto, T. Mogami, and Y. Watabiki, “Transfer matrix formalism for two-dimensional quantum gravity and fractal structures of space-time,” Phys. Lett. B **306**, 19 (1993).
- [27] Y. Watabiki, “Construction of noncritical string field theory by transfer matrix formalism in dynamical triangulation,” Nucl. Phys. B **441**, 119 (1995).
- [28] J. Ambjørn and Y. Watabiki, “Scaling in quantum gravity,” Nucl. Phys. B **445**, 129 (1995).
- [29] S. Jain and S. D. Mathur, “World-sheet geometry and baby universes in 2D quantum gravity,” Phys. Lett. B **286**, 239 (1992).
- [30] V. G. Knizhnik, A. M. Polyakov, and A. B. Zamolodchikov, “Fractal structure of 2d-quantum gravity,” Mod. Phys. Lett. A **3**, 819 (1988).
- [31] F. David, “Conformal field theories coupled to 2-d gravity in the conformal gauge,” Mod. Phys. Lett. A **3**, 1651 (1988).
- [32] J. Distler and H. Kawai, “Conformal field theory and 2-D quantum gravity,” Nucl. Phys. B **321**, 509 (1989).
- [33] V. A. Kazakov, “Ising model on a dynamical planar random lattice: Exact solution,” Phys. Lett. A **119**, 140 (1986).
- [34] D. V. Boulatov and V. A. Kazakov, “The Ising model on a random planar lattice: The structure of the phase transition and the exact critical exponents,” Phys. Lett. B **186**, 379 (1987).
- [35] Z. Burda and J. Jurkiewicz, “The Ising model on a random lattice with a coordination number equal 3,” Act. Phys. Polon. B **20**, 949 (1989).
- [36] V. A. Kazakov, “Percolation on a fractal with the statistics of planar Feynman graphs: exact solution,” Mod. Phys. Lett. A **4**, 1691 (1989).

- [37] J. M. Daul, “ Q -states Potts model on a random planar lattice,” preprint hep-th/9502014 (unpublished).
- [38] B. Eynard and G. Bonnet, “The Potts- q random matrix model: loop equations, critical exponents, and rational case,” *Phys. Lett. B* **463**, 273 (1999).
- [39] P. Zinn-Justin, “The dilute Potts model on random surfaces,” *J. Stat. Phys.* **98**, 245 (2000).
- [40] M. Gaudin and I. Kostov, “ $O(n)$ model on a fluctuating planar lattice: some exact results,” *Phys. Lett. B* **220**, 200 (1989).
- [41] I. K. Kostov, “ $O(n)$ vector model on a planar random lattice: spectrum of anomalous dimensions,” *Mod. Phys. Lett. A* **4**, 217 (1989).
- [42] B. Eynard and J. Zinn-Justin, “The $O(n)$ model on a random surface: critical points and large-order behaviour,” *Nucl. Phys. B* **386**, 558 (1992).
- [43] B. Eynard and C. Kristjansen, “Exact solution of the $O(n)$ model on a random lattice,” *Nucl. Phys. B* **455**, 577 (1995).
- [44] B. Eynard and C. Kristjansen, “More on the exact solution of the $O(n)$ model on a random lattice and an investigation of the case $|n| > 2$,” *Nucl. Phys. B* **466**, 463 (1996).
- [45] C. F. Baillie and D. A. Johnston, “The XY model coupled to two-dimensional quantum gravity,” *Phys. Lett. B* **291**, 233 (1992).
- [46] C. F. Baillie and D. A. Johnston, “A numerical test of KPZ scaling: Potts models coupled to two-dimensional quantum gravity,” *Mod. Phys. Lett. A* **7**, 1519 (1992).
- [47] C. F. Baillie, W. Janke, and D. A. Johnston, “Solid on solid on fluid lattices,” *Phys. Lett. B* **318**, 424 (1993).
- [48] C. F. Baillie and D. A. Johnston, “2D $O(3)$ + 2D QG,” *Phys. Rev. D* **49**, 603 (1994).
- [49] D. A. Johnston, “Ising (anti-)ferromagnet on dynamical triangulations and quadrangulations,” *Phys. Lett. B* **314**, 69 (1993).

- [50] J. Ambjørn, G. Thorleifsson, and M. Wexler, “New critical phenomena in 2d quantum gravity,” Nucl. Phys. B **439**, 187 (1995).
- [51] J. Ambjørn, J. Jurkiewicz, and Y. Watabiki, “On the fractal structure of two-dimensional quantum gravity,” Nucl. Phys. B **454**, 313 (1995).
- [52] M. Bowick, V. John, and G. Thorleifsson, “The Hausdorff dimension of surfaces in two-dimensional quantum gravity coupled to Ising minimal matter,” Phys. Lett. B **403**, 197 (1997).
- [53] F. David, “A scenario for the $c > 1$ barrier in non-critical bosonic strings,” Nucl. Phys. B **487**, 633 (1997).
- [54] J. Ambjørn, K. N. Anagnostopoulos, and R. Loll, “Crossing the $c = 1$ barrier in 2d Lorentzian quantum gravity,” Phys. Rev. D **61**, 044010 (2000).
- [55] R. J. Baxter, *Exactly Solved Models in Statistical Mechanics* (Academic Press, London, 1982).
- [56] E. H. Lieb and F. Y. Wu, “Two-dimensional ferroelectric models,” in *Phase Transitions and Critical Phenomena*, C. Domb and M. S. Green, eds., (Academic Press, London, 1972), Vol. 1, p. 331.
- [57] V. Pasquier, “Lattice derivation of modular invariant partition functions on the torus,” J. Phys. A **20**, L1229 (1987).
- [58] P. di Francesco, H. Saleur, and J.-B. Zuber, “Generalized Coulomb-gas formulation for two-dimensional critical models based on $SU(2)$ coset construction,” Nucl. Phys. B **300**, 393 (1988).
- [59] R. J. Baxter, “Eight-vertex model in lattice statistics,” Phys. Rev. Lett. **26**, 832 (1971).
- [60] R. J. Baxter, “Partition function of the eight-vertex lattice model,” Ann. Phys. (N.Y.) **70**, 193 (1972).
- [61] F. Rys, “Über ein zweidimensionales klassisches Konfigurations-Modell,” Helv. Phys. Acta **36**, 537 (1963).
- [62] E. H. Lieb, “Exact solution of the F model of an antiferroelectric,” Phys. Rev. Lett. **18**, 1046 (1967).

- [63] J. M. Kosterlitz and D. J. Thouless, "Ordering, metastability and phase transitions in two-dimensional systems," *J. Phys. C* **6**, 1181 (1973).
- [64] J. M. Kosterlitz, "The critical properties of the two-dimensional *XY* model," *J. Phys. C* **7**, 1046 (1974).
- [65] K. Binder and A. P. Young, "Spin glasses: Experimental facts, theoretical concepts, and open questions," *Rev. Mod. Phys.* **58**, 801 (1986).
- [66] *Spin Glasses and Random Fields*, A. P. Young, ed., (World Scientific, Singapore, 1997).
- [67] P. A. Lee and T. V. Ramakrishnan, "Disordered electronic systems," *Rev. Mod. Phys.* **57**, 287 (1985).
- [68] R. Albert and R.-L. Barabási, "Statistical mechanics of complex networks," *Rev. Mod. Phys.* **74**, 47 (2002).
- [69] A. B. Harris, "Effect of random defects on the critical behaviour of Ising models," *J. Phys. C* **7**, 1671 (1974).
- [70] M. Aizenmann and J. Wehr, "Rounding of first-order phase transitions in systems with quenched disorder," *Phys. Rev. Lett.* **62**, 2503 (1989).
- [71] J. M. Luck, "A classification of critical phenomena on quasi-crystals and other aperiodic structures," *Europhys. Lett.* **24**, 359 (1993).
- [72] P. Zinn-Justin, "The six-vertex model on random lattices," *Europhys. Lett.* **50**, 15 (2000).
- [73] I. Kostov, "Exact solution of the six-vertex model on a random lattice," *Nucl. Phys. B* **575**, 513 (2000).
- [74] C. F. Baillie and D. A. Johnston, "Square gravity," *Phys. Lett. B* **357**, 287 (1995).
- [75] J. Ambjørn, P. Bialas, J. Jurkiewicz, Z. Burda, and B. Petersson, "Effective sampling of random surfaces by baby universe surgery," *Phys. Lett. B* **325**, 337 (1994).

- [76] H. G. Evertz, “The loop algorithm,” in *Numerical Methods for Lattice Quantum Many-Body Problems*, D. J. Scalapino, ed., (Perseus Books, Cambridge, MA, 2000), p. 146.
- [77] P. A. M. Dirac, *Z. Phys. Sov. Union* **3**, 64 (1933).
- [78] R. P. Feynman, “Space-time approach to non-relativistic quantum mechanics,” *Rev. Mod. Phys.* **20**, 367 (1948).
- [79] H. Kleinert, *Path Integrals in Quantum Mechanics, Statistics, and Polymer Physics*, 2nd ed. (World Scientific, Singapore, 1995).
- [80] T. Goto, “Relativistic quantum mechanics of one-dimensional mechanical continuum and subsidiary condition of dual resonance model,” *Prog. Theor. Phys.* **46**, 1560 (1971).
- [81] L. Brink, P. di Vecchia, and O. Hove, “A locally supersymmetric and reparametrization invariant action for the spinning string,” *Phys. Lett. B* **65**, 471 (1976).
- [82] A. M. Polyakov, “Quantum geometry of bosonic strings,” *Phys. Lett. B* **103**, 207 (1981).
- [83] B. Hatfield, *Quantum Field Theory of Point Particles and Strings* (Addison-Wesley, Redwood City, 1992).
- [84] D. Schlingemann, “From Euclidean field theory to quantum field theory,” *Rev. Math. Phys.* **11**, 1151 (1999).
- [85] J. Ambjørn and R. Loll, “Non-perturbative Lorentzian quantum gravity, causality and topology change,” *Nucl. Phys. B* **536**, 407 (1998).
- [86] J. Ambjørn, J. Jurkiewicz, and R. Loll, “A non-perturbative Lorentzian path integral for gravity,” *Phys. Rev. Lett.* **85**, 924 (2000).
- [87] R. Loll, “Discrete Lorentzian quantum gravity,” *Nucl. Phys. B (Proc. Suppl.)* **94**, 96 (2001).
- [88] M. Nakahara, *Geometry, Topology and Physics* (Institute of Physics Publishing, Bristol, 1990).
- [89] H. M. Farkas and I. Kra, *Riemannian Surfaces* (Springer, Berlin, 1980).

- [90] A. Lasota and M. C. Mackey, *Chaos, Fractals and Noise — Stochastic Aspects of Dynamics* (Springer, Berlin, 1994).
- [91] P. Billingsley, *Convergence of Probability Measures* (Wiley, New York, 1968).
- [92] B. Simon, *Functional Integration and Quantum Physics* (Academic Press, New York, 1979).
- [93] T. Regge, “General relativity without coordinates,” *Nuovo Cimento* **19**, 558 (1961).
- [94] W. Beirl and B. A. Berg, “Is there quantum gravity in two dimensions?,” *Nucl. Phys. B* **452**, 415 (1995).
- [95] H. Hagura, “Dynamical Regge calculus as lattice gravity,” *Nucl. Phys. B (Proc. Suppl.)* **94**, 704–707 (2001).
- [96] G. Ponzano and T. Regge, “Semiclassical limit of Racah coefficients,” in *Spectroscopic and Group Theoretical Methods in Physics*, F. Bloch, S. G. Cohen, A. De-Shalit, S. Sambursky, and I. Talmi, eds., (North-Holland, Amsterdam, 1968), p. 1.
- [97] H. W. Hamber, “Simplicial quantum gravity,” In *1984 Les Houches Summer School, Session XLIII*, (North-Holland, Amsterdam, 1986).
- [98] H. W. Hamber and R. M. Williams, “Higher derivative quantum gravity on a simplicial lattice,” *Nucl. Phys. B* **248**, 392 (1984).
- [99] H. W. Hamber and R. M. Williams, “Erratum,” *Nucl. Phys. B* **260**, 747 (1985).
- [100] H. W. Hamber and R. M. Williams, “Simplicial quantum gravity with higher derivative terms: Formalism and numerical results in four dimensions,” *Nucl. Phys. B* **269**, 712 (1986).
- [101] W. Beirl, E. Gerstenmeyer, and H. Markum, “Influence of the measure on simplicial quantum gravity in four dimensions,” *Phys. Rev. Lett.* **59**, 713 (1992).
- [102] C. Holm and W. Janke, “Fixed versus random triangulations in 2D simplicial Regge calculus,” *Phys. Lett. B* **390**, 59 (1997).

- [103] H. W. Hamber, “Smooth and rough phases of quantized gravity,” Nucl. Phys. B (Proc. Suppl.) **30**, 751 (1993).
- [104] C. Holm and W. Janke, “Measuring the string susceptibility in 2D simplicial quantum gravity using the Regge approach,” Nucl. Phys. B **477**, 465 (1996).
- [105] C. Holm and W. Janke, “Ising spins on a gravitating sphere,” Phys. Lett. B **375**, 69 (1996).
- [106] W. Beirl, E. Gerstenmeyer, H. Markum, and J. Riedler, “The well-defined phase of simplicial quantum gravity in four dimensions,” Phys. Rev. D **49**, 5231 (1994).
- [107] M. E. Agishtein and A. A. Migdal, “Simulations of four-dimensional simplicial quantum gravity,” Mod. Phys. Lett. A **7**, 1039 (1992).
- [108] M. E. Agishtein and A. A. Migdal, “Critical behaviour of dynamically triangulated quantum gravity in four dimensions,” Nucl. Phys. B **385**, 395 (1992).
- [109] J. Ambjørn, B. Durhuus, J. Fröhlich, and P. Orland, “The appearance of critical dimensions in string theories,” Nucl. Phys. B **270**, 457 (1986).
- [110] J. Ambjørn, B. Durhuus, and J. Fröhlich, “The appearance of critical dimensions in string theories (II),” Nucl. Phys. B **275**, 161 (1986).
- [111] M. Carfora and M. Marzuoli, “Entropy estimates for simplicial quantum gravity,” J. Geom. and Phys. **16**, 9 (1995).
- [112] M. Carfora and M. Marzuoli, “Holonomy and entropy estimates for dynamically triangulated manifolds,” J. Math. Phys. **36**, 6353 (1995).
- [113] C. Bartoci, U. Bruzzo, M. Carfora, and M. Marzuoli, “Entropy of random coverings and 4-D quantum gravity,” J. Geom. and Phys. **18**, 247 (1996).
- [114] F. David, “Randomly triangulated surfaces in -2 dimensions,” Phys. Lett. B **159**, 303 (1985).
- [115] N. Kawamoto, V. A. Kazakov, Y. Saeki, and Y. Watabiki, “Fractal structure of two-dimensional gravity coupled to $c = -2$ matter,” Phys. Rev. Lett. **68**, 2113 (1992).

- [116] J. Ambjørn, K. N. Anagnostopoulos, T. Ichihara, L. Jensen, N. Kawamoto, Y. Watabiki, and K. Yotsuji, “The quantum space-time of $c = -2$ gravity,” Nucl. Phys. B **511**, 673 (1998).
- [117] B. Durhuus, J. Fröhlich, and T. Jonsson, “Critical behaviour in a model of planar random surfaces,” Nucl. Phys. B **240**, 453 (1984).
- [118] P. Bialas and Z. Burda, “Phase transition in fluctuating branched geometry,” Phys. Lett. B **384**, 75 (1996).
- [119] J. Jurkiewicz and A. Krzywicki, “Branched polymers with loops,” Nucl. Phys. B **392**, 291 (1997).
- [120] J. Ambjørn and B. Durhuus, “Regularized bosonic strings need extrinsic curvature,” Phys. Lett. B **118**, 253 (1987).
- [121] J. B. Hartle and S. W. Hawking, “Wave function of the universe,” Phys. Rev. D **28**, 2960 (1983).
- [122] J. Ambjørn, J. Jurkiewicz, and Y. M. Makeenko, “Multiloop correlators for two-dimensional quantum gravity,” Phys. Lett. B **251**, 517 (1990).
- [123] J. Ambjørn and Y. M. Makeenko, “Properties of loop equations for the Hermitian matrix model and for two-dimensional quantum gravity,” Mod. Phys. Lett. A **5**, 1753 (1990).
- [124] P. Ginsparg, “Matrix models of 2D gravity,” Lectures given July 22–25, 1991 at Trieste summer school, preprint hep-th/9112013.
- [125] M. Kaku, *Quantum Field Theory* (Oxford University Press, Oxford, 1993).
- [126] C. F. Baillie, W. Janke, D. A. Johnston, and P. Plecháč, “Spin glasses on thin graphs,” Nucl. Phys. B **450**, 730 (1995).
- [127] C. F. Baillie, N. Dorey, W. Janke, and D. A. Johnston, “The Villain model on thin graphs,” Phys. Lett. B **369**, 123 (1996).
- [128] D. Johnston and P. Plecháč, “Vertex models on Feynman diagrams,” Phys. Lett. A **248**, 37 (1998).

- [129] D. A. Johnston, J.-P. Kownacki, and A. Krzywicki, “Random geometries and real space renormalization group,” Nucl. Phys. B (Proc. Suppl.) **42**, 728 (1995).
- [130] Z. Burda, J.-P. Kownacki, and A. Krzywicki, “Towards a non-perturbative renormalization of Euclidean quantum gravity,” Phys. Lett. B **356**, 466 (1995).
- [131] J. Ambjørn, D. Boulatov, J. L. Nielsen, J. Rolf, and Y. Watabiki, “The spectral dimension of 2-d quantum gravity,” JHEP **9802**, 010 (1998).
- [132] N. Fukuma, N. Ishibashi, H. Kawai, and V. John, “Two-dimensional quantum gravity in temporal gauge,” Nucl. Phys. B **427**, 139 (1994).
- [133] N. Ishibashi and H. Kawai, “A background independent formulation of non-critical string theory,” Phys. Lett. B **352**, 75 (1995).
- [134] E. Brézin and V. A. Kazakov, “Exactly solvable field theories of closed strings,” Phys. Lett. B **236**, 144 (1990).
- [135] M. R. Douglas and S. H. Shenker, “Strings in less than one dimension,” Nucl. Phys. B **335**, 635 (1990).
- [136] D. J. Gross and A. Migdal, “Nonperturbative two-dimensional quantum gravity,” Phys. Rev. Lett. **64**, 127 (1990).
- [137] W. Janke and D. A. Johnston, “Ising and Potts models on quenched random gravity graphs,” Nucl. Phys. B **578**, 681 (2000).
- [138] W. Janke and D. A. Johnston, “Non-self averaging in autocorrelations for Potts models on quenched random gravity graphs,” J. Phys. A **33**, 2653 (2000).
- [139] J. Zinn-Justin, *Quantum Field Theory and Critical Phenomena* (Clarendon Press, Oxford, 1996).
- [140] W. Janke and D. A. Johnston, “The wrong kind of gravity,” Phys. Lett. B **460**, 271 (1999).
- [141] D. Friedan, Z. Qiu, and S. Shenker, “Conformal invariance, unitarity, and critical exponents in two dimensions,” Phys. Rev. Lett. **52**, 1575 (1984).
- [142] Y. Watabiki, “Analytic study of fractal structure of quantized surface in two-dimensional quantum gravity,” Prog. Theor. Phys. Suppl. **114**, 1 (1993).

- [143] N. Ishibashi and H. Kawai, “String field theory of $c \leq 1$ noncritical strings,” *Phys. Lett. B* **322**, 67 (1994).
- [144] J. Ambjørn and K. N. Anagnostopoulos, “Quantum geometry of 2-d gravity coupled to unitary matter,” *Nucl. Phys. B* **497**, 445 (1997).
- [145] V. A. Kazakov, “Exact solution of the Ising model on a random two-dimensional lattice,” *JETP Lett.* **44**, 133 (1986).
- [146] Z. Burda and J. Jurkiewicz, “Ising model on a random lattice with a topology of a torus,” *Phys. Lett. B* **214**, 425 (1988).
- [147] M. Bowick, S. Catterall, and G. Thorleifsson, “Minimal dynamical triangulations of random surfaces,” *Phys. Lett. B* **391**, 305 (1997).
- [148] V. A. Kazakov, M. Staudacher, and T. Wynter, “Exact solution of discrete two-dimensional R^2 gravity,” *Nucl. Phys. B* **471**, 309 (1996).
- [149] D. Bessis, C. Itzykson, and J. B. Zuber, “Quantum field theory techniques in graphical enumeration,” *Adv. Phys.* **1**, 109 (1980).
- [150] A. Khurana, “Planar diagrams — some enumerative results,” *J. Phys. A* **18**, 2415 (1985).
- [151] G. 't Hooft, “Counting planar diagrams with various restrictions,” *Nucl. Phys. B* **538**, 389 (1999).
- [152] A. Schneider and T. Filk, “On the universality of matrix models for random surfaces,” *Eur. Phys. J. C* **8**, 523 (1999).
- [153] K. Binder and D. W. Heermann, *Monte Carlo Simulation in Statistical Physics — An Introduction* (Springer, Berlin, 1988).
- [154] *Quantum Fields on the Computer*, M. Creutz, ed., (World Scientific, Singapore, 1992).
- [155] D. P. Landau and K. Binder, *A Guide to Monte Carlo Simulations in Statistical Physics* (Cambridge University Press, Cambridge, 2000).
- [156] M. Gross and S. Varsted, “Elementary moves and ergodicity in D -dimensional simplicial quantum gravity,” *Nucl. Phys. B* **378**, 367 (1992).

- [157] J. W. Alexander, “The combinatorial theory of complexes,” *Ann. Math.* **31**, 292 (1930).
- [158] V. Pachner, *Europ. J. Combinatorics* **12**, 129 (1991).
- [159] D. V. Boulatov and V. A. Kazakov, “Summing Feynman graphs by Monte Carlo: planar φ^3 -theory and dynamically triangulated random surfaces,” *Phys. Lett. B* **214**, 581 (1988).
- [160] M. E. Agishtein and A. A. Migdal, “Numerical study of two point correlation function and Liouville field properties in two-dimensional quantum gravity,” *Mod. Phys. Lett. A* **6**, 1863 (1991).
- [161] M. E. Agishtein and A. A. Migdal, “Geometry of two-dimensional quantum gravity: numerical study,” *Nucl. Phys. B* **350**, 690 (1991).
- [162] J. F. Wheeler, “The critical exponents of crystalline random surfaces,” *Nucl. Phys. B* **458**, 671 (1996).
- [163] M. G. Harris and J. F. Wheeler, “Multiple Ising spins coupled to 2d quantum gravity,” *Nucl. Phys. B* **427**, 111 (1994).
- [164] A. Gibbons, *Algorithmic Graph Theory* (Cambridge University Press, Cambridge, 1985).
- [165] J. M. Drouffe and C. Itzykson, “Random geometry and the statistics of two-dimensional cells,” *Nucl. Phys. B* **235**, 45 (1984).
- [166] S. Catterall, G. Thorleifsson, M. Bowick, and V. John, “Scaling and the fractal geometry of two-dimensional quantum gravity,” *Phys. Lett. B* **354**, 58 (1995).
- [167] G. Thorleifsson, “Three-dimensional simplicial gravity and degenerate triangulations,” *Nucl. Phys. B* **538**, 278 (1999).
- [168] U. Wolff, “Collective Monte Carlo updating for spin systems,” *Phys. Rev. Lett.* **62**, 361 (1989).
- [169] A. D. Sokal, “Bosonic algorithms,” in *Quantum Fields on the Computer*, M. Creutz, ed., (World Scientific, Singapore, 1992), p. 211.
- [170] S. Brandt, *Statistical and Computational Methods in Data Analysis*, 2nd ed. (North Holland, Amsterdam, 1976).

- [171] R. H. Swendsen and J.-S. Wang, "Nonuniversal critical dynamics in Monte Carlo simulations," *Phys. Rev. Lett.* **58**, 86 (1987).
- [172] J. Ambjørn, P. Bialas, Z. Burda, J. Jurkiewicz, and B. Petersson, "Search for scaling dimensions for random surfaces with $c = 1$," *Phys. Lett. B* **342**, 58 (1995).
- [173] D. A. Lavis and G. M. Bell, *Statistical Mechanics of Lattice Systems 1 — Closed-Form and Exact Solutions*, 2nd ed. (Springer, Berlin, 1999).
- [174] H. G. Evertz, G. Lana, and M. Marcu, "Cluster algorithm for vertex models," *Phys. Rev. Lett.* **70**, 875 (1993).
- [175] J. C. Slater, "Theory of the transition in KH_2PO_4 ," *J. Chem. Phys.* **9**, 16 (1941).
- [176] E. H. Lieb, "Residual entropy of square ice," *Phys. Rev.* **162**, 162 (1967).
- [177] B. Sutherland, "Two-dimensional hydrogen bonded crystals without the ice rule," *J. Math. Phys.* **11**, 3183 (1970).
- [178] C. Fan and F. Y. Wu, "General lattice model of phase transitions," *Phys. Rev. B* **2**, 723 (1970).
- [179] E. H. Lieb, "Exact solution of the two-dimensional Slater KDP model of a ferroelectric," *Phys. Rev. Lett.* **19**, 108 (1967).
- [180] B. Sutherland, "Exact solution of a two-dimensional model for hydrogen-bonded crystals," *Phys. Rev. Lett.* **19**, 103 (1967).
- [181] M. Suzuki, "New universality of critical exponents," *Prog. Theor. Phys.* **51**, 1992 (1974).
- [182] C. Fan and F. Y. Wu, "Ising model with second-neighbour interactions. I. Some exact results and an approximate solution," *Phys. Rev.* **179**, 560 (1969).
- [183] J. E. Hirsch, R. L. Sugar, D. J. Scalapino, and R. Blankenbecler, "Monte Carlo simulations of one-dimensional fermion systems," *Phys. Rev. B* **26**, 5033 (1982).
- [184] H. F. Trotter, *Proc. Am. Math. Soc.* **10**, 545 (1959).

- [185] M. Suzuki, "Relationship between d -dimensional quantal spin systems and $(d+1)$ -dimensional Ising systems. Equivalence, critical exponents and systematic approximants of the partition function and spin correlations," *Prog. Theor. Phys.* **46**, 1337 (1971).
- [186] D. Kandel and E. Domany, "General cluster Monte Carlo dynamics," *Phys. Rev. B* **43**, 8539 (1991).
- [187] N. Kawashima and J. E. Gubernatis, "Dual Monte Carlo and cluster algorithms," *Phys. Rev. E* **51**, 1547 (1995).
- [188] H. G. Evertz and M. Marcu, "The loop-cluster algorithm for the case of the 6 vertex model," *Nucl. Phys. B (Proc. Suppl.)* **30**, 277 (1993).
- [189] H. G. Evertz and M. Marcu, "Vertex models and quantum spin systems: a nonlocal approach," in *Computer Simulations in Condensed Matter Physics VI*, D. P. Landau, K. K. Mon, and H. B. Schüttler, eds., (Springer, Berlin, 1993), p. 109.
- [190] R. G. Edwards and A. D. Sokal, "Generalization of the Fortuin-Kasteleyn-Swendsen-Wang representation and Monte Carlo algorithm," *Phys. Rev. D* **38**, 2009 (1988).
- [191] C. M. Fortuin and P. W. Kasteleyn, "On the random-cluster model: I. Introduction and relation to other models," *Physica* **57**, 536 (1972).
- [192] M. Weigel, W. Janke, and C.-K. Hu, "Random-cluster multihistogram sampling for the q -state Potts model," *Phys. Rev. E* **65**, 036109 (2002).
- [193] W. Janke, "Monte Carlo simulations of spin systems," in *Computational Physics*, K. H. Hoffmann and M. Schreiber, eds., (Springer, Berlin, 1996), p. 10.
- [194] S. Skiena, *Implementing Discrete Mathematics: Combinatorics and Graph Theory With Mathematica* (Perseus Books, Cambridge, MA, 1990).
- [195] O. Foda and B. Nienhuis, "The Coulomb gas representation of critical RSOS models on the sphere and the torus," *Nucl. Phys. B* **324**, 643 (1989).
- [196] B. Nienhuis, "Coulomb gas formulation of two-dimensional phase transitions," in *Phase Transitions and Critical Phenomena*, C. Domb and J. L. Lebowitz, eds., (Academic Press, London, 1987), Vol. 11, p. 1.

- [197] M. Aizenmann and B. Nachtergaele, “Geometric aspects of quantum spin states,” *Comm. Math. Phys.* **164**, 17 (1994).
- [198] J. Kondev and C. L. Henley, “Kac-Moody symmetries of critical ground states,” *Nucl. Phys. B* **464**, 540 (1996).
- [199] A. A. Belavin, A. M. Polyakov, and A. B. Zamolodchikov, “Infinite conformal symmetry in two-dimensional quantum field theory,” *Nucl. Phys. B* **241**, 333 (1984).
- [200] J. L. Cardy, “Conformal invariance,” in *Phase Transitions and Critical Phenomena*, C. Domb and J. L. Lebowitz, eds., (Academic Press, London, 1987), Vol. 11, p. 55.
- [201] M. Henkel, *Conformal Invariance and Critical Phenomena* (Springer, Berlin/Heidelberg/New York, 1999).
- [202] D. A. Huse, “Exact exponents of infinitely many new multicritical points,” *Phys. Rev. B* **30**, 3908 (1984).
- [203] G. E. Andrews, R. J. Baxter, and P. Forrester, “Eight vertex SOS model and generalized Rogers-Ramanujan type identities,” *J. Stat. Phys.* **35**, 193 (1984).
- [204] V. Pasquier, “Two-dimensional critical systems labelled by Dynkin diagrams,” *Nucl. Phys. B* **285**, 162 (1987).
- [205] P. di Francesco, P. Mathieu, and D. Sénéchal, *Conformal Field Theory* (Springer, Berlin, 1997).
- [206] V. G. Kac, *Infinite Dimensional Lie Algebras*, 2nd ed. (Cambridge University Press, Cambridge, 1985).
- [207] V. Pasquier, “Operator content of the ADE lattice models,” *J. Phys. A* **20**, 5707 (1987).
- [208] V. S. Dotsenko, J. L. Jacobsen, and M. Picco, “Classification of conformal field theories based on Coulomb gases. Application to loop models,” *Nucl. Phys. B* **618**, 523 (2001).
- [209] J. Villain, “Theory of one- and two-dimensional magnets with an easy magnetization plane. II. The planar, classical, two-dimensional magnet,” *J. Physique* **36**, 581 (1975).

- [210] W. Janke and K. Nather, “High-precision Monte Carlo study of the two-dimensional XY Villain model,” *Phys. Rev. B* **48**, 7419 (1993).
- [211] W. Janke, “Logarithmic corrections in the two-dimensional XY model,” *Phys. Rev. B* **55**, 3580 (1997).
- [212] H. J. F. Knops, “Exact relation between the solid-on-solid model and the XY model,” *Phys. Rev. Lett.* **39**, 766 (1977).
- [213] R. Savit, “Duality in field theory and statistical systems,” *Rev. Mod. Phys.* **52**, 453 (1980).
- [214] H. van Beijeren, “Exactly solvable model for the roughening transition of a crystal surface,” *Phys. Rev. Lett.* **38**, 993 (1977).
- [215] M. den Nijs, “Extended scaling relations for the magnetic critical exponents of the Potts model,” *Phys. Rev. B* **27**, 1674 (1983).
- [216] S. O. Warnaar, B. Nienhuis, and K. A. Seaton, “New construction of solvable lattice models including an Ising model in a field,” *Phys. Rev. Lett.* **69**, 710 (1992).
- [217] E. Domany, M. Schick, J. S. Walker, and R. B. Griffith, “Classification of continuous order-disorder transitions in adsorbed monolayers,” *Phys. Rev. B* **18**, 2209 (1981).
- [218] B. Nienhuis, “Exact critical point and critical exponents of $O(n)$ models in two dimensions,” *Phys. Rev. Lett.* **49**, 1062 (1982).
- [219] J. L. Jacobsen and J. Kondev, “Field theory of compact polymers on the square lattice,” *Nucl. Phys. B* **532**, 635 (1998).
- [220] J. Kondev, J. de Gier, and B. Nienhuis, “Operator spectrum and exact exponents of the fully packed loop model,” *J. Phys. A* **29**, 6489 (1996).
- [221] I. Kostov, “The ADE face models on a fluctuating planar lattice,” *Nucl. Phys. B* **326**, 583 (1989).
- [222] I. K. Kostov, “Strings with discrete target space,” *Nucl. Phys. B* **376**, 539 (1992).

- [223] I. Kostov, “Gauge invariant matrix model for the \hat{A} - \hat{D} - \hat{E} closed strings,” *Phys. Lett. B* **297**, 74 (1992).
- [224] I. Kostov and M. Staudacher, “Multicritical phases of the $O(n)$ model on a random lattice,” *Nucl. Phys. B* **384**, 459 (1992).
- [225] R. J. Baxter, “Equivalence of the Potts model or Whitney polynomial with an ice-type model,” *J. Phys. A* **9**, 397 (1976).
- [226] S. Dalley, “The Weingarten model à la Polyakov,” *Mod. Phys. Lett. A* **7**, 1651 (1992).
- [227] D. J. Gross and I. R. Klebanov, “One-dimensional string theory on a circle,” *Nucl. Phys. B* **344**, 475 (1990).
- [228] D. J. Gross and I. R. Klebanov, “Vortices and the nonsinglet sector of the $c = 1$ matrix model,” *Nucl. Phys. B* **354**, 459 (1990).
- [229] S. Dalley, “The Kosterlitz-Thouless phenomenon on a fluid random surface,” *Nucl. Phys. B* **422**, 605 (1994).
- [230] D. Johnston, “Symmetric vertex models on planar random graphs,” *Phys. Lett. B* **463**, 9 (1999).
- [231] V. A. Kazakov and P. Zinn-Justin, “Two-matrix model with ABAB interaction,” *Nucl. Phys. B* **546**, 647 (1999).
- [232] V. L. Berezinskii, “Destruction of long-range order in one-dimensional and two-dimensional systems with a continuous symmetry group. II. Quantum systems,” *Zh. Eksp. Teor. Fiz.* **61**, 1144 (1971).
- [233] N. D. Mermin and H. Wagner, “Absence of ferromagnetism or antiferromagnetism in one- or two-dimensional isotropic Heisenberg models,” *Phys. Rev. Lett.* **17**, 1133 (1966).
- [234] P. C. Hohenberg, “Existence of long-range order in one and two dimensions,” *Phys. Rev.* **158**, 383 (1967).
- [235] C. Itzykson and J.-M. Drouffe, *Statistical Field Theory* (Cambridge University Press, Cambridge, 1989).

- [236] M. E. Barber, “Finite-size scaling,” in *Phase Transitions and Critical Phenomena*, C. Domb and J. L. Lebowitz, eds., (Academic Press, New York, 1983), Vol. 8, p. 146.
- [237] R. Gupta, J. DeLapp, G. G. Batrouni, G. C. Fox, C. F. Baillie, and J. Apostolakis, “Phase transition in the 2D XY model,” *Phys. Rev. Lett.* **61**, 1996 (1988).
- [238] U. Wolff, “Collective Monte Carlo updating in a high precision study of the x - y model,” *Nucl. Phys. B* **322**, 759 (1989).
- [239] R. G. Edwards, J. Goodman, and A. D. Sokal, “Multigrid Monte-Carlo. II. 2-dimensional XY -model,” *Nucl. Phys. B* **354**, 289 (1991).
- [240] D. J. Amit, Y. Y. Goldschmidt, and S. Grinstein, “Renormalisation group analysis of the phase transition in the 2D Coulomb gas, Sine-Gordon theory and XY -model,” *J. Phys. A* **13**, 585 (1980).
- [241] L. P. Kadanoff and A. B. Zisook, “Correlation functions on the critical line of the two-dimensional planar model: logarithms and corrections to scaling,” *Nucl. Phys. B* **180**, 61 (1981).
- [242] R. J. Baxter, “Spontaneous staggered polarization of the F model,” *Phys. Rev. B* **1**, 2199 (1970).
- [243] R. J. Baxter, “Exact isotherm for the F model in direct and staggered electric fields,” *Phys. Rev. B* **1**, 2199 (1970).
- [244] G. Mazzeo, G. Jug, A. C. Levi, and E. Tosatti, “Sublattice order parameter in the BCSOS model: a finite-size Monte Carlo study,” *J. Phys. A* **25**, L967 (1992).
- [245] M. Hasenbusch, M. Marcu, and K. Pinn, “High precision verification of the Kosterlitz-Thouless scenario,” preprint hep-lat/9207019 (unpublished).
- [246] A. C. Levi and M. Kotrla, “Theory and simulation of crystal growth,” *J. Phys.: Condens. Matter* **9**, 299 (1997).
- [247] J. Ambjørn, P. Bialas, and J. Jurkiewicz, “Connected correlators in quantum gravity,” *JHEP* **9902**, 005 (1999).

- [248] J. Jurkiewicz, A. Krzywicki, B. Petersson, and S. Söderberg, “Ising spins on a dynamically triangulated random surface,” *Phys. Lett. B* **213**, 511 (1988).
- [249] J. Ambjørn, K. N. Anagnostopoulos, T. Ichihara, L. Jensen, N. Kawamoto, Y. Watabiki, and K. Yotsuji, “Quantum geometry of topological gravity,” *Phys. Lett. B* **397**, 177 (1997).
- [250] J. Ambjørn, K. N. Anagnostopoulos, and G. Thorleifsson, “The quantum spacetime of $c > 0$ 2d gravity,” *Nucl. Phys. B (Proc. Suppl.)* **63**, 742 (1998).
- [251] P. di Francesco, H. Saleur, and J.-B. Zuber, “Critical Ising correlation functions in the plane and on the torus,” *Nucl. Phys. B* **290**, 527 (1987).
- [252] L. P. Kadanoff and A. C. Brown, “Correlation functions on the critical lines of the Baxter and Ashkin-Teller models,” *Ann. Phys. (N.Y.)* **121**, 318 (1979).
- [253] H. J. F. Knops and L. W. J. den Ouden, “Renormalization connection between eight-vertex operators and Gaussian operators,” *Ann. Phys. (N.Y.)* **138**, 155 (1982).
- [254] F. C. Alcaraz, M. N. Barber, and M. T. Batchelor, “Conformal invariance, the XXZ chain and the operator content of two-dimensional critical systems,” *Ann. Phys. (N.Y.)* **182**, 280 (1988).
- [255] A. Klümper, T. Wehner, and J. Zittartz, “Conformal spectrum of the six-vertex model,” *J. Phys. A* **26**, 2815 (1993).
- [256] S. Catterall, J. B. Kogut, and R. L. Renken, “The XY model on a dynamical random lattice,” *Nucl. Phys. B* **408**, 427 (1993).
- [257] M. Hasenbusch, G. Lana, M. Marcu, and K. Pinn, “Cluster algorithm for a solid-on-solid model with constraints,” *Phys. Rev. B* **46**, 10472 (1992).
- [258] J. Ambjørn, S. Jain, and G. Thorleifsson, “Baby universes in 2-d quantum gravity,” *Phys. Lett. B* **307**, 34 (1993).
- [259] C. F. Baillie and D. A. Johnston, “Multiple Potts models coupled to two-dimensional quantum gravity,” *Phys. Lett. B* **286**, 44 (1992).
- [260] F. Markopoulou and L. Smolin, “Causal evolution of spin networks,” *Nucl. Phys. B* **508**, 409 (1997).

- [261] J. Ambjørn, K. N. Anagnostopoulos, and R. Loll, “On the phase diagram of 2d Lorentzian Quantum Gravity,” Nucl. Phys. B (Proc. Suppl.) **83**, 733 (2000).
- [262] M. Fisz, *Wahrscheinlichkeitsrechnung und Mathematische Statistik* (Deutscher Verlag der Wissenschaften, Berlin, 1989).
- [263] O. Narayan and A. P. Young, “Convergence of Monte Carlo simulations to equilibrium,” Phys. Rev. E **64**, 021104 (2001).
- [264] N. Metropolis, A. W. Rosenbluth, M. N. Rosenbluth, A. H. Teller, and E. Teller, “Equation of state calculations by fast computing machines,” J. Chem. Phys. **21**, 1087 (1953).
- [265] M. B. Priestley, *Spectral Analysis and Time Series* (Academic Press, London, 1996).
- [266] A. D. Sokal and L. E. Thomas, “Exponential convergence to equilibrium for a class of random walk models,” J. Stat. Phys. **54**, 797 (1989).
- [267] N. Madras and A. D. Sokal, “The Pivot algorithm: a highly efficient Monte Carlo method for selfavoiding walk,” J. Stat. Phys. **50**, 109 (1988).
- [268] T. W. Anderson, *The Statistical Analysis of Time Series* (Wiley, New York, 1994).
- [269] H. Flyvbjerg and H. G. Petersen, “Error estimates on averages of correlated data,” J. Chem. Phys. **91**, 461 (1989).
- [270] B. Efron, *The Jackknife, the Bootstrap and Other Resampling Plans* (Society for Industrial and Applied Mathematics [SIAM], Philadelphia, 1982).
- [271] B. Efron and R. J. Tibshirani, *An Introduction to the Bootstrap* (Chapman and Hall, Boca Raton, 1998).
- [272] B. A. Berg, “Double jackknife bias corrected estimators,” Comput. Phys. Commun. **69**, 7 (1992).
- [273] M. Weigel and W. Janke, “Universal amplitudes in the finite-size scaling of three-dimensional spin models,” Phys. Rev. Lett. **82**, 2318 (1999).

- [274] M. Weigel and W. Janke, “Monte Carlo study of the scaling of universal correlation lengths in three-dimensional $O(n)$ spin models,” *Phys. Rev. B* **62**, 6343 (2000).
- [275] A. M. Ferrenberg and R. H. Swendsen, “New Monte Carlo technique for studying phase transitions,” *Phys. Rev. Lett.* **61**, 2635 (1988).
- [276] A. M. Ferrenberg and R. H. Swendsen, “New Monte Carlo technique for studying phase transitions,” *Phys. Rev. Lett.* **63**, 1658(E) (1989).
- [277] <http://www.opengl.org>.
- [278] R. E. Tarjan and J. Hopcroft, “Efficient planarity testing,” *J. ACM* **21**, 549 (1974).
- [279] R. Sedgewick, *Algorithms in C++* (Addison-Wesley, Reading, Mass., 1992).

Acknowledgements

The research reported in this thesis was funded by a Ph.D. fellowship of the “Graduiererkolleg Quantum Field Theory” of the DFG. International exchange and participation in conferences related to the subject of this thesis were supported by the DAAD through the research grant 313-ARC-XII-98/41, the EC network HPRN-CT-1999-000161 “Discrete Random Geometries: From Solid State Physics to Quantum Gravity” and the ESF network “Geometry and Disorder: From Membranes to Quantum Gravity”.

Concerning the scientific content of this thesis, my thanks in the first place are due to my Ph.D. supervisor Wolfram Janke for the numerous discussions in the last years and his constant interest in the progress of this thesis. However tight his schedule was, he could always spare the time for a chat about scientific or personal issues. I also acknowledge fruitful discussions about problems related to the work presented in this thesis with P. Bialas, Z. Burda, D. A. Johnston and V. A. Kazakov. I am thankful to my colleagues at the ITP for the stimulating and homely atmosphere.

For insisting on the belief that there is a non-scientific part of life I would like to thank my singing and drinking colleagues Holger, Michael, Niels, Robert, Thomas, Torsten and Tina. I am deeply indebted to my parents and my sister, who supported me financially, mentally and emotionally through all the years of my growing-up and education and thus allowed me to come to this point. Finally, I thank my love Daniela for existing and having so much understanding for an apparent imbalance between working and private life.

Curriculum Vitae

Personal Details

Name	Martin Weigel
Date of birth	September 06, 1972
Place of birth	Neustadt a. d. Weinstraße
Nationality	German
Marital status	unmarried, no children
Address	Paul-List-Str. 18, 04103 Leipzig, Germany
Telephone	+49-341-21 222 71
E-mail	Martin.Weigel@itp.uni-leipzig.de

Education

08.1979 – 06.1983	basic school Bornheim/Dammheim
08.1983 – 06.1992	high-school “Max-Slevogt” Landau, degree “Abitur” with overall grade 1.0
10.1992 – 03.1998	study of physics at the University “Johannes-Gutenberg” Mainz
03.1997 – 03.1998	diploma thesis on “ <i>Numerical tests of conjectures of conformal field theory for three-dimensional systems</i> ” in the condensed matter theory group, supervisor: Prof. Dr. K. Binder
03.1998	finals with overall grade “sehr gut” (excellent)
03.1995 – 03.1998	philosophy and business science studies at Mainz University

Ph.D. Study

since 05.1998	graduate studies at the University of Leipzig, Ph.D. thesis on “ <i>Vertex models on random graphs</i> ” in the computer-oriented quantum-field theory group, supervisor: Prof. Dr. W. Janke
---------------	---